Wave breaking at high wind speeds and its effects on air-sea gas transfer

Sophia E. Brumer

Submitted in partial fulfillment of the

requirements for the degree

of Doctor of Philosophy

in the Graduate School of Arts and Sciences

Columbia University

2017

Abstract

Wave breaking at high wind speeds and its effect on air-sea gas transfer

Sophia E. Brumer

Gravity waves are ubiquitous at the surface of the ocean and play a key role in the coupled ocean-atmosphere system. These wind generated waves, for which gravity provides the restoring force, influence the kinematics and dynamics of the upper ocean and lower atmosphere. Their breaking injects turbulence into the upper ocean, generates bubble plumes and sea-spray thus transferring energy, momentum, heat and mass between the atmosphere and the ocean. In the anthropocene, with CO_2 driving the warming trend and the ocean acting as the main carbon sink, it is imperative to understand the complex physical controls of air-sea gas transfer. Large uncertainties still remain under high wind speed conditions where wave breaking processes are dominant. This dissertation seeks to shed light onto the dependence of wave breaking and air-sea gas transfer on environmental parameters. It further explores process based models of air-sea gas transfer that explicitly account for the breaking related processes.

Air entraining breaking waves are easily detectable as bright features on the ocean surface composed of foam and subsurface bubble plumes. These features, termed whitecaps, arise at wind speed as as low as 3 m s^{-1}. The whitecap coverage (W) has been recognized as a

useful proxy for quantifying wave breaking related processes. It can be determined from shipboard, air-borne and satellite remote sensing. W is most commonly parameterized as a function of wind speed, but previous parameterizations display over three orders of magnitude scatter. Concurrent wave field and flux measurements acquired during the Southern Ocean Gas Exchange (SO GasEx) and the High Wind Gas exchange Study (HiWinGS) projects permitted evaluation of the dependence of W on wind speed, wave age, wave steepness, mean square slope, as well as on wave-wind and breaking Reynolds numbers. W was determined from over 600 high frequency visible imagery recordings of 20 minutes each. Wave statistics were computed from in situ and remotely sensed data as well as from a WAVEWATCH-III® hind cast. The first ship-borne estimates of W under sustained wind speeds (U_{10N}) of 25 m s^{-1} were obtained during HiWinGS. These measurements suggest that W levels off at high wind speed, not exceeding 10% when averaged over 20 minutes. Combining wind speed and wave height in the form of the wave-wind Reynolds number resulted in closely agreeing models for both datasets, individually and combined. These are also in good agreement with two previous studies. When expressing W in terms of wave field statistics only or wave age, larger scatter is observed and/or there is little agreement between SO GasEx, HiWinGS, and previously published data. The wind–speed-only parameterizations deduced from the SO GasEx and HiWinGS datasets agree closely and capture more of the observed W variability than Reynolds number parameterizations. However, these wind-speed-only models do not agree as well with previous studies than the wind-wave Reynolds numbers.

The ability to quantify air-sea gas transfer hinges on parameterizations of the gas transfer velocity k. k represents physical mass transfer mechanisms and is usually parameterized as a non-linear function of wind forcing. Previous eddy-covariance measurements and models based on the global radio carbon inventory led to diverging parameterizations with both cubic and quadratic wind speed dependence. At wind speeds above 10 m s^{-1} these parameterizations differ considerably and measurements display large scatter. In an attempt to reduce uncertainties in k, explored empirical parameterizations that incorporate both

wind speed and sea state dependence via breaking and wave-wind Reynolds numbers, were explored. Analysis of concurrent eddy covariance gas transfer and measured wave field statistics supplemented by wave model hindcasts shows for the first time that wave-related Reynold numbers collapse four open ocean datasets that have a wind speed dependence of CO_2 transfer velocity ranging from lower than quadratic to cubic. Wave-related Reynolds number and wind speed show comparable performance for parametrizing DMS which, because of its higher solubility, is less affected by bubble-mediated exchange associated with wave breaking.

While single parameter models may be readily used in climate studies, their application is gas specific and may be limited to select environments. Physically based parameterizations that incorporate multiple forcing factors allow to model the gas transfer of gases with differing solubility for a wide range of environmental conditions. Existing mechanistic models were tested and a novel framework to model gas transfer in the open ocean in the presence of breaking waves is put forward. This analysis allowed to update NOAA's Coupled Ocean-Atmosphere Response Experiment Gas transfer algorithm (COAREG) and exposed limitation of other existing physically based parameterizations. The newly proposed mechanistic model incorporates both the turbulence and bubble mediated transfer. It is based on various statistics determined from the breaking crest length distribution ($\Lambda(c)$). $\Lambda(c)$ was obtained by tracking the advancing front of breaking waves in the high frequency videos taken during HiWinGS. Testing the mechanistic model with the HiWinGS dataset shows promising results for both CO_2 and DMS, though it does not perform better than COAREG. Uncertainties remain in the quantification of bubble cloud which are at the core of the formulation of the bubble mediated transfer and additional field measurements are necessary to characterize bubble plume properties in the open ocean.

Table of Contents

List of Figures

List of Tables

Acknowledgments

I have had the pleasure to interact and work with many people during my graduate studies whom I wish to recognize here. My advisor, Christopher Zappa, deserves a special mention for exposing me to a wide variety of projects all of which greatly contributed to my comprehension of the field. I am grateful for these opportunities and thank you for teaching me the importance of self-reliance. I would equally like to thank Adam Sobel and Arnold Gordon for their unequivocal encouragement and support as committee members. To my external committee members Jim Edson and Bill Asher, thank you for thoroughly reviewing this dissertation, for providing useful feedback and for the insightful discussion during the defense.

Mike Banner who shared my office a couple of months a year discussing wave breaking physics, theater, music, and current affairs. I am grateful for your guidance throughout and your continuous interest in my professional development.

A big thank you to John Dugan who led the RIDE experiment which became my first project at Lamont and whom I wish could have been around to mentor me longer. Steven Anderson, also from Areté Associates, with whom I continue to enjoy working on the RIDE dataset.

I owe a tremendous amount of gratitude to the HiWinGS team and my co-authors: Ian Brooks, Byron Blomquist, Chris Fairall, Barry Huebert, Ming-Xi Yang, Ludovic Bariteau, Helen Czerski, Adrian Matei, Robin Pascal and everyone else working on HiWinGS. It was a pleasure looking for bad weather at sea with you. Thank you for your continuous input and critical review of my manuscripts.

To the rest of the air-sea interactions team at Lamont (past and present): Scott Brown, Deb LeBel, Carson Witte, Una Miller, Tae Siek Rhee, and Daniel Kiefhaber thank you for your assistance with instrumentation and analysis, for all the fruitful discussions, and for the laughs.

Let's not forget the usual suspects. Maman, Papa, Anna, Irène, Ioan et les petites, merci. You provided me with unfailing support, guidance and continuous encouragement and I would

have not have made it so far without you. Ramón, no words would do justice to the role you played. Know that I am grateful to you and your family.

Asmi, Winnie, and Anirban, we will always have Ithaca. Your friendship made my time here much sweeter. Claudia, thank you for always leaving your door open for me. Catherine, Angel, and Julius for the company in class and beyond. Nora, Etienne, Tarini, and Nandini the lunches behind the cafe were always fun.

My graduate work was supported by the National Science Foundation, the Office of Naval Research, and the department of Earth and Environmental Sciences of the Graduate School of Arts and Sciences. The UNOLS organization provided the ships for our experiments. The captain and crew of the *R/V Knorr* deserve a special mention for facilitating our research in rough seas.

À ma famille,

Chapter 1

Introduction

1.1 The Big Picture

In the current age of anthropogenic climate change, it is imperative to reduce uncertainties in climate predictions to allow for sound mitigation and adaptation guidelines. Poor understanding of the complex physical controls of air-sea exchanges under high winds, in particular with respect to the uptake and release of greenhouse gases and particulate material (aerosols and pollutants), remains a source of uncertainties in biogeochemical models and climate predictions. Greenhouse gases trap the thermal radiation leaving the Earth's surface, thereby warming the lower atmosphere. They are responsible for keeping the averaged surface air temperature above freezing thus permitting life on Earth as we know it. Carbon dioxide (CO_2) is the most important greenhouse gas besides water vapor. This is not because of its greenhouse potential per molecule, but rather on account of its abundance [*Myhre et al.*, 2013]. Its atmospheric concentration has risen drastically, from $\sim$ 275 ppm to over 400 ppm, since the industrial revolution in the 18^{th} century (Figure 1.1) and has resulted in radiative warming leading to global climate change.

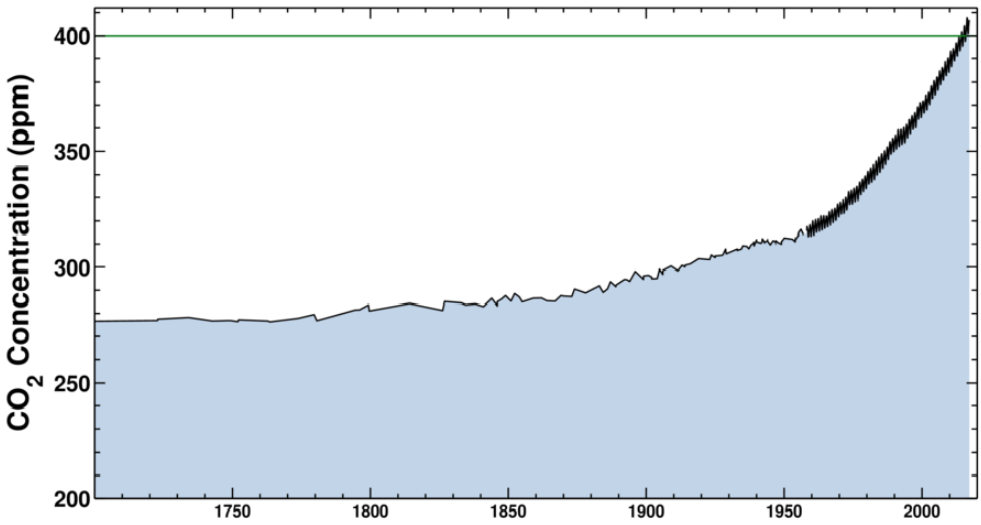

Figure 1.1: Atmospheric CO_2 concentrations 1700-present. Data pre 1985 is estimated from ice-cores. Concentrations from 1985 to present are measured at the Mauna Loa Observatory. Due to human-produced emissions, CO_2 levels in Earth's atmosphere have been rapidly rising since the beginning of the Industrial Revolution and nowadays are crossing 400 ppm (400.01 ppm on 25 May 2013), equaling a 44% increase when compared to pre-industrial CO_2 concentrations of around 275 ppm. The green horizontal line indicates the level on 01 March 2017: 406.78 ppm. Source: Scripps Institution of Oceanography (https://scripps.ucsd.edu/programs/keelingcurve/).

1.1.1 CO_2

While some of the CO_2 is produced naturally, the observed increased is human-induced. It is the result of fossil fuel burning, land use changes and cement production [*Boden et al.*, 2011; *Houghton*, 1999]. A simplified version of the global carbon cycle is shown in Figure 1.2, illustrating the sizes of the different carbon reservoirs and fluxes. Taking up ∼25% of the emitted anthropogenic CO_2, the ocean acts as the main carbon sink [*Archer*, 2005]. It has an overall larger carbon inventory than the land biosphere with both abiotic inorganic and biological cycling mechanisms at play. As CO_2 enters the ocean it dissolves into carbonic acid (H_2CO_3) most of which disassociate into bicarbonate (HCO_3^-) and carbonate (CO_3^{2-}). This disassociation results in the release of hydrogen ions which increase ocean acidity with devastating consequences for oceanic ecosystems. As CO_2 reacts with water, only a small fraction remains as dissolved CO_2 within the surface ocean. The ocean thus has a natural buffering capacity. However, as the ocean becomes more acidic, seawater will become less

effective in disassociation CO_2. The chemical enhancement of the rate of transfer of CO_2 across the air-sea interface resulting from its dissolution and dissociation is thought to be minimal and only be important in low turbulent, high pH (basic) conditions [*Wanninkhof and Knox*, 1996].

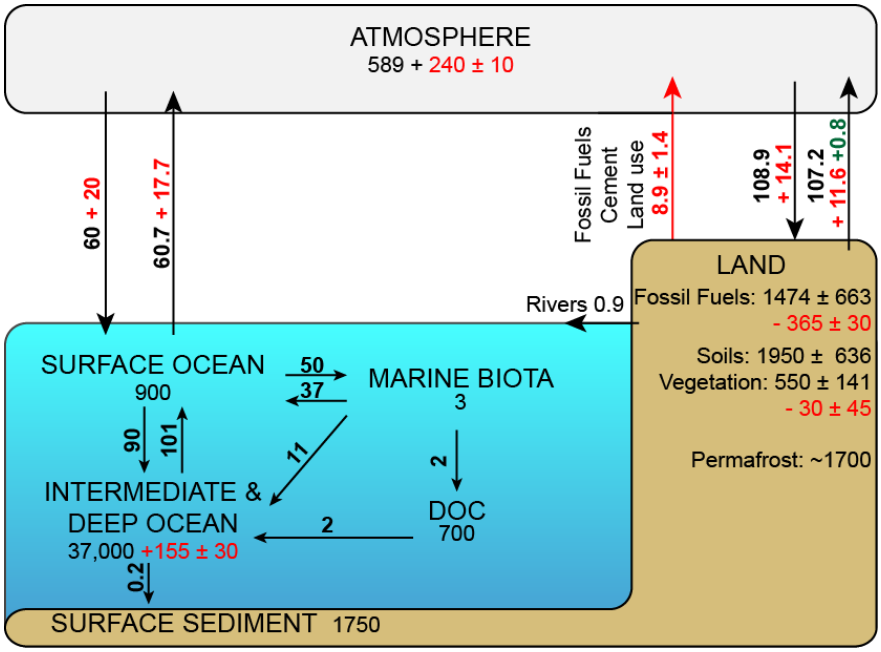

Figure 1.2: Simplified illustration of the global carbon cycle, adapted from *Ciais et al.* [2013]. Reservoir mass numbers and annual exchange fluxes are given in PgC (1015 gC) and PgC yr^{-1}, respectively. Black numbers refer to pre-industrial values (before 1750). Red flux numbers represent annual anthropogenic fluxes averaged over the years 2000–2009 and red reservoir numbers depict cumulative changes of anthropogenic carbon between 1750 and 2011 (90% confidence interval).

Dissolved inorganic carbon (DIC) is transported in the ocean as a tracer by the meridional overturning circulation. As the solubility of CO_2 increases with decreasing temperature, cold high latitude waters typically absorb CO_2 and DIC is subducted in deep water formation regions. Conversely, DIC is upwelled in equatorial waters and CO_2 is released to the atmosphere in warm tropical regions. This pathway by which carbon is transported between the surface and the deep ocean is known as the solubility pump. Other important mechanisms controlling the inventory of carbon in the ocean are the biological pumps [*Volk and Hoffert*, 1985]. The organic carbon pump involves uptake of DIC by biota in the euphotic surface waters; via photosynthesis they produce particulate and dissolved organic carbon (POC

and DOC). As POC sinks through the water column, some is re-mineralized, some enters the marine food web and a fraction may reach the seafloor becoming marine sediments. The $CaCO_3$ counter pump involves the formation of calcium carbonate ($CaCO_3$) shells and skeletons by marine organisms in surface waters. This process uses up bicarbonate and releases CO_2 into the surrounding water. At depth, $CaCO_3$ particles either undergo dissolution or marine sediments. Globally, the biological $CaCO_3$ production is estimated to contribute to about 75 ppm of the atmospheric CO_2 concentration [*Broecker and Peng*, 1986].

It is expected that the ocean will ultimately account for the major part of removal of atmospheric CO_2 through inorganic buffering and $CaCO_3$ sediment dissolution. However, the net uptake is small compared to the gross up and downward fluxes and large uncertainties remain in future estimates of the air-sea carbon flux [*Heinze et al.*, 2015]. In order to limit warming over the 21st century to less than 2℃ relative to pre-industrial levels, as agreed to during the 2015 Paris climate conference, atmospheric CO_2 concentrations should not surpass 450 ppm in 2100 [*Pachauri et al.*, 2014]. This means that atmospheric CO_2 concentrations must only be permitted to rise an additional 50 ppm. However, inter-model spread in cumulative oceanic carbon sink ranges from 320 to 635 Pg-C for the scenario that matches current emissions most closely [*Pachauri et al.*, 2014]. This 315 Pg-C difference in ocean sink translates to over a 100 ppm difference in atmospheric CO_2 by the end of the 21st century which double the desired limit of 50 ppm.

1.1.2 DMS

In order to improve the overall predictive capabilities of global climate model forecasts, and ultimately predictions of climate change, the physics of gas transfer across the atmosphere-ocean interface have to be better understood. Air-sea interaction parameterizations need to be developed and validated for a wider range of physical conditions. Adequate characterization of gas transfer across the air-sea interface is not only essential to quantify local and global sinks and sources of CO_2 but also to budget many other trace gases that influence Earth's

radiation. These include, among others, marine aerosol precursors such as dimethyl sulfide (DMS).

DMS is released into the upper ocean and subsequently to the atmosphere as a product of the breakdown of certain dimethylsulphoniopropionate synthesizing phytoplanktons, such as coccolithophorids. Once in the atmosphere, DMS is oxidized to form sulfur dioxide and methane sulphinic acid. These contribute to the formation sulfate aerosols. These aerosols act as cloud condensation nuclei which increase the number of cloud droplets, the liquid water content of clouds, and the cloud area. As such, they may be responsible for raising the top of the atmosphere albedo promoting reflection of incoming sunlight. In a warmer climate, the growth rate of phytoplankton may be enhanced through physiological effects related to warmer temperatures. As a result more DMS may be produced, increasing sulfate aerosol concentrations, raising the cloud cover and albedo thus leading to a cooler climate. This negative feedback is knows as the CLAW hypothesis, named after the initials of the originating authors [*Charlson et al.*, 1987]. It has however also been proposed that in a warmer climate, phytoplankton growth will be inhibited as the world oceans will become more stratified which would hinder the cycling of nutrients from the deep ocean to its productive euphotic zone [*Lovelock*, 2007]. This in turn could result in a reduction of DMS production ultimately leading to increase warming. These two opposite feedback scenarios are illustrated in Figure 1.3.

Modeling efforts, laboratory work and most importantly observations conducted to verify the CLAW hypothesis have uncovered no evidence for a DMS-controlled biota-climate feedback which has led *Quinn and Bates* [2011] to conclude that is is time to retire the hypothesis. Still, there seems to be no consensus on future trends and the sea-air DMS flux is poorly constrained with estimates ranging from 16 to 54 Tg yr^{-1} of sulphur [*Kettle and Andreae*, 2000]. Several modeling studies suggest an increase in DMS by the end of the 21^{st} century under enhanced greenhouse gas conditions [*Penner et al.*, 2001; *Gabric et al.*, 2004; *Bopp et al.*, 2004] resulting in a small negative climate feedback and to global warming of about

-0.05 W m^{-2}. Other studies [*Gunson et al.*, 2006] conclude that changes in temperature and irradiance will impact DMS emission negatively. It is important to note here that these studies rely on gas transfer parameterizations determined for CO_2, which will be shown to not be applicable to DMS.

1.2 Processes at the Air-Sea Interface

As illustrated in Figure 1.4, a myriad of processes are at play at the air-sea interface and have the potential to influence the exchange of momentum, heat, and material within the dynamically coupled ocean-atmosphere system. These will be briefly described here and a subset of the processes relevant in the high latitude open ocean under high wind conditions will be explored further in the next sections and throughout the dissertation.

Upper ocean dynamics is dominated by processes that range several orders of spatio-temporal scales. Small-scale, wind-shear generated turbulence coexists with large scale turbulence associated with buoyant plumes and wave-generated coherent structures. Both large and small scale turbulence disrupts the molecular sublayer allowing for more efficient

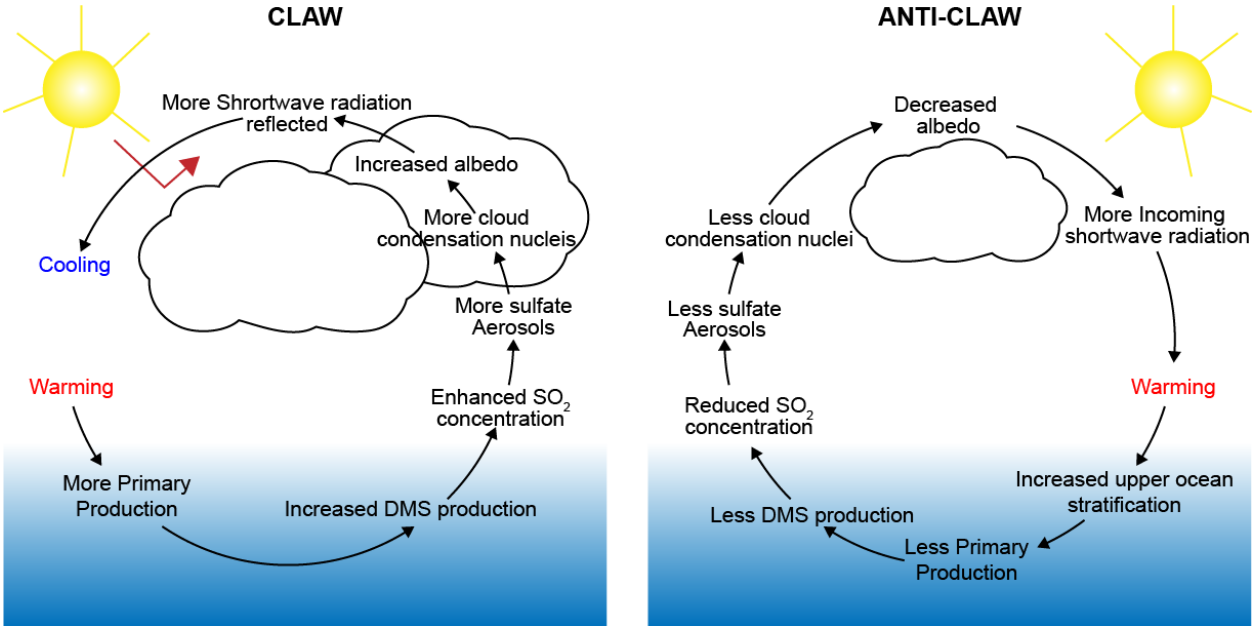

Figure 1.3: Illustration of DMS climate feedbacks

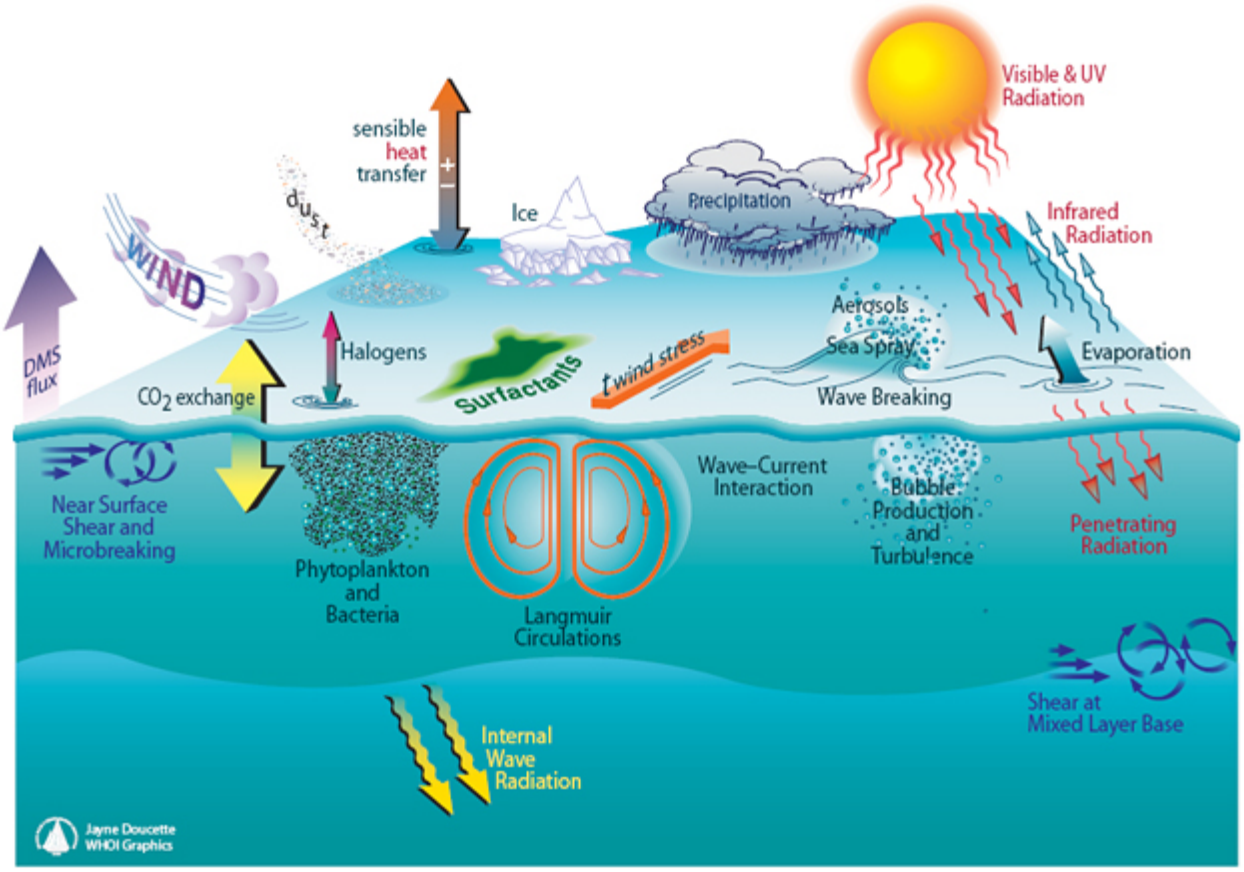

Figure 1.4: Depiction of processes operating at the air-sea interface and in the upper ocean mixed layer. Many of these processes vary on time scales ranging from seconds to decades and remain poorly understood. (Illustration by Jayne Doucette, Woods Hole Oceanographic Institution)

gas transfer across the air-sea surface.

Buoyancy-driven turbulence arises as the surface is cooled, i.e. there is a net heat flux from the ocean to the atmosphere. This net flux ensues from the local balance between the incoming short wave solar radiation, the outgoing long wave (infrared) radiation, as well as the sensible and latent (evaporation) heat fluxes. Surface cooling can lead to large scale convection that extends the bottom of the mixed layer, below which stability suppresses turbulence [*Csanady*, 1997].

Surface gravity waves are formed as the wind blows over the ocean. They are ubiquitous at the air-sea interface and have the potential to alter both upper ocean and lower atmosphere dynamics. The mean particle drift of surface waves, known as the Stokes drift, sets up a current in the along-wave direction which decays rapidly with depth. Near the surface it may

become substantial (∼1 m/s) and its interaction with the Coriolis effect adds a potentially non-negligible term to the momentum balance that governs the mean ocean circulation. The interaction between the Stokes drift and wind-driven surface shear currents results in Langmuir circulation [*Langmuir*, 1938]. These counter-rotating vortices, roughly parallel to the wind direction, can easily be detected at the ocean surface as the surface convergence regions between the vortices trap algea, surfactants, foam and debris in along-wind bands. Complex interactions also exist between surface gravity waves and small or large scales currents [*Peregrine*, 1976] leading to inhomogeneities in the wave field. Indeed, a mean flow in the opposing direction of the wave field propagation may lead to formation of rogue waves and promote wave breaking [*Romero et al.*, 2017].

Wave breaking leads to enhanced upper ocean turbulence and bubble cloud formation which will be discussed in greater detail throughout the dissertation. It also results in sea spray production. These saline droplets are a pathway by which both volatile and non-volatile material can be transported from the ocean to the lower atmosphere. Sea spray is generated by two mechanisms: 1) film and jet droplets result from bubble bursting at the sea surface and 2) spume droplets are produced by the wind tearing off the crest of a waves [*Veron*, 2015; *Andreas*, 2004]. The lager spume droplets remain airborne only for short periods of time ranging from seconds to minutes, but have significant impact on the latent and sensible heat transfer [*Andreas*, 1992]. Smaller droplets may have a lifespan of hours or days in the marine atmosphere. Sea spray may enhance outgasing as ejected droplets evaporate, but may also increase the net ocean uptake as larger droplets may absorb gases prior to falling back into the ocean. The relative importance of spray in air-sea gas exchange has yet to be quantified and will not be discussed further here due to lack of direct measurements.

Model experiments have suggested that, while insignificant on global scale, rain may have significant impact on regional air-sea CO_2 fluxes [*Komori et al.*, 2007; *Turk et al.*, 2010]. Precipitation may impact fluxes through increased near surface turbulence and alteration of the surface layer density stratification. Lab experiments and models studies indicate that

rain enhances the air-sea gas flux due to increased near surface turbulence [*Ho et al.*, 2000]. This was found to be valid both in freshwater and saltwater. However, in saltwater at low to intermediate wind speeds, the less dense rain water remains at the surface and inhibit vertical mixing thus dampening the gas flux effect of rain [*Ho et al.*, 2007]. Further laboratory studies revealed that rain and wind effects combine non-linearly to enhance air-water gas exchange with rain contributing significantly only at low wind speeds [*Harrison et al.*, 2012]. No special consideration for rainy conditions will be made here as the majority of measurements discussed in this dissertation were taken under stormy, rainy conditions.

The impacts of sea-ice on air-sea gas exchange are manifold and opposite. Although ice acts as a physical barrier inhibiting the exchange, it is also associated with enhanced turbulence due to convection and current shear which promotes air-sea fluxes [*Loose et al.*, 2014, 2016]. Laboratory experiments (Zappa et al., *in preparation*) suggest that increased ice floe concentrations enhances gas transfer due to enhanced turbulence. This study implies that the gas transfer first increases with floe concentration up to a certain point after which concentration starts inhibiting turbulence and transfer. Eddy covariance measurements reveal a linear relationship between ice cover and transfer [*Butterworth and Miller*, 2016]. Gas was also shown to permeate through the ice leading to a non negligible flux that is however not distinguishable from the air-sea flux in eddy covariance measurements [*Else et al.*, 2011; *Miller et al.*, 2011; *Delille et al.*, 2014]. No further consideration on sea ice will be made as non of the data presented here was taken within proximity of it.

Finally, the role of phytoplankton and bacteria in the biological carbon pump and the DMS cycles were elucidated in the previous section. It is also important to note that they are the primary source for naturally occurring oceanic surfactants [*Garrett*, 1967]. Surfactants are organic compounds with amphillic characteristics having both hydrophobic and hydrophilic end members both of natural/biological and human origin[*Garrett*, 1967]. Containing both water-soluble and water-insoluble components, they preferentially remain at air-water boundaries such as the air-sea interface and the surfaces of bubbles. Their presence

alters surface tension and reduce the sea surface roughness and suppress turbulence in the viscous boundary layer thus having the potential to decrease surface shear stress induced bulk turbulence. They represent an additional drag force on bubbles rising through the water column, and have been shown to prolong the lifetime of foam at the water surface [e.g. *Garrett*, 1967; *Clift et al.*, 1978; *Jähne et al.*, 1984; *Callaghan et al.*, 2016]. Slicks or concentrated films of surfactants may retard gas transfer as they form either an insoluble layer or an additional liquid phase that adds resistance to mass transfer [*Springer and Pigford*, 1970; *Liss and Martinelli*, 1978]. Their impact is thought to be important only at low wind speeds. The surfactant laden surface micro layer is difficult to sample particularly under high wind and rough seas and its influence in all conditions remains an active field of research. Surfactants will not be considered further as the surface microlayer was not sampled during the experiments considered here.

1.3 Wave Breaking

As wind blows over the water surface, gravity waves are generated. These contribute to and modulate the energy, momentum, and mass fluxes between the ocean and the atmosphere [*Melville*, 1996]. The wave field at a given time (t) and geographic location (x, y) can be characterized by a directional wave height spectra $S(\theta, f)$, where f is the frequency and θ the direction of propagation. The spectrum S is related to the surface elevation η such that: $\langle \eta^2 \rangle = \iint S d\theta df$. Its evolution in time and space can be mathematically described by the radiative transfer equation [*Komen et al.*, 1994, 1984] which represents the balance of the energy transferred in, out, and within the wave field:

$$\frac{D}{Dt} S(x, y, t, \theta, f) = S_{in} + S_{dis} + S_{nl} \tag{1.1}$$

The term $\frac{D}{Dt}$ denotes the total time derivative: $\frac{D}{Dt} = \frac{\delta}{\delta t} + (\vec{c}_g + \vec{u})\vec{\nabla}$, where $\vec{u}$ is the current, $\vec{c}_g$ the propagation, i.e. group velocities, and $\vec{\nabla}$ is the horizontal divergence. The main source

of energy (S_{in}) is the wind, while wave energy is lost through dissipation (S_{dis}) primarily due to wave breaking. Nonlinear wave-wave interactions (S_{nl}) are responsible for the exchange of energy between wave components.

Whitecaps

The main proxy used to quantify breaking processes is the whitecap cover (W) which is easily detectable in near surface imagery from ships or aircrafts [e.g. *Monahan and O'Muircheartaigh*, 1980; *Callaghan and White*, 2009; *Callaghan et al.*, 2008a; *Goddijn-Murphy et al.*, 2011; *Bobak et al.*, 2011; *Kleiss and Melville*, 2010] and can be retrieved from satellite data [*Salisbury et al.*, 2013; *Anguelova and Webster*, 2006]. W has traditionally been parameterized as a non-linear function, most commonly a power-law, of the 10 m wind speed (U_{10}). Historical wind speed dependent parameterizations of W were reviewed by *Anguelova and Webster* [2006]. These exhibit several order of magnitude scatter, highlighting the large uncertainties in whitecap fraction and wave breaking parameterizations (Figure 1.5).

The total whitecap fraction W, includes foam generated during active, stage A, wave breaking as well as residual foam left behind by maturing, stage B waves. While the total fraction may be used to determine bubble mediated sea spray aerosol production and heat exchange [*Andreas*, 1998; *de Leeuw et al.*, 2011], it is the active portion (W_A) that needs to be considered to deduce dynamical processes such as momentum flux and turbulent mixing associated with breaking waves. Separating the active fraction of the total whitecap coverage from photographic imagery is a tedious process and no robust method has been developed up to date. Several studies [*Asher et al.*, 2002; *Kleiss and Melville*, 2010; *Monahan and Woolf*, 1989] distinguish between the active and residual whitecap fraction based on intensity/brightness/albedo thresholds. Such thresholds are however difficult to set without meticulous analysis of individual images. Recent effort include a crowd-sourcing technique by *Scanlon and Ward* [2013] in which separation is achieved manually based on visual inspection of the wave crest according to criterions of intensity, shape and texture.

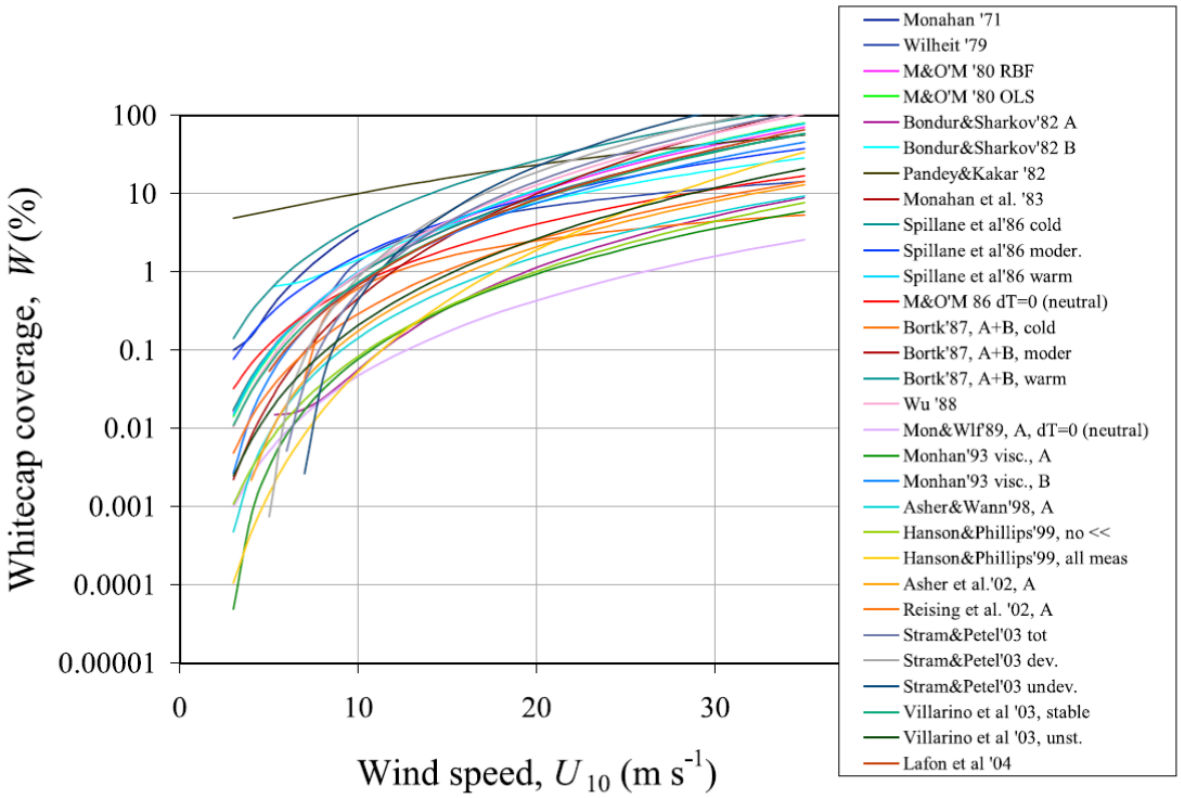

Figure 1.5: Wind speed dependent whitecap parameterizations suggested in the literature prior 2004. Figure 1 from *Anguelova and Webster* [2006]

Breaking Crest length distribution

While still images can be used to determine W, much more information can be extracted from videos. Higher frequency imaging allows not only to detect, but also to track the evolution of whitecaps and more importantly of breaking crest lengths. The breaking crest length and its propagation speed (c_{br}) have been recognized by *Phillips* [1985] as key to quantify not only the scale of breaking but also its kinematic and dynamic properties. This led him to introduce a statistical variable $\Lambda(c_{br})$ known as the breaking crest length distribution. In a laboratory experiment, towing a hydrofoil at constant speed and depth through channel, *Duncan* [1981] showed that the rate of energy loss per unit length of breaking crest is proportional to c_{br}^5, were c_{br} is the propagation speed of the crest. This led *Phillips* [1985] to postulate that depth integrated turbulent kinetic energy dissipation rate due to active breaking at scale c_{br} may be related to $\Lambda(c_{br})$ as follows:

$$\varepsilon(c_{br}) = bc_{br}^{5}\Lambda(c_{br})/g \tag{1.2}$$

where b is the effective strength parameter. Integration across wave scales, provides a direct estimate for the total kinetic energy flux into the water column mediated by wave breaking [*Zappa et al.*, 2016].

As recognized by *Anguelova and Hwang* [2016], W_A may be determined by combining the first moment of $\Lambda(c)$ with the duration of the breaking T:

$$W_A = \int Tc_{br}\Lambda(c_{br})dc_{br} \tag{1.3}$$

fractional surface turnover rate or breaking frequency first moment.

$$R = \int c_{br}\Lambda(c_{br})dc_{br} \tag{1.4}$$

1.4 Gas Transfer

The air-sea gas transfer can be divided into three processes: 1) a flux in the atmospheric viscous boundary layer between the bulk air and the air-side concentration boundary layer (CBL), 2) a flux across the interface between the air and water films, and 3) a flux in the water mass boundary layer between the aqueous CBL and bulk water. As the transfer across the interface occurs much faster than the transfer through either CBL, the air-sea flux is limited by the transport through the sublayers on either side of the interface. Whether the air or the water is most limiting depends on solubility. Sparingly soluble gases as CO_2 are water-side controlled.

The bulk gas flux (F_g) across the air-sea interface can be expressed as the product of the gas transfer velocity (k) and the air-sea concentration difference ($\Delta C = C_w - \alpha C_a$, where α

is the dimensionless Ostwald solubility coefficient):

$$F_g = k\Delta C = kK_0\Delta p, \tag{1.5}$$

where K_0 is the aqueous-phase solubility of the gas and Δp the partial pressure difference. The gas transfer velocity both incorporates the diffusivity of the gas in water (which varies for different gases, temperatures and salinities) and represents the dependence of the flux on physical forcing mechanisms. k is composed of both air and water phase transfer velocities and can be written in terms of water (k_w^{-1}) and air side (k_a^{-1}) resistance as:

$$k = \frac{1}{\frac{1}{k_w} + \frac{\alpha}{k_a}}. \tag{1.6}$$

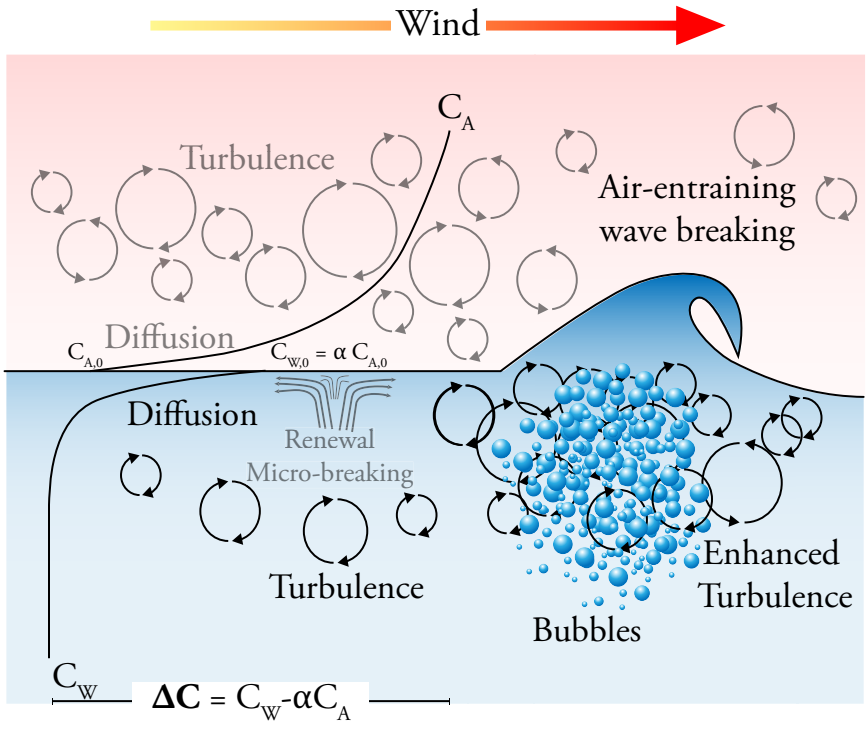

Figure 1.6: Illustration of the boundary layers at the air-sea interface and processes relevant to gas transfer.

Many studies have shown that the transfer velocity is regulated by the turbulence in the boundary layer which arises mainly from the friction of the air moving above the water surface

[*Jähne et al.*, 1987; *Komori et al.*, 1993]. k is therefore typically parameterized as a function of wind speed (U). One of the earliest parameterization came from *Liss and Merlivat* [1986] based on wind tunnel data [*Broecker et al.*, 1978; *Broecker and Siems*, 1984] and Rockland lake data [*Wanninkhof et al.*, 1985]. They considered 3 wind regimes corresponding to no waves, capillary waves and breaking waves and deduced a three piece linear dependency on U. Later, *Wanninkhof* [1992] suggested a U^2 dependency which can be backed by the physical, but not dimensional, argument that, at least for moderate winds, the surface wind stress, which drives surface renewal, increases as U^2. *Monahan and Spillane* [1984] proposed that gas transfer is directly related to whitecap coverage which they found to have a cubic dependency on wind speed. This idea was verified by lab work [*Asher et al.*, 1996] which showed a linear, gas specific, dependence of gas transfer with whitecaps. This work however did not explore the dependency of k on wind. Other studies also suggested a cubic dependency rationalized from the role of bubbles for low solubility gases which was supported by lab and field measurements [e.g., *Wanninkhof and McGillis*, 1999; *McGillis et al.*, 2001; *Prytherch et al.*, 2010].

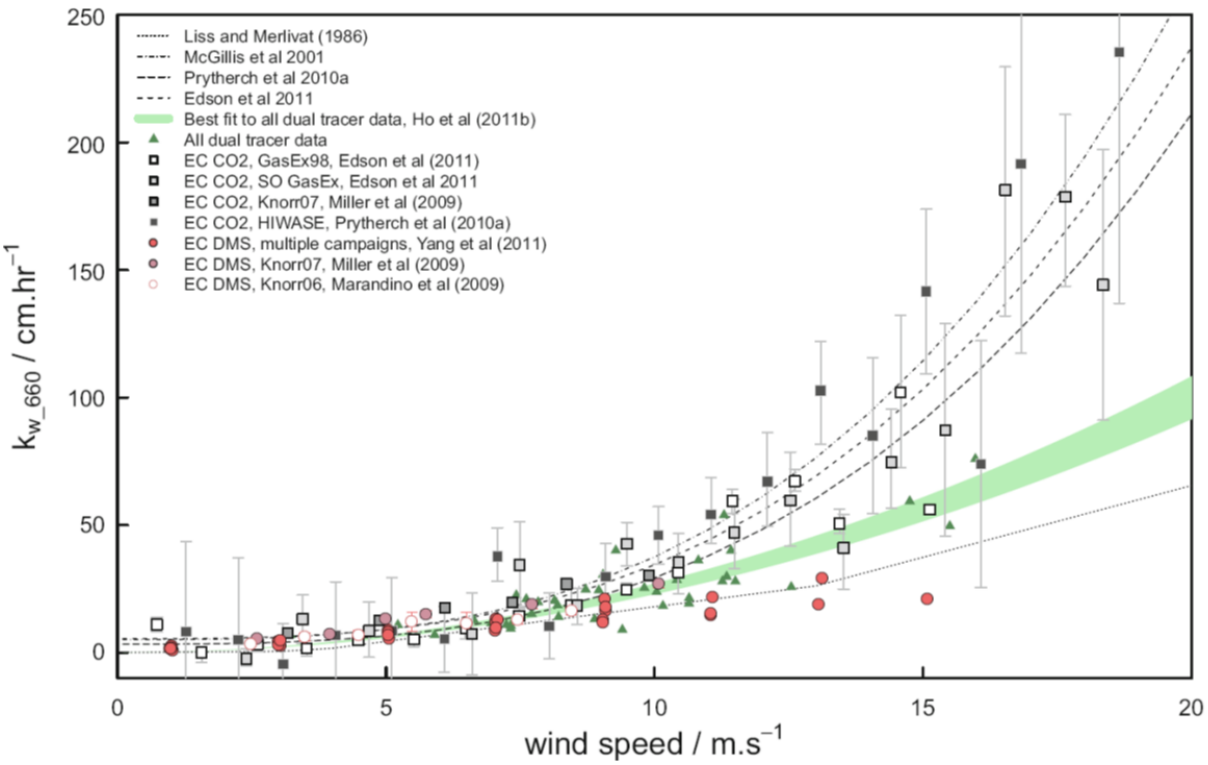

Figure 1.7: A comparison of different wind speed relationships of the water side transfer velocity, k_w. Measurements from eddy covariance techniques are presented [*Garbe et al.*, 2014].

The apparent non-linear dependency on wind means that short duration high wind events such as winter storms may have significant impact on the global mean gas flux. However, large uncertainties still remain, especially under high wind conditions. Indeed, already for wind speed of 7 m s^{-1} the uncertainty in k is 50% and exceeds 100% for wind speeds over 15 m s^{-1} [*Prytherch et al.*, 2010]. It is also important to note that the majority of wind based parameterization were determined from and tuned to the data rich temperate latitude [*Bourassa et al.*, 2013]. However, winds over the polar oceans are among the strongest in the world and the subpolar north Atlantic and the southern ocean that have been identified as primary locations of ocean uptake of CO_2 mainly due to it's greater solubility in cold water [*Sabine et al.*, 2004; *Takahashi et al.*, 2009]. Paucity of air-sea gas exchange measurements at high latitude hinders our ability to better constrain gas transfer velocity in such environment dominated by high winds, rough seas and spray.

Turbulent transport model for gas transfer velocities

Although to a first order gas transfer can be thought of to be controlled by wind speed, which is a primary driver of turbulence in the upper ocean, a large variety of environmental forcing and processes (wind, currents, rain, waves, breaking, surfactants, fetch, stability of both the atmospheric and ocean boundary layer) actually influence k and wind speed alone cannot capture the variability of air-water gas exchange. Several studies have used mechanistic approaches such as surface renewal [*Danckwerts*, 1951; *Komori et al.*, 1993] embody the turbulence driving gas exchange, but their applicability is limited to specific environmental conditions. Early work by *Banerjee et al.* [1968], *Lamont and Scott* [1970], and *Kitaigorodskii* [1984] showed that gas transfer can be modeled as a function of turbulent transport and diffusivity such that:

$$k \propto (\varepsilon \nu_w)^{(1/4)} Sc^{-1/2}, \tag{1.7}$$

where ε is the turbulent kinetic energy (TKE) dissipation rate and the Schmidt number ($Sc = D/\nu_w$) defined as the ratio of the kinematic viscosity of water (ν_w) to mass diffusivity D in water. Compiling data collected in a large tidal river, a macro-tidal estuary and from a coastal ocean site as well as in a "model" saltwater ocean at Biosphere 2 (Oracle, AZ USA), *Zappa et al.* [2007] showed that gas transfer rates vary linearly with the turbulent dissipation rate to the 1/4 power. This study demonstrated that turbulent kinetic energy dissipation is a good predictor for gas transfer in low to moderate winds. Whether this model can be extended to high wind, breaking wave conditions has yet to be verified.

Whitecapping and bubble-mediated transfer

At high wind speed, breaking waves become a key factor to take into account when estimating gas fluxes. Both theoretical and experimental studies suggest that wind waves and their breaking can significantly enhance gas exchange [*Farmer et al.*, 1993; *Watson et al.*, 1991; *Wallace and Wirick*, 1992; *Wanninkhof et al.*, 1995; *Woolf*, 1997]. However, robust

quantification of this enhancement still remains elusive. Breaking results in additional upper ocean turbulence and generation of bubble clouds. Bubbles offer a second pathway for gases between atmosphere and ocean, in addition to direct diffusion across the main interface. Gas may be injected into the water by first being encapsulated in a bubble and subsequently diffusing across the surface of the bubble. Similarly, gas may evade by diffusing into the bubble and escaping when the bubble surfaces and bursts. Smaller bubbles may also simply dissolve completely. The role of bubble-mediated transfer depends on gas solubility and is thought to be significant only for sparingly soluble gases such as CO_2 and DMS ($k \sim k_w$). Soluble gases such as acetone and even more so methanol, are largely air side controlled and bubble mediated transfer is thought to be negligible ($k \sim k_a$) [*Yang et al.*, 2014]. It has also been suggested that bubbles lead to a reduction of the transfer of amphiphilic marine compounds (having both polar and non-polar regions) such as DMS [*Vlahos and Monahan*, 2009]. The amphiphilic nature of DMS means that experiences different surface tension at the water-bubble interface which slows down it's dissolution. What is more, at high winds when bubble-bubble conllision is frequent, DMS may be transported to a sinking bubble furthrt delaying its transfer to the surface.

Efforts have been made towards including the effect of bubble mediate transfer in parameterizations of gas transfer to reduce the uncertainties around k estimates at high wind speed. In these parameterizations the bubble mediated transfer is modulated by the total whitecap coverage. Perhaps the best illustration of physical approach to parameterize the air-sea gas transfer is the NOAA/COARE (Coupled Ocean-Atmosphere Response Experiment) gas transfer model COAREG [*Fairall et al.*, 1996, 2000]. Initially developed for heat and momentum, COARE is a "bulk" algorithm of atmospheric boundary layer and surface interaction, utilizing mean measurements of meteorological parameters and SST. It was extended to include a kco2 parameterization [*Fairall et al.*, 2003; *Hare et al.*, 2004] based on a cool-skin model [*Soloviev and Schlüssel*, 1994] and subsequently adapted for DMS [*Blomquist et al.*, 2006] and ozone [*Bariteau et al.*, 2010; *Helmig et al.*, 2012]. With potential application to a

wide range of other gases [*Fairall et al.*, 2011; *Jeffery et al.*, 2010; *Johnson*, 2010; *Rowe et al.*, 2011] COAREG can be used to obtain global estimates of gas exchange using satellite SST along with near surface wind, temperature and humidity [*Jackson et al.*, 2012]. COAREG writes k as: $k = [(k_w + k_b)^{-1} + \alpha k_a^{-1}]^{-1}$, where k_b is the bubble mediated transfer velocity proposed by *Woolf* [1997] which is a direct function of W.

Another parameterization includes not only bubble effects but also enhancement arising from wave breaking generated turbulence [*Asher and Wanninkhof*, 1998]. It assumes the following functional form for k : $k = k_M + W(k_T - k_M) + Wk_B$, where k_T is the transfer velocity due to turbulence generated by wave breaking and k_M is the contribution of turbulence generated by all other processes. The bubble mediated transfer, k_B is parameterized following *Merlivat et al.* [1993]. k_T is a constant modulated by Sc and k_M is expressed as a linear function of wind speed equally modulated by Sc. Coefficients were estimated from lab experiments for both invasion and evasion, but had since recently not been verified against field data.

1.5 Motivation

In view of current climate change, it is essential to accurately quantify the sources and sinks of gases that impact Earth's radiative balance. Improving our understanding of air-sea gas fluxes will allow for improved future predictions as they are at the at the core of biogeochemical cycles. This in turn will permit informed mitigation strategies for climate change. Large uncertainties remain in current estimates of the air-sea gas transfer. These are particularly critical in high wind speed conditions where waves and their breaking dominate upper ocean dynamics. Waves are the "gearbox" coupling the atmosphere to the ocean and wave breaking plays an important role in air-sea exchange processes such as gas transfer. Its impact on gas transfer has yet to be quantified for both soluble and insoluble gases.

Previous studies lacked exhaustive wave field observations. This limited most studies to

only explore the dependence of the gas transfer velocities on the wind speed. As successful as wind-dependent models may be, they are not complete because they cannot fully account for the role played by surface waves and the state of the ocean in the gas transfer process. What is more, wind-speed only models for CO_2 diverge considerably at high wind speed having a wind-speed dependency ranging from quadratic to cubic. Within the last decade several multi institutional field campaigns aimed at collecting the data necessary to link gas transfer to sea state. This dissertation provides a collection of original analysis of two of these datasets that were focused on high wind conditions in areas recognized as critical for marine carbon uptake: the Southern Ocean and the North Atlantic.

1.6 Goals and Objectives

The 2008 Southern Ocean Gas Exchange Experiment (SO GasEX) and the 2013 High Wind Gas Exchange Study (HiWinGS) provide comprehensive datasets of micro meteorological flux estimates, physical and chemical measurements of the surface ocean and lower atmosphere complemented with various concurrent in situ and remotely sensed wave field observations. These were analyzed in the aim of understanding, parameterize and ultimately predict the gas transfer velocities of CO_2, dimethyl sulfide (DMS) among others under high wind regimes. The focus being on qualifying the role of wave breaking and incorporating it into gas transfer parameterizations. Their main objectives were to:

1. Understand the wind and sea state dependence of breaking to reduce the uncertainties around whitecapping which is the main proxy used to quantify breaking processes.
2. Evaluate the sea state dependence of the gas transfer velocities of gases of varying solubility and establish if wind and wave dependent parameter models can transcend the cubic-quadratic k conundrum.
3. Develop a new framework for process driven gas transfer modeling that incorporate wave breaking processes (bubbles and turbulence) based on breaking crest properties.

1.7 Scope of the Chapters

This dissertation comprises five Chapters and one Appendix. This first chapter introduced the broader context of this dissertation and motivates the present work. Additional background material can be found within individual chapters. Chapters 2 to 4 contain the results pertaining to the main topic of the dissertation while Appendix A consists of early work conducted by the author in the first years of her graduate studies at the Lamont-Doherty Earth Observatory at Columbia University.

Chapter 2 presents a first set of analysis of the visible imagery collected during two major experimental campaigns – the 2008 Southern Ocean Gas Exchange (SO GasEx) experiment and the 2013 High Wind Speed Gas Exchange Study (HiWinGS). This analysis focused on the total whitecap coverage observed during both experiments. Its goal was to find suitable parameters to quantify W through systematic investigation of the effect of wind and wave fields. It consists of a thorough literature review and is based on detailed analysis of omni-directional and directional wave spectra partitioning either directly measured or obtained from a wave model hindcast. This chapter has been accepted for publication in the *Journal of Physical Oceanography*: Brumer et al. On the dependence of Whitecap coverage on environmental parameters observed during HiWinGS and SO GasEx. Note that details of the wave data analysis and model/measurement comparison for HiWiNGS will appear in a separate paper, co-authored by the dissertation author.

Chapter 3 represents the key outcome of an investigation on the performance of simple, single parameter parameterizations for gas transfer velocities. This analysis was conducted in the effort of finding easily obtainable wave and wind related parameters that allow for improved representation of the gas transfer velocities than the current default wind speed only parameterizations. While a multitude of parameters were tested, such as was done in chapter 2, only the most promising ones are presented here. This work is under review in the *Geophysical Research Letters*: Brumer et al. Wave-related Reynolds number parameterizations

of CO_2 and DMS transfer velocities.

Chapter 4 is currently being prepared for submission for publication. The dissertation author is the primary investigator and author of this paper. It is based on a more in depth analysis of the visible imagery collected during the HiWinGS field campaign. Tracking of the breaking crest in the high frequency imagery allowed to determine breaking crest length distributions from which breaking frequency, active breaking faction, and turbulent kinetic energy dissipation, void fraction and bubble air flux were computed. A new framework for process based gas transfer modeling is proposed based on these statistics and tested against the measured gas transfer velocities of CO_2 and DMS. Performance of the framework is contrasted against that of other process based models of gas transfer.

In the fifth and final chapter, the major findings reported herein are summarized and some additional considerations regarding the results are noted. Finally, a proposal for future work is put forward.

Appendix A includes some work based on the Riverine Dynamics Experiment 2 - a two day field campaign in the Hudson River Estuary in 2010 conducted in collaboration with Areté Associates. In it, the author relates the scales of turbulence determined from IR imagery directly to the subsurface scales of turbulence demonstrating the ability to remotely estimate riverine flow rate, subsurface turbulence and bathymetry under low winds. This work was published as a peer reviewed article: Brumer, S.E., C.J. Zappa, S.P. Anderson and J.P. Dugan (2016). Riverine Skin Temperature Response to Subsurface Processes in Low Wind Speeds, J. Geophys. Res. Oceans, 121, doi:10.1002/2015JC010746

Chapter 2

Whitecap coverage dependence on wind and wave statistics as observed during SO GasEx and HiWinGS

A version of this chapter has been accepted for publication in the Journal of Physical Oceanography: Brumer, S. E., C. J. Zappa, I. M. Brooks, H. Tamura, S. M. Brown, B. W. Blomquist, C. W. Fairall, and A. Cifuentes-Lorenzen (2017). Whitecap coverage dependence on wind and wave statistics as observed during SO GasEx and HiWinGS.

2.1 Introduction

Whitecaps are the surface signature of air-entraining breaking waves consisting of subsurface bubble clouds and surface foam patches. They have been studied extensively since the late 1960s because of the role of bubbles in the air-sea exchange of gases, and the production of sea spray aerosols. They form under wind speeds as low as 3 m s^{-1} [*Hanson and Phillips*, 1999; *Monahan and O'Muircheartaigh*, 1986] and have been estimated to cover, on average, 1-4% of the global oceans [*Blanchard*, 1963, 1983]. Their high albedo makes them easily detectable locally with cameras set up on stable platforms [e.g. *Callaghan et al.*, 2008a; *Lafon*

et al., 2007, 2004; *Sugihara et al.*, 2007] as well as from ships [e.g. *Callaghan et al.*, 2008b; *Goddijn-Murphy et al.*, 2011] or planes [e.g. *Bobak et al.*, 2011; *Kleiss and Melville*, 2010]. Typically, monochrome visible sensors are used, but whitecap coverage (W) has also been determined from multi-spectral visible [*Randolph et al.*, 2016] and infrared [*Jessup et al.*, 1997] imagery. Globally, W can be inferred from satellite-borne microwave radiometers [e.g. *Anguelova and Webster*, 2006; *Salisbury et al.*, 2013].

Being such a readily observable quantity, W has been recognized as a promising proxy for quantifying wave breaking dependent processes that have complex impacts on the energy, momentum, heat, and mass transfer at the air-water interface. Large-scale wave breaking is the least understood key element in determining the evolution of wave fields and needs to be properly represented in wave models. It generates turbulent kinetic energy in the upper ocean, drives near surface mixing, and transfers energy from the wave system to surface currents and longer waves [*Cavaleri et al.*, 2007]. Breaking waves and their consequent whitecaps play a significant role in the climate system [*Cavaleri et al.*, 2012]. They directly influence the ocean surface albedo, and hence the surface radiation budget. It has been estimated that they contribute to a globally averaged cooling of about 0.03 W m^{-2} [*Frouin et al.*, 2001]. Because of their impact on albedo, whitecaps must be accounted for in remote sensing applications such as retrieval of surface wind [*Gaiser et al.*, 2004] and ocean color [*Gordon and Wang*, 1994].

Many studies have also shown that, through additional turbulence and bubble mediated transfer, wave breaking leads to enhanced air-sea transfer of gases [*Wallace and Wirick*, 1992; *Farmer et al.*, 1993; *Asher et al.*, 1995; *Asher and Wanninkhof*, 1998; *Monahan and Spillane*, 1984; *Woolf*, 1997; *Woolf et al.*, 2007]. These experiments led to several whitecap dependent gas transfer parameterizations. Furthermore, bursting of the bubbles at the surface injects sea spray aerosols into the atmosphere and the aerosol production flux is thought to be directly proportional to the whitecap coverage (*de Leeuw et al.* [2011] and references therein). These sea salt aerosols play an important role in the earth's radiation budget. They are cloud

condensation nuclei influencing the microphysical and radiative properties of clouds. They are also direct scatterers of solar radiation [*Andreae and Rosenfeld*, 2008; *Haywood et al.*, 1999].

W has traditionally been parameterized as a non-linear function, most commonly a power law, of the 10-meter wind speed (U_{10}) which is easily and routinely measured and modeled. The first empirical function suggested was a simple two coefficient power law [*Monahan*, 1971]:

$$W(U_{10}) = aU_{10}^{n}. \tag{2.1}$$

Later, a new functional form was proposed that accounts for a minimum wind speed threshold below which no whitecaps are observed [*Monahan*, 1993; *Asher and Wanninkhof*, 1998], and forced a cubic dependence on wind speed ($n = 3$):

$$W(U_{10}) = a[U_{10} - b]^{n}. \tag{2.2}$$

The cubic wind speed dependence was adopted based on the hypothesis that W is strongly related to the energy flux from the wind which scales as u_*^3 [*Phillips*, 1985; *Wu*, 1988], where u_* is the air-side friction velocity. However, a cubic dependence on wind speed is questionable and there is no reason not to allow for a tunable exponent. Indeed, satellite derived W display a dependence on wind speed closer to quadratic [*Salisbury et al.*, 2013] while most recent non-thresholded power-law fits suggest an exponent greater than 3 (Table 2.1).

Anguelova and Webster [2006] compiled parameterizations of W as a function of U_{10} found in the literature prior to 2005. The "wind-speed-only" parameterizations published since then are tabulated in Table 2.1 and plotted in Figure 2.1. While the historical parameterizations, summarized in *Anguelova and Webster* [2006], exhibit several orders of magnitude scatter, recent parameterizations can be seen to agree more closely between studies. A variety of different detection techniques used in the past could explain the majority of the scatter between previous studies. Recent advances in instrumentation, and the adoption of an automated

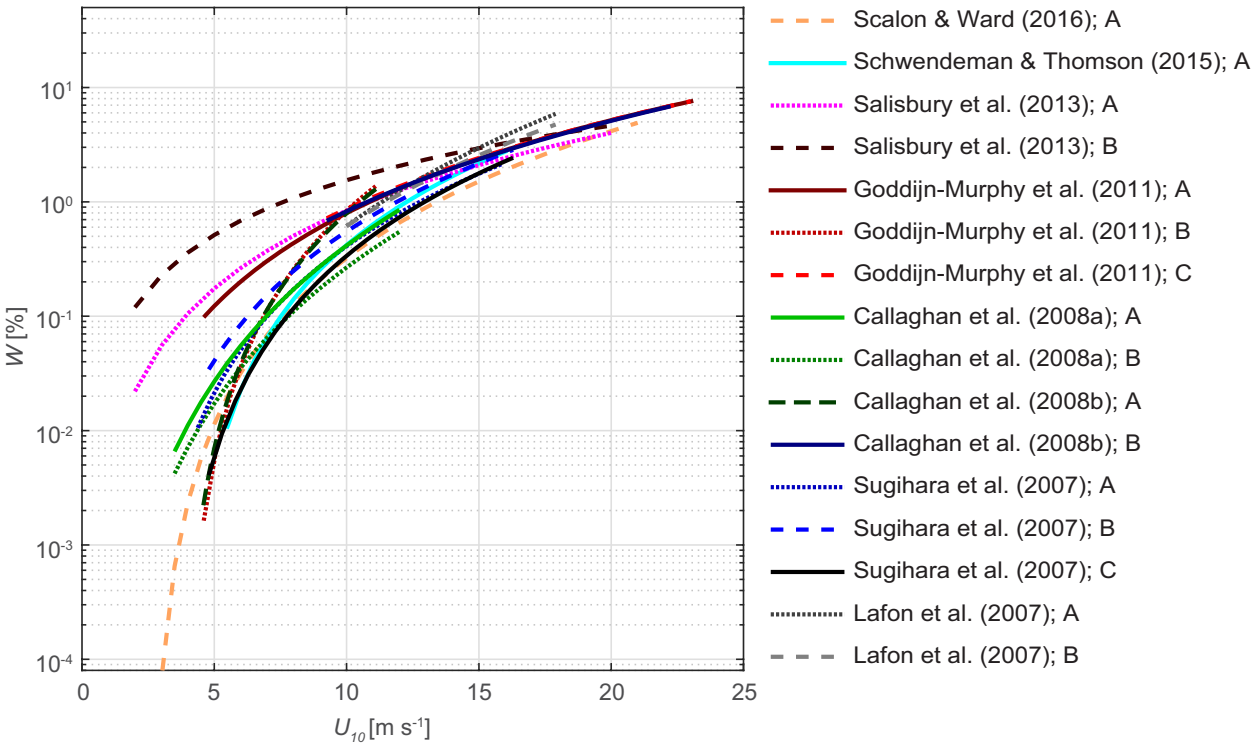

Figure 2.1: Parameterizations of Whitecap coverage (W) as a function of wind speed (U_{10}) published since 2004, see Table 2.1

and objective image processing algorithm [*Callaghan and White*, 2009] have resulted in more consistent whitecap detection. It is also important to note that parameterizations are typically used over a wind speed range that goes beyond the range from which any given parameterization was determined which may lead to significant errors. Individual projects sample only a limited set of environmental conditions and exhibit large scatter. This leads to different trends as determined from best fits and parameterizations that diverge from one study to the next. This divergence is exacerbated at the low and high wind speeds tails and extrapolating parameterizations beyond their valid range results in increased apparent scatter. However, at least from recent data, at a given wind speed scatter is comparable from one study to the next and the mean W do not differ significantly (see *de Leeuw et al.* [2011], Figure 2).

Remaining scatter suggests that wind speed alone does not account for all the observed W variability. Indeed, a multitude of factors have been recognized to affect wave breaking and

bubble lifetime and thereby influencing whitecap coverage [*Melville*, 1996; *Salisbury et al.*, 2013]. These include surfactants [*Frew*, 1997], salinity, sea surface temperature [*Spillane et al.*, 1986], atmospheric stability [*Myrhaug and Holmedal*, 2008; *Spillane et al.*, 1986], wind fetch and duration [*Myrhaug and Holmedal*, 2008], current shear, and long wave interaction [*Kraan et al.*, 1996]. The effects of these factors are more often than not studied separately. The typical approach is to group observations into several ranges of similar conditions based on one factor and compute different coefficients to the wind speed power laws for each range. *Salisbury et al.* [2013] looked at the variability in W after removing the dominant wind speed dependence and showed that the most important secondary factor is the wave state.

Since the scatter displayed by wind-speed-only parameterizations is thought to be largely due to varying wave conditions, parameterizations have emerged in the recent literature that account for both wind speed and sea state. These are summarized in Table 2.2 and Table 2.3. *Zhao and Toba* [2001] suggested that W is better constrained as a function of wind-sea Reynolds numbers than wind speed alone. The breaking-wave Reynolds number was first proposed by *Toba and Koga* [1986] and is defined as:

$$R_{B_w} = \frac{u_*^2}{\nu_w \omega_p} = \frac{2\pi u_*^2 cp}{\nu_w g} \tag{2.3}$$

where ν_w is the kinematic viscosity of water, and ω_p is the peak angular frequency of wind waves. *Zhao and Toba* [2001] introduced an alternative Reynolds number:

$$R_{H_a} = \frac{u_* H_s}{\nu_a} \tag{2.4}$$

where H_s the significant wave height and ν_a is the kinematic viscosity of air. Both *Zhao and Toba* [2001] and *Woolf* [2005] suggested that it is more appropriate to use ν_w rather than ν_a to characterize wave breaking in the open ocean and suggested:

$$R_{H_a} = \frac{u_* H_s}{\nu_w} \tag{2.5}$$

Although, these Reynolds numbers were originally defined for wind-seas, subsequent studies computed them with wave statistics from the full spectrum which may contain both swells and wind-sea [*Norris et al.*, 2013; *Goddijn-Murphy et al.*, 2011]. While R_{H_w} was termed the wave roughness Reynolds number in *Norris et al.* [2013], it will hereafter be referred to as the wave-wind Reynolds number to highlight that it incorporates both a wind and wave dependence. Note that the Reynolds numbers may also be able to account for the dependence on temperature and salinity as these dictate the kinematic viscosity [*Nayar et al.*, 2016; *Sharqawy et al.*, 2010].

The whitecap coverage has also been shown to depend on wave age (c_p/u_*, where c_p is the phase speed at spectral peak), with decreased W observed in old, swell-dominated seas compared to young, wind-wave seas [e.g. *Schwendeman and Thomson*, 2015a]. For transitional and shallow water waves, an inverse dependence of whitecap coverage on wave age has been observed [*Sugihara et al.*, 2007]. Based on the relation of W to the wave-breaking induced energy dissipation as proposed by *Komen et al.* [1994]; *Kraan et al.* [1996] deduced a relation between W and the integral wave steepness ($\bar{\alpha} = \bar{\omega}^4 g^{-2} \int E(\omega) d\omega$, where $\bar{\omega}$ is the mean angular frequency and E is the omnidirectional wave spectrum): $W = 24\bar{\alpha}^2$. Expressing $\bar{\alpha}$ as a function of wave age, they deduced a wave age dependent parameterization of W. Multiple later studies [*Callaghan et al.*, 2008b; *Guan et al.*, 2007; *Lafon et al.*, 2007, 2004; *Schwendeman and Thomson*, 2015a] have determined additional power law parameterizations of whitecap coverage as a function of wave age. These are tabulated in Table 2.3. Note that *Schwendeman and Thomson* [2015a] gave coefficients for the inverse wave age and the parameterization reported in Table 2.3 were computed by fitting a power law to their parameterization.

Fewer studies suggested parameterizations of W as a function of the turbulent kinetic energy dissipation (ε). This is because only a few studies have been undertaken in which both the near surface ε and whitecap coverage were measured [*Schwendeman and Thomson*, 2015a]. Such parameterizations will not be addressed in this chapter.

The idea that wave breaking occurs once a critical local steepness is reached dates back over a century [*Stokes*, 1880] and is at the core of many probability models of wind-wave breaking. However, few studies have related W to steepness since *Kraan et al.* [1996]. While local steepness is difficult to measure, average wave steepness parameters are easy to compute from 1D wave spectra based on a characteristic wave height (H) and wave number (k):

$$s = \frac{Hk}{2} \tag{2.6}$$

Typically, either the peak or mean wavenumbers are considered, and the peak, mean or significant wave heights are used to compute S [*Kleiss and Melville*, 2010; *Schwendeman and Thomson*, 2015a]. However, whitecaps are typically associated with steeper and shorter waves than the dominant or mean wave system which often corresponds to swell. It has therefore been argued that a measure of the mean square slope (mss) as suggested by *Banner et al.* [2002] is a more appropriate measure. The mss is calculated as:

$$mss = \int \frac{(2\pi f)^4 E(f)}{g^2} df \tag{2.7}$$

where $E(f)$ is the omnidirectional wave spectral energy density. The frequency range over which the mean square slope is evaluated is typically chosen as the equilibrium range spanning $\sqrt{2}f_m \leq f \leq \sqrt{5}f_m$ [*Schwendeman and Thomson*, 2015a], where f_m is the mean frequency computed as:

$$f_m = \frac{\int f E(f) df}{\int E(f) df} \tag{2.8}$$

Schwendeman and Thomson [2015a] found the mss most promising for improving W parameterization, especially when normalized by directional spread ($\Delta\theta$, [*Kuik et al.*, 1988]) and frequency bandwidth (Δf).

Few parameterizations other than wind-speed-only have been rigorously tested beyond the original studies and not many datasets exist with concurrent W and wave field measurements.

The synergy of measurements taken during the Southern Ocean Gas Exchange Experiment (SO GasEx) and the recent High Wind Gas exchange Study (HiWinGS) offer unique datasets that facilitate testing of new and existing W parameterizations. In this paper, the dependence of whitecap coverage on wind speed and sea state conditions is investigated with the aim of improving whitecap parameterizations to be used in gas transfer and climate models. The SO GasEx and HiWinGS field campaigns are described in Section 2 along with details of supporting measurements and of the WAVEWATCH III® hind cast used to complement in situ wave observations. After a brief explanation of the image processing and wave field analysis methods in Section 3, the results are presented in Section 4 and discussed in Section 5. Section 6 summarizes key findings and provides recommendations for whitecap parameterizations and future studies.

2.2 Data

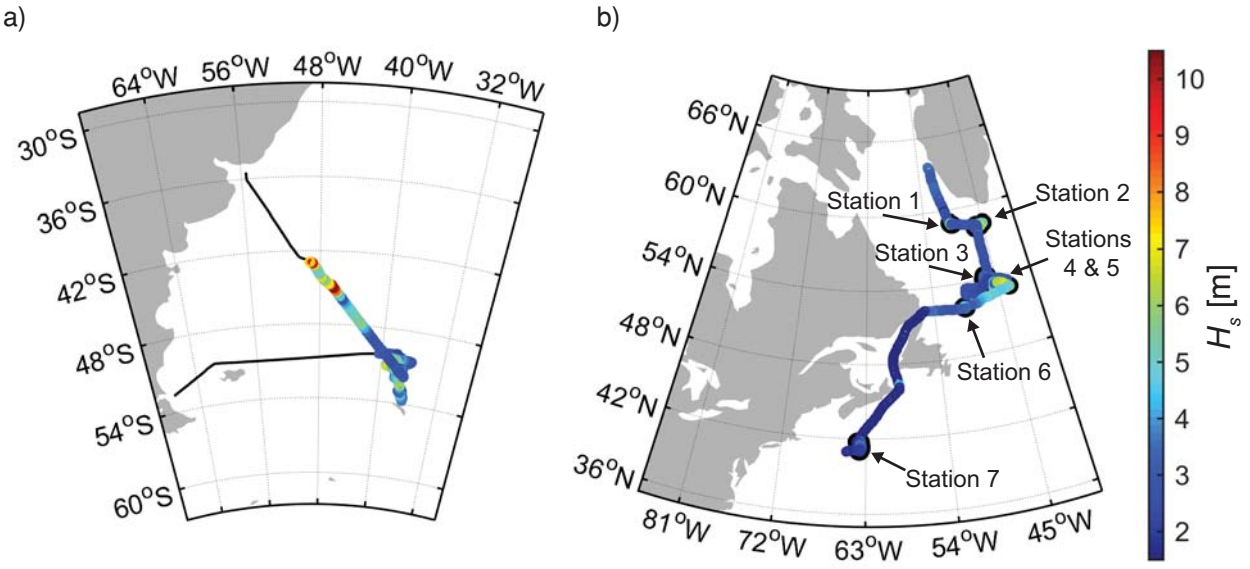

Figure 2.2: Ships tracks a) SO GasEx and b) HiWinGS; the color code shows the significant wave height [m]

2.2.1 The SO GasEx cruise

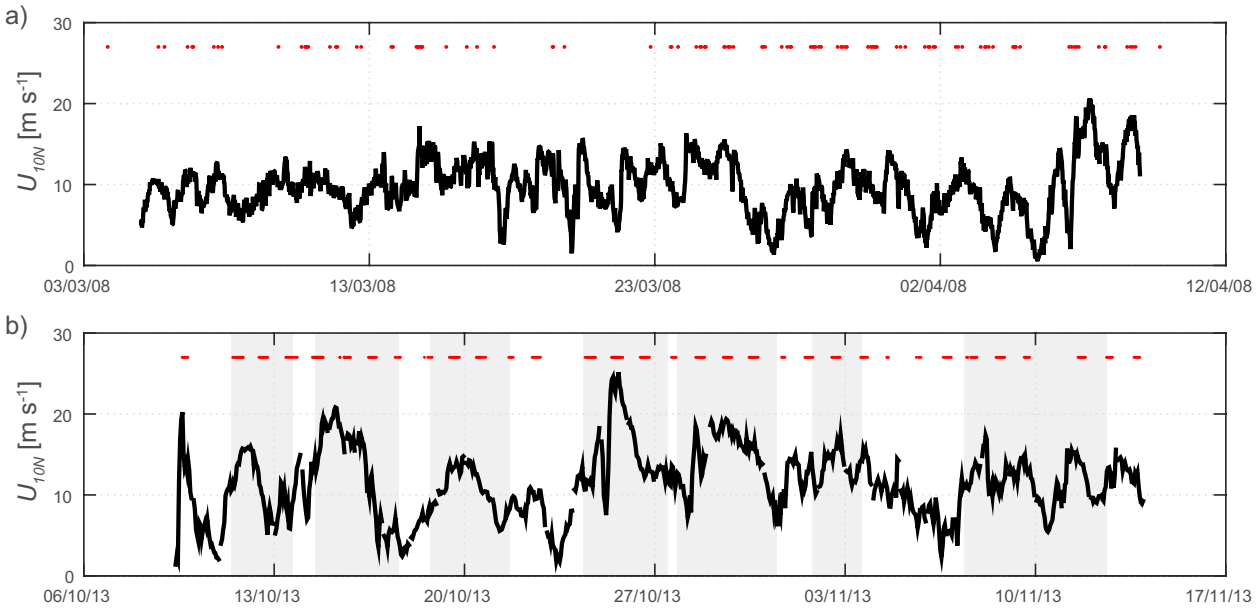

Figure 2.3: Wind speed time series; a) for SO GasEx, and b) for HiWinGS. The gray shading represents periods when the ship was on station during HiWinGS. The red lines correspond to periods of visible imagery recording.

The SO GasEx cruise was the third and most recent cruise of the US led GasEx series initiated in 1998. The main GasEx objective was to improve quantification of air-sea CO2 fluxes and gas transfer velocities. The aim of this third cruise was to examine these processes at higher wind speeds and obtain data in a previously unexplored region. The SO GasEx project focused on a study area around 51°S, 36°W, where the *R/V Ronald H. Brown* remained for 37 days having left Punta Arenas, Chile, on 28 February 2008 (Figure 2.2a). It is important to note that the ship was rarely stationary as deliberate tracer release surveys were conducted on site. The study location was chosen for its high wind speeds and large air-water pCO_2 difference. The average U_{10N} measured in the main study location was 9.7±3.2 m s^{-1}, and a maximum wind speed of 20.7 m s^{-1} was recorded during transit back to Uruguay where the cruise ended on 9 April 2008 (Figure 2.3a). In order to avoid a storm between 13 and 17 March, the *R/V Ronald H. Brown* moved temporarily into the lee of South Georgia Island. Water temperatures in the study site varied between 5℃ and 7℃ increasing to 14℃ in the

transit legs. For further details about SO GasEx, see *Ho et al.* [2011]; *Edson et al.* [2011] and *Cifuentes-Lorenzen et al.* [2013].

2.2.2 The HiWinGS cruise

With the aim of gaining new insights into poorly understood aspects of air-sea interaction under high winds, the HiWinGS cruise objective was to deploy direct measurements of trace gas and physical fluxes together with a suite of wave physics and sea state observations. The HiWinGS cruise took place on board the *R/V Knorr*, in the North Atlantic, (Figure 2.2b) departing Nuuk, Greenland, on 9 October 2013 and ending at Woods Hole, USA on 14 November 2013. The ship's track was chosen based on daily analysis of weather maps and forecasts from the European Centre for Medium-Range Weather Forecast model provided by the Icelandic Met Office as well as from PassageWeather.com with the aim of maximizing the amount of time spent in the strongest winds. Along the track, the ship stopped at several stations for buoy deployments. While on station, the ship was positioned bow pointing into the wind for the duration of each storm.

The ship remained in the Labrador Sea, south of Greenland, for the first $\sim$ 20 days of the cruise. Sea surface temperature and salinity were around 6-8℃ and 34-34.5 psu, respectively, at the first 6 stations (Figure 2.2b). The ship then transitioned through the Gulf of St Lawrence from 4 to 6 November 2013, and the last station was south of Nova Scotia where warmer and higher salinity Gulf Stream waters were encountered with SST of 20℃ and salinity of 36 psu. Wind speeds exceeded 15 m s^{-1} 25% of the time amounting to a total of 189 hours of wind speeds above 15 m s^{-1} of which 48 hours had wind speeds greater than 20 m s^{-1}. On 25 October 2013 (station 4), wind speeds exceeded 25 m s^{-1} with gusts of 35 m s^{-1} in the early stages of what became known as the St. Jude's day storm (Figure 2.3b).

2.2.3 Visible Imagery

During SO GasEx a total of 216 20-minute video segments were recorded, while during the HiWinGS cruise over 500 20-minute segments were recorded, of which 50 were taken during the St. Jude's day storm. For both experiments, the imaging system consisted of two obliquely-angled Imperx model Lynx 1M48 digital video cameras with a sensing array of 1000 x 1000 elements of 7.4 μm. These were mounted on the flying bridge of the *R/V Knorr* and *R/V Brown* at a height above the water line of 14.7 m and 25 m, respectively. For both experiments, one of the cameras was directed starboard while the other one was mounted on the port side to accommodate all lighting conditions. During HiWinGS, wide field-of-view lenses (68.7° FOV; 6 mm focal length) were used, whereas during SO GasEx lenses with 9 mm focal length and a FOV of 36.6° were used. The visible cameras ran at a frame rate of 20 Hz during HiWinGS and 5 Hz during SO GasEx.

The imaging system was improved for HiWinGS by the addition of Inertial Motion Units (IMU) mounted on the same metal plate as the cameras to record the pitch, roll and yaw angles of the cameras. An Xsens model MTi IMU was mounted on the port side system while a 3DM-GX2 model MicroStrain IMU was affixed to the starboard camera mount. The Xsens, which has an angular resolution of 0.05°, recorded at ∼100 Hz, while the MicroStrain, which has an angular resolution of <0.1°, recorded at 50 Hz. Both sensors have a dynamic accuracy of ±2.0°.

2.2.4 Meteorological Measurements

Momentum, energy, and buoyancy fluxes were obtained via direct eddy covariance measurements during both SO GasEx and HiWinGS, along with mean measurements of wind speed, wind direction, air temperature, humidity, pressure, and downwelling solar and IR radiation. The University of Connecticut Direct Covariance Flux System (Uconn DCFS; [*Edson et al.*, 1998, 2004] and the NOAA/ESRL/PSD system [*Blomquist et al.*, 2006; *Fairall*

et al., 2003] were deployed during SO GasEx. These were mounted on the jackstaff of the *R/V Brown* at a height of 18 m above the surface and consisted of 3 fast response Gill R-3 sonic anemometers, and 5 infrared gas analyzers (Li-Cor LI-7500) sampling at 20 Hz. Additionally, the systems included a GPS compass and Systron-Donner "Motion-Pak" used to correct for ship motion as described by *Edson et al.* [1998]. For a detailed description of the setup, the reader is referred to *Edson et al.* [2011]. The NOAA/ESRL/PSD wind-motion system was also used during HiWinGS. It was mounted on the bow mast at 16 m above the water line with fast response sensors set to sample at 10 Hz. Two additional sonic anemometers were deployed, a Gill model r^2 from the University of Hawaii (UH) on the foremast at 15 m and a Gill Windmaster Pro from Plymouth Marine Laboratory on the main mast, some distance behind the bow. While the measurements are mostly consistent between systems, only the measurements from the UH sonic and the Motion-Pak are considered here as the NOAA system suffered a power outage during the St. Jude storm that put several instruments out of action. Direct eddy covariance fluxes and bulk fluxes from the COARE3.5 algorithm [*Edson et al.*, 2013; *Fairall et al.*, 2003, 2011] were computed over 15 minute intervals for SO GasEx and hourly for HiWinGS.

2.2.5 1D and Directional Wave Spectra

In situ and remotely sensed measurements Directional ocean wave spectra were obtained with a Wave and Surface Current Monitoring System (WaMoS®) during SO GasEx [*Cifuentes-Lorenzen et al.*, 2013; *Lund et al.*, 2017]. These measurements are based on the radar backscatter of sea clutter in which the wave patterns are distinguishable. The system used the unfiltered output from a marine X-Band radar mounted on the flying bridge of the *R/V Brown* operating at 9.41 GHz to determine wave and surface current parameters. The WaMoS® has the capability to resolve two-dimensional maps of the surface elevation, and allowed for continuous day and night real-time measurements even in rough seas, and harsh weather conditions. WaMoS® provides directional wave spectra and individual wave state

components at scales of $\mathcal{O}$(100 m).

During HiWinGS, a Datawell DWR-4G Waverider buoy of 0.4 m diameter was deployed while on station for the duration of each major storm system. The Waverider uses the Doppler shift of the GPS signal carrier wave to obtain a direct measurement of its velocity in 3 dimensions at 1.28 Hz. These are integrated to obtain a time series of the 3-dimensional displacement, from which directional wave spectra can be derived. The spectral frequency range resolved by the Waverider covers 0.025 Hz to 0.6 Hz, corresponding to waves of wavelength greater than 4.3 m. During most deployments, the Waverider was left to drift freely within 5 km of the ship. The Waverider was tethered to the ship with a 200 m polypropylene line during the first deployment due to operational restrictions and during the largest storm (station 4) due to severe wind and wave conditions that would not have allowed the ship to stay within radio contact of the buoy. While the tether remained slack and the buoy was kept outside of the ships wake on the first deployment, it regularly dragged the buoy under water during the peak wind period on station 4. This led to loss of GPS reception and poor data quality during part of the St. Jude storm. These data were discarded from subsequent analysis.

In addition, short to moderate gravity waves were measured using a Riegl laser altimeter (model LD90-3100VHS) during both experiments. The laser operates at a wavelength of 0.9 μm (near infrared), with a beam divergence of 2.7 mrad that corresponds to a footprint on the ocean surface of 2.65 cm at a range of 10 m. The manufacturer-specified measurement accuracy is $\mathcal{O}$(2.0 cm) with a precision of $\mathcal{O}$(0.25 cm). The LD-90 laser altimeter data independently characterized spatial and temporal properties of the wave height field resolved down to $\mathcal{O}$(20 cm) wavelengths [*Zappa et al.*, 2012].

The Reigl was mounted on the jackstaff of the *R/V Knorr* at about 14.4 m during HiWinGS and on the jackstaff of the *R/V Brown* at 10 m above the mean water level during SO GasEx. Internal processing provided range to surface measurements at 10 Hz which were corrected for the ship's heave following *Cifuentes-Lorenzen et al.* [2013] to provide the wave

surface displacement. Midway through HiWinGS, after the St. Jude storm on 25 October 2013 at station 4 (see Figure 2.2), the Riegl stopped functioning due to a power distribution failure.

2.2.6 WAVEWATCH III®hind cast

As flux measurements were taken continuously during the HiWinGS cruise and visible imagery was taken regularly during daylight periods regardless whether the ship was steaming or on station, the in situ wave data were complemented by a model hind cast. Version 3.14 of the Wavewatch-III® (WW3; Tolman 2009) was used to compute the hind cast for the duration of the cruise from 1 October to 15 November 2013 (2.5 months). The model domain was set to cover the North Atlantic (0°-70°N and 100°W-15°E) with a latitudinal and longitudinal grid resolution of 0.2°. Bottom topography and coastlines were taken from the ETOPO2 dataset that provides 2 minute gridded elevations/bathymetry for the world. The wave model was forced by 6-hourly surface wind fields from the National Centers for Environmental Prediction/Climate Forecast System Reanalysis (NCEP/CFSR) product [*Saha et al.*, 2010] which has a horizontal resolution of ∼38 km (Gaussian Grid: T382).

WW3 solves the wave spectral balance equation which dictates the evolution of the wave field based on the sum of source terms consisting of the energy transferred to the waves by the wind (S_{in}), the energy lost through dissipation due to wave breaking (S_{dis}), and nonlinear wave-wave energy transfers (S_{nl}):

$$\frac{DN}{Dt} = \frac{S_\Sigma}{\sigma} = \left(S_{in} + S_{dis} + S_{nl}\right)/\sigma \tag{2.9}$$

where $N = N(t, x, y, f, \theta)$ is the wave action density spectrum, S_Σ the sum of source terms, and σ the intrinsic (radian) frequency. The term $\frac{DN}{Dt}$ denotes the total time derivative: $\frac{DN}{Dt} = \partial N/\partial t + \nabla_x((c_x + u)N) + \nabla_i(c_i N)$, where u is the current, c_x the propagation, i.e. group velocities in geographical space (x, y) and c_i the propagation velocities in spectral

space (f, θ).

For the HiWinGS hind cast, the source terms proposed by *Tolman and Chalikov* [1996] were used and the surface wind speed at 10 m elevation was modified to account for the instability of the atmospheric boundary layer (the "effective" wind speed; *Tolman et al.* [2002]). Being a third-generation model, WW3 allows for a punctual, although approximate, representation of S_{nl} for which the discrete interaction approximation (DIA) method was chosen [*Hasselmann et al.*, 1985]. For spatial propagation of the wave spectrum, the default third-order advection scheme was used.

The spectral space was discretized using 35 frequencies ranging from 0.04 Hz to 1.05 Hz in 10% steps ($f_{i+1} = 1.1 f_i$, where i is a discrete grid counter) with 36 directions ($\Delta\theta = 10°$). An f^{-5} spectral tail outside the model frequency range was assumed, as per default WW3 settings. The directional wave spectra from the hind cast were stored every 30 minutes along 4 trajectories following the ship's track.

2.3 Methods

2.3.1 Image Analysis

Initial visual quality control led to removal of runs that were affected by sun glare, or taken in otherwise poor light conditions. Runs were also removed based on the presence of birds that tend to be falsely identified as whitecaps. The first step of the image analysis was to crop the images in order to avoid the ship's wake when the ship was steaming and to remove the horizon from the field of view. An example of images taken while on station during HiWinGS is shown in Figure 2.4a. Before applying the typical brightness threshold (Callaghan and White 2009) to the images, all background gradients were removed. This was achieved in a two-step process: the images are pre-thresholded to identify any pixel with brightness greater than 3.25 standard deviations above the mean, then the row and column means are computed ignoring the high brightness pixels and these means were subtracted from each

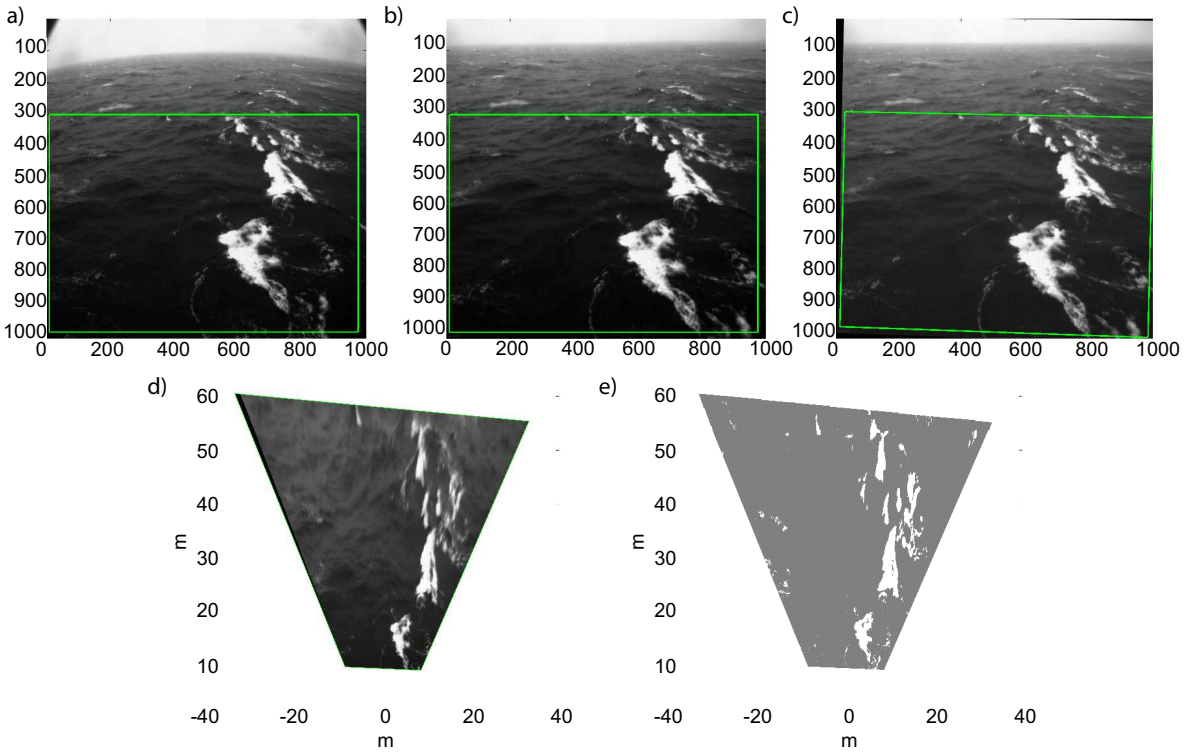

Figure 2.4: Steps of the image processing: a) raw image, b) lens calibration, c) roll and yaw correction, d) projection based on incidence angle and height of camera assuming flat surface and e) thresholded and projected image

pixel. Pre-thresholding avoids brightness bleeding when removing background gradients.

Removing background gradients was found to greatly improve subsequent whitecap detection via the typical automated brightness threshold techniques. A test dataset was used to evaluate the effectiveness of flattening the background intensity gradient for removing biases arising from varying brightness and exposure settings. This dataset consisted of imagery taken over the course of two days during HiWinGS from two Mobotix MX-M24M IP cameras with 32 mm lenses, providing a 60° field of view, on the starboard side of the *R/V Knorr* with closely matched fields of view. One camera setting remained unchanged during the test while the target brightness and exposure settings were changed on the other one. Ignoring the background gradients resulted in up to a factor 4 difference between W determined from the two cameras, removing them reduced the difference to a factor of 0.7 to

1.04.

Whitecaps were then isolated in the pre-processed rectified images by the automated whitecap extraction (AWE) algorithm *Callaghan and White* [2009] which computes the most suitable brightness threshold for each individual image based on the derivatives of an image structure function. The AWE algorithm has been used successfully to analyze large datasets [*Callaghan et al.*, 2008a,b; *Goddijn-Murphy et al.*, 2011; *Scanlon and Ward*, 2013, 2016; *Schwendeman and Thomson*, 2015a; *Schwendeman et al.*, 2014] and has been shown to provide robust W results.

The thresholded images are orthorectified to compute W. This is achieved by first correcting for lens distortion based on intrinsic parameters determined using the Camera Calibration Toolbox for Matlab®[*Bouguet*, 2015]. The effect of the lens distortion can clearly be seen in the non-cropped raw imagery in Figure 2.4a and its correction in Figure 2.4b. Then, geo-rectification is performed by applying the 3D rotation matrix based on the roll, pitch, and yaw angles [*Holland et al.*, 1997; *Schwendeman and Thomson*, 2015b]. This step is illustrated on the raw imagery in Figure 2.4c and Figure 2.4d. Finally the thresholded images are interpolated onto the regular georectified grid with pixel dimensions of 0.01 m^2 (Figure 2.4e), W is determined for each image and an average W is computed for each 20-minute segment.

At this point an additional quality control step was undertaken and a cumulative whitecap coverage W_{CA} was computed based on the whitecap coverage (W_{frame}) determined from a single frame (F), normalized by the 20-minute averaged whitecap coverage (W_{20min}):

$$W_{CA_{norm}}(F) = \frac{W_{CA}(F)}{W_{20min}} = \left(\Sigma_{i=1}^{F} \frac{W_{frame}(i)}{i} \right) / W_{20min} \tag{2.10}$$

Time series of $W_{CA_{norm}}$ show that for the most part $W_{CA_{norm}}$ converges quickly towards unity staying within 1 standard deviation bounds ± 0.3 and ± 0.17 after 10 and 15 minutes, respectively (Figure 2.5). Several runs, however, do not appear to converge within 20 minutes.

Non-converging $W_{CA_{norm}}$ were identified based on standard deviation bounds computed from $W_{CA_{norm}}$ of the entire dataset for a given time (or frame number). Data was flagged if it fell outside the 2 standard deviation bound after 15 minutes and excluded from subsequent analysis. There does not seem to be a clear dependence of the convergence time on wind speed or wave age which could require a wind and sea state dependent averaging timescale. Note that an alternative approach to evaluate convergence of W can be found in *Callaghan et al.* [2008a].

After removing these data, the 20-minute W estimates were averaged to give hourly estimates on the same time intervals as the fluxes yielding 97 and 176 hourly means for SO GasEx and HiWinGS, respectively. Note that when comparing W to wave statistics, the number of hourly concurrent data points is 73 for SO GasEX and 172 for HiWinGS which is further reduced to 34 and 138 when considering wind seas for SO GasEx and HiWinGS, respectively.

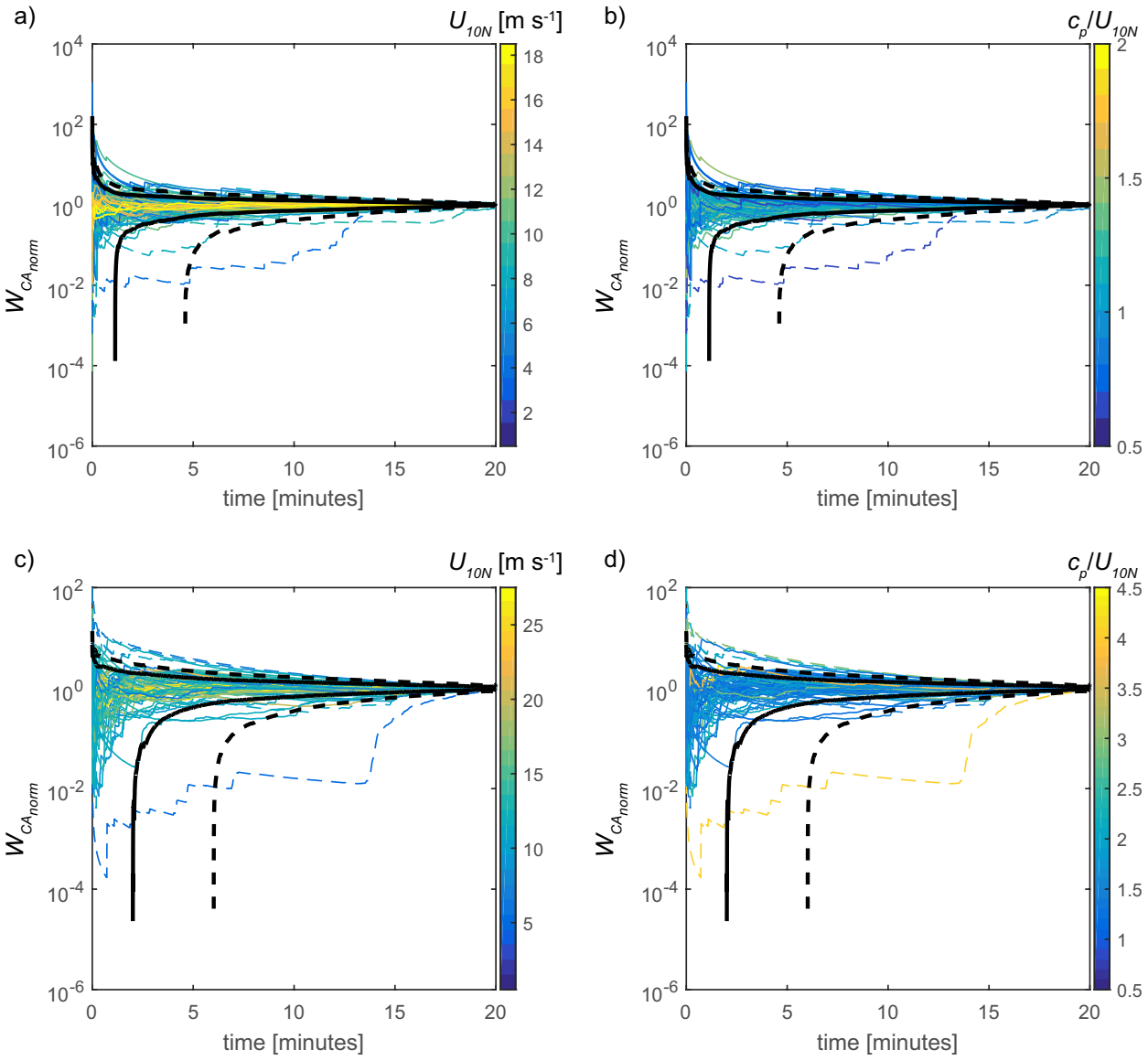

Figure 2.5: Time series of the normalized cumulative whitecap coverage WCA_norm color-coded by wind speed (a,c) and wave age (b,d) for SO GasEx (a,b) and HiWinGS (c,d). The black solid and dashed lines represent the one and two standard deviations bounds computed from WCA_norm of the respective datasets for a given time. Non-converging WCA_norm are represented by lines that fall outside of the 2 standard deviations bound after 15 minutes for more than 3 minutes

While an IMU was mounted in each camera housing during the HiWinGS campaign recording the rotation angles that allow for projection and scaling of the images, this was not the case during SO GasEx. Instead, rotation angles were determined by tracking the horizon (Schwendeman and Thomson 2015a). In order to test the performance of the horizon tracking algorithm, it was applied to the HiWinGS imagery and the computed angles were

plotted against those computed from the IMUs. As shown in Figure 2.6, the horizon tracking algorithm is successful at retrieving the roll and pitch angles. However, it generates erroneous attitude angles easily detectable as spikes in the pitch and roll time series. Depending on the type of analysis to be subsequently performed on the imagery, individual frames may be discarded or de-spiking algorithms [e.g. *Mori et al.*, 2007] may be applied.

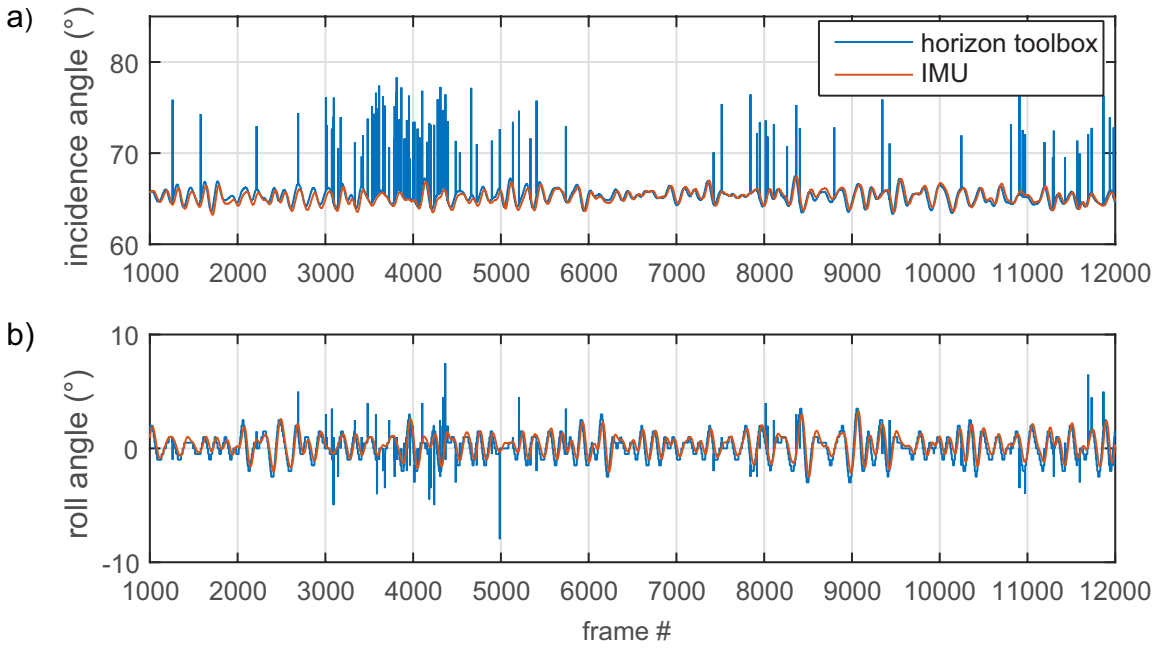

Figure 2.6: Time series of the a) incidence and b) roll angles measured by the IMU (orange) and determined by the horizon tracking toolbox (blue).

2.3.2 Wave-field Statistics

Wave field statistics were determined both from the directional spectra given by the Waverider, the WAMOS, and the WW3 hind cast and the 1D spectra obtained from the Riegl. The raw 3D displacement measurements of the Waverider were used to compute hourly spectra using the DIWASP toolbox [*Johnson*, 2012] to match the time scale of the other data. Half hourly wave spectra obtained from the four WW3 hind cast tracks were averaged to get hourly spectra. Figure 2.7 shows the spectrogram and an example of a directional spectrum from the WAMOS, those from the Waverider and WW3 are shown in Figure 2.8.

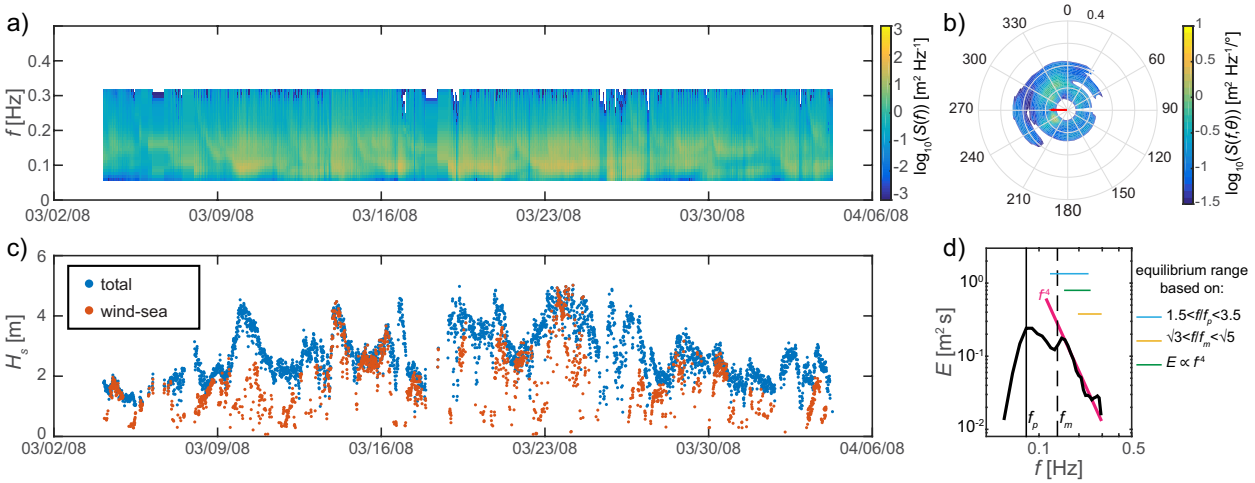

Figure 2.7: WAMOS measurements taken during SO GasEx: a) the spectragram, b) an example of a directional wave spectra, c) the time series of the significant wave height computed from the total spectrum and the wind-sea partition, and d) the omnidirectional wave spectra computed from b) with vertical lines depicting the peak and mean frequencies and horizontal lines showing equilibrium ranges based on the peak frequency, the mean frequency and portion of the spectra proportional to the frequency to the power -4

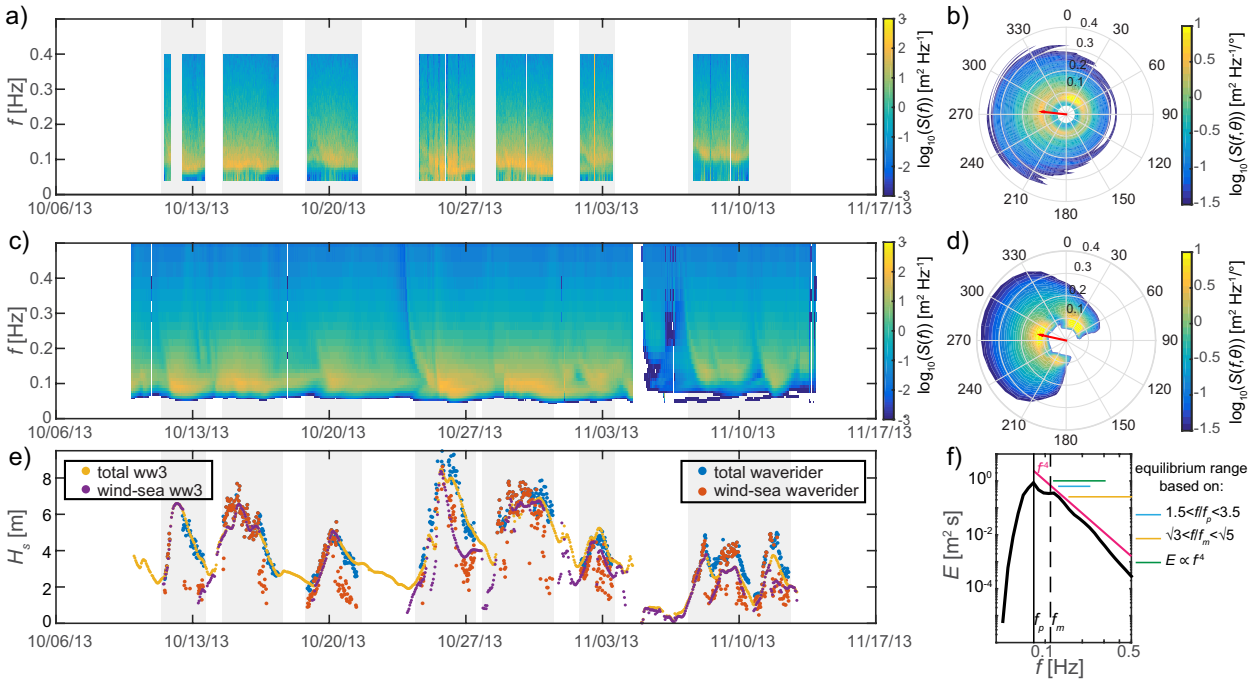

Figure 2.8: Wave field measurements and model hind cast for HiWinGS. a) and c) show spectrograms from the waverider and from the WAVEWATCH III® hind cast, respectively. Examples of directional wave spectra from the waverider, and from the WAVEWATCH III® hind cast corresponding to the same time are shown in b) and d). The time series of the significant wave heights computed from the total spectrum and the wind-sea partition of both the waverider and the model hind cast is shown in e), and d) depicts the omnidirectional wave spectra computed from d) with vertical lines depicting the peak and mean frequencies and horizontal lines showing equilibrium ranges based on the peak frequency, the mean frequency and portion of the spectra proportional to the frequency to the power -4. The grey shading in a), b), and e) indicates periods when the *R/V Knorr* was on station.

Wave statistics were first computed from 1D spectra measured by the Riegl or from the directionally integrated spectra of the WAMOS, Waverider and WW3 using a standard processing method. Similarly, a standard protocol was applied to the directional spectra to separate wind seas and swell and to get wave statistics for individual wave groups [*Hanson and Phillips*, 2001]. The computed wave statistics include the peak (f_p) and mean (f_m) frequencies, the peak and mean phase velocities (c_p and c_m, respectively) as well as the significant ($H_s = 4\left[\int E(f)df\right]^{1/2}$), peak ($H_p = 4\left[\int_{0.7f_p}^{1.3f_p} E(f)df\right]^{1/2}$) and mean ($H_m = 4\left[\int_{0.7f_m}^{1.3f_m} E(f)df\right]^{1/2}$) wave height of the entire wave field or individual wave system. When computing statistics for individual systems, we distinguish between wind-sea and swells, merging systems so as to have at the most a single wind sea and a single swell system.

No comparison of the statistics obtained from the different datasets is discussed here. Inter-comparison of various wave measurements and validation of the WW3 hind cast for HiWinGS will be reported in a separate paper along with a detailed description of the analysis methods applied to the directional spectra. An inter-comparison between the Riegl and WAMOS data recorded during SO GasEx can be found in *Cifuentes-Lorenzen et al.* [2013], while *Lund et al.* [2017] show a comparison of wind-sea and swell statistics obtained from WAMOS and WW3 for SO GasEx. As the statistics obtained from the various datasets are consistent for each experiment, results are reported based on WAMOS and WW3 statistics to allow usage of the full range of whitecap data.

2.3.3 Determination and evaluation of parameterizations

Wind and wave dependent parameterizations are determined through weighted least square fits of binned data for each dataset individually and combined. The binning was done using the equi-density method with each bin containing 7 data points, rather than at set regular intervals of wind and/or wave statistics. The reciprocal of the standard error in each bin was used as weights. Two fit statistics are reported to help evaluate the parameterizations:

1. The root mean square error ($rmse = \sqrt{\Sigma(W_{obs} - W_{param})^2/N}$), where W_{obs} are the hourly estimates of W, W_{param} are the W obtained from the parameterizations and N the number of estimates), and

2. The correlation coefficients ($r^2 = 1 - (\Sigma(\log_{10}(W_{obs} - \log_{10} W_{param})^2)/\Sigma(\log_{10} W_{obs} - (\log_{10} W_{obs})^2$, where the overbar represents the dataset average) are computed based on the *log*-residual as in *Schwendeman and Thomson* [2015a] so as to equally weight data points across orders of magnitude.

Note that all fits were performed in linear space and both W and the $rmse$ are reported in %. Note also that no consistent way of computing the $rmse$ has been used in the literature and

that these therefore are not directly comparable to previous studies such as *Schwendeman and Thomson* [2015a] and *Goddijn-Murphy et al.* [2011].

2.4 Results

2.4.1 Whitecap dependence on wind speed alone

Following the traditional approach, the dependence of W on wind speed alone is assessed. As seen in Figure 2.9a, the So GasEx and HiwinGS data fall within the recent wind speed only parameterizations reported in the literature since 2004. Results of the weighted least-square fit to a thresholded power law (Eq. 2.2) are listed in Table 2.5 along with the appropriate fit statistics. The power law fits to the individual and combined datasets agree closely with exponents closer to 1 than 3. It appears that the whitecap coverage saturates at high wind speeds ($U_{10N} > 22.5$ m s^{-1}). The fit to the combined dataset most closely follows that suggested by *Salisbury et al.* [2013] based on the 10 GHz microwave satellite data. The *rmse* between the best fits determined here and the 10 GHz parameterization of *Salisbury et al.* [2013] is around 0.1%. The next closest parameterization is that of Goddijn-Murphy et al. (2011, Eq. A, Table 2.1) with and *rmse* to the best fit to the combined data set of 1.4%. The *rmse* between the best fits determined here and the other parameterizations plotted in Figure 2.9a average around 2%.

Following the same approach as before, parameterizations of W as functions of the friction velocity were determined from the data. These are shown in Figure 2.9b and listed in Table 2.5. Parameterizations from previous studies plotted here are summarized in Table 2.4. Based on the fit statistics, there does not seem to be an improvement in using the friction velocity over the 10-m neutral wind speed. Again, the exponents of the thresholded power laws suggest a closer to linear than cubic relationship between W and u_*.

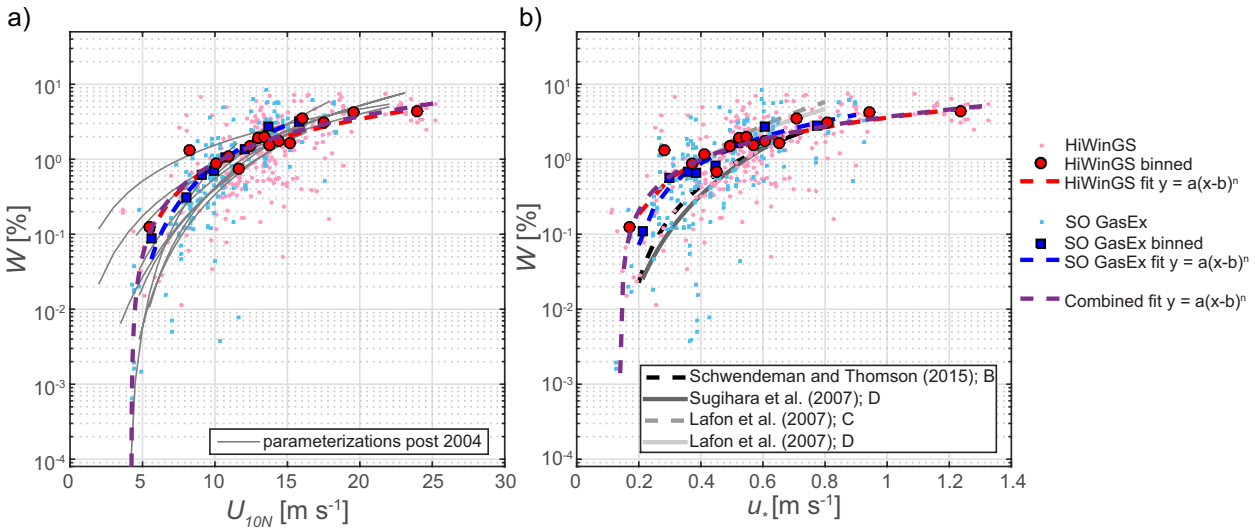

Figure 2.9: Whitecap coverage (W) as a function of a) the 10 m neutral wind speed (U_{10N}) and b) the friction velocity (u_*). The small light red dots show the hourly averaged whitecap coverage computed from the HiWinGS dataset, while the small blue squares are the 30 minute averaged whitecap coverage computed from the SO GasEx dataset. The blue squares and red circles show averages of 7 neighboring points for SO GasEx and HiWinGS, respectively. These are used to compute the best fit shown by the dashed red and blue lines. The dark purple lines show the best fits to the binned combined data. The gray lines correspond to the parameterizations summarized in Table 2.1 and Table 2.4

2.4.2 Whitecap dependence on sea state alone

In terms of pure sea state parameterization, the relationship between W and various forms of wave steepness parameters (S) and (mss) were investigated. These statistics were computed from entire spectra as well as from the wind-sea-only spectral partition. To compute S, three distinct wave heights (H_s, H_m, and H_p) were considered in combination with the two wave numbers (k_p and k_m) computed via the linear deep water dispersion relation ($k = (2\pi f)^2/g$) from the peak and the mean frequency, respectively.

Simple power laws of the form $W(X) = aX^n$ were found to be more suitable than thresholded power laws for these statistics. The computed fits are listed in Table 2.6 along with the appropriate statistics. Based on the correlation coefficients (r^2), steepness and slope parameters are poorer predictors for W than wind speed. Negative r^2 suggest that the model performs worse than a horizontal line. The root mean square errors ($rmse$) are also generally

higher than for the wind only fits. In general, very poor fits were obtained for SO GasEx. Of the wave steepness predictors, $(H_s k_m)/2$ gives the best fit for HiWinGS. Normalizing the mss by the directional spread and the frequency bandwidth yields only slightly improved fits. These two fits are shown in Figure 2.10. They correspond to the steepness estimate and the normalized mss that were shown to best fit the Northeast (NE) Pacific data published by *Schwendeman and Thomson* [2015a]. While the HiWinGS data appear to fall along the best fit suggested by *Schwendeman and Thomson* [2015a] when plotted against the wave steepness $(H_s k_m)/2$, significantly higher W were observed over less steep waves during SO GasEx than by Schwendeman and Thomson in the NE Pacific. More importantly, the SO GasEx data show very little variation of W with wave steepness, regardless of the wave statistics used. Neither dataset shows much variation with mss whether normalized or not. Considering only the wind-sea part of the spectrum does not improve the fits or increase the sensitivity of W to the slope estimates.

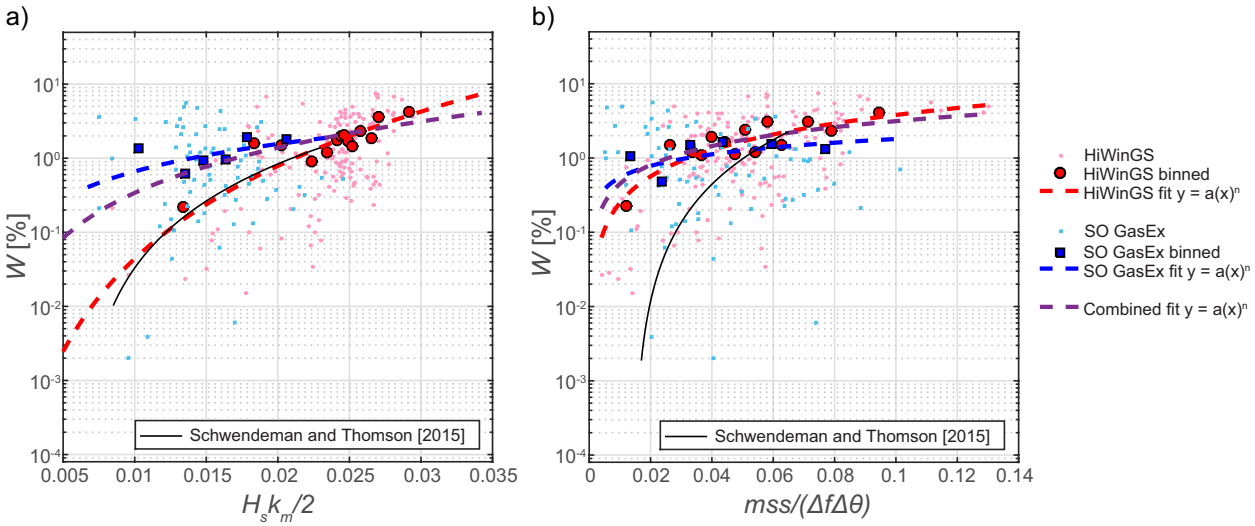

Figure 2.10: Whitecap coverage (W) as a function of a) mean wave steepness and b) mean square steepness. The small light red dots show the hourly averaged whitecap coverage computed from the HiWinGS dataset, while the small blue squares are the 30 minute averaged whitecap coverage computed from the SO GasEx dataset. The blue squares and red circles show averages of 7 neighboring points for SO GasEx and HiWinGS, respectively. These are used to compute the best fit shown by the dashed red and blue lines. The dark purple lines show the best fits to the binned combined data. The black lines correspond to parameterizations of *Schwendeman and Thomson* [2015a]

2.4.3 Combined influence of wind and wave field on Whitecap coverage

The first metric considered that includes the combined effect of wind and wave field is the wave age. The wave age has been derived both in terms of u_* and U_{10N} as well as from the mean and peak phase speeds (c_m and c_p) of both the wind-sea and total spectra. As for the wave slope parameters, a non-thresholded power law fit was computed for the various wave age estimates (see Table 2.7). Shown in Figure 2.11 are W plotted against the wave age expressed both in terms of U_{10N} and u_* and the peak velocity of the total and wind-sea wave field. While overall better fits were found when the wave-age was expressed as a function of c_m, as was the case in *Schwendeman and Thomson* [2015a], plots of the wave-age as a function of c_p are shown here to illustrate how the SO GasEx and HiWinGS data compare to previous studies that addressed the wave-age dependence of W.

Both datasets in Figure 2.11a agree once more with that of *Schwendeman and Thomson* [2015a], and W is higher than reported in all other studies for a given wave age. Interestingly, when considering wind seas alone (Figure 2.11b and 2.11d), the two datasets presented here no longer show matching trends, and the SO GasEx W is lower than the HiWinGS W for a given wave age. The W magnitude for a given wave age during HiWinGS is similar for the total and the wind-sea derived wave age because the wind-sea partition often contained the dominant peak. Since swell was typically dominant during SO GasEx, the change in W magnitude between total wave age and wind-sea wave age suggests less breaking occurs when a young wind sea was superimposed on swell than in an overall young sea. The wave-wind and breaking-wave Reynolds numbers are the second type of non-dimensional parameters historically used to parameterize W including both wind and sea state dependence. When computing the wave-wind Reynolds numbers (R_{H_w}), the significant (H_s), mean (H_m), and peak (H_p) wave heights were considered. Similarly, when computing the breaking-wave Reynolds number (R_{B_w}), the peak (ω_p) and mean (ω_m) angular velocities were considered.

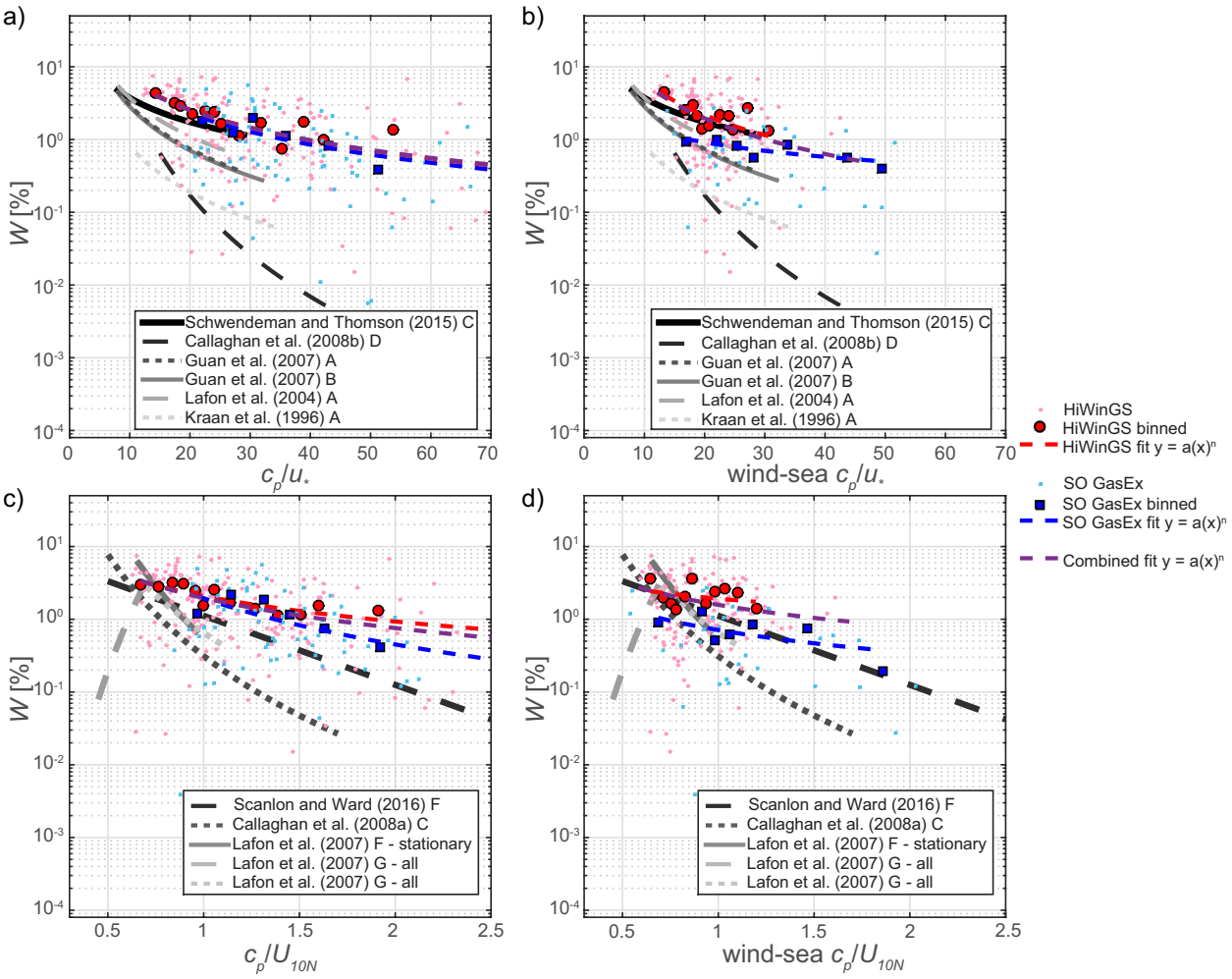

Figure 2.11: Whitecap coverage (W) as a function of wave age a) c_p/u_*, b) c_p/u_* using the wind-sea spectral peak, c) c_p/U_{10N} using the wind-sea spectral peak, and d) c_p/U_{10N} whitecap coverage. The small light red dots show the hourly averaged whitecap coverage computed from the HiWinGS dataset, while the small blue squares are the 30 minute averaged whitecap coverage computed from the SO GasEx dataset. The blue squares and red circles show averages of 7 neighboring points for SO GasEx and HiWinGS, respectively. These are used to compute the best fit shown by the dashed red and blue lines. The dark purple lines shows the best fit to the binned combined data. The black and gray lines correspond to the parameterizations summarized in Table 2.3

Again, both the full spectrum and the wind-sea only statistics were considered and least square fits were used to determine non-thresholded power laws relating W to the Reynolds numbers. The viscosities were computed based on the ships underway temperature and salinity measurements using the MATLAB Seawater Thermophysical Properties Library [*Nayar et al.*, 2016; *Sharqawy et al.*, 2010]. Results are summarized in Table 2.8 and Table 2.9. Two examples are shown in Figure 2.12. Overall, the wave-wind Reynolds number fits show

very good agreement between the datasets as well as with the findings of *Goddijn-Murphy et al.* [2011] and *Scanlon and Ward* [2016]. The *rmse* between the fits determined here and for Goddijn-Murphy et al.(2011; Eqs. D and E in Table 2.2), and for Scanlon and Ward (2016; Eq. B in Table 2.2) all average around 0.8%. Note that the parameterization of *Zhao and Toba* [2001] had to be adapted for this plot as they compute the wave-wind Reynolds number using the air viscosity rather than the water viscosity. A nominal ν_a to ν_w ratio of 11.03 was chosen. For R_{B_w}, there is poorer agreement between datasets as well as with prior studies, though scatter appears to be reduced (c.f. r^2 in Table 2.9 vs. those in Table 2.8). Note again that previous parameterizations were adapted as the breaking Reynolds number has typically been reported in terms of the air rather than the water viscosity.

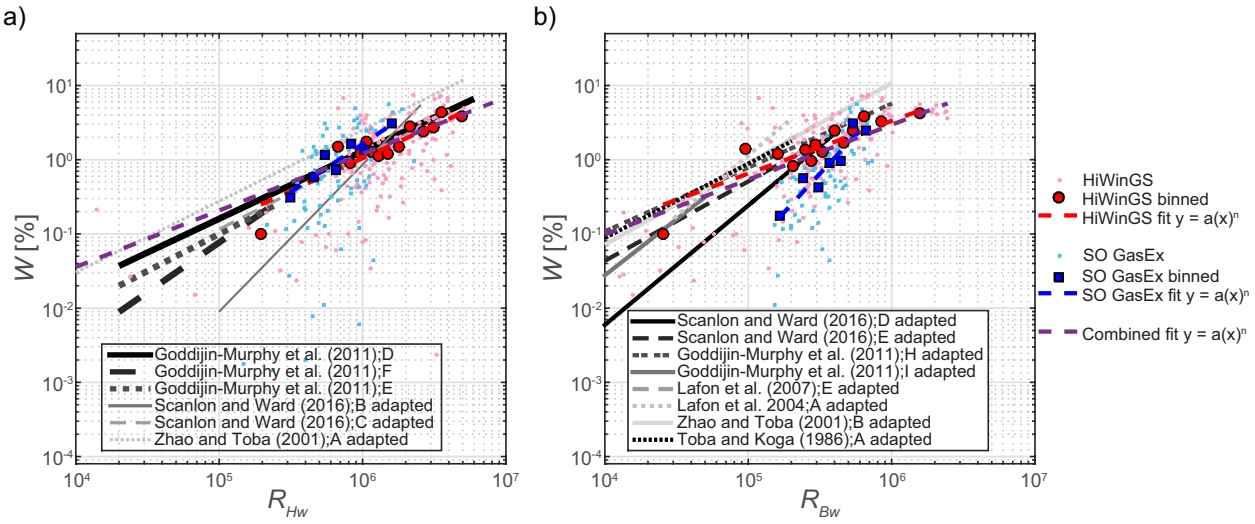

Figure 2.12: Whitecap coverage (W) as a function of a) wave-wind and b) breaking-wave Reynolds number computed from the significant wave height and peak angular velocity of the entire wave spectrum. The small light red dots show the hourly averaged whitecap coverage computed from the HiWinGS dataset, while the small blue squares are the 30 minute averaged whitecap coverage computed from the SO GasEx dataset. The blue squares and red circles show averages of 7 neighboring points for SO GasEx and HiWinGS, respectively. These are used to compute the best fit shown by the dashed red and blue lines. The dark purple lines shows the best fit to the binned combined data. The black and gray lines correspond to the parameterizations summarized in Table 2.2

2.4.4 Multiple parameter model

As mentioned in section 2.4.3, the dependence of W on wind and wave field parameters can be studied through dimensionless parameters. It is apparent that W may depend on (c,ρ_a,ρ_w,u,H,k,Γ,χ), where ρ_a and ρ_w are the densities of air and water, respectively, u is the wind speed or friction velocity, H a characteristic wave height, k a characteristic wavenumber, Γ the surface tension and χ the wind fetch.

Considering non-dimensional scaling, the whitecap coverage can be written as:

$$W = f\left(\frac{\rho_a}{\rho_w}, \frac{c}{u}, S, Re, F, Bo\right) \tag{2.11}$$

Here, c/u is the wave age, S is a measure of the wave steepness, Re the wave-wind or breaking-wave Reynolds number (see equations 2.3, 2.4 and 2.1), F the dimensionless fetch ($F = g\chi/(c_p^2$) or $F = g\chi/(u_*^2)$), and Bo the Bond number ($Bo = \Delta\rho g\Gamma^{-1}$), where g is the acceleration due to gravity,. The dimensionless group ρ_a/ρ_w is approximately constant and can be ignored. As waves small enough to be directly affected by surface tension (Γ) are not resolved in the measurements, the Bond number dependence is ignored. Furthermore, not having a measure of fetch, waves will be assumed to be fetch unlimited. This leads to a simplified model:

$$W = f\left(\frac{c}{u}, S, Re\right) \tag{2.12}$$

Assuming a power law dependence of W on the non-dimensional numbers, we can rewrite (Eq. 2.12) as follows:

$$W = aX, \text{ where } X = \left(\frac{c}{u}\right)^{\alpha} S^{\beta} Re^{\gamma} \tag{2.13}$$

The coefficients α, β, and γ can be found by minimizing a squared-difference cost function. This is done by taking the log on both sides of eq. 2.13 and solving the following linear regression:

$$\log_{10} W = \log_{10} a + \alpha \log_{10}(c/u) + \beta \log_{10} S + \gamma \log_{10} Re. \tag{2.14}$$

Choosing $S = (H_m k_m)/2$, $Re = (u_* H_m)/\nu_w$, and a wave age expressed in term of the friction velocity and the mean phase speed computed from the whole wave spectrum, coefficients were computed for each dataset individually and combined. The model determined from the combination of both datasets is shown in Figure 2.13. The coefficients resulting from the linear regressions are quite different for each dataset and regressions suggest that including the steepness does not significantly improve the model (Table 2.10). Indeed, T statistics suggest that $\beta = 0$ at a 91.4%, 24.7% and 77.6% confidence level for HiWinGS, SO GasEx, and the two combined. Fit statistics ($r^2 = 0.52$; $rmse \sim 1.39$) suggest that multiple parameters capture more of the variability in the observed W than single parameter wind and wave dependent models. Lack of agreement between the regression results, however, does not support using a multi non-dimensional parameter model as expressed by equation 2.14. Note that both the wave age and the Reynolds numbers combine wind and wave characteristic, but have opposite impacts on W. It may therefore be more physically intuitive to combine only one of these two non-dimensional number with the pure sea state parameter that is steepness. However statistically, combining only two non-dimensional numbers rather than 3 led to poorer results. As the Reynolds numbers capture most of the variance of W of the non-dimensional numbers considered here, $W(S, Re)$ is a better model than $W(S, c/u)$.

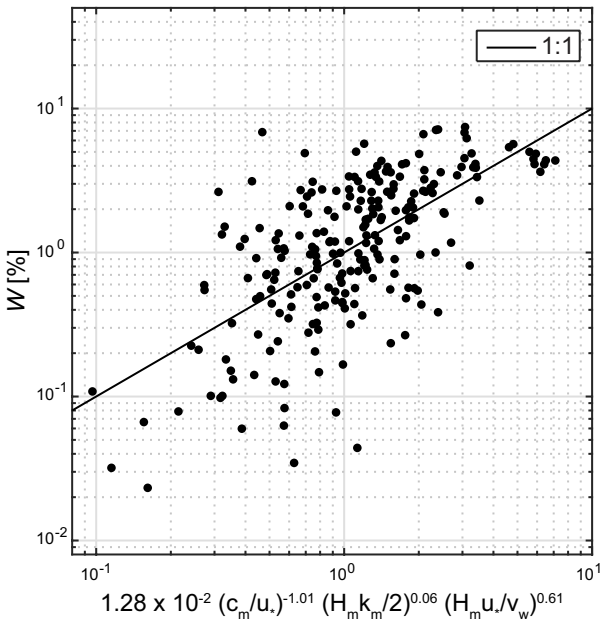

Figure 2.13: Scatter plot of the measured whitecap coverage (W) plotted against the multiple parameter model:$W = a\,(c_m/u_*)^{\alpha}\,(H_m k_m/2)^{\beta}\,(H_m u_*/\nu_w)^{\gamma}$. In black the 1:1 line

2.5 Discussion

Careful considerations need to be made before using parameterizations beyond their range of validity. Extrapolations, while often unavoidable, increase uncertainties and may lead to erroneous results. Ongoing efforts and targeted field campaigns allow for an ever-wider range of environmental conditions to be sampled, and a combined dataset will lead to more precise and universal parameterizations. New parameterizations should clearly state the range for which they are valid. This was done for the results reported here and as far as possible for the parameterizations compiled from the existing literature.

Prior studies not only differ in the whitecap detection algorithms used, but also in the application of appropriate image projection and scaling. In order to evaluate the impact of image scaling on the whitecap coverage estimate, we compared results from SO GasEx computed with or without scaling. For a given frame, image scaling significantly alters W, however, when computing 20-minute averaged W the impact of scaling appears to average out. The scaling has minimal impact when considering over 6000 frames as illustrated in Figure

2.14. Recording attitude angles and geo-rectifying images is therefore not essential when computing W, but is critical when tracking breakers such as for determining the breaking crest length distribution.

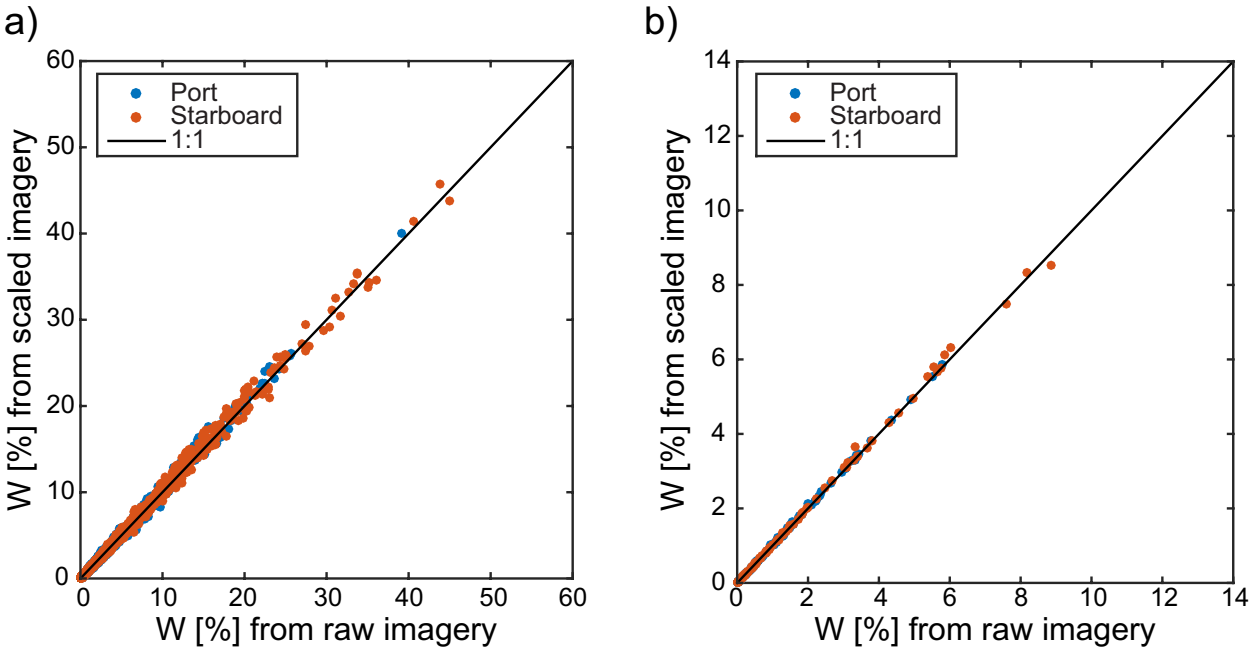

Figure 2.14: Scatter plots of the whitecap coverage (W) estimated from the scaled and non-scales imagery a) individual frames, and b) 20 minute averages

When considering wind speed only (Figure 2.9a) and wave-wind Reynolds number (Figure 2.12a) parameterizations, the level of agreement between the two datasets analyzed in this study with existing parameterizations is remarkable. Close agreement between these two datasets and recently published parameterizations gives confidence in the recently-developed and now commonly-used thresholding technique, and it may be valuable to reanalyze old datasets with the same method if possible. The additional step of removing background gradients before running the AWE (Section 2.3.1), ensures removal of biases arising from varying light conditions and camera exposure and brightness settings. A similar approach was put forward by *Mironov and Dulov* [2008]. Agreement between the WW3 hind cast wave statistics and in-situ observations is also remarkable (Figure 2.8). This should encourage reanalysis of wave dependent whitecap parameterizations for earlier datasets using hind casts to complement measurements, to evaluate them over a wider range of conditions.

Recent wind-speed-only total whitecap parameterizations showing less scatter than previously suggested for intermediate to high wind speeds. When considered within their originally defined wind speed range, they fall within 30% of their average, spanning an order of magnitude, for $U_10 > 10$ m s^{-1}. Note that the datasets presented here are much larger than those obtained from previous field experiments. Therefore, a larger amount of variability may be expected. Indeed, the data presented here displays variability similar to that of the combined historical datasets (c.f. *Albert et al.* [2016], Figure 1), which is greater than reported in individual studies. Significant scatter of up to 2 orders of magnitude remains in hourly W observations at many wind speeds and further studies are necessary to thoroughly understand it. While surfactants have been shown to prolong the lifetime of foam at the water surface [e.g., *Garrett*, 1967; *Callaghan et al.*, 2016] and their spatial inhomogeneity may account for some of the observed scatter for a given wind speed and sea state, they are difficult to measure under wind speeds greater than 10 m s^{-1} [*Cunliffe and Wurl*, 2014]. Technological development and more observations are evidently needed.

Targeted sampling under high winds and young sea conditions during HiWinGS extended the upper limit of the validity range for wind only whitecap parameterizations to 25 m s^{-1}. It is important to note here that unlike the majority of previous studies, the neutral 10-m wind speed was considered here. Both *Goddijn-Murphy et al.* [2011] and *Salisbury et al.* [2013] used equivalent neutral winds and, therefore maybe not surprisingly, match the parameterizations determined in the current study the best. The neutral wind speed and friction velocity along with non-dimensional numbers calculated from them are the only quantities that account for varying atmospheric stability conditions and therefore allow for true comparison from one dataset to the next. The differences in whitecap parameterizations arising from the stability dependence and correction has been evaluated by *Paget et al.* [2015].

As hinted to by *Schwendeman and Thomson* [2015a] and *Callaghan et al.* [2008b], W is seen to level off at high wind speed (c.f. Figure 2.1 and Figure 2.9a), not exceeding 10% when averaged over a 20 minute to hourly period. To evaluate W saturation at high winds,

linear fits were performed through the high wind speed data points and T-tests were used to determine if the slopes were significantly different than zero. T-tests reveal that for $U_{10N} >$ 18 m s^{-1} (26 hourly averages), the slope of W vs. U_{10N} is significantly different than zero only at a 14% confidence level, i.e. W is near constant. If the lower wind speed bound is reduced to 17.5 m s^{-1}, the confidence that the slope is significantly different than zero is raised to 74% and for $U_{10N} > 17$ m s^{-1} it is at 92%. Analysis of a very small number of visible images of the sea surface taken under hurricanes equally implied that W remains near constant for $U_{10} > 24$ m s^{-1} [*Holthuijsen et al.*, 2012]. Note that under high wind speeds, streaks of foam and especially spray dominate and *Holthuijsen et al.* [2012] did not include streaks in their W estimate making it more representative of the active whitecap coverage than the total coverage considered here. Widespread spray coverage at high wind speed may render whitecap and streak detection more difficult in imagery. There may be, therefore, a practical upper wind speed limit to the current image analysis technique.

The datasets analyzed here display a weaker wind speed dependence than most previous studies, except for *Salisbury et al.* [2013]. This weak wind speed dependence of W may be attributed to the low sea surface temperatures, averaging around 5-8℃, in which most of the measurements were taken. Only during the last station during HiWinGS did temperature exceed 10℃ while surface water temperatures during SO GasEX did not exceed 14℃. Early work by *Monahan and O'Muircheartaigh* [1986] provided evidence of a weaker dependence of W on U for SSTs of 16℃ compared to 32℃, but the increase of W with SST at a given wind speed was found to be modest. They analyzed 5 datasets including that collected by *Bortkovskii* [1987] which displays a strong positive dependence of W on SST and a near linear dependence of W on wind speed for SST less than 3℃. *Monahan and O'Muircheartaigh* [1986] argued that the water temperature will impact the exponent of the $W(U)$ power-law and suggested that for SSTs around 10℃ the exponent is around 2, while for SSTs warmer than 22℃ the exponent is greater than 3. The weaker wind speed dependence in cold waters is reflected in the latitudinal variation of the dependence of W on U shown by *Monahan et al.*

[2015] which is supported by *Salisbury* [2014] who demonstrated that using a power-law wind speed dependence with an exponent of 3.41 leads to overestimation of W at high latitudes. *Wu* [1988] suggested that rather than affecting the exponent, temperature affects a, the slope of the power-law Eq. (2.2), though no systematic trends were found. It was further argued that all coefficients of the power-law vary with temperature, with the strongest temperature dependence in the exponent [*Albert et al.*, 2016]. Cold waters suppress the rate of breaking, but increase the lifetime of bubbles and foam patches thus having the potential to enhance or reduce W [*Bortkovskii and Novak*, 1993]. Opposite trends in temperature dependence of air entrainment have been found in laboratory studies [*Hwang et al.*, 1991; *Salter et al.*, 2014; *Callaghan et al.*, 2014]. As individual field campaigns rarely sample a wide range of environmental parameters, it is essential to compile all existing data to detect trends and caution is advisable in determining trends from reduced datasets.

Continued improvement of whitecap parameterizations requires consideration of more than wind speed, specifically including statistics of the variable wave field. This motivated the concurrent measurement of whitecaps, winds, and wave field during SO GasEx and HiwinGS. Purely wave-dependent parameterizations that express W as a function of wave steepness or mean square slope within the equilibrium range do not give improved results over the wind-speed-only parameterizations. Nor does the wave age parameterization provide a better fit. The wave-wind Reynolds number based parameterizations show tighter correlations and better inter-dataset agreement than wave age and wave-only parameterizations. More wind and sea state conditions should be sampled to establish any limitations to these relationships. The breaking Reynolds number captures more of the variability in individual datasets, but R_{B_w} displays less inter-dataset agreement. Reynolds number functions have also been shown to provide better models of sea-spray aerosol fluxes than wind speed alone, with R_{H_w} explaining twice as much of total variance in direct measurements [*Norris et al.*, 2013]. While the Reynolds numbers have been typically computed using the friction velocity, the HiWinGS and SO GasEx data suggest that using the neutral 10 m wind speed lead to similar fit statistics

for W.

Energy weighted or mean statistics (f_m, H_m, k_m and c_m)are regularly chosen as being more representative of the breaking waves rather than peak statistics (f_p, H_p, k_p and c_p) which often correspond to the swell in multimodal spectra [*Sutherland and Melville*, 2015]. *Schwendeman and Thomson* [2015a] show that mean statistics are better predictors for W parameterizations further encouraging their use. The use of energy-weighted statistics of the wind-sea partition was motivated by the observation that most whitecaps are associated with waves even shorter than the mean [*Gemmrich et al.*, 2008]. This study, however, only suggests marginal improvement of fit statistics using mean wave field statistics.

As stated in the introduction, mss is computed over the equilibrium range. The existence of such a range, where sources and sinks are in balance was postulated by *Phillips* [1985]. Based on measurements by *Toba* [1973], *Phillips* [1985] proposed an analytical expression for the energy spectrum within that range which is characterized by a f^{-4} spectral shape. Bounds for the equilibrium range were later suggested by *Donelan* [1985] as $1.5f_p$ and $3.5f_p$. The upper bounds however seemed to be dictated by the highest frequency resolved by the measurements rather than the end of the range in which the spectrum is proportional to f^{-4}. Indeed, the equilibrium range was found to extend further: up to $6f_p$ [*Toba*, 1973] or 0.35 to 0.4 Hz in *Thomson et al.* [2013] for f_p generally less than 0.1 Hz. Furthermore, the upper limit of the equilibrium range is not always easily detectable with no visible shift in slope of $E(f)$ at the transition between the equilibrium and the saturation ranges.

The SO GasEx and HiWinGS datasets suggest that for multimodal spectra, particularly when the winds increase and wind-seas start appearing, $1.5f_p < f < 3.5f_p$ incorporates the wind sea peak, while $\sqrt{2}f_m \leq f \leq \sqrt{5}f_m$ usually falls beyond the wind-sea peak. This is illustrated in Figure 2.7d. What is more, the equilibrium range defined in terms of f_m, also extends to higher frequencies, and its upper limit falls within those observed by *Thomson et al.* [2013]. Determining the equilibrium range based on sections of the spectra beyond f_p that most closely decays as f^{-4} led to highly variable results with little agreement between

WW3 and the waverider. The mss computed over that range showed less correlation with W than the mss computed over $\sqrt{2}f_m \leq f \leq \sqrt{5}f_m$.

Finally, alignment of the swell and the wind sea was considered during the analysis by differentiating between periods of pure wind sea and pure swell as well as following, cross, and counter swell as defined in *Sugihara et al.* [2007]. This analysis did not, however, result in distinct trends for the different alignments and is consequently not shown here.

2.6 Conclusion

Analysis of visible imagery, flux and wave data collected during SO GasEx and HiWinGS allowed for evaluation of existing whitecap coverage parameterizations. Considering the two datasets separately and computing best fits for each individually facilitates critical assessment of the parameterizations discussed in this study, which are further verified by comparison to published parameterizations. Based on this work and recent studies reviewed herein, it is apparent that wind speed only parameterizations show very little scatter for winds above 10 m s^{-1} and are able to capture the observed variability of W well. The neutral wind speed or friction velocity should be used for those parameterizations. Of all the wave–only, and wind and wave dependent parameterizations tested here, the wave-wind Reynolds number parameterizations appear to be the most universally applicable ones as suggested by the close agreement between the best fits determined from the individual and combined datasets which are further in good agreement with those of *Goddijn-Murphy et al.* [2011] and *Scanlon and Ward* [2016]. Although wave-wind Reynolds number parameterizations capture somewhat less of the observed variability in W, they are in closer agreement to previous studies than wind-only parameterizations. When wave field statistics are readily available, wave-wind Reynolds number parameterizations should be used. Such statistics do not have to be derived from directional spectra as separating wind seas from swell does not appear to yield significantly better representation of W. Results from this study do not support a more

complex multi-parameter whitecap coverage model based on non-dimensional scaling.

Table 2.1: Parameterizations of Whitecap coverage [%] as a function of wind speed (since 2004).

Reference	Eq.	Formula	Wind speed range [m s^{-1}]	Sea state	Data Set
Scanlon and Ward [2016]	A	$W(U_{10}) = 7.84 \times 10^{-4}(U_{10N} - 2.56)^3$	$1 < U_{10} \leq 21$		Knorr11 & SOAP 2012
Schwendeman and Thomson [2015a]	A	$W(U_{10}) = 2.81 \times 10^{-3}(U_{10} - 3.87)^{2.76}$	$5.5 < U_{10} \leq 16$		North Pacific cruises 2012 & 2015
Salisbury et al. [2013]	A	$W_{10}(U_{10}) = 4.6 \times 10^{-3}U_{10}^{2.26}$	$2 < U_{10} \leq 20$		satellite W - 10 Ghz
	B	$W_{37}(U_{10}) = 3.97 \times 10^{-2}U_{10}^{1.59}$			satellite W - 37 Ghz
Goddijn-Murphy et al. [2011]	A	$W(U_{10}) = 15.9 \times 10^{-4}U_{10}^{2.7}$	$4.6 < U_{10} < 23.09$		
	B	$W(U_{10}) = 35.7 \times 10^{-4}(U_{10} - 3.83)^3$	$U_{10} < 11.5$		MAP W; in situ winds
	C	$W(U_{10}) = 46.9 \times 10^{-5}(U_{10} + 2.28)^3$	$U_{10} > 9.25$		
Kleiss and Melville [2010]	A	$W(U_{10}) = 6.58 \times 10^{-7}U_{10}^{4.9}$	$13 < U_{10} < 20.2$	fetch limited	GOTEX
	B	$W(U_{10}) = 5.83 \times 10^{-4}(U_{10} - 5.9)^3$			
Callaghan et al. [2008b]	A	$W(U_{10}) = 4.66 \times 10^{-5}U_{10}^{3.95}$	$3.5 < U_{10} < 12$	mixed seas	Coastal site at
	B	$W(U_{10}) = 2.99 \times 10^{-5}U_{10}^{3.95}$	$3.5 < U_{10} < 12$	swell dominated	Martha's Vineyard
Callaghan et al. [2008a]	A	$W(U_{10}) = 3.18 \times 10^{-3}(U_{10} - 3.7)^3$	$4.6 < U_{10} \leq 11.25$		MAP campaign
	B	$W(U_{10}) = 4.82 \times 10^{-4}(U_{10} + 1.98)^3$	$9.25 < U_{10} \leq 23.09$		
Sugihara et al. [2007]	A	$W(U_{10}) = 8.04 \times 10^{-4}(U_{10} - 2.01)^3$	$4.37 < U_{10} < 16.35$	all	Shirahama observation tower
	B	$W(U_{10N}) = 8.57 \times 10^{-4}(U_{10N} - 1.34)^3$	$4.79 < U_{10N} < 16.57$	pure wind-sea	
	C	$W(U_{10N}) = 1.09 \times 10^{-3}(U_{10N} - 3.24)^3$	$4.79 < U_{10N} < 16.57$	other	
Lafon et al. [2007]	A	$W(U_{10}) = 8.1 \times 10^{-5}U_{10}^{3.88}$	$10 \leq U_{10} \leq 17.9$	stationary	EMMA Campaign
	B	$W(U_{10}) = 1.9 \times 10^{-4}U_{10}^{3.51}$		all	Toulon-Hyeres bay

Table 2.2: Parameterizations of Whitecap coverage as a function of the friction velocity (since 2004).

Reference	Eq.	Formula	Wind speed range [m s^{-1}]	sea state conditions	Data Set
Schwendeman and Thomson [2015a]	B	$W(u_*) = 6.82(u_* - 1.39 \times 10^{-1})^{2.04}$	$0.2 < u_* \leq 0.75$		North Pacific cruises 2012 & 2015
Kleiss and Melville [2010]	C	$W(u_*) = 2u_*^{3.1}$	$0.46 \leq u_* \leq 0.79$	fetch limited	GOTEX
Sugihara et al. [2007]	D	$W(u_*) = 9.53(u_* - 0.074)^3$	$0.212 < u_* < 0.67$		Shirahama observation tower
Lafon et al. [2007]	C	$W(u_*) = 10.2 \times u_*^{2.53}$	$0.33 \leq u_* \leq 0.8$	stationary	EMMA Campaign Toulon-Hyeres bay
	D	$W(u_*) = 7.78 \times u_*^{2.29}$		all	

Table 2.3: Parameterizations of Whitecap coverage as a function of breaking and wave-wind Reynolds numbers.

Reference	Eq.	Formula	Range	Data set and comments
Scanlon and Ward [2016]	B	$W(R_{Ha}) = 1.1 \times 10^{-10} R_{Ha}^{1.98}$ (log − log fit)	$10^4 < R_{Ha} < 2.5 \times 10^5$	Knorr11 & SOAP 2012
	C	$W(R_{Ha}) = 1.4 \times 10^{-5} R_{Ha}^{0.98}$		
	D	$W(R_{Ba}) = 8.9 \times 10^{-8} R_{Ba}^{1.61}$ (log − log fit)	$2.1 \times 10^2 < R_{Ba} < 7 \times 10^4$	
	E	$W(R_{Ba}) = 2.7 \times 10^{-5} R_{Ba}^{1.07}$		
Goddijn-Murphy et al. [2011]	D	$W(R_{Hw}) = 4.51 \times 10^{-6} R_{Hw}^{0.91}$	$2 \times 10^4 < R_{Hw} < 6 \times 10^6$	MAP W; in situ wind; ECMWF wave stats; $R_{Hw\,w}$ computed based on wind sea H_s
	E	$W(R_{Hw}) = 10.2 \times 10^{-7} R_{Hw}$	$2 \times 10^4 < R_{Hw} < 2.5 \times 10^5$	
	F	$W(R_{Hw}) = 1.53 \times 10^{-8} R_{Hw}^{1.34}$	$2 \times 10^4 < R_{Hw} < 2.5 \times 10^5$ ($U_{10} < 8.6$)	
	G	$W(R_{Hw\,w}) = 11.3 \times 10^{-7} R_{Hw\,w}$		
	H	$W(R_{Ba}) = 28.6 \times 10^{-5} R_{Ba}^{0.86}$	$3 \times 10^2 < R_{Ba} < 10^5$	
	I	$W(R_{Ba}) = 8.28 \times 10^{-7} R_{Ba}^{1.51}$	$3 \times 10^2 < R_{Ba} < 5 \times 10^3$ ($U_{10} < 8.6$)	
Lafon et al. [2007]	E	$W(R_{Ba}) = 3.7 \times 10^{-5} R_{Ba}^{1.1}$	$6 \times 10^3 < R_{Ba} < 3 \times 10^4$	EMMA Campaign Toulon-Hyeres bay
Lafon et al. [2004]	A	$W(R_{Ba}) = 3.2 \times 10^{-7} R_{Ba}^{1.64}$	$3 \times 10^3 < R_{Ba} < 2 \times 10^4$	FETCH
Zhao and Toba [2001]	A	$W(R_{Ha}) = 4.02 \times 10^{-5} R_{Ha}^{0.96}$	$10^2 \leq R_{Ha} \leq 5 \times 10^5$	wind-wave tunnel, coastal and other field data from six different studies
	B	$W(R_{Ba}) = 3.88 \times 10^{-5} R_{Ba}^{1.09}$	$10^2 \leq R_{Ba} < 10^5$	
Toba and Koga [1986]	A	$W(R_{Ba}) = 8.9 \times 10^{-5} R_{Ba}$	$5 \times 10^2 < R_{Ba} < 2 \times 10^4$	wind-wave tunnel & oceanographic tower

Table 2.4: Parameterizations of Whitecap coverage as a function of wave age.

Reference	Eq.	Formula	Range	Data sets
Schwendeman and Thomson [2015a]	C	$W\left(\frac{c_p}{u_*}\right) = 47\left(\frac{c_p}{u_*}\right)^{-1.1}$	$8 < \frac{c_p}{u_*} < 29$	North Pacific cruises 2012 and 2015
	D	$W\left(\frac{c_m}{U_{10}}\right) = 8.48 \times 10^{-1}\left(\frac{c_m}{U_{10}}\right)^{-3.53}$		
	E	$W\left(\frac{c_m}{u_*}\right) = 9.33 \times 10^{2}\left(\frac{c_m}{u_*}\right)^{-1.945}$	$18 < \frac{c_m}{u_*} < 52$	
Kleiss and Melville [2010]	D	$W\left(\frac{c_p}{U_{10}}\right) = 2.98 \times 10^{-2}\left(\frac{c_p}{U_{10}}\right)^{-3.15}$	$0.6 \leq \frac{c_p}{U_{10}} \leq 1.45$	GOTEX
	E	$W\left(\frac{c_p}{u_*}\right) = 18^{2}\left(\frac{c_p}{u_*}\right)^{-2.71}$	$10 < \frac{c_p}{u_*} \leq 32$	
Callaghan et al. [2008b]	C	$W\left(\frac{c_p}{U_{10}}\right) = 3.11 \times 10^{-2}\left(\frac{c_p}{U_{10}}\right)^{-4.63}$	$0.5 \leq \frac{c_p}{U_{10}} \leq 1.7$	Coastal site at Martha's Vineyard
	D	$W\left(\frac{c_p}{u_*}\right) = 1.81 \times 10^{5}\left(\frac{c_p}{u_*}\right)^{-4.63}$	$15 \leq \frac{c_p}{u_*} \leq 48$	
Guan et al. [2007]	A	$W\left(\frac{c_p}{u_*}\right) = 2.97 \times 10^{2}\left(\frac{c_p}{u_*}\right)^{-2}$	$8 < \frac{c_p}{u_*} < 28$	FETCH
	B	$W\left(\frac{c_p}{u_*}\right) = 2.82 \times 10^{2}\left(\frac{c_p}{u_*}\right)^{-2}$	$8 < \frac{c_p}{u_*} < 32$	FETCH and Bohai Sea data sets
Lafon et al. [2007]	F	$W\left(\frac{c_p}{U_{10}}\right) = 0.54 \times \left(\frac{c_p}{U_{10}}\right)^{-5.75}$	$0.67 \leq \frac{c_p}{U_{10}} < 1$	EMMA Campaign Toulon-Hyeres bay
	G	$W\left(\frac{c_p}{U_{10}}\right) = \begin{cases} 70 \times \left(\frac{c_p}{U_{10}}\right)^{8.5} \\ 0.65 \times \left(\frac{c_p}{U_{10}}\right)^{-4.1} \end{cases}$	$0.52 \leq \frac{c_p}{U_{10}} \leq 0.69$ $0.69 < \frac{c_p}{U_{10}} < 1$	
Lafon et al. [2004]	B	$W\left(\frac{c_p}{u_*}\right) = 210\left(\frac{c_p}{u_*}\right)^{-1.75}$	$15 < \frac{c_p}{u_*} < 28$	
	C	$W\left(\frac{c_p}{u_*}\right) = 2 \times 10^{6}\left(\frac{c_p}{u_*}\right)^{-4.9}$	$8 < \frac{c_p}{u_*} < 28$	FETCH
	D	$W\left(\frac{c_p}{u_*}\right) = -0.187 \times \left(\frac{c_p}{u_*}\right) + 5.2$	$8 < \frac{c_p}{u_*} < 28$	
Kraan et al. [1996]	A	$W_A\left(\frac{c_p}{u_*}\right) = 96\left(\frac{c_p}{u_*}\right)^{-2.08}$	$11 \leq \frac{c_p}{u_*} \leq 34$	ASGASEX & Meetpost Nooordwjik coastal research platform

Table 2.5: Wind speed only parameterizations of whitecap coverage determined in this study. Fits were computed from the binned averages, but statistics are reported with respect to the hourly estimates. Note that W is expressed as a percentage as is its $rmse$. The correlation coefficients were computed in log space to give equal weight to the whitecap data across several orders of magnitude.

Experiment	best fit equation	range	r^2	$rmse$
HiWinGS	$W = 8.07 \times 10^{-2}(U_{10N} - 4.45)^{1.37}$	$5.46 \leq U_{10N} \leq 23.96$	0.51	1.35
SO GasEx	$W = 2.31 \times 10^{-2}(U_{10N} - 4.20)^{2.03}$	$5.61 \leq U_{10N} \leq 15.82$	0.34	0.96
Combined	$W = 7.38 \times 10^{-2}(U_{10N} - 4.23)^{1.42}$	$4.56 \leq U_{10N} \leq 25.10$	0.48	1.22
HiWinGS	$W = 4.24(u_* - 0.14)^{1.10}$	$0.17 \leq u_* \leq 1.27$	0.51	1.35
SO GasEx	$W = 5.84(u_* - 0.17)^{1.13}$	$0.21 \leq u_* \leq 0.77$	0.16	1.00
Combined	$W = 4.32(u_* - 0.14)^{1.09}$	$0.15 \leq u_* \leq 1.24$	0.37	1.24

Table 2.6: Wave steepness and mean square slope parameterizations of whitecap coverage (%) determined in this study. Wind-sea only statistics are denoted by a 'ws' subscript. Fits and data computed as for Table 2.5.

Predictor	Experiment	a	n	range	r^2	rmse
mss	HiWinGS	1.47E+04	1.63	1.43E-03 – 5.32E-03	0.16	1.61
	SO GasEx	5.40E+00	0.28	8.05E-04 – 4.59E-03	-0.11	1.32
	Combined	1.72E+02	0.82	6.48E-04 – 5.35E-03	-0.04	1.56
mss_{ws}	HiWinGS	4.42E+03	1.39	2.01E-03 – 6.84E-03	-0.08	1.64
	SO GasEx	2.81E+00	0.19	6.27E-04 – 3.80E-03	-0.13	0.72
	Combined	1.73E+03	1.22	3.87E-04 – 6.16E-03	0.00	1.54
$mss/\Delta\theta\Delta f$	HiWinGS	5.74E+01	1.16	1.04E-02 – 9.31E-02	0.19	1.49
	SO GasEx	3.67E+00	0.34	7.61E-03 – 7.04E-02	-0.18	1.32
	Combined	1.75E+01	0.75	5.25E-03 – 9.13E-02	0.13	1.48
$mss_{ws}/\Delta\theta\Delta f$	HiWinGS	4.76E+01	1.07	1.24E-02 – 1.16E-01	0.25	1.47
	SO GasEx	2.54E+00	0.25	5.10E-03 – 2.02E-02	-0.15	0.70
	Combined	3.68E+01	0.96	2.82E-03 – 1.10E-01	0.04	1.41
$H_s k_m/2$	HiWinGS	9.05E+06	4.16	1.34E-02 – 2.91E-02	0.21	1.54
	SO GasEx	1.91E+02	1.23	1.03E-02 – 2.06E-02	-0.19	1.30
	Combined	3.71E+03	2.02	8.83E-03 – 2.87E-02	0.05	1.48
$H_m k_m/2$	HiWinGS	3.08E+05	2.40	3.79E-03 – 7.77E-03	0.12	1.63
	SO GasEx	1.55E+02	0.94	3.15E-03 – 6.90E-03	-0.17	1.32
	Combined	1.70E+03	1.36	2.66E-03 – 7.72E-03	-0.05	1.57
$H_p k_p/2$	HiWinGS	5.98E+02	1.27	2.53E-03 – 1.67E-02	0.04	1.60
	SO GasEx	2.28E-01	-0.31	3.63E-03 – 1.21E-02	-0.11	1.30
	Combined	1.23E+02	0.91	2.37E-03 – 1.67E-02	-0.10	1.56

Table 2.7: Wave age parameterizations of whitecap coverage (%) determined in this study. Wind-sea only statistics are denoted by a 'ws' subscript.Fits and data computed as for 2.5.

Predictor	Experiment	a	n	range	r^2	rmse
c_p/U_{10N}	HiWinGS	2.09E+00	-1.17	0.67 – 2.59	0.08	1.58
	SO GasEx	1.94E+00	-2.11	0.97 – 3.17	0.06	1.24
	Combined	1.96E+00	-1.38	0.67 – 3.64	0.09	1.48
c_p/u_*	HiWinGS	1.76E+02	-1.41	14.22 – 80.22	0.24	1.47
	SO GasEx	1.57E+02	-1.41	21.98 – 79.03	-0.04	1.19
	Combined	1.57E+02	-1.38	14.22 – 106.58	0.13	1.39
$c_{p_{ws}}/U_{10N}$	HiWinGS	1.92E+00	-0.54	0.65 – 1.2	-0.11	1.76
	SO GasEx	7.11E-01	-1.04	0.69 – 1.86	-0.11	0.68
	Combined	1.58E+00	-1.02	0.58 – 1.72	-0.08	1.68
$c_{p_{ws}}/u_*$	HiWinGS	2.34E+02	-1.56	13.26 – 30.65	-0.01	1.63
	SO GasEx	6.65E+00	-0.66	16.9 – 49.47	-0.18	0.69
	Combined	2.61E+02	-1.63	12.14 – 47.78	0.04	1.54
c_m/U_{10N}	HiWinGS	1.35E+00	-1.4	0.52 – 1.88	0.1	1.61
	SO GasEx	1.31E+00	-3.64	0.81 – 2.27	0.3	0.98
	Combined	1.25E+00	-1.78	0.52 – 2.57	0.16	1.48
c_m/u_*	HiWinGS	1.57E+02	-1.51	10.65 – 57.66	0.23	1.51
	SO GasEx	2.82E+03	-2.42	18.55 – 58	0.13	1.01
	Combined	2.25E+02	-1.64	10.65 – 77.51	0.22	1.4
$c_{m_{ws}}/U_{10N}$	HiWinGS	1.77E+00	-0.52	0.48 – 0.95	-0.13	1.75
	SO GasEx	5.38E-01	-2.27	0.66 – 1.64	0	0.64
	Combined	1.08E+00	-1.42	0.41 – 1.51	0	1.64
$c_{m_{ws}}/u_*$	HiWinGS	1.26E+02	-1.48	9.82 – 24.07	0.02	1.67
	SO GasEx	3.57E+01	-1.22	16.8 – 43.85	-0.1	0.65
	Combined	9.99E+01	-1.44	8.11 – 40.25	0.12	1.54

Table 2.8: Wave-wind Reynolds number parameterizations of whitecap coverage (%) determined in this study. Wind-sea only statistics are denoted by a 'ws' subscript. Fits and data computed as for Table 2.5.

Predictor	Experiment	a	n	range	r^2	rmse
$u_* H_s/\nu_w$	HiWinGS	5.38E-06	0.88	1.95E+05 – 4.90E+06	0.35	1.39
	SO GasEx	3.16E-08	1.29	3.12E+05 – 1.59E+06	0.1	1.1
	Combined	3.21E-05	0.76	1.46E+05 – 6.00E+06	0.25	1.31
$u_* H_{s_{ws}}/\nu_w$	HiWinGS	2.75E-04	0.62	2.40E+05 – 6.73E+06	0.34	1.45
	SO GasEx	5.98E-05	0.72	2.44E+05 – 7.24E+05	-0.06	0.71
	Combined	9.91E-05	0.69	1.25E+05 – 4.29E+06	0.35	1.34
$u_* H_p/\nu_w$	HiWinGS	1.64E-05	0.82	1.45E+05 – 3.85E+06	0.33	1.41
	SO GasEx	8.83E-08	1.24	2.39E+05 – 1.22E+06	0.09	1.09
	Combined	5.65E-05	0.74	1.11E+05 – 4.69E+06	0.24	1.33
$u_* H_{p_{ws}}/\nu_w$	HiWinGS	3.77E-04	0.61	1.90E+05 – 5.19E+06	0.33	1.46
	SO GasEx	1.93E-07	1.18	2.18E+05 – 5.88E+05	-0.08	0.73
	Combined	7.03E-05	0.73	1.09E+05 – 3.43E+06	0.34	1.36
$u_* H_m/\nu_w$	HiWinGS	1.20E-05	0.91	5.50E+04 – 1.30E+06	0.36	1.42
	SO GasEx	2.10E-07	1.25	1.05E+05 – 5.25E+05	0.09	1.16
	Combined	5.80E-05	0.79	4.57E+04 – 1.59E+06	0.24	1.33
$u_* H_{m_{ws}}/\nu_w$	HiWinGS	4.64E-04	0.64	6.06E+04 – 1.70E+06	0.34	1.45
	SO GasEx	1.13E-04	0.75	5.22E+04 – 2.30E+05	0.04	0.74
	Combined	2.37E-04	0.7	2.15E+04 – 1.17E+06	0.35	1.35

Table 2.9: Breaking Reynolds number parameterizations of whitecap coverage (%) determined in this study. Wind-sea only statistics are denoted by a 'ws' subscript. Fits and data computed as for Table 2.5.

Predictor	Experiment	a	n	range	r^2	rmse
$\frac{u_*}{\omega_p \nu_w}$	HiWinGS	1.85E-04	0.71	2.54E+04 – 1.58E+06	0.42	1.4
	SO GasEx	2.10E-12	2.09	1.66E+05 – 6.60E+05	0.33	0.98
	Combined	1.08E-04	0.74	2.54E+04 – 2.04E+06	0.24	1.34
$\frac{u_*}{\omega_{pws} \nu_w}$	HiWinGS	2.50E-03	0.52	5.47E+04 – 1.99E+06	0.3	1.44
	SO GasEx	4.10E-06	0.98	1.38E+05 – 3.51E+05	0	0.68
	Combined	2.24E-04	0.7	4.70E+04 – 1.31E+06	0.28	1.36
$\frac{u_*}{\omega_m \nu_w}$	HiWinGS	2.39E-04	0.7	1.87E+04 – 1.17E+06	0.4	1.37
	SO GasEx	3.33E-11	1.92	1.40E+05 – 4.77E+05	0.33	0.93
	Combined	1.06E-04	0.76	1.87E+04 – 1.45E+06	0.23	1.32
$\frac{u_*}{\omega_{pws} \nu_w}$	HiWinGS	1.39E-03	0.58	4.47E+04 – 1.49E+06	0.31	1.42
	SO GasEx	1.93E-06	1.05	1.33E+05 – 2.84E+05	0.06	0.67
	Combined	1.70E-04	0.73	4.15E+04 – 9.62E+05	0.24	1.36

Table 2.10: Results of the linear regression: $W = a\,(c_m/u_*)^{\alpha}\,(H_m k_m/2)^{\beta}\,(H_m u_*/\nu_w)^{\gamma}$.

Experiment		Estimate	T-Stat	pValue
HiWinGS	a	1.43E-04	-2.56	1.13E-02
	α	-0.77	-3.73	2.62E-04
	β	-0.03	-0.11	9.14E-01
	γ	0.86	5.32	3.53E-07
SO GasEx	a	7.52E-05	-1.16	2.51E-01
	α	-1.33	-2.42	1.85E-02
	β	-0.66	-1.17	2.47E-01
	$\boldsymbol{\gamma}$	0.82	2.25	2.77E-02
Combined	a	1.28E-02	-1.84	6.72E-02
	α	-1.01	-5.44	1.40E-07
	β	0.06	0.29	7.76E-01
	γ	0.61	5.3	2.77E-07

Chapter 3

The Cubic-Quadratic k Conundrum

A version of this chapter was submitted as a Geophysical Research Letter: Brumer S. E., C. J. Zappa, B. W. Blomquist, C. W. Fairall, A. Cifuentes-Lorenzen, J. B. Edson, I. M. Brooks, and B. J. Huebert (2017). Wave-related Reynolds number parameterizations of CO_2 and DMS transfer velocities.

3.1 Introduction

Adequate characterization of gas transfer across the air-sea interface is not only essential to quantify local and global sinks and sources of carbon dioxide, CO_2, but also to budget many other trace gases that influence Earth's climate [*Carpenter et al.*, 2012]. These include, among others, marine aerosol precursors such as dimethyl sulfide, DMS [*Charlson et al.*, 1987].

The bulk gas flux (F_x) across the air-sea interface can be expressed as a function of the concentration difference (ΔC_x) across the air-water interface, and a kinematic parameter, the transfer velocity (k_x):

$$F_x = k_x \Delta C_x = k_x K_{0x}(p_{wx} - p_{ax}), \tag{3.1}$$

where K_{0x} is the solubility of the gas, x, in seawater, p_{ax} and p_{wx} are the partial pressures of

x in the air and surface water, respectively. k_x represents the mass transfer resistances of various physical forcing mechanisms and incorporates the dependence of the transfer on the diffusivity of the gas in water (which varies for different gases, temperatures and salinities).

Studies have shown that the interfacial transfer velocity is regulated by the turbulence in the air and water surface microlayers. This turbulence is generated by wind stress at the water surface and buoyancy effects [*Jähne et al.*, 1987; *Komori et al.*, 1993]. k is therefore typically parameterized as a function of wind speed (U). One of the earliest parameterizations [*Liss and Merlivat*, 1986] derived from various field and laboratory measurements was a three piece linear function of U, corresponding to wind regimes in which no waves, capillary waves, or breaking waves are present. For simplicity and practical reasons, the impacts of waves were later no longer considered explicitly and a single quadratic [*Wanninkhof*, 1992] or cubic [*McGillis et al.*, 2001; *Wanninkhof and McGillis*, 1999] function linking k to U were adopted for all sea states.

Current climate modeling studies most commonly use quadratic wind speed parameterizations for k [*Arora et al.*, 2013; *Wanninkhof*, 1992]. These models parameterizations are tuned to give the correct result for the global radiocarbon carbon budget over yearly or decadal timescales [*Sweeney et al.*, 2007; *Wanninkhof*, 1992, 2014] and provide an important constraint for global studies, but have an uncertain relationship to transfer mechanisms over limited temporal and spatial scales. Recent eddy-covariance measurements [*Garbe et al.*, 2014] highlight the inadequacy of wind speed only parameterizations for gas transfer velocities. For wind speeds above 10 m s^{-1} observations display substantial scatter, and individual wind speed dependent parameterizations diverge; this can be attributed to a variety of environmental conditions and processes, particularly those associated with surface waves. The complex interplay of these processes means that wind speed alone cannot capture the variability of air-water gas exchange. For winds over 7 m s^{-1}, breaking waves become a key factor to consider when estimating gas fluxes. Both theoretical and experimental studies suggest that wind waves and their breaking can significantly enhance gas exchange

[*Woolf*, 1997]. Breaking results in additional upper ocean turbulence and generation of bubble clouds. Bubbles offer a second pathway for gas transfer between the atmosphere and ocean in addition to direct diffusion across the main interface. Their influence increases with decreasing solubility leading to significantly enhancement of the transfer of sparingly soluble gases such as CO_2 under wave breaking conditions.

The main proxy used to quantify breaking processes is the whitecap fraction (W) which is detectable in near surface imagery from ships or aircrafts (e.g.,*Brumer et al.* [2017] and references therein) and can be retrieved from satellite data [*Anguelova and Webster*, 2006]. This has led to parameterizations in which the total [*Zhao et al.*, 2003] or bubble mediated [*Woolf*, 1997, 2005] gas transfer velocities are expressed as a function of W. Similarly to k, W is typically modeled as a non-linear function of wind speed. However, several studies have shown that W can be better constrained by a function of breaking (R_B) and wave-wind (R_H) Reynolds numbers [*Goddijn-Murphy et al.*, 2011; *Zhao and Toba*, 2001]. *Norris et al.* [2013] provided further evidence that wave-breaking related processes may be showed that R_H better constrained by Reynolds numbers than by wind speed alone, showing R_H to be a more adequate predictor for sea-spray aerosol flux – which results from breaking waves – than did wind speed alone. These Reynolds numbers incorporate both wave field and wind speed dependence. The breaking Reynolds number is defined as: $R_{B_w} = (u_*^2)/\nu_w\omega_p)$, where ν_w is the viscosity of water, and ω_p is the peak angular frequency of the wave energy spectrum and u_* is the friction velocity. The use of the water viscosity is denoted by the "w" subscript. The wave-wind Reynolds number can be written as: $R_{H_w} = (u_* H_s)/\nu_w$, where H_s is the significant wave height.

Zhao et al. [2003] combined a parameterization that expresses k_{CO_2} as a power law of W based on data from *Wanninkhof et al.* [1995] and the relation of W and R_B from *Zhao and Toba* [2001]. They deduced:

$$k_{660} = 0.13 R_{B_a}^{0.63}, \tag{3.2}$$

where k_{660} is the gas velocity normalized to a Schmidt number, Sc, of 660 in units of cm h^{-1}.

Note that they used the air viscosity (ν_a) rather than the water viscosity for their Reynolds number calculations, hence the "a" subscript. Using wind tunnel data from *Jähne et al.* [1985], they further suggested:

$$k_{660} = 0.25 R_{B_a}^{0.67}. \tag{3.3}$$

Woolf [2005] built on his earlier model [*Woolf*, 1997] which separates breaking (k_b), whitecap-dependent, from non-breaking (k_0, u_* and Sc-dependent) contributions and expressed k as:

$$k = k_0 + k_b = 1.57 \times 10^{-4} u_* (600/Sc)^{1/2} + 2 \times 10^{-5} R_{H_w}. \tag{3.4}$$

Note, this model does not explicitly account for the solubility dependence of k_b, but is consistent with measurements of CO2 transfer at 20°C. Equation may therefore only be used for low solubility gases such as CO_2, requires extending for other gases [*Jeffery et al.*, 2010]. These relationships were determined for growing wind sea conditions. Recent studies [*Brumer et al.*, 2017; *Goddijn-Murphy et al.*, 2011] showed that statistics computed from the total wave spectra, including swells, captured observed variability in W at least equally well than wind-sea only statistics hinting to an extended applicability of Reynolds number parameterizations. To date few gas transfer measurements have been made with concurrent wave physics observations and the universality of these parameterizations has yet to be assessed. In this chapter, results from four field projects will be used to evaluate the utility of Reynolds number parameterizations for CO_2 and DMS and their performance in contrasted to that of wind-only relationships.

3.2 Data and Methods

3.2.1 GasEx-98

The GasEx-98 cruise was the first of the three Gas Exchange experiments and was conducted in the North Atlantic (46°6'N, 20°55'W) on the *R/V Ronald H. Brown* in May and June 1999.

Air-sea gas exchange was estimated from deliberate dual tracer release as well as direct eddy covariance measurements of CO_2 under wind speeds up to $\sim$15 m s^{-1}. These direct covariance fluxes were reported in [*McGillis et al.*, 2001] and hourly gas transfer velocities derived from these measurements will be used for this study. No wave measurements were made during GasEx-98. Instead, wave field statistics were computed from a WAVEWATCHIII®(WW3) global hindcast obtained from the database of the French Research Institute for Exploitation of the Sea (IFREMER) where 3-hourly statistics derived from the total spectrum with a 0.5° spatial resolution are stored. For this hindcast, the model was forced with wind fields from The Climate Forecast System Reanalysis [*Saha et al.*, 2010] and ST4-TEST471 source term parameterizations were used [*Rascle and Ardhuin*, 2013]. Fields of H_s and f_p were interpolated first in space onto the ship's track and then in time to match gas transfer velocities.

3.2.2 SO GasEx

The SO GasEx cruise took place on board the *R/V Ronald H. Brown* in the South Atlantic (51°S, 36°W) from February 28th to April 9th, 2008. Two multi-day, dual-gas tracer experiments were performed along with continuous eddy covariance measurements of CO_2 and DMS fluxes. A Riegl laser altimeter (model LD90-3100VHS) and a Wave and Surface Current Monitoring System (WAMOS®II) provided wave field data. Wind speeds averaged 9.7$\pm$3.2 m s^{-1} with a maximum of $\sim$18 m s^{-1} during periods of trustworthy gas transfer measurements. The tracer experiment results are published in *Ho et al.* [2011] and will not be considered here. Description of the momentum and CO_2 flux measurements can be found in*Edson et al.* [2011], along with a critical assessment on data quality. The DMS measurements are described in *Yang et al.* [2011] and the analysis of the wave measurements was reported by *Cifuentes-Lorenzen et al.* [2013] and *Lund et al.* [2017]. For this analysis hourly averages of the gas transfer velocities and wave statistics will be considered. The WAMOS resolves the directional wave, whereas the Riegl provides only onmidirectional information. Wave

field statistics are consistent between the Riegl and WAMOS, but WAMOS allows separation of wind-sea and swell components.

As the WAMOS was not running during the large storm that occurred during the SO GasEx return transit and the Riegl data are not reliable when the ship is moving, the wave data were suplemented by a WAVEWATCH-III® global hindcast from the IFREMER database. For this hindcast, the model was forced with ECMWF winds and ST4-TEST471 source term was used. *Lund et al.* [2017] found excellent agreement between the WAMOS and this hindcast for SO GasEX. As for GasEx-98, the 3-hourly hindcast fields of H_s and f_p derived from the total spectrum were interpolated first in space onto the ship's track and then in time to match gas transfer velocity estimates. For this study WAMOS statistics will be the primary data source and WW3 output will be used only for the last 5 days of flux measurements to allow inclusion of the storm event encountered on the return transit to Uruguay.

3.2.3 Knorr11

The Knorr11 cruise took place in the North Atlantic Ocean (41.53°N, 70.68°W) between June 25th and July 18th, 2011 aboard the *R/V Knorr*. The study region was selected for its high biological productivity and phytoplankton blooms. Wind speeds sampled during the cruise range from 2 to 20 m s^{-1}. The eddy covariance measurements of air–sea CO_2 and DMS fluxes have been reported by *Miller et al.* [2010], *Bell et al.* [2013], and *Bell et al.* [2017]. Omnidirectional surface wave spectra were obtained using an ultrasonic altimeter mounted at the end of a steel pole lowered through one of hawsehole on the bow of the ship [*Christensen et al.*, 2013]. An IMU mounted on the bow mast allowed for motion correction of the one-dimensional altimeter measurements. The significant wave heights measured during Knorr11 agree well with the 6-hourly, 0.1 horizontal resolution ECMWF Reanalysis ERA Interim and Satellite observations from AVISO regardless of whether the ship was on station or not. Good agreement was found between the measured and modeled peak frequencies while

on station. Estimates of ω_p while underway are therefore discarded. Two hourly averaged estimates of the gas transfer velocities of CO_2 and DMS and wave field statistics will be used here.

3.2.4 HiWinGS

The High Wind Gas exchange Study (HiWinGS) built on experiences and lessons from the three prior GasEx experiments with the goal of further improving physics-based air-sea gas transfer parameterizations for high winds and breaking-wave conditions. The HiWinGS cruise took place aboard the *R/V Knorr* in the North Atlantic between October 9$^{\text{th}}$ and November 14$^{\text{th}}$, 2013. Direct eddy correlation fluxes during HiWinGS include CO_2, DMS, acetone, and methanol [*Yang et al.*, 2014]. Instrumentation and methods for DMS and CO_2 flux measurements are described in *Blomquist et al.* [2010] and *Blomquist et al.* [2014]. The wave field was monitored with a Riegl laser altimeter (model LD90-3100VHS) and a Datawell DWR-4G Waverider buoy. Buoy wave measurements were only acquired on-station (approximately 68% of the cruise duration) and are supported and supplemented by a WW3 hindcast for the entire period of the cruise. The WW3 hindcast is described and an inter-comparison between the various wave measurements and the model hindcast will be reported in a separate HiWinGS submission. As the statistics computed from the hindcast match the buoy measurements well and provide the most complete dataset, they will be used for the results reported here.

3.2.5 Computation of wave-field statistics

Wave field statistics were computed from the directional wave spectra obtained from the WAMOS and WW3 hindcasts. Separation of the wind-sea and swell systems was achieved based on *Hanson and Phillips* [2001]. While hourly gas transfer velocities were computed for SO GasEx, WAMOS spectra and statistics were computed over 10.25 minutes and averaged to match the gas transfer velocity time resolution. For HiWinGS, the hindcast statistics were

obtained half hourly for each of 4 grid points around the ship position and averaged to give a single hourly time series matching the gas fluxes. The significant wave height is defined as follows: $H_s = 4[\int E(f)df]^{1/2}$, where $E(f)$ is either the total omnidirectional wave spectrum or the wind-sea partition. The peak angular velocity is determined from the peak frequency of each system of the whole spectrum: $\omega_p = 2\pi f_p$. In what follows, statistics computed from the wind-sea partition are denoted by a "ws" subscript.

3.2.6 Determination and evaluation of gas transfer velocity parameterizations

The gas transfer velocities of CO_2 ($k_{CO_{2_{660}}}$) and DMS ($k_{DMS_{660}}$) were referenced to a Schmidt number of 660 which corresponds to that of CO_2 at 20℃Using $k_{660} = k_{measured}\left(\frac{660}{Sc_{measured}}\right)^{-0.5}$. For each experiment and gas, seven different parameterizations are considered. Quadratic ($k = aU_{10N}^2 + b$), cubic ($k = aU_{10N}^3 + b$), and power-law ($k = aU_{10N}^n$) dependence on wind speed were evaluated as well as power-law dependence ($k = aR_x^n$) on the wave-wind and breaking Reynolds numbers computed from the total wave spectra and wind-sea partition only. Note, for GasEx-98 and the return transit leg of SO GasEx no wind-sea statistics could be determined. Also, no DMS measurements were taken during GasEx-98. Combining all data, a final set of parameterization is suggested.

Coefficients (a, b and n) were determined through weighted least-square regressions using equi-density bins containing 15 data points. The weights were set to equal the reciprocal of the variance in each bin. For the wind-sea statistics for $k_{CO_{2_{660}}}$ where bins were decreased to 5 data points due to the paucity of data available from the SO GasEx experiment. In order to compare the performance of the different parameterizations, three metrics are considered:

1. the variation of the exponent "n" among the four datasets,
2. the correlation coefficient (r^2), and
3. the root mean square error ($rmse$).

Both the r^2 and $rmse$ and were computed with respect to the hourly data.

3.3 Results

Key results and parameterizations determined from the four individual and the combined datasets are summarized below. Coefficients for various best-fit functions are reported in Tables 3.1 and 3.1 for CO_2 and DMS, respectively.

3.3.1 CO_2

Figure 3.1a shows the measured gas transfer velocities of CO_2 plotted against the neutral 10-m wind speed. The different dependencies of the $k_{CO_{2_{660}}}$ on U_{10N} observed during the 4 experiments are immediately apparent. While both GasEx datasets show close to cubic wind speed dependence with power-law fit exponents of 2.53 and 2.67 for GasEx-98 and SO GasEx, respectively, a power law with an exponent of 1.62 is the best fit to HiWinGS data. The Knorr11 dataset displays the weakest wind speed dependence with a power-law exponent of 1.46. The near-cubic dependences of $k_{CO_{2_{660}}}$ with U_{10N} are in agreement with those reported in *Edson et al.* [2011] and *McGillis et al.* [2001] for the two GasEx datasets. Quadratic parameterizations reported in *Wanninkhof* [1992] or *Ho et al.* [2006] under-predict all but the Knorr11 $k_{CO_{2_{660}}}$.

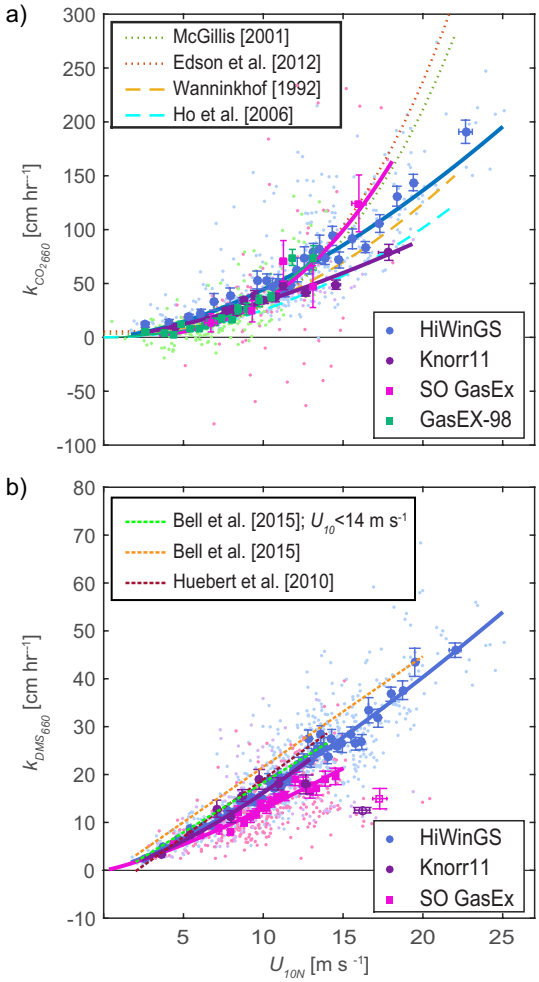

Figure 3.1: Measured gas transfer velocity of a) CO_2 and b) DMS, adjusted to a Schmidt number of 660 and plotted against 10 m neutral wind speed (U_{10N}). The smaller dots represent individual hourly and two-hourly estimates and the larger symboles are averages of equidensity bins of 15 data points. The solid lines represent best fits of power laws of the form $k = ax^n$. Examples of published cubic ($k = aU_{10}^3 + b$) and quadratic ($k = aU_{10}^2 + b$) parameterizations derived from CO_2 datasets are represented by dotted and dashed lines, respectively. Examples of published linear wind-speed dependent parameterization ($k = aU10 + b$) derived from DMS measurements are represented by dashed lines in b). The open symboles in b) represent outliers in the SO GasEx and Knorr11 datasets that cannot be reconciled by neither wind speed nor Reynolds numbers.

The wave-wind Reynolds number, computed from the total wave spectrum (Figure 3.2a), collapses the observations from all three experiments to a single curve with reduced scatter:

$$k_{CO_{2_{660}}} = 2.04 \times 10^{-4} R_{H_w}^{0.88} \tag{3.5}$$

with $r^2 = 0.65$ and $rmse = 29.38$ for all three datasets combined. These fit statistics are

slightly better than those obtained from wind-only fits (Table 3.1, Eq. p25). Equation 3.5 captures 58%, 31%, 63% and 69% of the observed variability in the GasEx-98 ($rmse$ = 16.40), SO GasEx ($rmse$ = 59.2), Knorr11 ($rmse$ = 13.86) and HiWinGS ($rmse$ = 27.83) measurements, respectively. A wind speed only power-law parameterization based on the combined dataset captures 60%, 25%, 70%, and 64% of the observed variability in the GasEx-98 ($rmse$ = 16.3), SO GasEx ($rmse$ = 61.57), Knorr11 ($rmse$ = 15.99), and HiWinGS ($rmse$ = 30.11) measurements, respectively.

Note that not only were more measurements taken during HiWinGS than during the other two experiments, but they were also spread over a wider range of wave and wind conditions. These combined fits are therefore mostly driven by the HiWinGS data. Nevertheless, fits to individual data sets also demonstrate the improved inter-dataset agreement with wave-wind Reynolds number compared to wind only. Power-law exponents of these fits, ranging from 0.66 (Knorr11) to 1.11 (GasEx-98), show less spread than those of wind speed power laws. Again, project specific wave-wind Reynolds number fits suggest marginal improvement compared to the best individual wind-only fits in terms of r^2 for HiWinGS and SO GasEx.

The breaking Reynolds number (Figure 3.2c), collapses the datasets, with power law exponents ranging from 0.52 (Knorr11) to 0.79 (GasEx-98). However, scatter is increased in comparison to the wind-wave Reynolds number for all experiments but GasEx-98. The best fit obtained from the combination of the datasets is:

$$k_{CO_{2_{660}}} = 9.05 \times 10^{-3} R_{B_w}^{0.69} \tag{3.6}$$

with $r^2 = 0.59$ and $rmse = 31.67$ for all four datasets combined. Equation 3.6 6 captures 32%, 27%, 89%, and 65% of the observed variability in the GasEx-98 ($rmse$ = 22.02), SO GasEx ($rmse$ = 60.51), Knorr11 ($rmse$ = 19.21), and HiWinGS ($rmse$ = 29.35) measurements, respectively. As for the wave-wind Reynolds number, the close match between the combined and dataset specific fit statistics attest to the inter data set agreement of these Reynolds

number parameterizations.

Utilizing only the wind-sea part of the spectrum to compute the significant wave height and peak angular frequencies does not lead to improved inter-dataset agreement based on project specific fits (Figure 3.2b, d). Compared to full sea state Reynolds numbers, the scatter is increased for $R_{H_{ws}}$ for which the best fit (eq. 3.7) only captures 47% of the variability and there is improvement for $R_{B_{ws}}$ which captures 62% (eq. 3.8) of the variability of the SO GasEx and HiWinGS data combined. The *rmse* values are 36.6 (eq. 3.7) and 30.5 (eq. 3.8).

$$k_{CO_{2_{660}}} = 1.65 \times 10^{-2} R_{H_{w_{ws}}}^{0.59} \tag{3.7}$$

$$k_{CO_{2_{660}}} = 3.45 \times 10^{-2} R_{B_{w_{ws}}}^{0.6} \tag{3.8}$$

Equations 7 and 8 can explain 48% and 66% of the variability in the HiWinGS data. Very few good measurements of $k_{CO_{2_{660}}}$ were taken during SO GasEx when a wind sea was present so that best fits determined from both datasets are again mainly driven by the HiWinGS dataset and project specific fits for SO GasEX have $r^2 \leq 0.05$. Note that for HiWinGS, fits and statistics for $R_{B_{w_{ws}}}$ are very similar to those for R_{B_w}.

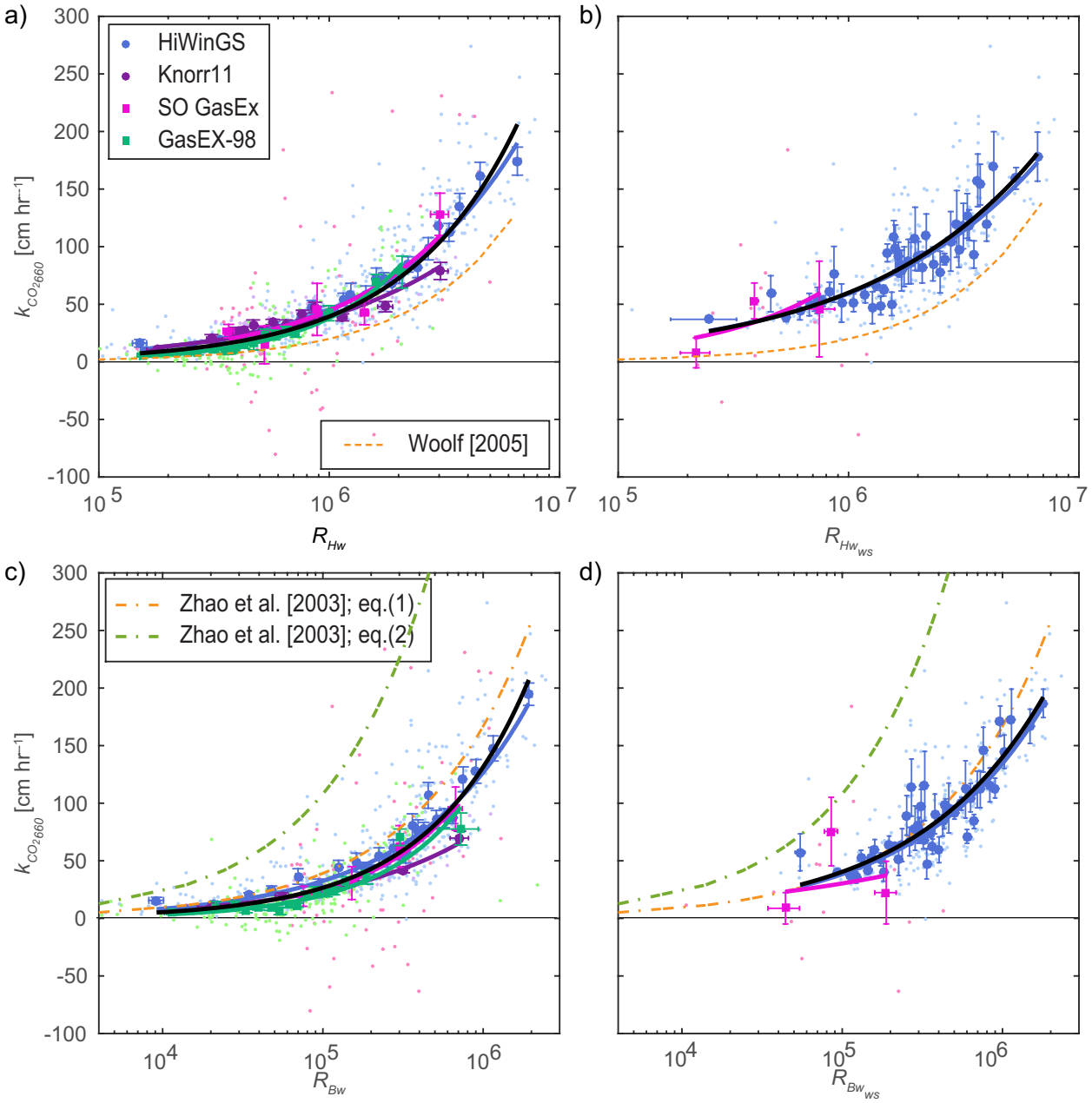

Figure 3.2: Measured gas transfer velocity of CO_2 adjusted to a Schmidt number of 660 plotted against a) the wave-wind Reynolds number based on H_s computed from the total spectrum, b) the wave-wind Reynolds number based on H_s computed from the wind-sea partition of the wave spectrum, c) the breaking Reynold number computed from the total spectrum, and d) the breaking Reynold number computed from the wind-sea partition of the wave spectrum. The smaller dots represent individual hourly and two hourly estimates, the larger symboles are averages of equidensity bins of 15 data points for a) and c) and 5 points for b) and d). The solid green, pink, and purple, blue, and black lines represent best fits of power laws of the form $k = ax^n$, for Gasex-98, SO GasEx, Knorr11, HiWinGS, and all the data, respectively

3.3.2 DMS

$k_{DMS_{660}}$ measured during SO GasEx was significantly lower than that measured during HiWinGS for a given wind speed (Figure 1b). The Knorr11 measurements agree with those from HiWinGS for wind speeds less than 10 m s^{-1}, however for U_{10N} >15 m s^{-1} they match the lower SO GasEx values. The data recorded when U_{10N} exceeded 15 m s^{-1} during SO GasEx and Knorr11 appear as outliers in Figure 3.1b as well as in Figure 3.3a, c. They correspond to unfilled bin average data points in those figures. The SO GasEx outliers were measured during the return transit leg and the Knorr11 outliers were measured at the last station under high wind and wave height conditions. No directional wave data are available to separate wind-seas from swells for these outliers. They are therefore excluded from 3.3b, d. Sea state, whitecap, and basic environmental conditions have not allowed to explain those outliers so that they are excluded from subsequent analysis and proposed parameterizations.

Ignoring SO GasEx data taken on the return transit and Knorr11 data taken during U_{10N} >14 m s^{-1} allows for better overall inter-data agreement with a power-law function of wind-speed alone capturing 70% of the variability in the combined data with $rmse$ of 5.77. $k_{DMS_{660}}$ increases close to linearly with wind speed with power-law exponent ranging from 1.28 to 1.4. A power-law function of R_{H_w} can capture 57% of the combined variability with $rmse = 6.78$:

$$k_{DMS_{660}} = 1.95 \times 10^{-2} R_{H_w}^{0.49}. \tag{3.9}$$

A power-law function of R_{B_w} can account for 63% of the variability in both data sets with $rmse$ of 6.41:

$$k_{DMS_{660}} = 5.36 \times 10^{-2} R_{H_w}^{0.47}. \tag{3.10}$$

Considering wind seas only leads to divergence in the individual best fits for the two data sets. The combined fits are:

$$k_{DMS_{660}} = 9.95 \times 10^{-2} R_{H_{wws}}^{0.39} \tag{3.11}$$

$$k_{DMS_{660}} = 1.29 \times 10^{-1} R_{B_{w_{ws}}}^{0.41} \tag{3.12}$$

with comparable statistic to eq. 3.9 and eq. 3.10 (for eq. 3.11: $r^2 = 0.57$ and $rmse = 7.17$; for eq. 3.12: $r^2 = 0.63$ and $rmse = 6.64$). As noted above, the none of the Knorr11 nor the high wind SO GasEx data were not included in these fits.

When considering the thre datasets individually, expressing $k_{DMS_{660}}$ as a function of Reynolds numbers does not lead to better fit statistics than wind only fits. Indeed, for SO GasEX a wind speed power-law dependence can capture 45% of the variability while a breaking Reynolds number dependence only captures 25% when ignoring the above mentioned outliers. For Knorr11, the wind speed and R_{B_w} perform comparably well, allowing to account for 38% and 39% of the observed variability for $U_{10N} < 14$ m s^{-1}. For HiWinGS, the wind speed only parameterization performs only slightly better than the R_{B_w} one with 75% compared to 72%. Power law exponents for the individual HiWnGS and SO GasEX fits are more comparable for wind speed (1.29, 1.27) and for R_{B_w} (0.44, 0.4) than for R_{H_w} (0.47, 0.4). It is possible that the potential improvement in fit statistics using Reynolds number instead of wind speed is offset by the greater sampling error in determining R_{B_w}.

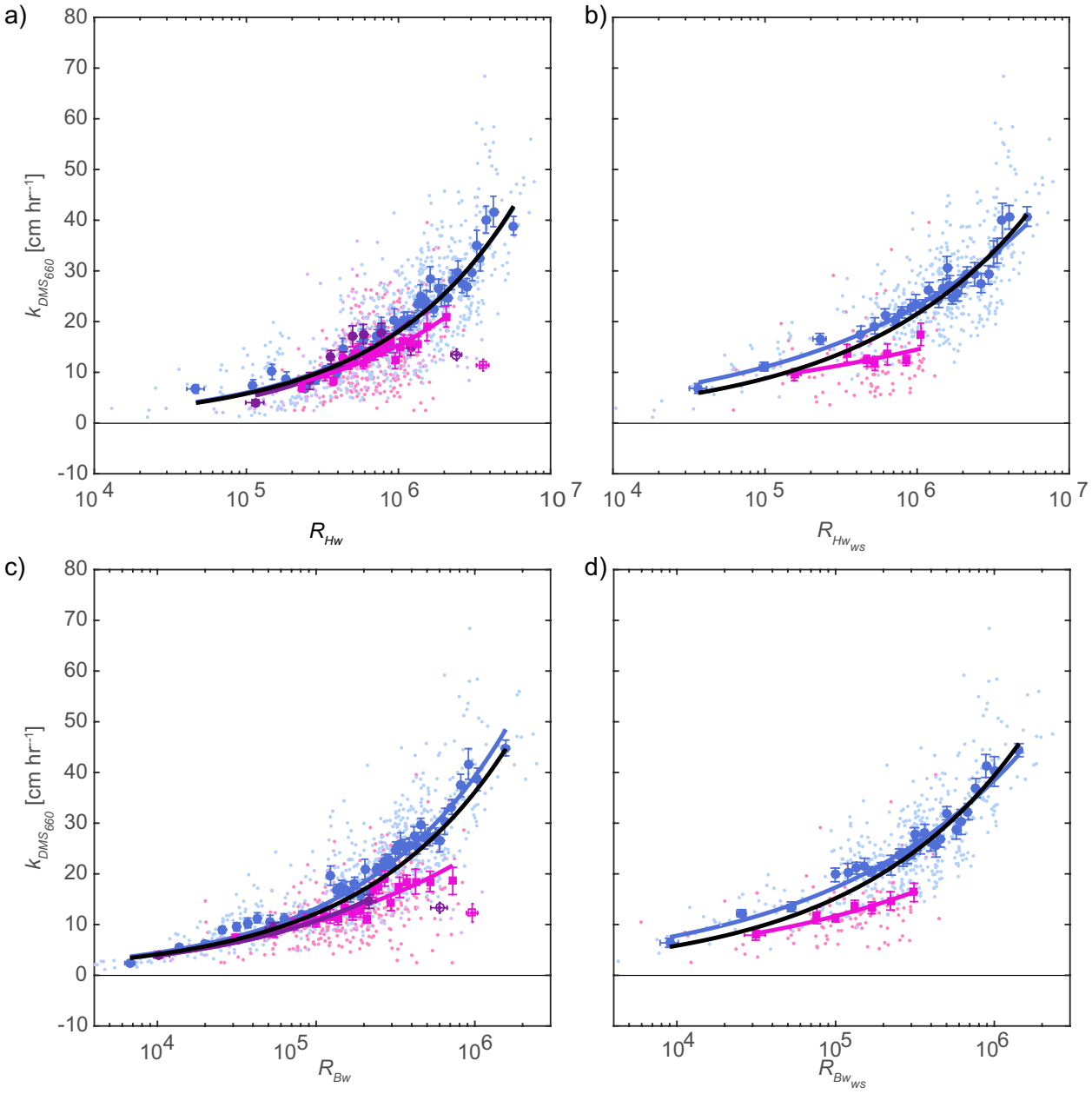

Figure 3.3: Measured gas transfer velocity of DMS adjusted to a Schmidt number of 660 plotted against a) the wave-wind Reynolds number based on H_s computed from the total spectrum, b) the wave-wind Reynolds number based on H_s computed from the wind-sea partition of the wave spectrum, c) the breaking Reynold number computed from the total spectrum, and d) the breaking Reynold number computed from the wind-sea partition of the wave spectrum. The smaller dots represent individual hourly and two hourly estimates, the larger symbols are averages of equidensity bins of 15 data points. The solid pink, and purple, blue, and black lines represent best fits of power laws of the form $k = ax^n$, for SO GasEx, Knorr11, HiWinGS, and all the data, respectively. The open symbols represent outliers in the SO GasEx and Knorr11 datasets that cannot be reconciled by neither wind speed nor Reynolds numbers.

3.4 Discussion

Wind-only gas transfer velocity parameterizations display significant disagreement between different studies [*Garbe et al.*, 2014; *Goddijn-Murphy et al.*, 2012; *McGillis et al.*, 2001; *Wanninkhof*, 1992]. While implementing different wind-only parameterizations for CO_2 may result in comparable globally averaged gas transfer velocities, the parameterization choice was shown to have significant impact on global and regional fluxes [*Fangohr and Woolf*, 2007; *Wrobel and Piskozub*, 2016]. In light of current efforts to include wave processes in Earth System models (e.g., *Li et al.* [2016], *Qiao et al.* [2013]), it is time to update the traditional wind-only gas transfer parameterizations to sea state dependent ones and assess uncertainties linked to parameterization choice.

Parameterizations that incorporate the dependence of wind and sea state in the form of a wave-wind and breaking Reynolds number provide coherent agreement between the GasEx-98, SO GasEx, Knorr11, and HiWinGS datasets for CO_2, and the majority of the DMS data. This study therefore strongly suggests that expressing k as a simple function of a wave-related Reynolds number will lead to improved parameterizations regional and global models relative to wind-only parameterizations. Global fields of significant wave heights and peak angular velocities are routinely computed by operational wave prediction centers, making wave-wind and breaking Reynolds number based parameterizations convenient to implement and test on a global scale. The relationship between k and other wave statistics such as the wave age, bulk slope, and the mean square steepness was also examined but did not reveal any significant trends.

Although the current study is not a comprehensive analysis of all available eddy covariance CO_2 and DMS gas transfer data, the datasets analyzed here are representative of the observed variability. They were chosen because they span a wide range of wind speeds with strongly differing dependency. They are also, to the best of our knowledge, the only available gas transfer datasets with in situ wave field measurements. Seeing how well wave model hindcast

perform, this study may be extended for other existing CO_2 and DMS datasets [*Bell et al.*, 2015; *Blomquist et al.*, 2006; *Huebert et al.*, 2004; *Marandino et al.*, 2007, 2008, 2009; *Miller et al.*, 2009]. However, results will likely not vary much as other datasets do not span a wider wind speed range than the ones considered here and where taken under lower wind speeds where there is less discrepancies in k.

CO_2 and DMS have dimensionless Ostwald solubilites of $\sim$1 and $\sim$20, which strongly influence the fraction of total transfer resistance represented by bubble-mediated and air-side mechanisms. The less soluble a gas, the more its air-sea flux depends on the transfer resistance in the aqueous boundary layer and bubble mediated mechanisms. This explains why k_{DMS} is smaller than k_{CO_2} at high wind speeds, where wave breaking leads to generation of bubble clouds, and thus the need for different, single parameter models for gases of different solubilities. One could a priori expect DMS to be less sea state dependent than CO_2 as its increased solubility means that its transfer velocity depends less on bubble mediated transfer. Weaker dependence on sea state may account for the increased scatter observed in the relationship between both the wave-wind and breaking Reynolds numbers and $k_{DMS_{660}}$. Sea state, represented as either the significant wave height or wave age ($\beta = g/(\omega_p u_*) = R_{B_w}(g\nu_w)/u_*^3$) does not reconcile outliers in the SO GasEx and Knorr11 DMS dataset. These suppressed gas transfer velocities at high wind speeds were observed in high wave height conditions, i.e. high R_{H_w} and more work is needed to understand these observation. *Bell et al.* [2013] suggested that air-flow separation at the crests of large waves may suppress the transfer of gas and explain the low k_{DMS} values treated as outliers here.

Early studies [*Toba and Koga*, 1986; *Zhao and Toba*, 2001; *Zhao et al.*, 2003] which relate breaking conditions, whitecapping, and gas transfer velocities to Reynolds numbers focus on wind-sea statistics, ignoring the importance of swell. It is typically assumed that wave breaking is governed by the wind sea component of the wave spectrum, and that properties of the wind sea partition are most relevant for air-sea processes. This study, however, suggests that consideration of swell is important for gas transfer. Indeed, considering only the wind-sea

partition of the wave spectra did not reduce the scatter in k, yielding poor fits that differ substantially between datasets. Arguably this could be due to the paucity of data collected under wind-sea conditions especially during SO GasEx or the difficulty of separating wind sea and swell. More data are needed to verify this. However, non-breaking wave induced mixing has been shown to significantly contribute to upper ocean turbulence through Langmuir circulation [*Fan and Griffies*, 2014; *Li et al.*, 2016]. This suggests mixing that arises from all components of the wave spectra should be considered. Furthermore, if air-flow separation over large waves indeed inhibits gas transfer, the swell component needs to be considered. Reynolds numbers computed from the full spectrum can however not account for this effect.

The Reynolds number parameterizations determined in this study differ from previously published parameterizations [*Woolf*, 2005; *Zhao et al.*, 2003] using the wind-sea partition or the total spectra. This can partially be attributed to the whitecap data used to tune previous parameterizations. The W parameterization used by *Zhao and Toba* [2001] overestimates W measured during both experiments resulting in overestimated gas transfer velocities. The parameterization of *Woolf* [2005] underestimates the measured transfer velocities of CO_2 though it is loosely based on the relation between W and R_{H_a} determined by *Zhao and Toba* [2001]. The issue here comes primarily from the relation used between the bubble mediated transfer and W based on *Woolf* [1997], but may also be attributed to the expression of the non-breaking transfer used. The coefficients of the 1997 bubble mediated transfer model are best guess values which were tuned in *Woolf* [2005] to match a range of observed functions given the assumption that wave fetch is the primary controlling parameter for W. The model may therefore not be adequate for the open ocean. Note also that we established that these earlier W data and the parameterizations differ greatly from recent observations [*Brumer et al.*, 2017] in part due to the different techniques employed, and in part due to different wind/wave environments (pure wind vs. mixed seas, lab or fetch limited vs. open ocean waves).

3.5 Conclusion

Consideration of the breaking or wind wave Reynolds numbers allows for improved single parameter models of the gas transfer velocity of DMS and CO_2 relative to wind speed only parameterizations. The Reynolds number- based parameterizations appear to be more universally valid, collapsing the data of the GasEx-98, SO GasEx, Knorr11, and HiWinGS experiments onto closely matching power law dependences, while wind only parameterizations vary greatly between datasets. For CO_2 they also, for the most part, capture slightly more of the observed variability than the traditional wind only ones. Unlike previous studies that relied on the combination of unrelated datasets and more or less sound relations between Reynolds numbers, whitecap fraction and gas transfer velocities, these are the first Reynold number parameterizations determined directly from concurrent eddy covariance measurements of gas fluxes and modeled or remotely sensed wave field statistics.

Table 3.1: Least square fit results of the wind speed and Reynolds number dependence of the gas transfer velocity of CO_2 referenced to a Schmidt number of 660.

Eq.	Experiment	Form	a	n	r^2	$rmse$
p1	GasEx-98	$k = a(U_{10N})^n$	1.06E-01	2.53	0.62	15.44
p2		$k = a(U_{10N})^2 + n$	3.46E-01	-1.3	0.6	16.43
p3		$k = a(U_{10N})^3 + n$	3.14E-02	3.48	0.63	15.3
p4		$k = a(R_{H_w})n$	7.97E-06	1.11	0.57	16.23
p5		$k = a(R_{B_w})^n$	2.27E-03	0.79	0.28	22.38
p6	SO GasEx	$k = a(U_{10N})^n$	7.27E-02	2.67	0.25	60.81
p7		$k = a(U_{10N})^2 + n$	4.79E-01	-11.01	0.25	60.88
p8		$k = a(U_{10N})^3 + n$	2.80E-02	4.78	0.25	60.86
p9		$k = a(R_{H_w})^n$	6.10E-04	0.81	0.31	58.96
p10		$k = a(R_{B_w})^n$	5.75E-03	0.73	0.27	60.46
p11		$k = a(R_{H_{w_{ws}}})^n$	6.72E-04	0.84	0.05	64.43
p12		$k = a(R_{B_{w_{ws}}})^n$	7.45E-02	0.51	0.01	58.2
p13	Knorr11	$k = a(U_{10N})^n$	1.15E+00	1.46	0.71	9.23
p14		$k = a(U_{10N})^2 + n$	2.56E-01	5.78	0.69	10.15
p15		$k = a(U_{10N})^3 + n$	1.55E-02	11.45	0.64	12.55
p16		$k = a(R_{H_w})^n$	4.11E-03	0.66	0.64	10.68
p17		$k = a(R_{B_w})^n$	6.33E-02	0.52	0.9	7.22
p18	HiWinGS	$k = a(U_{10N})^n$	1.07E+00	1.62	0.63	29.87
p19		$k = a(U_{10N})^2 + n$	3.32E-01	9.23	0.64	29.68
p20		$k = a(U_{10N})^3 + n$	1.74E-02	18.47	0.61	31.88
p21		$k = a(R_{H_w})^n$	1.25E-03	0.76	0.69	27.13
p22		$k = a(R_{B_w})^n$	3.63E-02	0.59	0.66	28.73
p23		$k = a(R_{H_{w_{ws}}})^n$	2.33E-02	0.57	0.48	34.69
p24		$k = a(R_{B_{w_{ws}}})^n$	7.73E-02	0.54	0.55	33.01
p25	Combined	$k = a(U_{10N})^n$	4.78E-01	1.91	0.61	29.77
p26		$k = a(R_{H_w})^n$	2.04E-04	0.88	0.65	29.38
p27		$k = a(R_{B_w})^n$	9.05E-03	0.69	0.59	31.67
p28		$k = a(R_{H_{w_{ws}}})^n$	1.64E-02	0.59	0.47	36.66
p29		$k = a(R_{B_{w_{ws}}})^n$	5.70E-02	0.56	0.53	34.94

Table 3.2: Least square fit results of the wind speed and Reynolds number dependence of the gas transfer velocity of DMS referenced to a Schmidt number of 660.

Eq.	Experiment	Form	a	n	r^2	$rmse$
p30	SO GasEx	$k = a(U_{10N})^n$	7.31E-01	1.25	0.25	5.8
p31		$k = a(U_{10N})^2 + n$	8.51E-02	3.95	0.2	6.44
p32		$k = a(U_{10N})^3 + n$	5.69E-03	6.2	0.13	7.81
p33		$k = a(R_{H_w})^n$	3.75E-02	0.44	0.18	5.93
p34		$k = a(R_{B_w})^n$	1.91E-01	0.35	0.25	5.63
p35		$k = a(R_{H_{w_{ws}}})^n$	8.22E-01	0.21	0.08	6.11
p36		$k = a(R_{B_{w_{ws}}})^n$	3.72E-01	0.3	0.22	5.62
p37	Knorr11	$k = a(U_{10N})^n$	6.45E-01	1.4	0.38	6.02
p38		$k = a(U_{10N})^2 + n$	1.40E-01	2.11	0.34	6.47
p39		$k = a(U_{10N})^3 + n$	1.11E-02	3.78	0.26	7.3
p40		$k = a(R_{H_w})^n$	7.62E-03	0.56	0.2	6.82
p41		$k = a(R_{B_w})^n$	7.14E-02	0.44	0.39	6.27
p42	HiWinGS	$k = a(U_{10N})^n$	8.23E-01	1.3	0.75	5.67
p43		$k = a(U_{10N})^2 + n$	1.07E-01	3.78	0.73	6.23
p44		$k = a(U_{10N})^3 + n$	5.53E-03	6.4	0.65	7.96
p45		$k = a(R_{H_w})^n$	2.28E-02	0.48	0.62	6.97
p46		$k = a(R_{B_w})^n$	5.73E-02	0.47	0.71	6.04
p47		$k = a(R_{H_{w_{ws}}})^n$	2.80E-01	0.32	0.54	6.97
p48		$k = a(R_{B_{w_{ws}}})^n$	3.22E-01	0.35	0.63	6.29
p50	Combined	$k = a(U_{10N})^n$	7.42E-01	1.32	0.62	6.51
p51		$k = a(R_{H_w})^n$	1.95E-02	0.49	0.57	6.78
p52		$k = a(R_{B_w})^n$	5.36E-02	0.47	0.63	6.41
p53		$k = a(R_{H_{w_{ws}}})^n$	9.95E-02	0.39	0.57	7.17
p54		$k = a(R_{B_{w_{ws}}})^n$	1.29E-01	0.41	0.63	6.64

Chapter 4

Mechanistic formulations of gas transfer resulting from wave breaking

Evaluation of existing mechanistic formulations of gas transfer reported in this chapter were the author's contribution to *Blomquist et al.* [2017]. The new framework proposed herein and corresponding results are not yet finalized for publication.

4.1 Introduction

Surface waves act similar to a "gearbox" coupling the ocean and the atmosphere. Their breaking has the potential to considerably impact air-sea exchanges and upper-ocean dynamics. Surface waves gain their energy from the wind blowing over the surface of the ocean and as they break transfer energy, momentum, heat, and gases from the atmosphere to the ocean. Breaking also results in wave energy dissipation which leads to enhanced turbulent kinetic energy in the near surface layer. Indeed, breaking wave dissipation rates have been shown to be roughly 5–1000 times greater than wall layer scaling [*Agrawal et al.*, 1992; *Gemmrich*, 2010; *Sutherland and Melville*, 2015; *Terray et al.*, 1996]. Additionally, air-entraining breaking waves foster aerosol production by generating sea-spray and result in bubble clouds that allow for an additional path way for gas transfer.

Of particular interest to this study are the enhancements to the turbulent kinetic energy (TKE) and bubble clouds associated with breaking waves which are thought to promote the transfer of gases. Large scatter is observed in gas transfer velocities (k) of sparingly soluble gases at high wind speeds, where wave breaking dominates upper ocean dynamics. This scatter suggests that k can no longer be modeled as a function of wind speed alone and may be due to variability in wave breaking. Bubble mediated transfer is known to be important for sparingly soluble gases such as CO_2 and efforts have been made to account for the impact of bubbles in physical process based models [*Fairall et al.*, 2011; *Goddijn-Murphy et al.*, 2016; *Asher et al.*, 1996]. However, only one of these models explicitly considers the contribution of wave breaking turbulence [*Asher et al.*, 1996; *Asher and Wanninkhof*, 1998]. The recent HiWinGS cruise provides an unprecedented dataset to test process based models. It also allows the exploration of an alternative framework to estimate k for gases with different solubility based on the characteristics of breaking waves.

Section 4.2 provides an outline of the general form of the proposed model followed by a review of *Phillips* [1985]'s theoretical framework used to characterize the kinematic, dynamic and energetic properties of breaking waves as well as the derivation of quantities key to air-sea gas transfer. In section 4.3 the image analysis technique to extract breaking wave statistics is described. The wave breaking statistics determined from the HiWinGS imagery are then presented in section 4.4 after which existing process based models are evaluated and the new framework is tested. Finally results and limitations of the proposed framework are discussed in section 4.5.

4.2 Proposed Gas Transfer Model

The model accounts for the contribution of the turbulence driven (k_ε) and the bubble mediated (k_b) transfers:

$$k = k_\varepsilon + k_b \tag{4.1}$$

Various mechanistic approaches were suggested by which turbulence promotes the transfer of gases. These invoke concepts of surface renewal [*Higbie*, 1935; *Danckwerts*, 1951; *Lamont and Scott*, 1970; *Komori et al.*, 1993], surface penetration [*Harriott*, 1962; *Atmane et al.*, 2004] and surface divergence [*McCready et al.*, 1986; *Banerjee and MacIntyre*, 2004; *Banerjee et al.*, 2004; *McKenna and McGillis*, 2004; *Turney et al.*, 2005] and their ‘ is limited to a constrained set of environmental conditions. A form of k_ε was derived from boundary layer scaling. The flux of gas (F_g) follows Fick's law of diffusion:

$$F_g = D\frac{\partial C}{\partial z} = \frac{D}{\delta_z}(C_w - \alpha C_a) = k_\varepsilon(C_w - \alpha C_a) \tag{4.2}$$

Where D is the diffusivity, δ_Z a characteristic surface boundary length scale, α the Ostwald solubility coefficient and C_a, C_w the air and water concentrations, respectively. This allows to rewrite k_ε as:

$$k_\varepsilon = \frac{D}{\delta_z} \tag{4.3}$$

Using the Batchelor length scale $\delta_Z \propto \left(\frac{\nu_w D^2}{\varepsilon}\right)^{1/4}$, which is the characteristic turbulent microscale for a passive scalar [*Batchelor*, 1959], the following relationship between k and ε was derived [*Banerjee et al.*, 1968; *Kitaigorodskii*, 1984]:

$$k_\varepsilon \propto (\varepsilon\nu_w)^{\frac{1}{4}} Sc^{-0.5} \tag{4.4}$$

where ν_w is the water viscosity, and Sc is the Schmidt number defined as the ratio of the water viscosity and the mass diffusivity D ($Sc = \nu_w/D$).

Bubble mediated transfer is typically expressed as function of the bubble volume flux (F_a) or the void fraction (v) [*Woolf*, 1997; *Woolf et al.*, 2007]. Two commonly used form are those suggested by *Woolf* [1997]. The simplest one is:

$$k_b \propto F_a \alpha^{-1} \left(1 + \left(\frac{Sc^{-0.5}}{14\alpha}\right)^{1/1.2}\right)^{-1.2} \tag{4.5}$$

Based on laboratory work by *Cipriano and Blanchard* [1981], *Woolf* [1997] first suggests that:

$$F_a = 6.25 \times W \text{ [m(m}^2 \text{ s)}^{-1}\text{]} = 2250 \times W \text{ [cm/h]} \tag{4.6}$$

Where W is the total whitecap cover expressed as a fraction. Later in the paper, Woolf uses $F_a = 2450W$ which is the value adopted by subsequent studies.

The model based on eq. 4.5 does not account for the potential "suffocation" effect of bubbles within dense clouds. This effect was suggested to arise from the fact that bubbles evolve within a finite volume of water with relatively small interstitial space which has limited capacity to take up gases, thus restricting the bubble mediated transfer [*Woolf et al.*, 2007]. An alternate form for k_b, labeled as the "dense plume model" was therefor proposed:

$$\begin{aligned} k_b &= W \times X \frac{F_{a_{1\%}}}{\alpha}(1 + (X\chi)^{1/1.2})^{-1.2} \\ X &= \alpha F_{w_{1\%}}/(\alpha F_{w_{1\%}} + F_{a_{1\%}}) \\ \chi &= \frac{Sc^{-0.5}}{14\alpha} \end{aligned} \tag{4.7}$$

$F_{a_{1\%}}$ is the volume flux of air for 1% whitecap cover, i.e $F_{a_{1\%}} = F_a/W$, which *Woolf et al.* [2007] set to equal 24.5 cm/h. $F_{w_{1\%}}$ is the volume flux of water within bubble plume relative to $F_{a_{1\%}}$ and is related to $F_{a_{1\%}}$ through the void fraction:

$$v = \frac{F_{a_{1\%}}}{F_{a_{1\%}} + F_{w_{1\%}}}. \tag{4.8}$$

Note that through out this framework, a Schmidt number exponent of 0.5 is used which is in accordance with open ocean scaling. The exponent was suggested to vary between 1/2 for wavy, surfactant free conditions to 2/3 for flat, film covered surfaces. It may therefor need adjustment for coastal applications.

4.2.1 Phillips' [1985] Spectral Framework

Laboratory experiments by *Duncan* [1981, 1983], in which a breaking wave was created by a hydrophoil towed at constant speed and depth, revealed a relationship between energy dissipated by steady breaking wave and its speed:

$$\varepsilon_l \propto \frac{\rho_w c_h^5}{g}, \tag{4.9}$$

where ε_l is the energy dissipation per crest length, ρ_w is the water density, g is the gravitational acceleration, and c_h the speed of a towed hydrofoil which corresponds to the speed of the breaking crest length $c_h \sim c_{br}$.

Phillips [1985] introduced the spectral density of the breaking crest length per unit area $\Lambda(c)$, where c is the phase speed. Based on the previously mentioned experiments, he proposed:

$$\varepsilon = \int S_{ds}(c)dc = \int b(c)\rho_w g^{-1} c^5 \Lambda(c)dc \tag{4.10}$$

where S_{ds} is the spectral dissipation term from the radiative transfer equation that describes the evolution of the wave field and $b(c)$ is the spectral breaking strength.

For wave numbers larger than the peak, *Phillips* [1985] further postulated that a spectral equilibrium exists in which all source terms, i.e. the nonlinear energy flux, wind forcing, and energy dissipation from breaking waves are in balance, proportional, and of similar magnitude. This allowed him to derive the following functional form for the spectral dissipation term in the equilibrium range:

$$S_{ds}(c) = (4\gamma\beta^3) I(3p) \rho_w u_*^3 c^{-1} \tag{4.11}$$

where γ, β, and p are constants, and I is a directional weight function:

$$I(3p) = \int_{-\pi/2}^{\pi/2} (cos\theta)^{3p} d\theta \tag{4.12}$$

From eq. 4.10 and 4.11, the following form of the breaking crest length distribution emerges:

$$\Lambda(c) = (4\gamma\beta^3) I(3p) b^{-1} u_*^3 g c^{-6} \tag{4.13}$$

Which suggest that within the equilibrium range $\Lambda(c)$ decreases as c^{-6}.

Recognizing the value of the breaking crest length distribution to infer breaking wave characteristics and subsequently air-sea interaction processes, multiple studies have been undertaken to obtain direct measurements of both $\Lambda(c)$ and ε. The first measurements of $\Lambda(c)$ were made by *Phillips et al.* [2001] using a marine radar. Later studies have used digital video camera to track breaking waves from stable platforms [*Gemmrich et al.*, 2008, 2013; *Schwendeman et al.*, 2014; *Sutherland and Melville*, 2013, 2015; *Thomson et al.*, 2009; *Zappa et al.*, 2012] and planes [*Kleiss and Melville*, 2010]. Techniques to derive the breaking crest length distribution from the imagery vary greatly. These are reviewed and discussed in *Banner et al.* [2014]. Here the initial velocity method is adopted, in which the phase velocity c is equated to a fixed reference velocity that corresponds to initial breaker-front velocity of each breaking event (c_{br}) as was originally chosen by *Phillips* [1985]. Following *Gemmrich et al.* [2008, 2013], the breaking crest length distribution $\Lambda(c_{br})$ for a given speed range (c_b, $c_b + \Delta c$) is then obtained from:

$$\Lambda(c_{br}) = \sum L_{br} t_{br} / (T A \Delta c_{br}) \tag{4.14}$$

where L_{br} is the characteristic breaking segment length, t_{br} duration of an individual breaking crest event (based on the time a breaker is tracked in imagery), A is the area of the field of view and T the total duration of observation.

4.2.2 Estimating the turbulent kinetic energy dissipation rate

To estimate the turbulent kinetic energy dissipation rate from the breaking crest length distribution, one unknown remains: the spectral breaking strength $b(c)$. Wave systems produced in laboratory experiments are narrow-banded and $b(c)$ is assumed to be independent of scale. It was found to vary with wave steepness [*Banner and Peirson*, 2007; *Drazen et al.*, 2008; *Melville*, 1994]. Ocean waves are however rarely narrow-banded,and modeling studies suggest that that $b(c)$ may scale with wave age [*Banner and Morison*, 2010; *Romero et al.*, 2012].

No measurements of $b(c)$ exist to date. This encouraged to define a scale-independent, effective breaking strength coefficient (b_{eff}):

$$b_{eff} = \frac{\varepsilon}{\rho_w g^{-1} \int c^5 \Lambda(c) dc} \tag{4.15}$$

This leads to:

$$\varepsilon(c) = b_{eff} c^5 \Lambda(c)/g \tag{4.16}$$

Reviewing all existing breaking crest length distribution and coinciding upper ocean dissipation rate measurements, *Zappa et al.* [2016] determined the following wave-age dependent of b_{eff}:

$$b_{eff} = 3.48 \times 10^{-3} - 4.69 \times 10^{-5} \frac{c_p}{u_*} \tag{4.17}$$

4.2.3 Estimating the Bubble Volume flux and Void fraction

Estimation of the bubble volume flux and void fractions are based on relations determined from novel direct numerical simulations (DNS) of three-dimensional breaking waves that resolve bubble scales [*Deike et al.*, 2016]. One of the key finding from this DNS study is that total volume of air entrained by a breaking wave (V_a) is directly proportional to the breaking

crest length (L_{br}) and the breaking speed to the power 5:

$$V_a = Bb_{eff}\frac{L_{br}c_{br}^5}{U_b g^2} \tag{4.18}$$

Where B is a dimensionless constant, and U_b is a dissipation-weighted vertical mean velocity which corresponds to the average rise velocity of the bubble plume. This relation stems from the core assumption that the global (integrating over space and time of the event) work done against buoyancy forces in entraining the bubbles is proportional to the mechanical energy dissipated where B is the proportionality factor. U_b scales as the rise velocity in clean water [*Woolf and Thorpe*, 1991] of a bubble of radius equal to the mean of the bubble distribution. Not knowing the bubble distribution, a constant U_b equal to 10 cm s^{-1} is assumed here based on *Asher et al.* [1997].

From eq. 4.18, a volume flux per unit area (F_a) can be estimated by summing the total volume of air entrained by each breaker observed during a single video recording and dividing by the area of the field of view (A) and the total time of observations (T).

$$\begin{aligned} F_a &= \frac{\sum V_a}{AT} \\ &= b_{eff}B\frac{\sum L_{br}c_{br}^5}{ATU_b g^2} \end{aligned} \tag{4.19}$$

Alternatively, F_A may be expressed as a combination of the fifth moment of the breaking crest length distribution and the breaking duration (τ_{br}):

$$F_a = \frac{b_{eff}B}{U_b g^2}\int \frac{1}{\tau_{br}(c)}\Lambda(c)c^5 dc \tag{4.20}$$

This form assumes that the duration of the breaker is a function of the breaker speed. As proposed by *Kleiss* [2009], based on laboratory and field data [*Thorpe and Hall*, 1983; *Rapp and Melville*, 1990], τ_{br} can be related to the period of the breaking wave which may be

expressed in terms of the phase speed c via the deep water dispersion relation:

$$\tau_{br} \propto \frac{2\pi}{g} c \tag{4.21}$$

The phase speed of the breaking wave has been shown to be closely related to the speed of the breaking crest c_{br} with $c_{br}/c \sim 0.8 - 0.9$. *Kleiss* [2009] suggest $\tau_{br} = 0.25 c_{br}$.

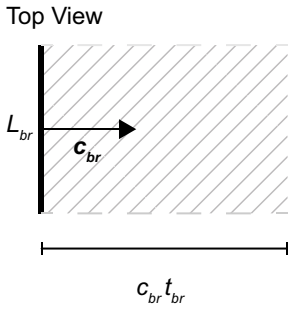

Figure 4.1: Sketch illustrating the assumption that the swept out area is related to the length of breaking L_{br}, the translation $c_{br}t_{br}$

The void fraction for a given breaking wave (v_{br}) can be estimated from V_a, the surface area of active breaking (A_{br}), which is proportional to the breaking crest length times the "swept out" length of the breaker ($L_{br} \times c_{br}t_{br}$, see Figure 4.1), and the depth of the bubble plume (h):

$$\begin{aligned} v_{br} &= \frac{V_a}{A_{br}h} \\ &= b_{eff}\frac{B}{U_b g^2}\frac{L_{br}c_{br}^5}{L_{br}c_{br}t_{br}h} \\ &= b_{eff}\frac{B}{U_b g^2}\frac{c_{br}^4}{t_{br}h} \end{aligned} \tag{4.22}$$

The time averaged void fraction is then:

$$v = \frac{\sum v_{br}t_{br}}{T} \tag{4.23}$$

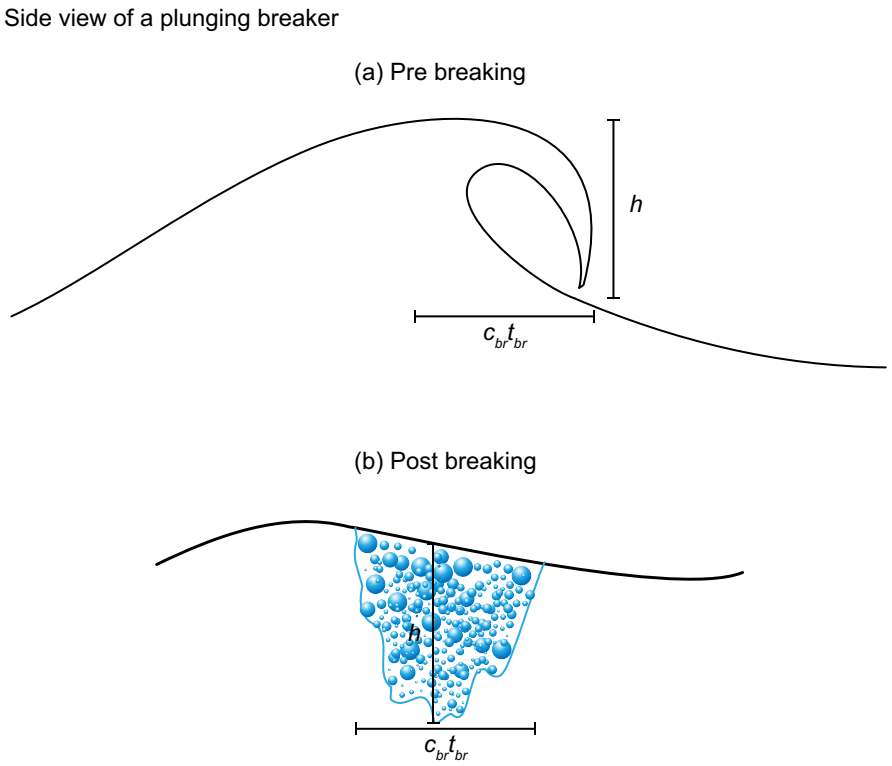

Figure 4.2: Sketch of the assumed geometry of (a) a plunging breaker, and (b) the subsequent bubble plume.

The bubble plume depth remains elusive, but may be assumed to be proportional to the significant wave height of the wind-sea ($H_{s_{ws}}$) or to the "swept out" length of the breaker ($c_{br}t_{br}$). Figure 4.2 illustrates the assumed geometry of a plunging breaker and the subsequent bubble plume. The two estimates are then given by:

1. assuming $h \propto H_{s_{ws}}$ [e.g., *Rapp and Melville*, 1990; *Lamarre and Melville*, 1991; *Baldy and Bourguel*, 1987]:

$$v_1 \propto \frac{b_{eff} B}{H_{s_{ws}} T U_b g^2} \sum c_{br}^4. \tag{4.24}$$

2. assuming $h \propto c_{br}t_{br}$ [e.g., *Deike et al.*, 2016]:

$$v_2 \propto \frac{b_{eff} B}{T U_b g^2} \sum \frac{c_{br}^3}{t_{br}}. \tag{4.25}$$

Note that both forms are independent of the breaking crest length and cannot be expressed

in terms of moments of the breaking crest length distribution.

4.3 Data Analysis Methods

Description of the data sets can be found in sections 2.2.2, 2.2.3, and 3.2.4. The high frequency visible imagery taken during the HiWinGS field campaign will be exploited further here in combination with the CO_2 and DMS gas transfer velocity estimates obtained during the cruise.

4.3.1 Tracking breaking crests

As for determining the total whitecap fraction (see section 2.3.1), all background gradients present in the images were removed prior to any further analysis. The images were then corrected for lens distortion and re-projected using the roll, pitch and yaw angles measured by the IMUs. Finally, they were interpolated onto a regular grid with pixel resolution of 0.1 m. The area of the field of view A was $\sim$1100 m^2 and the total duration of observation T was around 19 minutes. The first 1000 frames of each run was ignored due to an apparent drift in the IMU data each time the instruments were started up.

The breaking crest lengths were tracked following the method developed by *Gemmrich et al.* [2008]. In order to bring out the advancing side of the whitecap two consecutive rectified and projected images are differenced. As whitecaps are brighter than the background, the advancing front is distinguishable by high positive values, while the rear side is negative in the differenced image. The differenced images are thresholded based on image intensity (I) using $I/\max(I) > 0.6$ and transformed into binary images where the breaking crests have pixels equal to 1 and the rest is set to 0.

Using Matlab's image processing toolbox, a series of morphological operations are then applied to the binary frames to insure that crest do not contain holes and to link crests that are close together into a single one. Finally, each crest is identified and approximated‘

as ellipse. This allows to determine the coordinates of the center of mass (x_i, y_i) of each crest, as well as the length major and minor axis (L_i, m_i, respectively), their area (A_{br}), and orientation ϕ_i.

At this stage crests that have an area smaller than 1.5 m^2 are removed. The remaining crests are then tracked from one differenced frame to the next. Matching the crests in consecutive differenced frames is based on:

1. propagation direction of the centers of mass of $\pm$ 90° relative to the ship's orientation which was pointed into the wind.

2. a propagation speed less than 1.2 times the phase speed of the waves at spectral peak.

3. change in area and major axis length less than 25%

4. orientations of the major axes within 15°

Theoretical minimum detectable crest advancement speed is dictated by the pixel resolution and the frame rate. A pixel resolution of 0.1 m at 20 Hz would only allow to track waves traveling at a speed greater than 5 m s^{-1}. Therefore the imagery was down-sampled to 10 Hz, reducing the resolvable propagation speed to 1 m s^{-1}. Note howevver that the coordinates of the center of masses are determined withing fractions of pixels propagation speeds smaller than 1 m s^{-1} can result from the analysis.

4.4 Results

4.4.1 Breaking crest length distributions

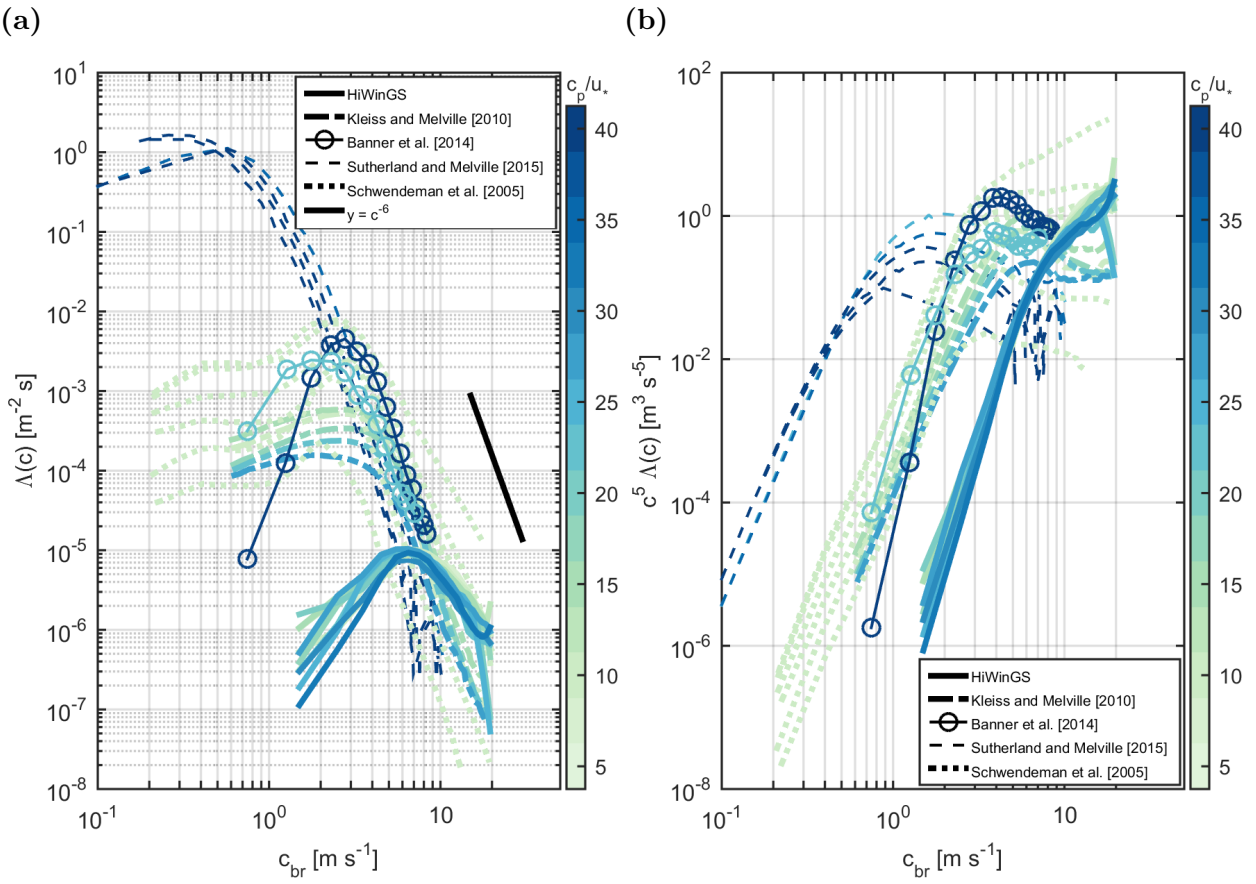

Figure 4.3: (a) Breaking crest length distributions and (b) their fifth moment as a function of the breaking crest speed color-coded by wave age ($\frac{c_p}{u_*}$).

Figure 4.3a shows the breaking crest length distributions as a function of the breaking speed computed from the HiWinGS data set color-coded by wave age ($\frac{c_p}{u_*}$). Figure 4.3b shows their fifth moment. Also shown are some of the previous breaking crest length determined from visible imagery. The first field measurements of $\Lambda(c)$ were made by *Phillips et al.* [2001] using backscatter measurements from and X-Band radar (not shown). Later *Kleiss and Melville* [2010] used air-borne imagery taken during the 2004 GOTEX experiment off the Pacific coast

of southern Mexico in the Gulf of Tehuantepec. The waves observed during GOTEX were fetch limited and wave ages ranged from 8 to 31 under wind speeds of 10 to 25 m s^{-1}.

Two further open ocean datasets were gathered by *Gemmrich et al.* [2013] from *R/P FLIP* in 2008 in the Santa Barbara Channel (SBC) and in 2009 in the Pacific Ocean (PO) south of Hawaii during the Office of Naval Research (ONR)-sponsored Radiance in a Dynamic Ocean (RaDyO) experiments [*Zappa et al.*, 2012]. A characteristic breaking crest length distribution from each of the RaDyO experiment was re-produced by *Banner et al.* [2014] and is shown in Figure 4.3. Young seas with mean wave age of 22.3 ($18.3 < \frac{c_p}{u_*} < 25$) were observed in SBC under varying wind speed where diurnal sea breezes led to U_{10} of up to 12 m s^{-1}. In contrast, closer to fully developed wind-seas were recorded in PO with mean wave age of 48.1 ($45 < \frac{c_p}{u_*} < 51.7$) under wind speeds averaging around 9.1 m s^{-1}. Note that a sea is considered fully developed when the energy flux inputted by the wind equal that lost by dissipation which occurs at $cp/u_* \sim 35$ [*Steele et al.*, 2009] or $cp/U_{10} \sim 1.2$ assuming $u_*/U_{10} \sim 0.035$.

Schwendeman et al. [2014] extracted breaking crest length distributions from shipboard imagery taken in 2011 in the Strait of Juan de Fuca, north of Sequim, Washington, aboard the *R/V Robertson*. They observed a developing young wind sea ($\frac{c_p}{u_*} \sim 10$) in a strongly forced, short fetch environment with wind speeds ranging from 9.7 to 18.0 m s^{-1}.

The last dataset is that published by *Sutherland and Melville* [2015] which combines measurements made in the North Pacific Ocean aboard *R/P FLIP*, during the 2010 ONR-sponsored High Resolution Air–Sea Interaction (HiRes) and the 2009 RaDyO experiments and those taken off the Southern California coast (SoCal) in 2010. Low to moderate wind conditions were observed during SoCal with wind speeds up to 9 m s^{-1}, while strong winds of up to 17 m s^{-1} were recorded during HiRes. Wave ages reported by *Sutherland and Melville* [2015] range from ∼34 to ∼250, but only data for $\frac{c_p}{u_*} < 80$ are plotted here.

Note that much younger seas and higher winds were sampled during HiWinGS than during most of the previous field experiments outlined above. It is also important to note

that different analysis techniques were used by the different groups. Only the two RaDyO datasets reported in *Gemmrich et al.* [2013] and *Banner et al.* [2014] were analyzed with the technique used here. The discrepancies arising from the various analysis techniques and choices in independent variables (in particular c_{br}) used to compute the breaking crest length distributions were highlighted by *Banner et al.* [2014] and will not be discussed further here. Nevertheless, these systematic differences have to be taken into consideration when comparing the breaking crest length distributions plotted here.

As noted by *Banner et al.* [2014], measurements of $\Lambda(c)$ have not provided definite support for Eq. 4.13, and departures from the -6 power-law exponent of c in the equilibrium range have been reported. The slope of the equilibrium tail of the breaking crest length distributions determined from the current analysis of the HiWinGS data set appears often less steep than stipulated by Eq. 4.13.

4.4.2 TKE dissipation, active breaking coverage, bubble volume flux and void fraction

The turbulent kinetic energy dissipation rates computed from the breaking crest length distributions span almost 2 orders of magnitude and is seen to increase with wind speed as expected (Figure 4.4). However, there appears to be much scatter in the derived ε leading to low correlations with both U_{10N} and W ($r^2 = 0.33$ and $r^2 = 22$, respectively). The breaking and wave-wind Reynolds numbers appear to capture more of the variability in ε (43% and 44%, respectively). The bubble volume flux (Figure 4.5) equally increases with wind speed. It correlates very poorly with the total whitecap coverage ($r^2 = 0.22$). Dividing F_a by the observe W, an average $F_{a_{1\%}}$ of 1.39 $\times 10^5$ cm hr^{-1} is found. This is 56.74 times larger than that suggested by *Woolf* [1997]. The breaking and wave-wind Reynolds numbers are able to capture 41% of the variability in F_a. The void fraction computed according to Eq. 4.24, with a proportionality constant equal to 1, does not appear to scale with any wind or wave field statistics. It ranges from 0.015 to 0.59 and averages around 0.18.Using Eq. 4.25 leads

to comparable results (no shown). The turbulent kinetic energy dissipation rate and the bubble volume flux are highly correlated to active whitecap coverage W_A (Figure 4.7). W_A is computed from the first moment of $\Lambda(c)$ and the breaking duration τ_{br} and is proportional to the second moment of $\Lambda(c)$ [*Kleiss and Melville*, 2010]:

$$\begin{aligned} W_A &= \int \tau_{br} \Lambda(c) c dc \\ &\sim 0.25 \int \Lambda(c) c.^2 dc \end{aligned} \tag{4.26}$$

W_A is able to capture 48% of the variability in the void fraction. However, unlike suggested by previous studies, W_A does not appear to vary much with wind speed. Estimates of W_A for wind speeds under 15 m s^{-1} match levels determined in previous studies but is an order of magnitude smaller at higher wind speeds. It is not clear at this stage whether the observed discrepancies are an artifact of the image analysis techniques. *Kleiss and Melville* [2010] computed W_A from the breaking crest length distribution (their Eq. 20 and 21) and from thresholded images (their Eq. 18 and 19). *Scanlon and Ward* [2016] crowd-sourced their image analysis and W_A was determined by eye based on brightness, texture and shape guidelines [*Scanlon and Ward*, 2013]. Measurements in *Kleiss and Melville* [2010] and [*Scanlon and Ward*, 2013] were done at wind speeds reaching up to ∼20 m s^{-1}.

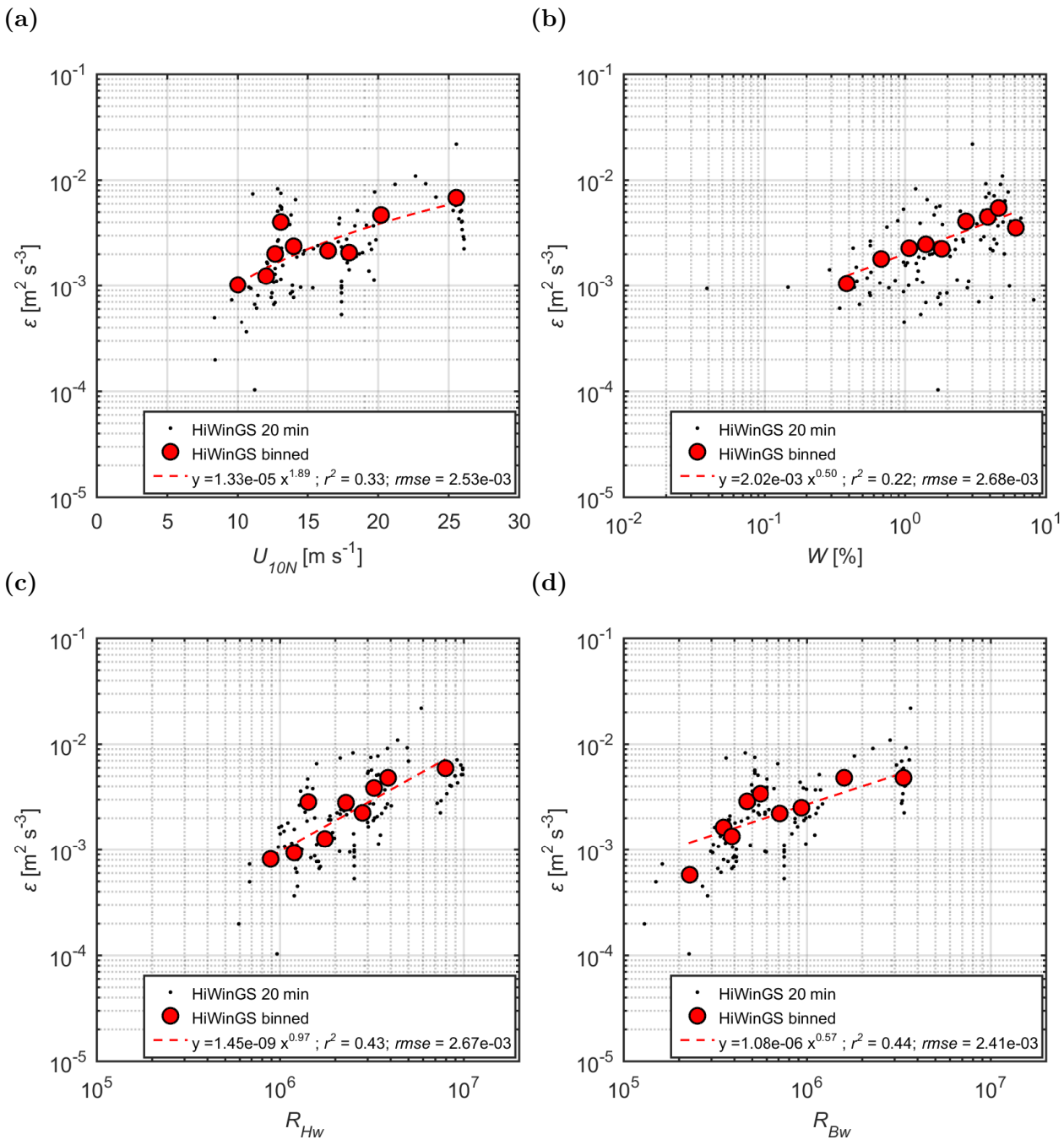

Figure 4.4: The turbulent kinetic energy dissipation rate (ε) plotted as a function of (a) the 10 m neutral wind speed, (b) the total whitecap coverage, (c) the wave-wind Reynolds number computed using the significant wave height of the onmi-directional spectra and (d) the Breaking Reynold number computed using the peak angular frequency of the onmi-directional spectra. The small dots represent statistics computed from individual 20 minute videos and the red dots are averages over equi-density bins. The red dashed line is the best power law fit.

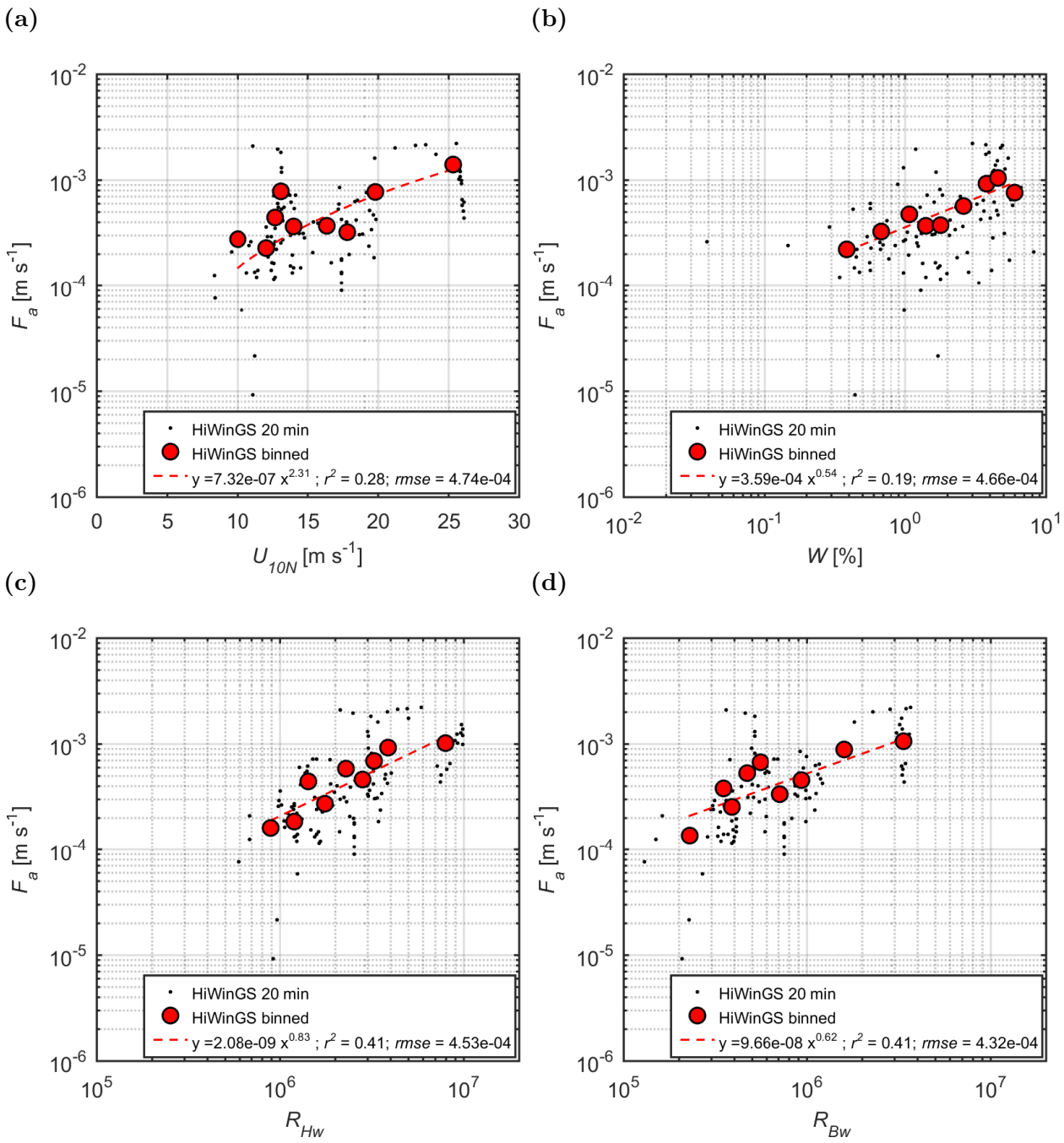

Figure 4.5: The bubble air volume flux (F_a) plotted as a function of (a) the 10 m neutral wind speed, (b) the total whitecap coverage, (c) the wave-wind Reynolds number computed using the significant wave height of the onmi-directional spectra and (d) the Breaking Reynold number computed using the peak angular frequency of the onmi-directional spectra. The small dots represent statistics computed from individual 20 minute videos and the red dots are averages over equi-density bins. The red dashed line is the best power law fit.

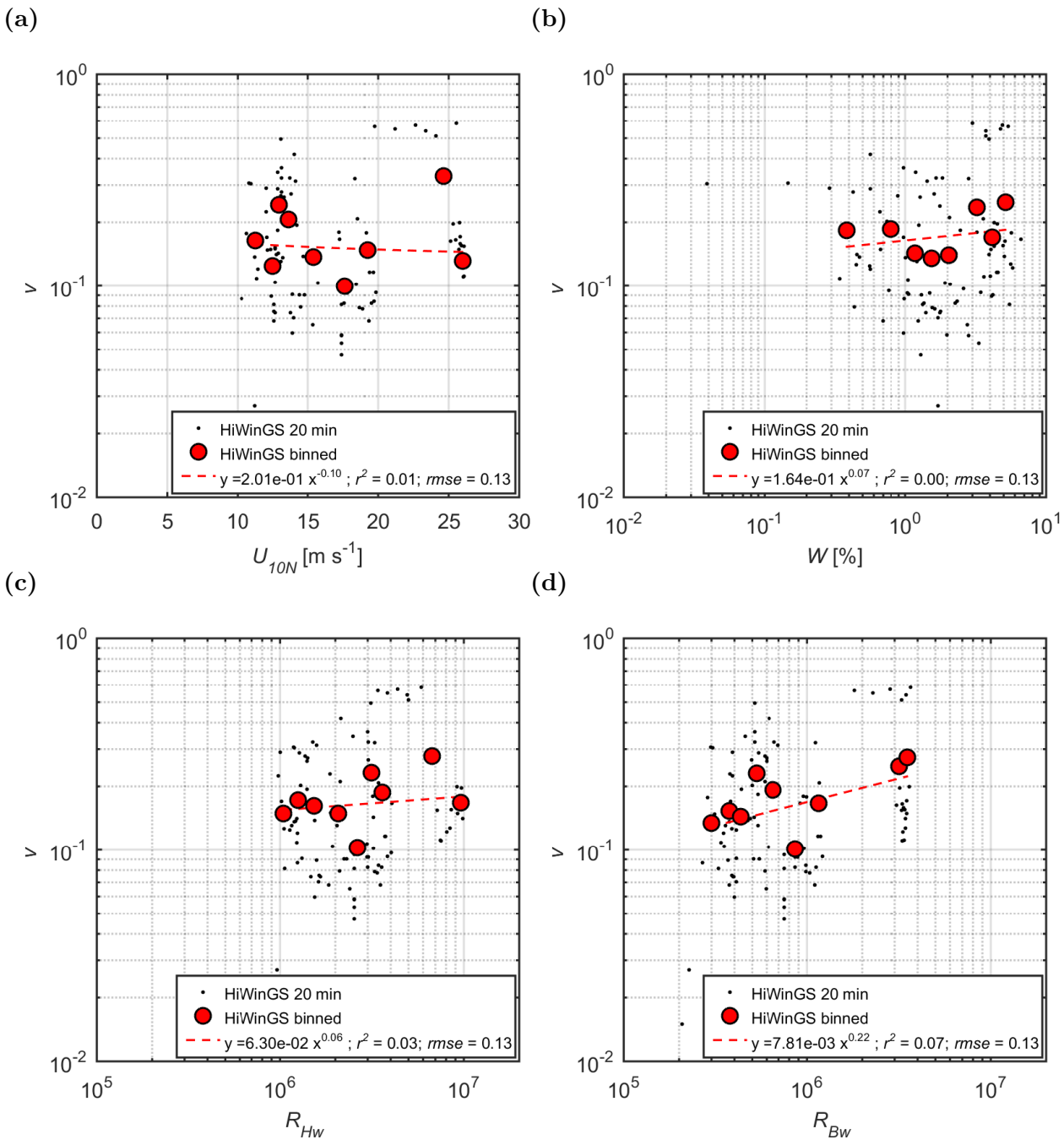

Figure 4.6: The turbulent Void fraction (v) plotted as a function of (a) the 10 m neutral wind speed, (b) the total whitecap coverage, (c) the wave-wind Reynolds number computed using the significant wave height of the onmi-directional spectra and (d) the Breaking Reynold number computed using the peak angular frequency of the onmi-directional spectra. The small dots represent statistics computed from individual 20 minute videos and the red dots are averages over equi-density bins. The red dashed line is the best power law fit.

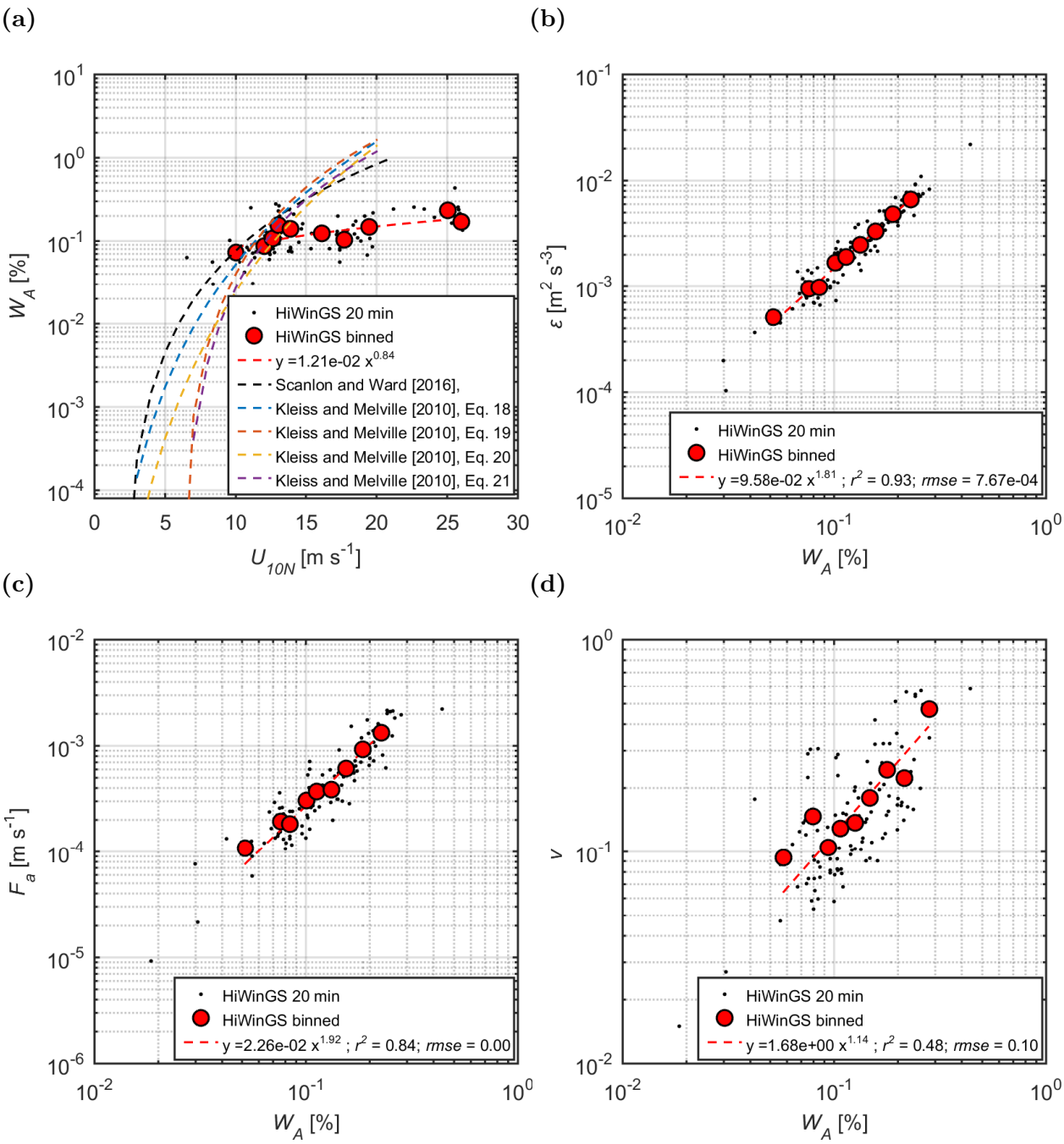

Figure 4.7: The active breaking coverage (W_A) plotted as a function of (a) the 10 m neutral wind speed, (b) turbulent kinetic energy dissipation rate plotted against W_A, (c) the bubble air volume flux plotted against W_A and (d) void fraction plotted against W_A. The small dots represent statistics computed from individual 20 minute videos and the red dots are averages over equi-density bins. The red dashed line is the best power law fit.

4.4.3 Previous process based models of gas transfer

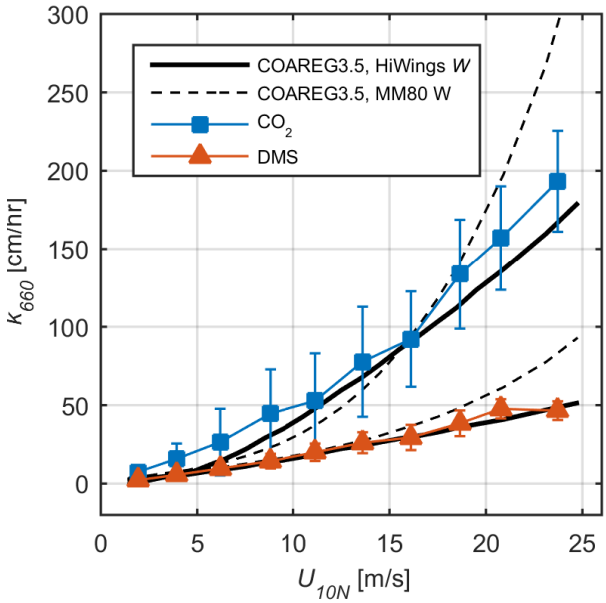

Figure 4.8: Gas transfer velocities of CO_2 and DMS referenced to a Schmidt number of 660 plotted against the neutral 10 m wind speed. The blue squares and brick colored triangles represent the bin averaged measured velocities of CO_2 and DMS, respectively. The thin dashed black lines show the NOAA/COAREG output using the original formulation with the W parameterization of *Monahan and O'Muircheartaigh* [1980]. The solid black lines show the output of the updated NOAA/COAREG with the wind-speed only parameterization determined from the HiWinGS dataset *Blomquist et al.* [2017].

NOAA's Coupled Ocean-Atmosphere Response Experiment Gas transfer algorithm (COAREG) is the first of the existing process based model evaluated here. It incorporates parameterizations of the air-side and the water-side transfer as well as the bubble mediated transfer. The formulation of the latter is based on Eq.4.5 with $F_a = 2450W$. It was originally tuned using the whitecap parameterization by *Monahan and O'Muircheartaigh* [1980] which has a greater than cubic wind speed dependency. The HiWinGS data, however, show a near linear dependence of W on U_{10N} as seen in Chapter 2 (Figure 2.9a and Table 2.5). This led to an overestimate of the gas transfer velocities, especially at wind speeds above 20 m s^{-1} (Figure 4.8). Using the wind speed only W parameterization determined from the HiWinGS dataset and adjusting the proportionality coefficient in Eq.4.5 (B_{COAREG}) leads to improved results

for both CO_2 and DMS (Figure 4.8). The wave-wind Reynolds number W parameterization further allows to capture more of the observed variability in the gas transfer velocities.

Three other process based models exist in the literature. *Asher and Wanninkhof* [1998], hereafter A98, proposed a model that includes not only bubble effects, but also enhanced gas transfer arising from wave breaking generated turbulence. It assumes the following functional form:

$$k = k_M(1 - W_f) + W_f k_T + W_f k_B \tag{4.27}$$

where $W_f = W/100$, k_T is the transfer velocity due to turbulence generated by wave breaking and k_M is the contribution of turbulence generated by all other processes. In A98, k_B is parameterized following *Merlivat et al.* [1993]:

$$k_B = [\frac{a_1}{\alpha} + b_1 \alpha^{-m} Sc^{-n}] \tag{4.28}$$

k_T is a constant modulated only by Sc ($k_T = 1.152 \times 10^{-5} Sc^{-1/2}$) and k_M is expressed as a linear function of wind speed equally modulated by the Sc ($k_M = 47 U_{10} Sc^{-1/2}$). Coefficients for Eq. 4.28 were estimated from lab experiments for both invasion and evasion.

As can be seen in Figure 4.9(a, b), A98 overestimates the gas transfer velocity of CO_2 and DMS for wind speeds over $\sim$12 m s^{-1}. The bubble-mediated transfer modeled by A98 is smaller than COAREG's (Figure 4.9(c, d)), but the non-wave breaking inter-facial transfer is larger such that ignoring the wave breaking turbulence mediated transfer ($(k_T - k_M)W_f$) A98 closely follows COAREG and the data for CO_2, but not for DMS.

Liang et al. [2013], hereafter L13, proposed another formulation of the bubble mediated transfer of sparingly soluble gases to be used in combination with the air and water-side resistances of COAREG:

$$k_{kL13} = 1.98 \times 10^6 u_{*w}^{2.76} (Sc/660)^{-2/3} \tag{4.29}$$

where u_{*w} is the water-side friction velocity ($u_{*w} = \sqrt{\rho_a/\rho_w}u_*$). L13 has no solubility dependence and is not adequate for DMS. It also over estimates the gas transfer velocity of CO_2 as k_{kL13} exceeds COAREG's for $U_{10} > 17$ m s^{-1}.

More recently, *Goddijn-Murphy et al.* [2016], hereafter GM16, put forward a hybrid model that uses the bubble-mediated transfer parameterizations suggested by *Woolf* [1997] and *Woolf et al.* [2007] (Eqs. 4.5 and 4.7) with a proportionality coefficient equal to 1 and $F_a = 2450W$. The non-bubble mediated transfer in GM16 is parameterized as a linear function of wind speed based on a linear fit through k_{660} measurements of DMS for wind speeds between 2 and 13 m s^{-1} ($k_0 = 2.6U_{10} - 5.7$). While GM16 successfully capture the magnitude of DMS gas transfer, it severely underestimates that of CO_2 due to its bubble mediated transfer being too small.

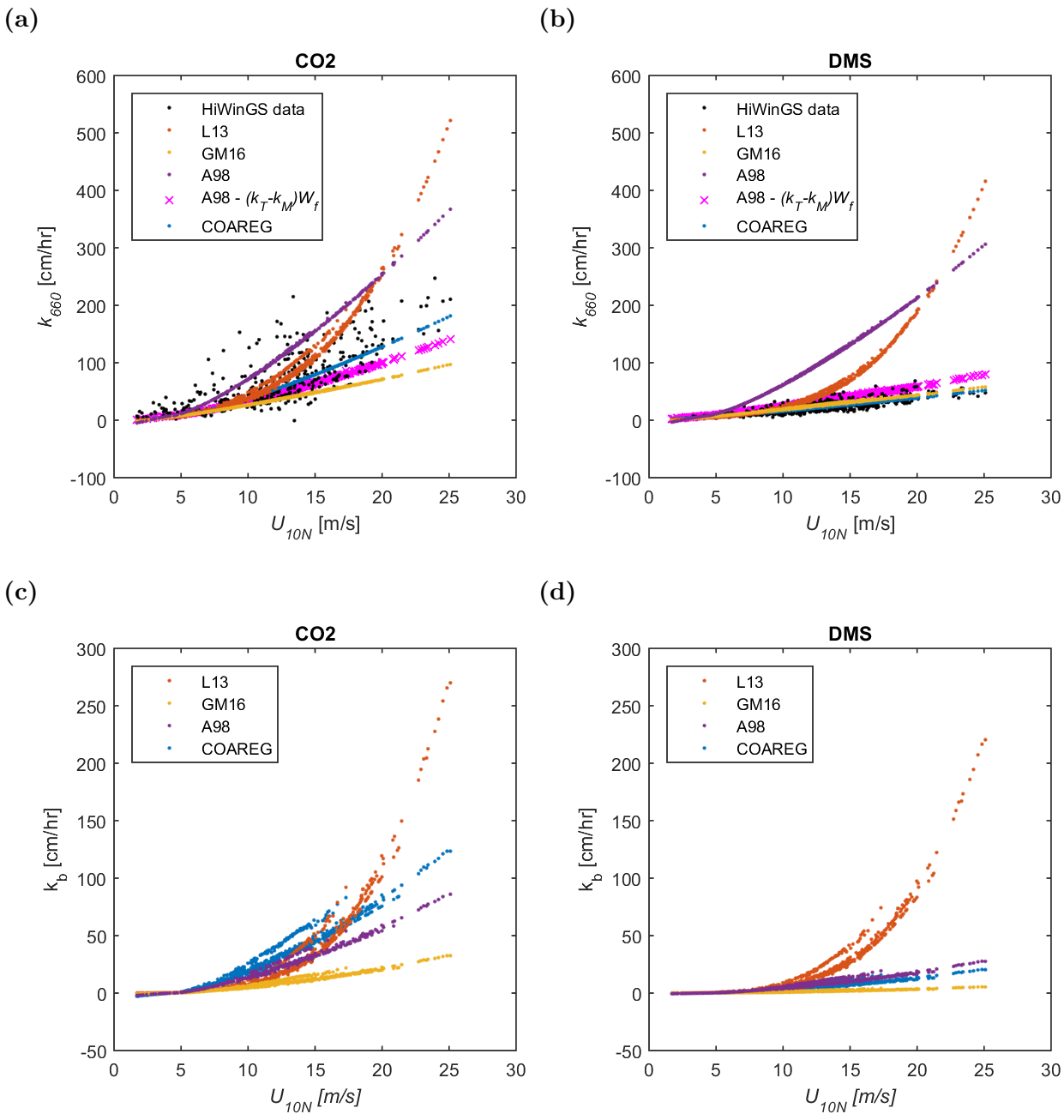

Figure 4.9: The gas transfer velocities measured during HiWinGS of (a) CO_2 and (b) DMS as well as the modeled bubble mediated transfer velocities for (c) CO_2 and (d) DMS all referenced to a Schmidt number of 660 plotted against the 10 m neutral wind speed. Plotted over the data (black dots) are existing process based gas transfer models: in blue, labeled L13, that of *Liang et al.* [2013]; in orange, labeled GM16, that of *Goddijn-Murphy et al.* [2016]; in yellow, labeled A98, that of *Asher and Wanninkhof* [1998], and in purple the COAREG [*Fairall et al.*, 2011] updated based on HiWinGS by *Blomquist et al.* [2017]. The magenta crosses show the transfer velocities given by A98 without the wave breaking turbulence contribution.

4.4.4 Testing the proposed framework

To test the proposed framework outline in Section 4.2, a linear regression was performed with the measured gas transfer velocities of CO_2 and DMS and the right hand sides of Eq. 4.4 and Eq. 4.5 which will be referred to as K_ε and K_{b1_χ}, respectively. Note that the bubble mediated transfer K_{b1_χ} is solubility and gas dependent. The turbulent transfer component is Schmidt number (diffusivity) dependent and in this case gas independent as the transfer velocities are all scaled to $Sc = 660$. Solving:

$$k = aK_\varepsilon + bK_{b1_\chi} \tag{4.30}$$

gives $a = 0.34$ and $b = 0.06$. Results are shown in Figure 4.10a. Output of the COAREG algorithm for matching measurements are shown in Figure 4.10b allowing to evaluate the relative performance of the mechanistic model proposed by Eq. 4.1. Equation 4.30 is only able explain 45% of overall variability in the gas transfer velocities. The correlations to the transfer velocities of CO_2 and DMS individually are worse, particularly for DMS. In contrast COAREG is able to reproduce 79% and 91% of the transfer velocities of CO_2 and DMS, respectively. Using the right hand side of Eq. 4.7, with the void fraction estimated based on Eq. 4.24 instead of K_{b1_χ} leads to very poor overall correlations ($r^2 \sim 0.1$) on account of the large scatter in the void fraction estimates.

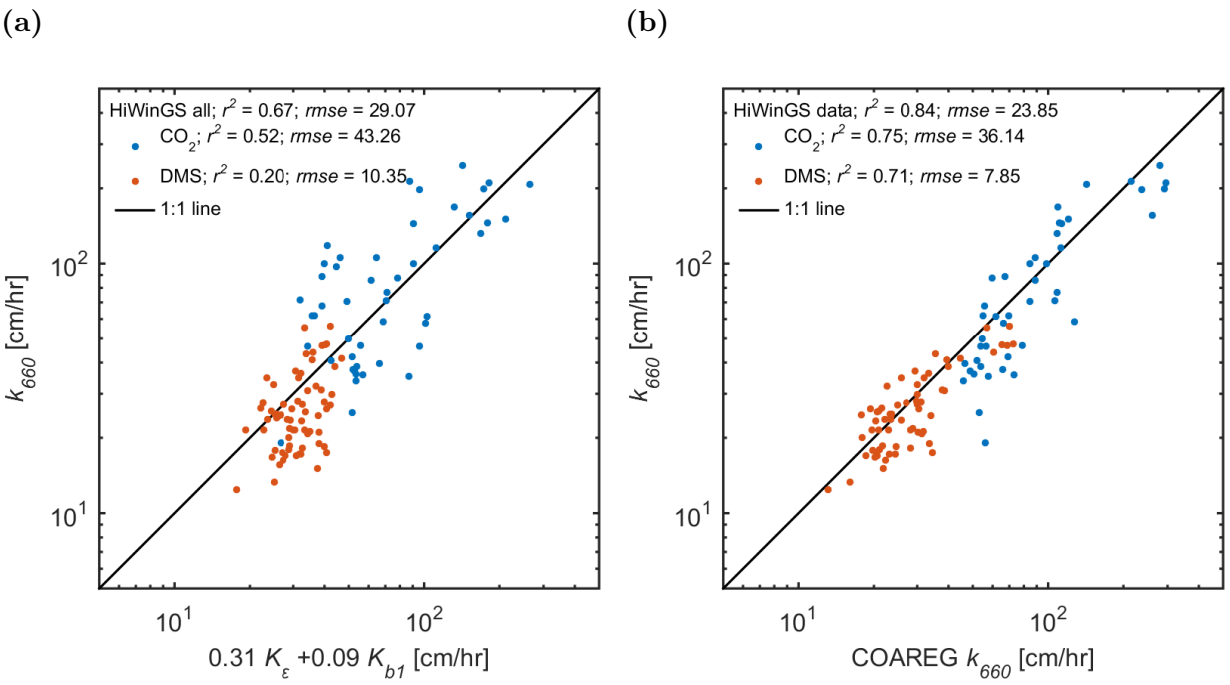

Figure 4.10: The measured gas transfer velocities of CO_2 (blue) and DMS (brick) measured during HiWinGS, referenced to a Schmidt number of 660, plotted against (a) the model proposed in Eq. 4.1 and (b) the NOAA/COAREG.

4.5 Discussion

Several sources of uncertainties remain in the estimation of the breaking crest length distribution and the derived breaking statistics. As the cameras set up on the *R/V Knorr* were set up looking at the breaking wave at an incidence angle of ∼65°, the 3D nature of oceanic waves may have led to parts of the breaking crest to be hidden from the cameras' view. This was likely less of a problem in previous datasets as those acquired from the *R/P Flip* [*Gemmrich et al.*, 2013; *Sutherland and Melville*, 2015] or from airborne imagery [*Kleiss and Melville*, 2010] in which camera were mounted to look straight down onto the ocean surface. The displacement of breaking waves with shorter wavelength than the underlying long waves is advected by than the orbital motion of long waves. In order to extract the phase speed of the breaking wave which is what *Phillips* [1985]'s spectral framework calls for, a Doppler correction has to be applied to the estimates derived from the imagery [see *Gemmrich et al.*, 2013; *Kleiss and Melville*, 2010]. To do so requires knowledge of the long wave amplitude (a)

and frequency (ω) [*Gemmrich et al.*, 2008]. Ideally, these should be measured locally such as by a Riegl altimeter located close or within the field of view of the camera. Such data was not available for the whole duration of the HiWinGS experiment, instead the correction was made based on spectral properties derived from the WAVEWATCH-III hindcast. It worth noting however, that the Doppler correction was shown to produce only modest changes to breaking crest length distribution [*Gemmrich et al.*, 2013]. Another source of uncertainty arises from the limited field of view of the imagery which does not always allow to track the full life-cycle of a breaking wave. Estimation of the duration of a breaking event therefore relies on the assumption that it is proportional to the period of the breaking wave (see Eq. 4.21).

The formulations of the bubble air volume flux and void fraction contain several unknowns. The first unknown is the bubble cloud constant B was set to 0.1 in accordance to *Deike et al.* [2016, 2017]. B was determined from laboratory data from *Duncan* [1981], *Lamarre and Melville* [1991] and *Deane and Stokes* [2002] for time averaged volumes of air entrained $\bar{V}$ by a single breaking wave ranging several orders of magnitude ($10^{-7} < \bar{V} < 10^{-1}$ m^3). The relationship however does not hold for $\bar{V} < 10^{-5}$ m^3 and it is unclear how these scale for open ocean conditions. The other unknown is the dissipation-weighted vertical mean bubble plume rise velocity (U_b). A constant U_b of 10 cm s^{-1} was assumed in the analysis presented above. It corresponds to the rise terminal rise velocity of clean bubble of radius of 450 μm according to *Woolf and Thorpe* [1991]. It is of the same order of magnitude as the rise velocity measured in a tank by [*Asher et al.*, 1997] which average within the first 6 seconds around 8 cm s^{-1} in sea-water.

Deike et al. [2017] found the following relationship for the dissipation-weighted velocity U_b:

$$U_b \sim h/\tau_{br} \tag{4.31}$$

where h is the height of the wave at the time of breaking. While h is not measured directly it may be approximated as the significant height of the wind-sea ($H_{s_{ws}}$). The proportionality

factor has however yet to be established. Since

$$H_{s_{ws}}$$

is on the order of 0.1-8 m and τ_{br} on the order of 1-10 s, a proportionality coefficient equal to 1, as suggested by *Deike et al.* [2017], would lead to rise velocities ranging from a couple of centimeters a second to over a meter a second which is clearly too high. Equation 4.31 allows to re-write Eq. 4.20 as:

$$F_a \propto \frac{b_{eff} B}{H_{s_{ws}} g^2} \int \Lambda(c) c^5 dc \tag{4.32}$$

This form, however, offers no advantage over Eq. 4.20 in terms of uncertainties as the proportionality coefficient remains unknown and leads to more scattered estimates of K_{b1_χ}.

The functional form of the proposed model for k (Eq. 4.1) is a linear combination of parameterizations of transfer velocities arising from different processes. As such, it follows the form adopted by previous studies outlined in section 4.4.3. Unlike in COAREG, it does not take into account the air-side transfer and may therefore only be applicable to sparingly soluble gases. This could also explain its poorer performance for DMS. No distinction is made between the turbulence mediated transfer due to wave breaking and other processes as is done in *Asher and Wanninkhof* [1998]. This is because computing the dissipation using the effective breaking strength gives an integrated estimate of the turbulence in the upper ocean at the given whitecap coverage. Indeed, b_{eff} was determined from the combination of breaking crest length distribution estimates and measures of the upper ocean turbulence that include both the wave breaking turbulence injection and the background turbulence [*Zappa et al.*, 2016]. The form of the bubble mediated transfer used in *Asher and Wanninkhof* [1998] could not be used for this study because 1) a wider variety of solubility have to be considered to estimate the coefficients and there are more unknowns than gases available, and 2) accounts for wave breaking only via W. *Asher and Wanninkhof* [1998] developed their model using laboratory W which may have led to unrealistic estimates of both the bubble

and the wave breaking turbulence mediate transfers (Wk_b and Wk_T in Eq. 4.27) . However, one could easily use Eq. 4.28 with the coefficients determined by *Asher and Wanninkhof* [1998] to estimate K_{b1_χ} in Eq. 4.30.

Both *Woolf* [1997], *Woolf et al.* [2007] and *Goddijn-Murphy et al.* [2016] assumed that the left and right hand side terms of eq. 4.5 are equal rather than proportional. In the NOAA-COAREG algorithm [*Fairall et al.*, 2011] the proportionality constant (B_{COARE}) was originally tuned to the SO GasEx data and set to 1.8. Note that there are two tunable parameters in the NOAA-COAREG algorithm's formulation of the water-side transfer coefficient: one for the bubble mediated and another for the turbulent molecular component. These empirical adjustement factors cannot be set independently and further depend on the choice of the W parameterization used. The original value of B_{COARE} was determined using the *Monahan and O'Muircheartaigh* [1980] W parameterization which we have shown to highly over estimate W at high wind speeds. Based on the HiWinGS data set, *Blomquist et al.* [2017] updated both tuning parameters and found $B_{COARE} = 3.8$ provides better model results. The proportional factor b found through regression in Section 4.4.4 is 0.06 is consistent with B_{COARE} given that the bubble air volume flux estimated from the breaking crest length distribution is 56.74 times bigger than that assumed in COAREG. Indeed, $56.74 \times 0.09 = 5 \sim B_{COARE}$ ($B_{COARE} \times 2450\ W \sim 0.06\ F_a$).

The proportionality coefficient a that multiplies K_ε to give k_ε is very close to that determined in previous studies. The study by *Zappa et al.* [2007] which is based data collected in a large tidal river, a macro-tidal estuary and from a coastal ocean site as well as in a "model" saltwater ocean at Biosphere 2 (Oracle, AZ USA) suggested $a = 0.4$. The first open ocean verification of the functional form of k_ε suggest $a = 0.12$-1.46 depending on the depth at which the turbulent kinetic dissipation rate measurements were taken and the approach used to extrapolate these measurements to the surface [*Esters et al.*, 2017]. Note that in this study different values of a were determined for CO_2 and DMS as the transfer velocities of these gases cannot be reconciled without taking bubble mediated transfer into account.

While fitting the transfer velocities separately may have led to improved fir statistics, it would defeat the goal of finding an unified model for both gases.

Although the assumed functional form follows the typical approach used in other process based models, it may not be entirely correct. Indeed, it is not the gas transfer velocities that should be combined linearly, but rather the bubble and turbulence mediated fluxes ($F_g = F_\varepsilon + F_b$). The partial pressure of a gas within a bubble is higher than that in the atmosphere due to the pressure caused by the surface tension of the bubble skin, which can be estimated from the Young–Laplace equation and hydrostatic pressure of the surrounding water. Estimation of this excess pressure a bubble requires knowledge of the bubble size distribution as a function of depth and time.

Chapter 5

Conclusion and Future work

5.1 Key Outcomes

The dependence of the whitecap coverage on wind and wave field characteristics was evaluated in Chapter 2 based on measurements acquired during the Southern Ocean Gas Exchange (SO GasEx) and the High Wind speed Gas exchange Study (HiWinGS) projects. High frequency ship-borne visible imagery were analyzed along side concurrent in situ eddy covariance flux measurements and wave field observations complemented by a WAVEWATCH-III® hind cast. The HiWinGS data set represents the first ship-borne measurements of W under sustained wind speeds (U_{10N}) of 25 m s^{-1}, extending the validity range of wind and wave dependent W parameterizations. Treating both datasets individually or as a combined dataset allowed critical assessment of the universality of the parameterizations obtained. A thorough literature review further provides a reference base for the results. There is remarkable inter-dataset agreement of the average dependence of W on wind speed alone and on wave-wind Reynolds numbers. The data further shows good agreement with two previous studies [*Goddijn-Murphy et al.*, 2011; *Salisbury et al.*, 2013] both for the wind-speed only and the wave-wind Reynolds number dependence of W. An important common trait of these studies is the use wind statistics that account for atmospheric stability effects.

While wind-speed-only models capture more of the observed W variability than Reynolds number parameterizations, the latter display is better inter-dataset agreement for both the current and the aforementioned previous studies. When expressing W in terms of wave field statistics only or wave age, larger scatter is observed and there is little agreement between SO GasEx, HiWinGS, and previously published data. The data also does not support the use of a multi-parameter model based on the combination of non-dimensional numbers that incorporate both wind and wave field variables. An interesting feature of the high wind speed measurements is the apparent leveling off of W for wind speeds above 18 m s^{-1}. The data suggest that W does not exceed 10% when averaged over 20 minutes to 1 hour. Such a leveling off had been previously proposed based on a small data sample and more data is needed to corroborate these observations.

Having recognized the usefulness of wind and wave related Reynolds numbers for use in simple single parameter models of wave breaking related processes such as W, Chapter 3 explores their applicability to air-sea gas transfer. Four distinct open ocean data sets were analyzed: GasEx-98, SO GasEx, Knorr11, and HiWinGS. These data cover a wide range of environmental conditions and the measured gas transfer velocity of CO_2 differ considerably: both SO GasEx and GasEx-98 display a cubic wind speed dependence, while the HiWinGS dataset displays a quadratic dependence. Expressing the gas transfer velocity, k as a function of breaking and wave-wind Reynolds numbers, R_B and R_H, respectively, allowed to collapse the three open ocean datasets. This is the first successful approach to reconcile diverging CO_2 gas transfer measurements. It highlights the necessity of taking into account sea state when estimating the transfer of sparingly soluble gases such as CO_2. In contrast, for DMS, parameterizations based on wave-related Reynolds number or wind speed alone perform comparably well. This is because DMS is more soluble than CO_2 and bubble-mediated exchange associated with wave breaking accounts for only a small fraction of the net air-sea transfer of DMS.

In Chapter 4, various physically based parameterizations were tested and a novel framework

was put forward to model gas transfer in the open ocean in the presence of breaking waves. NOAA's Coupled Ocean-Atmosphere Response Experiment Gas transfer algorithm was updated based on the whitecap coverage presented in Chapter 2 and the gas transfer velocities of CO_2 and DMS measured during HiWinGS. Shortcomings of other physically based parameterizations were revealed. The proposed framework incorporates both the turbulence and bubble mediated transfer. It is based on various statistics determined from the breaking crest length distribution, such as the turbulent kinetic energy dissipation rate, the bubble volume flux and the void fraction. In the last decade multiple field campaigns have aimed to apply the spectral framework proposed by *Phillips* [1985] to quantify wave breaking properties. They have provided a robust link between the breaking crest length distribution to the turbulent kinetic energy dissipation rate. Only recently has a study extended the application of the *Phillips* [1985] framework allowing estimations of bubble cloud properties from the breaking crest length distribution. This study is based on DNS and laboratory observations and many sources of uncertainties remain. It was applied to the HiWinGS data but we currently lack the necessary field measurements to corroborate the results. Nevertheless, the novel mechanistic approach to model gas transfer shows promise and will be explored further.

5.2 A proposal for future work

The necessity of including surface gravity waves in climate models to improve the representation of upper ocean dynamics has become evident and recent efforts have led to significant advances in model development. However, studies to date have solely focused on the physical impact of wave induced mixing on the mixed layer [e.g., *Wu et al.*, 2015; *Belcher et al.*, 2012; *Li et al.*, 2016]. The proposed study will be a first effort to address the biogeochemical impacts of wave induced mixing. It will build on the understanding of the impact of the wave field and wind-wave breaking on gas transfer developed in this dissertation. In particular,

it will take advantage of the improved gas transfer velocity parameterizations developed from the analysis of concurrent sea state, wave breaking and gas flux measurements taken during the HiWinGS, SO GasEx and GasEx-98 experiments. Two parametric forms will be considered:

1. Expressing k as a power-law function of wave-wind and breaking Reynolds (Re) numbers: $k = aRe^b$ which results in better inter-dataset agreement than wind-speed only parameterizations.

2. Expressing k as a function of the upper ocean turbulent kinetic energy dissipation rate ($k \propto (\varepsilon\nu_w)^{\frac{1}{4}}Sc^{-0.5}$). This functional form is based on turbulent transport arguments [*Lamont and Scott*, 1970; *Banerjee et al.*, 1968; *Kitaigorodskii*, 1984] and was previously demonstrated to be valid in low to moderate winds [*Zappa et al.*, 2007; *Esters et al.*, 2017]. Its validity in high wind and strong breaking wave conditions was demonstrated in the previous chapter based on ε determined from breaking crest length distributions .

Choice of gas transfer parameterization has been shown to significantly impact global and regional fluxes [e.g., *Boutin et al.*, 2002; *Fangohr and Woolf*, 2007; *Wrobel and Piskozub*, 2016]. It is therefore essential to update current default wind speed only parameterization in climate models and assess the model sensitivity to these new, wave dependent, parameterizations. The proposed study will be the first first to assess the impact of these novel wave dependent parameterizations, thus constraining uncertainties caused by parameterization choice. This could provide valuable guidance as to the processes necessary to include in future Coupled Model Intercomparison Projects.

Waves contribute to upper-ocean turbulence not only through their breaking, but also via Langmuir circulation, Stokes drift interaction with the Coriolis force, and stirring by non-breaking waves [*Wu et al.*, 2015]. Poor representation of wave mixing in ocean and climate models leads to systematic and substantial errors in the modeled mixed layer depth (MLD) as well as surface and subsurface temperatures [*Shu et al.*, 2011]. Taking into account

even only non-breaking wave induced vertical mixing results in a more realistic upper ocean thermal structure and MLD [*Qiao et al.*, 2004; *Song et al.*, 2012; *Qiao et al.*, 2010]. Langmuir turbulence has also been shown to have significant impacts leading to enhanced ventilation in the Southern Hemisphere and warming of the subsurface water over the majority of the global ocean thus reducing both MLD and subsurface ocean temperature biases [*Belcher et al.*, 2012; *Li et al.*, 2016]. Variations in the mixed layer stratification are strongly linked to variations in the vertical structure of state variables of the carbonate system which have significant implications on the $p\mathrm{CO}_{2_w}$ and thereby on the air-sea gas flux [*Fan and Griffies*, 2014; *Arruda et al.*, 2015; *Mahadevan et al.*, 2004].

While it takes about a year for the mixed layer to equilibrate its $p\mathrm{CO}_2$ with the atmosphere, the solubility pump operates over much longer timescales. On climate timescales the main rate-limiting process for air-sea gas exchange is the transfer of carbon between the upper mixed layer and deep waters and the solubility pump becomes important. To what extent it is affected by wave induced mixing has yet to be established.

Taking advantage of current modeling advances of coupling wave models to earth system models (ESM) and recent field measurements analyzed in this dissertation, I am proposing to:

1. Evaluate model sensitivity to gas transfer velocity parameterizations. This will addressed by incorporating wave dependent parameterizations derived from HiWinGS, Knorr11, SO GasEX, and GAsEX-98 datasets (see parametric forms enumerated above) and compare output to that obtained when using the traditional wind only parameterizations [e.g., *Wanninkhof*, 1992].

2. Investigate how wave induced changes in mixed layer properties impacts the evolution of surface and mixed layer $p\mathrm{CO}_{2_w}$ and consequently the air-sea flux of CO_2 on climate timescales.

For both objectives several approaches may be considered with varying levels of complexity

and computational cost. Ideally, a set of fully or partially coupled wave-ESM model runs will be compared to non-coupled ones. Partially coupled runs will include only one type of wave induced mixing (non-breaking stirring, breaking, Langmuir, or Stokes drift) allowing to evaluate relative importance. To alleviate the computational cost of coupling a third generation a third generation model such as WAVEWATCH-III in an ESM, wave statistics could be based on a wave climatology with perturbations related to wind perturbation with respect to a wind climatology. Alternatively, running a simplified wave model [*Donelan et al.*, 2012] may also be considered.

Bibliography

Abarbanel, H. D. I., D. D. Holm, J. E. Marsden, and T. Ratiu (1984), Richardson-number criterion for the nonlinear stability of 3-dimensional stratified flow, *Physical Review Letters*, *52*(26), 2352–2355, doi:DOI10.1103/PhysRevLett.52.2352.

Abood, K. A. (1974), Circulation in the hudson estuary, *Annals of the New York Academy of Sciences*, *250*(1), 39–111.

Adrian, R., C. Meinhart, and C. Tomkins (2000), Vortex organization in the outer region of the turbulent boundary layer, *Journal of Fluid Mechanics*, *422*, 1–54.

Agrawal, Y. C., E. A. Terray, M. A. Donelan, P. A. Hwang, A. Williams III, W. M. Drennan, K. K. Kahma, and S. A. Kitaigorodskii (1992), Enhanced dissipation of kinetic energy beneath surface waves, *Nature*, *359*(6392), 219–20.

Albert, M. F. M. A., M. D. Anguelova, A. M. M. Manders, M. Schaap, and G. de Leeuw (2016), Parameterization of oceanic whitecap fraction based on satellite observations, *Atmos. Chem. Phys.*, *16*(21), 13,725–13,751, doi:10.5194/acp-16-13725-2016.

Allen, J. (1985), *Principles of Physical Sedimentology*, George Allen and Unwin, London.

Andreae, M. O., and D. Rosenfeld (2008), Aerosol–cloud–precipitation interactions. part 1. the nature and sources of cloud-active aerosols, *Earth-Science Reviews*, *89*(1–2), 13–41, doi:http://dx.doi.org/10.1016/j.earscirev.2008.03.001.

Andreas, E. L. (1992), Sea spray and the turbulent air-sea heat fluxes, *J. Geophys. Res.*, *97*, 11,429–11,441.

Andreas, E. L. (1998), A new sea spray generation function for wind speeds up to 32 m s-1, *J. Phys. Ocean.*, *28*, 2175– 2184.

Andreas, E. L. (2004), Spray stress revisited, *Journal of Physical Oceanography*, *34*(6), 1429–1440, doi:10.1175/1520-0485(2004)034⟨1429:SSR⟩2.0.CO;2.

Anguelova, M. D., and P. A. Hwang (2016), Using energy dissipation rate to obtain active whitecap fraction, *Journal of Physical Oceanography*, *46*(2), 461–481, doi:10.1175/jpo-d-15-0069.1.

Anguelova, M. D., and F. Webster (2006), Whitecap coverage from satellite measurements: A first step toward modeling the variability of oceanic whitecaps, *J. Geophys. Res.*, *111*(C03017), doi:10.1029/2005JC003,158.

Archer, D. (2005), Fate of fossil fuel co_2 in geologic time, *Journal of Geophysical Research: Oceans*, *110*(C9), C09S05, doi:10.1029/2004JC002625.

Arora, V. K., G. J. Boer, P. Friedlingstein, M. Eby, C. D. Jones, J. R. Christian, G. Bonan, L. Bopp, V. Brovkin, P. Cadule, T. Hajima, T. Ilyina, K. Lindsay, J. F. Tjiputra, and T. Wu (2013), Carbon–concentration and carbon–climate feedbacks in cmip5 earth system models, *Journal of Climate*, *26*(15), 5289–5314, doi:10.1175/jcli-d-12-00494.1.

Arruda, R., P. H. R. Calil, A. A. Bianchi, S. C. Doney, N. Gruber, I. Lima, and G. Turi (2015), Air-sea co_2 fluxes and the controls on ocean surface pco_2 seasonal variability in the coastal and open-ocean southwestern atlantic ocean: a modeling study, *Biogeosciences*, *12*(19), 5793–5809, doi:10.5194/bg-12-5793-2015.

Asher, W. E., and R. Wanninkhof (1998), The effect of bubble-mediated gas transfer on

purposeful dual-gaseous tracer experiments, *Journal of Geophysical Research*, *103*(C5), 10,555–60.

Asher, W. E., L. M. Karle, B. Higgins, P. Farley, C. Sherwood, W. Gardiner, R. Wanninkhof, H. Chen, T. Lantry, M. Steckley, E. Monahan, Q. Wang, and P. Smith (1995), *Measurement of gas transfer, whitecap coverage, and brightness temperature in a surf pool: An overview of WABEX-93*, Heidelberg, Germany.

Asher, W. E., L. M. Karle, B. J. Higgins, P. J. Farley, E. C. Monahan, and I. S. Leifer (1996), The influence of bubble plumes on air-seawater gas transfer velocities, *Journal Of Geophysical Research*, *101*(C5), 12,027–12,041.

Asher, W. E., L. M. Karle, and B. J. Higgins (1997), On the differences between bubble-mediated air-water gas transfer in freshwater and seawater, *Journal of Marine Research*, *55*, 813–845.

Asher, W. E., J. Edson, W. McGillis, R. Wanninkhof, D. T. Ho, and T. Litchendorf (2002), *Fractional area whitecap coverage and air-sea gas transfer velocities measured during Gas Ex-98*, pp. 199–205, AGU, Geophysical Monograph 127, Washington, DC.

Atmane, M. A., W. E. Asher, and A. T. Jessup (2004), On the use of the active infrared technique to infer heat and gas transfer velocities at the air-water free surface, *Journal of Geophysical Research*, *109*, C08S14, doi:10.1029/2003JC001805.

Baldy, S., and M. Bourguel (1987), Bubbles between the wave trough and wave crest levels, *Journal of Geophysical Research: Oceans*, *92*(C3), 2919–2929, doi:10.1029/JC092iC03p02919.

Banerjee, S., and S. MacIntyre (2004), The air-water interface: Turbulence and scalar exchange, *Advances in coastal and ocean engineering*, *9*, 181.

Banerjee, S., D. S. Scott, and E. Rhodes (1968), Mass transfer to falling wavy liquid films in turbulent flow, *Industrial and Engineering Chemistry Fundamentals*, *7*(1), 22–27.

Banerjee, S., D. Lakehal, and M. Fulgosi (2004), Surface divergence models for scalar exchange between turbulent streams, *International Journal of Multiphase Flow*, *30*(7), 963 – 977, doi:http://dx.doi.org/10.1016/j.ijmultiphaseflow.2004.05.004, a Collection of Papers in Honor of Professor G. Yadigaroglu on the Occasion of his 65th Birthday.

Banner, M. L., and R. Morison (2010), Refined source terms in wind wave models with explicit wave breaking forecasts. part i. model framework and validation against field data, *Ocean Modelling*, *33*, 177–189, doi:10.1016/j.ocemod.2010.01.002.

Banner, M. L., and W. Peirson (2007), Wave breaking onset and strength for two-dimensional deep water wave groups, *J. Fluid Mech.*, *585*, 93–115.

Banner, M. L., J. Gemmrich, and D. Farmer (2002), Multiscale measurements of ocean wave breaking probability, *J. Phys. Oceanogr.*, *32*, 3364–3375.

Banner, M. L., X. Barthelemy, F. Fedele, M. Allis, A. Benetazzo, F. Dias, and W. Peirson (2014), Linking reduced breaking crest speeds to unsteady nonlinear water wave group behavior, *Physical Review Letters*, *112*(11), 114,502, doi:10.1103/PhysRevLett.112.114502.

Bariteau, L., D. Helmig, C. W. Fairall, J. E. Hare, J. Hueber, and E. K. Lang (2010), Determination of oceanic ozone deposition by ship-borne eddy covariance flux measurements, *Atmospheric Measurement Techniques*, *3*(2), 441–455.

Batchelor, G. K. (1953), *The theory of homogeneous turbulence*, Cambridge university press.

Batchelor, G. K. (1959), Small-scale variation of convected quantities like temperature in turbulent fluid. part 1. general discussion and the case of small conductivity, *J. Fluid Mech.*, *5*, 113–133.

Belcher, S. E., A. L. M. Grant, K. E. Hanley, B. Fox-Kemper, L. Van Roekel, P. P. Sullivan, W. G. Large, A. Brown, A. Hines, D. Calvert, A. Rutgersson, H. Pettersson, J.-R. Bidlot, P. A. E. M. Janssen, and J. A. Polton (2012), A global perspective on langmuir turbulence in the ocean surface boundary layer, *Geophysical Research Letters*, *39*(18), L18,605, doi: 10.1029/2012GL052932.

Bell, R. E., R. D. Flood, S. Carbotte, W. B. F. Ryan, C. McHugh, M. Cormier, R. Versteeg, H. Bokuniewicz, V. L. Ferrini, J. Thissen, and et al. (2006), *Benthic habitat mapping in the Hudson River Estuary*, pp. 51–64, Cambridge University Press, Cambridge.

Bell, T. G., W. De Bruyn, S. D. Miller, B. Ward, K. Christensen, and E. S. Saltzman (2013), Air-sea dimethylsulfide (dms) gas transfer in the north atlantic: Evidence for limited interfacial gas exchange at high wind speed, *Atmospheric Chemistry and Physics*, *13*(21), 11,073–11,087, doi:10.5194/acp-13-11073-2013.

Bell, T. G., W. De Bruyn, C. A. Marandino, S. D. Miller, C. S. Law, M. J. Smith, and E. S. Saltzman (2015), Dimethylsulfide gas transfer coefficients from algal blooms in the southern ocean, *Atmospheric Chemistry and Physics*, *15*(4), 1783–1794, doi:10.5194/ acp-15-1783-2015.

Bell, T. G., S. Landwehr, S. D. Miller, W. J. de Bruyn, A. Callaghan, B. Scanlon, B. Ward, M. Yang, and E. S. Saltzman (2017), Estimation of bubbled-mediated air/sea gas exchange from concurrent dms and co_2 transfer velocities at intermediate-high wind speeds, *Atmos. Chem. Phys. Discuss.*, *2017*, 1–29, doi:10.5194/acp-2017-85.

Best, J. (2005), The fluid dynamics of river dunes: A review and some future research directions, *Journal of Geophysical Research: Earth Surface*, *110*, F04S02, doi:10.1029/ 2004JF000218.

Blanchard, D. C. (1963), The electrification of the atmosphere by particles from bubbles in

the sea, *Progress in Oceanography*, *1*, 73–202, doi:http://dx.doi.org/10.1016/0079-6611(63)90004-1.

Blanchard, D. C. (1983), *The Production, Distribution, and Bacterial Enrichment of the Sea-Salt Aerosol*, pp. 407–454, Springer Netherlands, Dordrecht, doi:10.1007/978-94-009-7169-1_7.

Blomquist, B. W., C. W. Fairall, B. J. Huebert, D. J. Kieber, and G. R. Westby (2006), Dms sea-air transfer velocity: Direct measurements by eddy covariance and parameterization based on the noaa/coare gas transfer model, *Geophysical Research Letters*, *33*, L07,601, doi:10.1029/2006GL025735.

Blomquist, B. W., B. J. Huebert, C. W. Fairall, and I. C. Faloona (2010), Determining the sea-air flux of dimethylsulfide by eddy correlation using mass spectrometry, *Atmospheric Measurement Techniques*, *3*(1), 1–20.

Blomquist, B. W., B. J. Huebert, C. W. Fairall, L. Bariteau, J. B. Edson, J. E. Hare, and W. R. McGillis (2014), Advances in air-sea co_2 flux measurement by eddy correlation, *Boundary-Layer Meteorology*, *152*(3), 245–276, doi:10.1007/s10546-014-9926-2.

Blomquist, B. W., S. E. Brumer, C. W. Fairall, B. J. Huebert, C. J. Zappa, I. M. Brooks, M. Yang, L. Bariteau, J. Prytherch, J. E. Hare, H. Czerski, A. Matei, and R. Pascal (2017), Wind speed and sea state dependencies of air-sea gas transfer: results from the highwind speed gas exchange study (hiwings), *Journal of Geophysical Research: Oceans*, (submitted).

Bobak, J. P., W. E. Asher, D. J. Dowgiallo, and M. D. Anguelova (2011), Aerial radiometric and video measurements of whitecap coverage, *IEEE Transactions on Geoscience and Remote Sensing*, *49*(6), 2183–2193, doi:10.1109/TGRS.2010.2103565.

Boden, T., G. Marland, and R. Andres (2011), Global, regional, and national fossil-fuel co_2 emissions, carbon dioxide information analysis center, oak ridge national laboratory, *US Department of Energy, Oak Ridge, Tenn., USA.*, doi:10.3334/CDIAC/00001_V2011.

Bopp, L., O. Boucher, O. Aumont, S. Belviso, J.-L. Dufresne, M. Pham, and P. Monfray (2004), Will marine dimethylsulfide emissions amplify or alleviate global warming? a model study, *Canadian Journal of Fisheries and Aquatic Sciences*, *61*(5), 826–835.

Bortkovskii, R. S. (1987), *Air-Sea Exchange of Heat and Moisture During Storms*, 193 pp., Springer, New York.

Bortkovskii, R. S., and V. A. Novak (1993), Statistical dependencies of sea state characteristics on water temperature and wind-wave age, *Journal of Marine Systems*, *4*(2), 161–169, doi:http://dx.doi.org/10.1016/0924-7963(93)90006-8.

Bouguet, J.-Y. (2015), Camera calibration toolbox for matlab.

Bourassa, M. A., S. T. Gille, C. Bitz, D. Carlson, I. Cerovecki, C. A. Clayson, M. F. Cronin, W. M. Drennan, C. W. Fairall, R. N. Hoffman, G. Magnusdottir, R. T. Pinker, I. A. Renfrew, M. Serreze, K. Speer, L. D. Talley, and G. A. Wick (2013), High-latitude ocean and sea ice surface fluxes: Challenges for climate research, *Bulletin of the American Meteorological Society*, *94*(3), 403–423, doi:10.1175/BAMS-D-11-00244.1.

Boutin, J., J. Etcheto, L. Merlivat, and Y. Rangama (2002), Influence of gas exchange coefficient parameterisation on seasonal and regional variability of co2 air-sea fluxes, *Geophysical Research Letters*, *29*(8), 23–1–23–4, doi:10.1029/2001GL013872.

Broecker, H. C., and W. Siems (1984), *The Role of Bubbles for Gas Transfer from Water to Air at Higher Windspeeds: Experiments in the Wave-Wave Facility in Hamburg*, pp. 229–236, D. Reidel, Norwell, MA.

Broecker, H. C., J. Petermann, and W. Siems (1978), The influence of wind on co_2 exchange in a wind-wave tunnel, including the effects of monolayers, *Journal of Marine Research*, *36*, 595–610.

Broecker, W. S., and T.-H. Peng (1986), Carbon cycle: 1985 glacial to interglacial changes in the operation of the global carbon cycle, *Radiocarbon*, *28*(2A), 309–327, doi:10.1017/S0033822200007414.

Brumer, S. E., C. J. Zappa, I. M. Brooks, H. Tamura, S. M. Brown, B. Blomquist, C. W. Fairall, and A. Cifuentes-Lorenzen (2017), Whitecap coverage dependence on wind and wave statistics as observed during so gasex and hiwings, *Journal of Physical Oceanography*, doi:DOI:10.1175/JPO-D-17-0005.1.

Butterworth, B. J., and S. D. Miller (2016), Air-sea exchange of carbon dioxide in the southern ocean and antarctic marginal ice zone, *Geophysical Research Letters*, *43*(13), 7223–7230.

Callaghan, A. H., and M. White (2009), Automated processing of sea surface images for the determination of whitecap coverage, *Journal of Atmospheric and Oceanic Technology*, *26*, 383–394, doi:10.1175/2008JTECHO634.1.

Callaghan, A. H., G. B. Deane, and M. D. Stokes (2008a), Observed physical and environmental causes of scatter in whitecap coverage values in a fetch-limited coastal zone, *J. Geophys. Res.*, *113*, C05,022, doi:10.1029/2007JC004453.

Callaghan, A. H., G. d. Leeuw, L. Cohen, and C. D. O'Dowd (2008b), Relationship of oceanic whitecap coverage to wind speed and wind history, *Geophys. Res. Lett.*, *35*, L23,609, doi:10.1029/2008GL036165.

Callaghan, A. H., M. D. Stokes, and G. B. Deane (2014), The effect of water temperature on air entrainment, bubble plumes, and surface foam in a laboratory breaking-wave analog, *Journal of Geophysical Research: Oceans*, *119*(11), 7463–7482, doi:10.1002/2014JC010351.

Callaghan, A. H., G. B. Deane, and M. D. Stokes (2016), Laboratory air-entraining breaking waves: Imaging visible foam signatures to estimate energy dissipation, *Geophysical Research Letters*, *43*(21), 11,320–11,328, doi:10.1002/2016GL071226.

Carpenter, L. J., S. D. Archer, and R. Beale (2012), Ocean-atmosphere trace gas exchange, *Chemical Society Reviews*, *41*(19), 6473–6506, doi:10.1039/c2cs35121h.

Cavaleri, L., J. H. G. M. Alves, F. Ardhuin, A. Babanin, M. Banner, K. Belibassakis, M. Benoit, M. Donelan, J. Groeneweg, T. H. C. Herbers, P. Hwang, P. A. E. M. Janssen, T. Janssen, I. V. Lavrenov, R. Magne, J. Monbaliu, M. Onorato, V. Polnikov, D. Resio, W. E. Rogers, A. Sheremet, J. McKee Smith, H. L. Tolman, G. van Vledder, J. Wolf, and I. Young (2007), Wave modelling – the state of the art, *Progress in Oceanography*, *75*(4), 603–674, doi:http://dx.doi.org/10.1016/j.pocean.2007.05.005.

Cavaleri, L., B. Fox-Kemper, and M. Hemer (2012), Wind waves in the coupled climate system, *Bulletin of the American Meteorological Society*, *93*(11), 1651–1661, doi:10.1175/BAMS-D-11-00170.1.

Charlson, R. J., J. E. Lovelock, M. O. Andreae, and S. G. Warren (1987), Oceanic phytoplankton, atmospheric sulphur, cloud albedo and climate, *Nature*, *326*, 655–660.

Chickadel, C. C., A. R. Horner-Devine, S. A. Talke, and A. T. Jessup (2009), Vertical boil propagation from a submerged estuarine sill, *Geophysical Research Letters*, *36*(10), L10,601, doi:10.1029/2009GL037278.

Chickadel, C. C., S. A. Talke, A. R. Horner-Devine, and A. T. Jessup (2011), Infrared-based measurements of velocity, turbulent kinetic energy, and dissipation at the water surface in a tidal river, *IEEE Geoscience and Remote Sensing Letters*, *8*(5), 849–853, doi:10.1109/LGRS.2011.2125942.

Christensen, J., K. Krishna Kumar, E. Aldrian, S.-I. An, I. Cavalcanti, M. de Castro, W. Dong, P. Goswami, A. Hall, J. Kanyanga, A. Kitoh, J. Kossin, N.-C. Lau, J. Renwick, D. Stephenson, S.-P. Xie, and T. Zhou (2013), *Climate Phenomena and their Relevance for Future Regional Climate Change*, book section 14, p. 1217–1308, Cambridge University Press,

Cambridge, United Kingdom and New York, NY, USA, doi:10.1017/CBO9781107415324.028.

Ciais, P., C. Sabine, G. Bala, L. Bopp, V. Brovkin, J. Canadell, A. Chhabra, R. DeFries, J. Galloway, M. Heimann, C. Jones, C. Le Qu'er'e, R. Myneni, S. Piao, and P. Thornton (2013), *Carbon and Other Biogeochemical Cycles*, book section 6, p. 465–570, Cambridge University Press, Cambridge, United Kingdom and New York, NY, USA, doi:10.1017/CBO9781107415324.015.

Cifuentes-Lorenzen, A., J. B. Edson, C. J. Zappa, and L. Bariteau (2013), A multi-sensor comparison of ocean wave frequency spectra from a research vessel during the southern ocean gas exchange experiment, *J. Atmos. Oceanic Tech.*, *30*(12), 2907–2925, doi:10.1175/JTECH-D-12-00181.1.

Cipriano, R., and D. Blanchard (1981), Bubble and aerosol spectra produced by a laboratory "breaking wave", *J. Geophys. Res.*, *86*, 8085–8092.

Clift, R., J. R. Grace, and M. E. Weber (1978), *Bubbles, drops, and particles*, Courier Corporation.

Csanady, G. (1997), The "slip law" of the free surface, *Journal of Oceanography*, *53*(1), 67–80.

Cunliffe, M., and O. Wurl (2014), Guide to best practices to study the ocean's surface.

Danckwerts, P. V. (1951), Significance of liquid-film coefficients in gas absorption, *Industrial and Engineering Chemistry*, *43*(6), 1460–1467.

de Leeuw, G., E. L. Andreas, M. D. Anguelova, C. W. Fairall, E. R. Lewis, C. O'Dowd, M. Schulz, and S. E. Schwartz (2011), Production flux of sea spray aerosol, *Rev. Geophys.*, *49*, RG2001, doi:doi:10.1029/2010RG000349.

Deane, G. B., and M. D. Stokes (2002), Scale dependence of bubble creation mechanisms in breaking waves, *Nature*, *418*(6900), 839–844.

Deike, L., W. K. Melville, and S. Popinet (2016), Air entrainment and bubble statistics in breaking waves, *Journal of Fluid Mechanics*, *801*, 91–129, doi:10.1017/jfm.2016.372.

Deike, L., L. Lenain, and W. K. Melville (2017), Air entrainment by breaking waves, *Geophysical Research Letters*, *44*(8), 3779–3787, doi:10.1002/2017GL072883, 2017GL072883.

Delille, B., M. Vancoppenolle, N.-X. Geilfus, B. Tilbrook, D. Lannuzel, V. Schoemann, S. Becquevort, G. Carnat, D. Delille, C. Lancelot, L. Chou, G. S. Dieckmann, and J.-L. Tison (2014), Southern ocean co_2 sink: The contribution of the sea ice, *Journal of Geophysical Research: Oceans*, *119*(9), 6340–6355, doi:10.1002/2014JC009941.

Donelan, M. A. (1985), Directional spectra of wind-generated waves, *Philosophical transactions of the Royal Society of London. Series A: Mathematical, physical, and engineering sciences*, *315*(1534), 509–562, doi:10.1098/rsta.1985.0054.

Donelan, M. A., M. Curcic, S. S. Chen, and A. K. Magnusson (2012), Modeling waves and wind stress, *Journal of Geophysical Research: Oceans*, *117*(C11), doi:10.1029/2011JC007787.

Drazen, D., W. Melville, and L. Lenain (2008), Inertial scaling of dissipation in unsteady breaking waves, *J. Fluid Mech.*, *611*, 307–332.

Dugan, J. P., and C. C. Piotrowski (2012), Measuring currents in a coastal inlet by advection of turbulent eddies in airborne optical imagery, *J. Geophys. Res.*, *117*, C03,020, doi: doi:10.1029/2011JC007600.

Dugan, J. P., S. P. Anderson, C. C. Piotrowski, and S. B. Zuckerman (2014), Airborne infrared remote sensing of riverine currents, *IEEE Transactions on Geoscience and Remote Sensing*, *52*(7), 3895–3907.

Duncan, J. H. (1981), An experimental investigation of breaking waves produced by a towed hydrofoil, *Proceedings of the Royal Society of London, Series A*, *377*(1770), 331–48.

Duncan, J. H. (1983), The breaking and non-breaking wave resistance of a two-dimensional hydrofoil, *Journal of Fluid Mechanics*, *126*, 507–20.

Edson, J. B., A. A. Hinton, K. E. Prada, J. E. Hare, and C. W. Fairall (1998), Direct covariance flux estimates from mobile platforms at sea, *Journal of Atmospheric and Oceanic Technology*, *15*(2), 547–562.

Edson, J. B., C. J. Zappa, J. Ware, W. R. McGillis, and J. E. Hare (2004), Scalar flux profile relationships over the open ocean, *J Geophys. Res.*, *109*, C08S09, doi:10.1029/2003JC001960.

Edson, J. B., C. W. Fairall, L. Bariteau, C. J. Zappa, A. Cifuentes-Lorenzen, W. R. McGillis, S. Pezoa, J. E. Hare, and D. Helmig (2011), Direct covariance measurement of co_2 gas transfer velocity during the 2008 southern ocean gas exchange experiment: Wind speed dependency, *Journal of Geophysical Research – Oceans*, *116*(C4), C00F10, doi:10.1029/2011JC007022.

Edson, J. B., V. Jampana, R. A. Weller, S. P. Bigorre, A. J. Plueddemann, C. W. Fairall, S. D. Miller, L. Mahrt, D. Vickers, and H. Hersbach (2013), On the exchange of momentum over the open ocean, *Journal of Physical Oceanography*, *43*(8), 1589–1610, doi:10.1175/JPO-D-12-0173.1.

Else, B. G. T., T. N. Papakyriakou, R. J. Galley, W. M. Drennan, L. A. Miller, and H. Thomas (2011), Wintertime co_2 fluxes in an arctic polynya using eddy covariance: Evidence for enhanced air-sea gas transfer during ice formation, *Journal of Geophysical Research*, *116*, C00G03, doi:10.1029/2010JC006760.

Esters, L., S. Landwehr, G. Sutherland, T. G. Bell, K. H. Christensen, E. S. Saltzman, S. D. Miller, and B. Ward (2017), Parameterizing air-sea gas transfer velocity with dissipation, *Journal of Geophysical Research: Oceans*, *122*(4), 3041–3056, doi:10.1002/2016JC012088.

Fairall, C. W., E. F. Bradley, J. S. Godfrey, G. A. Wick, J. B. Edson, and G. S. Young (1996), Cool-skin and warm-layer effects on sea surface temperature, *Journal of Geophysical Research*, *101*(C1), 1295–1308.

Fairall, C. W., J. Hare, J. Edson, and W. McGillis (2000), Parameterization and micrometeorological measurement of air–sea gas transfer, *Bound.-Layer Meteor.*, *96*, 63–105.

Fairall, C. W., E. F. Bradley, J. E. Hare, A. A. Grachev, and J. B. Edson (2003), Bulk parameterization of air-sea fluxes: Updates and verification for the coare algorithm, *J. Climate*, *16*, 571–591.

Fairall, C. W., M. Yang, L. Bariteau, J. B. Edson, D. Helmig, W. McGillis, S. Pezoa, J. E. Hare, B. Huebert, and B. Blomquist (2011), Implementation of the coupled ocean-atmosphere response experiment flux algorithm with co_2, dimethyl sulfide, and o3, *J. Geophys. Res.*, *116*(C00F09), C00F09, doi:doi:10.1029/2010JC006884.

Fan, Y., and S. M. Griffies (2014), Impacts of parameterized langmuir turbulence and nonbreaking wave mixing in global climate simulations, *Journal of Climate*, *27*(12), 4752–4775, doi:10.1175/jcli-d-13-00583.1.

Fangohr, S., and D. K. Woolf (2007), Application of new parameterizations of gas transfer velocity and their impact on regional and global marine co_2 budgets, *Journal of Marine Systems*, *66*(1–4), 195–203, doi:http://dx.doi.org/10.1016/j.jmarsys.2006.01.012.

Farmer, D. M., C. L. McNeil, and B. D. Johnson (1993), Evidence for the importance of bubbles in increasing air-sea gas flux, *Nature*, *361*(6413), 620–3.

Farrar, J. T., C. J. Zappa, R. A. Weller, and A. T. Jessup (2007), Sea surface temperature signatures of oceanic internal waves in low winds, *Journal of Geophysical Research Oceans*, *112*, C06,014, doi:10.1029/2006JC003947.

Frew, N. M. (1997), *The role of organic films in air-sea gas exchange*, pp. 121–172, Cambridge University Press, Cambridge.

Frouin, R., S. F. Iacobellis, and P. Y. Deschamps (2001), Influence of oceanic whitecaps on the global radiation budget, *Geophysical Research Letters*, *28*(8), 1523–1526, doi: 10.1029/2000GL012657.

Gabioux, M., S. B. Vinzon, and A. M. Paiva (2005), Tidal propagation over fluid mud layers on the amazon shelf, *Continental Shelf Research*, *25*(1), 113–125, doi:http://dx.doi.org/10.1016/j.csr.2004.09.001.

Gabric, A. J., R. Simó, R. A. Cropp, A. C. Hirst, and J. Dachs (2004), Modeling estimates of the global emission of dimethylsulfide under enhanced greenhouse conditions, *Global Biogeochemical Cycles*, *18*(2), n/a–n/a, doi:10.1029/2003GB002183.

Gaiser, P. W., K. M. S. Germain, E. M. Twarog, G. A. Poe, W. Purdy, D. Richardson, W. Grossman, W. L. Jones, D. Spencer, G. Golba, J. Cleveland, L. Choy, R. M. Bevilacqua, and P. S. Chang (2004), The windsat spaceborne polarimetric microwave radiometer: sensor description and early orbit performance, *IEEE Transactions on Geoscience and Remote Sensing*, *42*(11), 2347–2361, doi:10.1109/TGRS.2004.836867.

Garbe, C. S., A. Rutgersson, J. Boutin, G. d. Leeuw, B. Delille, C. W. Fairall, N. Gruber, J. Hare, D. T. Ho, M. T. Johnson, P. D. Nightingale, H. Pettersson, E. S. Jacek Piskozub, W.-t. Tsai, B. Ward, D. K. Woolf, and C. J. Zappa (2014), *Transfer across the air-sea interface*, pp. 55–112, Springer Earth System Sciences, doi:10.1007/978-3-642-25643-1_2.

Garrett, W. D. (1967), Stabilization of air bubbles at the air-sea interface by surface-active material, *Deep Sea Research and Oceanographic Abstracts*, *14*(6), 661–672, doi: http://dx.doi.org/10.1016/S0011-7471(67)80004-4.

Gemmrich, J. R. (2010), Strong turbulence in the wave crest region, *J. Phys. Oceanogr.*, *40*, 583–595.

Gemmrich, J. R., M. L. Banner, and C. Garrett (2008), Spectrally resolved energy dissipation and momentum flux of breaking waves, *J. Phys. Oceanogr.*, *38*, 1296–1312.

Gemmrich, J. R., C. J. Zappa, M. L. Banner, and R. P. Morison (2013), Wave breaking in developing and mature seas, *Journal of Geophysical Research - Oceans*, *118*, 4542–4552, doi:10.1002/jgrc.20,334.

Geyer, W. R., and J. D. Smith (1987), Shear instability in a highly stratified estuary, *Journal of Physical Oceanography*, *17*(10), 1668–1679.

Giddings, S. N., D. A. Fong, and S. G. Monismith (2011), Role of straining and advection in the intratidal evolution of stratification, vertical mixing, and longitudinal dispersion of a shallow, macrotidal, salt wedge estuary, *Journal of Geophysical Research: Oceans*, *116*(C3), n/a–n/a, doi:10.1029/2010JC006482.

Goddijn-Murphy, L., D. K. Woolf, and A. H. Callaghan (2011), Parameterizations and algorithms for oceanic whitecap coverage, *Journal of Physical Oceanography*, *41*(4), 742–756.

Goddijn-Murphy, L., D. K. Woolf, and C. Marandino (2012), Space-based retrievals of air-sea gas transfer velocities using altimeters: Calibration for dimethyl sulfide, *Journal of Geophysical Research: Oceans*, *117*(C8), C08,028, doi:10.1029/2011JC007535.

Goddijn-Murphy, L., D. K. Woolf, A. H. Callaghan, P. D. Nightingale, and J. D. Shutler (2016), A reconciliation of empirical and mechanistic models of the air-sea gas transfer velocity, *Journal of Geophysical Research: Oceans*, *121*(1), 818–835, doi:10.1002/2015JC011096.

Gordon, C. M. (1975), Sediment entrainment and suspension in a turbulent tidal flow, *Marine Geology*, *18*(1), 57–64.

Gordon, H. R., and M. Wang (1994), Influence of oceanic whitecaps on atmospheric correction of ocean-color sensors, *Appl. Opt.*, *33*(33), 7754–7763, doi:10.1364/AO.33.007754.

Grass, A. (1971), Structural features of turbulent flow over smooth and rough boundaries, *Journal of Fluid Mechanics*, *50*(02), 233–255.

Guan, C., W. Hu, J. Sun, and R. Li (2007), The whitecap coverage model from breaking dissipation parametrizations of wind waves, *Journal of Geophysical Research: Oceans*, *112*(C5), C05,031.

Gunson, J. R., S. A. Spall, T. R. Anderson, A. Jones, I. J. Totterdell, and M. J. Woodage (2006), Climate sensitivity to ocean dimethylsulphide emissions, *Geophysical Research Letters*, *33*(7), n/a–n/a, doi:10.1029/2005GL024982.

Handler, R. A., G. B. Smith, and R. I. Leighton (2001), The thermal structure of an air-water interface at low wind speeds, *Tellus*, *53A*, 233–244.

Hanson, J. L., and O. M. Phillips (1999), Wind sea growth and dissipation in the open ocean, *Journal of Physical Oceanography*, *29*(8), 1633–1648, doi:10.1175/1520-0485(1999)029⟨1633:WSGADI⟩2.0.CO;2.

Hanson, J. L., and O. M. Phillips (2001), Automated analysis of ocean surface directional wave spectra, *Journal of Atmospheric and Oceanic Technology*, *18*(2), 277–293, doi:10.1175/1520-0426(2001)018⟨0277:AAOOSD⟩2.0.CO;2.

Hare, J. E., C. W. Fairall, W. R. McGillis, J. B. Edson, B. Ward, and R. Wanninkhof (2004), Evaluation of the national oceanic and atmospheric administration/coupled-ocean atmospheric response experiment (noaa/coare) air-sea gas transfer parameterization using gasex data, *J. Geophys. Res.*, *109*(C08S11), doi:10.1029/2003JC001,831.

Harriott, P. (1962), A random eddy modification of the penetration theory, *Chemical Engineering Science*, *17*, 149–154.

Harrison, E. L., F. Veron, D. T. Ho, M. C. Reid, P. Orton, and W. R. McGillis (2012),

Nonlinear interaction between rain- and wind-induced air-water gas exchange, *J. Geophys. Res.*, *117*, C03,034, doi:doi:10.1029/2011JC007693.

Hasselmann, S., K. Hasselmann, J. H. Allender, and T. P. Barnett (1985), Computations and parameterizations of the nonlinear energy transfer in a gravity-wave specturm. part ii: Parameterizations of the nonlinear energy transfer for application in wave models, *Journal of Physical Oceanography*, *15*(11), 1378–1391, doi:doi:10.1175/1520-0485(1985)015⟨1378:CAPOTN⟩2.0.CO;2.

Haywood, J. M., V. Ramaswamy, and B. J. Soden (1999), Tropospheric aerosol climate forcing in clear-sky satellite observations over the oceans, *Science*, *283*(5406), 1299–1303, doi:10.1126/science.283.5406.1299.

Heathershaw, A. D. (1974), "bursting" phenomena in the sea, *Nature*, *248*(5447), 394–395.

Heinze, C., S. Meyer, N. Goris, L. Anderson, R. Steinfeldt, N. Chang, C. Le Quéré, and D. C. Bakker (2015), The ocean carbon sink-impacts, vulnerabilities and challenges, *Earth System Dynamics*, *6*(1), 327.

Helmig, D., E. K. Lang, L. Bariteau, P. Boylan, C. W. Fairall, L. Ganzeveld, J. E. Hare, J. Hueber, and M. Pallandt (2012), Atmosphere-ocean ozone fluxes during the texaqs 2006, stratus 2006, gomecc 2007, gasex 2008, and amma 2008 cruises, *Journal of Geophysical Research: Atmospheres*, *117*(D4), D04,305, doi:10.1029/2011JD015955.

Higbie, R. (1935), The rate of absorption of a pure gas into a still liquid during short periods of exposure, *Trans. A.I.C.E.*, *31*, 365–389.

Ho, D., F. Veron, E. Harrison, L. F. Bliven, N. Scott, and W. R. McGillis (2007), The combined effect of rain and wind on air–water gas exchange: A feasibility study, *Journal of Marine Systems*, *66*, 150–160, doi:10.1016/j.jmarsys.2006.02.012.

Ho, D., C. L. Sabine, D. Hebert, D. S. Ullman, R. Wanninkhof, R. C. Hamme, P. G. Strutton, B. Hales, J. B. Edson, and B. R. Hargreaves (2011), Southern ocean gas exchange experiment: Setting the stage, *Journal of Geophysical Research - Oceans*, *116*(C4), C00F08, doi:10.1029/2010JC006852.

Ho, D. T., W. E. Asher, L. F. Bliven, P. Schlosser, and E. L. Gordan (2000), On the mechanisms of rain-induced air-water gas exchange, *J. Geophys. Res.*, *105*, 24,045–24,057.

Ho, D. T., C. S. Law, M. J. Smith, P. Schlosser, M. Harvey, and P. Hill (2006), Measurements of air-sea gas exchange at high wind speeds in the southern ocean: Implications for global parameterizations, *Geophys. Res. Lett.*, *33*, L16,611, doi:10.1029/2006GL026817.

Holland, K. T., R. A. Holman, T. C. Lippmann, J. Stanley, and N. Plant (1997), Practical use of video imagery in nearshore oceanographic field studies, *IEEE Journal of Oceanic Engineering*, *22*(1), 81–92.

Holthuijsen, L. H., M. D. Powell, and J. D. Pietrzak (2012), Wind and waves in extreme hurricanes, *Journal of Geophysical Research: Oceans*, *117*(C9), C09,003, doi:10.1029/2012JC007983.

Houghton, R. (1999), The annual net flux of carbon to the atmosphere from changes in land use 1850–1990, *Tellus B*, *51*(2), 298–313.

Howard, L. N. (1961), Note on a paper of miles,john,w., *Journal of Fluid Mechanics*, *10*(4), 509–512, doi:Doi10.1017/S0022112061000317.

Huebert, B. J., B. W. Blomquist, J. E. Hare, C. W. Fairall, J. E. Johnson, and T. S. Bates (2004), Measurement of the sea-air dms flux and transfer velocity using eddy correlation, *Geophysical Research Letters*, *31*, 1–4, doi:10.1029/2004GL021567.

Hurther, D., U. Lemmin, and T. E. (2007), Turbulent transport in the outer region of

rough-wall open-channel flows: the contribution of large coherent shear stress structures (lc3s), *Journal of Fluid Mechanics*, *574*(-1), 465–493, doi:10.1017/S0022112006004216.

Hwang, P. A., Y.-K. Poon, and J. Wu (1991), Temperature effects on generation and entrainment of bubbles induced by a water jet, *Journal of Physical Oceanography*, *21*(10), 1602–1605, doi:10.1175/1520-0485(1991)021⟨1602:TEOGAE⟩2.0.CO;2.

Jackson, D. L., G. A. Wick, and J. E. Hare (2012), A comparison of satellite-derived carbon dioxide transfer velocities from a physically based model with gasex cruise observations, *Journal of Geophysical Research: Oceans*, *117*(C4), C00F13, doi:10.1029/2011JC007329.

Jackson, R. G. (1976), Sedimentological and fluid-dynamic implications of the turbulent bursting phenomenon in geophysical flows, *Journal of Fluid Mechanics*, *77*(03), 531–560.

Jeffery, C. D., I. S. Robinson, and D. K. Woolf (2010), Tuning a physically-based model of the air–sea gas transfer velocity, *Ocean Modelling*, *31*(1–2), 28–35, doi:http://dx.doi.org/10.1016/j.ocemod.2009.09.001.

Jessup, A. T., C. J. Zappa, M. R. Loewen, and V. Hesany (1997), Infrared remote sensing of breaking waves, *Nature*, *385*(6611), 52–55.

Jähne, B., K. H. Fischer, J. Ilmberger, P. Libner, W. Weiss, D. Imboden, U. Lemnin, and J. M. Jaquet (1984), *Parameterization of Air/Lake Gas Exchange*, pp. 459–466, D. Reidel, Norwell, MA.

Jähne, B., T. Wais, L. Memery, G. Caulliez, L. Merlivat, K. O. Münnich, and M. Coantic (1985), He and rn gas exchange experiments in the large wind-wave facility of imst, *Journal of Geophysical Research*, *90*(C6), 11,989–97.

Jähne, B., G. Heinz, and W. Dietrich (1987), Measurement of the diffusion coefficients of sparingly soluble gases in water, *Journal of Geophysical Research*, *92*(C10), 10,767–10,776.

Johnson, D. (2012), Diwasp, a directional wave spectra toolbox for matlab®: User manual. research report wp-1601-dj (v1.1).

Johnson, E. D., and E. A. Cowen (2014), Remote monitoring of volumetric discharge based on surface mean and turbulent metrics, in *River Flow 2014 - the 7th International Conference on Fluvial Hydraulics*, EPFL.

Johnson, M. T. (2010), A numerical scheme to calculate temperature and salinity dependent air-water transfer velocities for any gas, *Ocean Sci.*, *6*(4), 913–932, doi: 10.5194/os-6-913-2010.

Katsaros, K. (1980), *Radiative sensing of sea surface temperature*, pp. 293–317, Plenum Press, New York.

Katsaros, K. B. (1977), The sea surface temperature deviation at very low wind speeds; is there a limit?, *Tellus*, *29*(3), 229–239.

Kettle, A. J., and M. O. Andreae (2000), Flux of dimethylsulfide from the oceans: A comparison of updated data sets and flux models, *Journal of Geophysical Research: Atmospheres*, *105*(D22), 26,793–26,808, doi:10.1029/2000JD900252.

Kitaigorodskii, S. A. (1984), On the fluid dynamical theory of turbulent gas transfer across an air-sea interface in the presence of breaking wind-waves, *Journal of Physical Oceanography*, *14*(5), 960–972.

Klaven, A. B. (1966), Investigation of the flow turbulent structure (in russian), *Trans. State Hydrol. Inst*, *136*, 65–76.

Klaven, A. B. (1968), Kinematic structure of the turbulent flow (in russian), *Trans. State Hydrol. Inst*, *147*, 134–141.

Klaven, A. B., and Z. D. Kopaliani (1973), Laboratory investigations of the kinematic

structure of turbulent flow over a rough bed (in russian), *Trans. State Hydrol. Inst*, *209*, 67–90.

Kleiss, J. M. (2009), Airborne observations of the kinematics and statistics of breaking waves, Ph.D. thesis, Scripps Institution of Oceanography–University of California.

Kleiss, J. M., and W. K. Melville (2010), Observations of wave breaking kinematics in fetchlimited seas, *J. Phys. Oceanogr.*, *40*, 2575–2604.

Kline, S. J., W. C. Reynolds, F. A. Schraub, and P. W. Runstadler (1967), The structure of turbulent boundary layers, *Journal of Fluid Mechanics*, *30*(4), 741–773.

Kolmogorov, A. N. (1991), Dissipation of energy in the locally isotropic turbulence, *Proceedings: Mathematical and Physical Sciences*, *434*(1890), 15–17.

Komen, G., S. Hasselmann, and K. Hasselmann (1984), On the existence of a fully developed wind-sea spectrum, *J. Phys. Ocean.*, *14*, 1271–1285.

Komen, G., L. Cavaleri, M. Donelan, K. Hasselmann, S. Hasselmann, and P. Janssen (1994), *Dynamics and Modelling of Ocean Waves*, 532 pp., Cambridge University Press, Cambridge.

Komori, S., R. Nagaosa, and Y. Murakami (1993), Turbulence structure and heat and mass transfer mechanism at a gas-liquid interface in a wind-wave tunnel, *Applied Scientific Research*, *51*, 423–427.

Komori, S., N. Takagaki, R. Saiki, N. Suzuki, and K. Tanno (2007), *The effect of raindrops on interfacial turbulence and air-water gas transfer*, p. 169–179, Springer.

Korchokha, Y. (1968), Investigation of the dune movement of sediments on the polomet river, *Sov. Hydrol.*, *11*, 541–559.

Kraan, G., W. A. Oost, and P. A. E. M. Janssen (1996), Wave energy dissipation by whitecaps, *Journal of Atmospheric and Oceanic Technology*, *13*(1), 262–267, doi:10.1175/1520-0426(1996)013⟨0262:WEDBW⟩2.0.CO;2.

Kudryavtsev, V. N., and A. V. Soloviev (1985), On the parameterization of the cold film on the ocean surface, *Izvestiya Academy of Science, USSR, Atmospheric and Ocean Physics*, *21*(2), 177–83.

Kuik, A. J., G. P. v. Vledder, and L. H. Holthuijsen (1988), A method for the routine analysis of pitch-and-roll buoy wave data, *Journal of Physical Oceanography*, *18*(7), 1020–1034, doi:10.1175/1520-0485(1988)018⟨1020:amftra⟩2.0.co;2.

Lafon, C., J. Piazzola, P. Forget, O. Le Calve, and S. Despiau (2004), Analysis of the variations of the whitecap fraction as measured in a coastal zone, *Boundary-Layer Meteorology*, *111*(2), 339–360, doi:10.1023/b:boun.0000016490.83880.63.

Lafon, C., J. Piazzola, P. Forget, and S. Despiau (2007), Whitecap coverage in coastal environment for steady and unsteady wave field conditions, *Journal of Marine Systems*, *66*(1–4), 38–46, doi:http://dx.doi.org/10.1016/j.jmarsys.2006.02.013.

Lamarre, E., and W. K. Melville (1991), Air entrainment and dissipation in breaking waves, *Nature*, *351*(6326), 469–72.

Lamont, J. C., and D. S. Scott (1970), An eddy cell model of mass transfer into the surface of a turbulent liquid, *A.I.Ch.E. J.*, *16*, 512–519.

Langmuir, I. (1938), Surface motion of water induced by wind, *Science*, *87*, 119–123.

Leibovich, S. (1983), The form and dynamics of langmuir circulations, *Annual Review Fluid Mechanics*, *15*, 391–427.

Li, Q., A. Webb, B. Fox-Kemper, A. Craig, G. Danabasoglu, W. G. Large, and M. Vertenstein (2016), Langmuir mixing effects on global climate: Wavewatch iii in cesm, *Ocean Modelling*, *103*, 145–160, doi:http://dx.doi.org/10.1016/j.ocemod.2015.07.020.

Liang, J.-H., C. Deutsch, J. C. McWilliams, B. Baschek, P. P. Sullivan, and D. Chiba (2013),

Parameterizing bubble-mediated air-sea gas exchange and its effect on ocean ventilation, *Global Biogeochemical Cycles*, *27*(3), 894–905, doi:10.1002/gbc.20080.

Liss, P., and F. Martinelli (1978), The effect of oil films on the transfer of oxygen and water vapour across an air-water interface, *Thalass Jugosl*, *14*, 215–220.

Liss, P. S., and L. Merlivat (1986), *Air-sea gas exchange rates: Introduction and synthesis*, pp. 113–127, Springer.

Liu, W. T., and J. A. Businger (1975), Temperature profile in the molecular sublayer near the interface of a fluid in turbulent motion, *Geophysical Research Letters*, *2*(9), 403–404.

Lombardo, C. P., and M. C. Gregg (1989), Similarity scaling of viscous and thermal dissipation in a convecting surface boundary layer, *Journal of Geophysical Research: Oceans*, *94*(C5), 6273–6284, doi:10.1029/JC094iC05p06273.

Loose, B., W. R. McGillis, D. Perovich, C. J. Zappa, and P. Schlosser (2014), A parameter model of gas exchange for the seasonal sea ice zone, *Ocean Science*, *10*(1), 17–28, doi:10.5194/os-10-17-2014.

Loose, B., A. Lovely, P. Schlosser, C. J. Zappa, W. R. McGillis, and D. Perovich (2016), Currents and convection cause enhanced gas exchange in the ice-water boundary layer, *Tellus B*, *68*, doi:10.3402/tellusb.v68.32803.

Lovelock, J. (2007), *The revenge of gaia: earth's climate crisis & the fate of humanity*, Basic Books.

Lund, B., C. J. Zappa, H. C. Graber, and A. Cifuentes-Lorenzen (2017), Shipboard wave measurements in the southern ocean, *Journal of Atmospheric and Oceanic Technology*, *in press*, doi:10.1175/JTECH-D-16-0212.1.

Mahadevan, A., M. Lévy, and L. Mémery (2004), Mesoscale variability of sea surface pco_2: What does it respond to?, *Global Biogeochemical Cycles*, *18*(1), doi:10.1029/2003GB002102.

Marandino, C. A., W. J. De Bruyn, S. D. Miller, and E. S. Saltzman (2007), Eddy correlation measurements of the air/sea flux of dimethylsulfide over the north pacific ocean, *Journal of Geophysical Research: Atmospheres*, *112*(D3), D03,301, doi:10.1029/2006JD007293.

Marandino, C. A., W. J. De Bruyn, S. D. Miller, and E. S. Saltzman (2008), Dms air/sea flux and gas transfer coefficients from the north atlantic summertime coccolithophore bloom, *Geophysical Research Letters*, *35*(23), L23,812, doi:10.1029/2008GL036370.

Marandino, C. A., W. J. De Bruyn, S. D. Miller, and E. S. Saltzman (2009), Open ocean dms air/sea fluxes over the eastern south pacific ocean, *Atmos. Chem. Phys.*, *9*(2), 345–356, doi:10.5194/acp-9-345-2009.

Matthes, G. H. (1947), Macroturbulence in natural stream flows, *Transactions, American Geophysical Union*, *28*(2), 255–265.

McCready, M. J., E. Vassiliadou, and T. J. Hanratty (1986), Computer simulation of turbulent mass transfer at a mobile interface, *AIChE Journal*, *32*(7), 1108–1115, doi:10.1002/aic.690320707.

McGillis, W. R., J. B. Edson, J. E. Hare, and C. W. Fairall (2001), Direct covariance air-sea co_2 fluxes, *Journal of Geophysical Research*, *106*(c8), 16,729–16,745.

McKenna, S. P., and W. R. McGillis (2002), Performance of digital image velocimetry processing techniques, *Experiments in Fluids*, *32*, 116–115, doi:10.1007/S003480100348.

McKenna, S. P., and W. R. McGillis (2004), Observations of flow repeatability and secondary circulation in an oscillating grid-stirred tank, *Physics of Fluids*, *16*(9), 3499–3502, doi:http://dx.doi.org/10.1063/1.1779671.

Melville, W. K. (1994), Energy dissipation by breaking waves, *Journal of Physical Oceanography*, *24*(10), 2041–9.

Melville, W. K. (1996), The role of surface-wave breaking in air-sea interaction, *Annual Review of Fluid Mechanics*, *28*, 279–321.

Melville, W. K., R. Shear, and F. Veron (1998), Laboratory measurements of the generation and evolution of langmuir circulations, *Journal of Fluid Mechanics*, *364*, 31–58.

Merlivat, L., L. Memery, and J. Boutin (1993), Gas exchange at the air-sea interface: present status. case of co_2, in *The Fourth International Conference on CO_2 in the OceansInst. Natl. des Sci. de l'Univers., Cent. Natl. de la Rech. Sci. Carqueiranne, FranceSept*, pp. 13–17.

Miles, J. W. (1961), On the stability of heterogeneous shear flows, *Journal of fluid mechanics*, *10*(04), 496, doi:10.1017/S0022112061000305.

Miller, L. A., G. Carnat, B. G. T. Else, N. Sutherland, and T. N. Papakyriakou (2011), Carbonate system evolution at the arctic ocean surface during autumn freeze-up, *Journal of Geophysical Research: Oceans*, *116*(C9), C00g04, doi:10.1029/2011JC007143.

Miller, S. D., C. Marandino, W. De Bruyn, and E. S. Saltzman (2009), Air-sea gas exchange of co_2 and dms in the north atlantic by eddy covariance, *Geophysical Research Letters*, *36*(15), 1–5, doi:10.1029/2009GL038907.

Miller, S. D., C. Marandino, and E. S. Saltzman (2010), Ship-based measurement of air-sea co_2 exchange by eddy covariance, *Journal of Geophysical Research: Atmospheres*, *115*(D2), D02,304, doi:10.1029/2009JD012193.

Mironov, A. S., and V. A. Dulov (2008), Detection of wave breaking using sea surface video records, *Meas. Sci. Technol.*, *19*(015405), doi:10.1088/0957–0233/19/1/015,405.

Monahan, E. C. (1971), Oceanic whitecaps, *Journal of Physical Oceanography*, *1*(2), 139–144, doi:10.1175/1520-0485(1971)001⟨0139:OW⟩2.0.CO;2.

Monahan, E. C. (1993), *Occurrence and Evolution of Acoustically Relevant Sub-Surface*

Bubble Plumes and their Associated, Remotely Monitorable, Surface Whitecaps, pp. 503–517, Springer Netherlands, Dordrecht, doi:10.1007/978-94-011-1626-8_37.

Monahan, E. C., and I. O'Muircheartaigh (1980), Optimal power-law description of oceanic whitecap coverage dependence on wind speed, *Journal of Physical Oceanography*, *10*(12), 2064–2099, doi:10.1175/1520-0485(1980)010⟨2094:OPLDOO⟩2.0.CO;2.

Monahan, E. C., and I. G. O'Muircheartaigh (1986), Whitecaps and the passive remote sensing of the ocean surface, *International Journal of Remote Sensing*, *7*(5), 627–642, doi:10.1080/01431168608954716.

Monahan, E. C., and M. C. Spillane (1984), *The role of oceanic whitecaps in air-sea gas exchange*, pp. 495–503, D. Reidel, Norwell, MA.

Monahan, E. C., and D. K. Woolf (1989), Comments on "variations of whitecap coverage with wind stress and water temperature", *Journal of Physical Oceanography*, *19*(5), 706–709.

Monahan, E. C., G. Hooker, and C. J. Zappa (2015), The latitudinal variation in the wind-speed parameterization of oceanic whitecap coverage; implications for global modelling of air-sea gas flux and sea surface aerosol generation, in *95th Annual American Meteorology Society Meeting, 19th Conference on Air-Sea Interaction, Phoenix, AZ.*

Mori, N., T. Suzuki, and S. Kakuno (2007), Noise of acoustic doppler velocimeter data in bubbly flows, *Journal of Engineering Mechanics*, *133*(1), 122–125, doi:doi:10.1061/(ASCE)0733-9399(2007)133:1(122).

Myhre, G., D. Shindell, F.-M. Br'eon, W. Collins, J. Fuglestvedt, J. Huang, D. Koch, J.-F. Lamarque, D. Lee, B. Mendoza, T. Nakajima, A. Robock, G. Stephens, T. Takemura, and H. Zhang (2013), *Anthropogenic and Natural Radiative Forcing*, book section 8, p. 659–740, Cambridge University Press, Cambridge, United Kingdom and New York, NY, USA, doi:10.1017/CBO9781107415324.018.

Myrhaug, D., and L. E. Holmedal (2008), Effects of wave age and air stability on whitecap coverage, *Coastal Engineering*, *55*(12), 959–966, doi:http://dx.doi.org/10.1016/j.coastaleng.2008.03.005.

Nayar, K. G., M. H. Sharqawy, L. D. Banchik, and J. H. Lienhard V (2016), Thermophysical properties of seawater: A review and new correlations that include pressure dependence, *Desalination*, *390*, 1–24, doi:http://dx.doi.org/10.1016/j.desal.2016.02.024.

Nepf, H. M., and W. R. Geyer (1996), Intratidal variations in stratification and mixing in the hudson estuary, *J Gephys. Res.*, *101*, 12,079–12,086.

Nezu, I., and H. Nakagawa (1993), Turbulence in open channels, *IAHR/AIRH Monograph. Balkema, Rotterdam, The Netherlands*.

Nimmo-Smith, W. A. M., S. A. Thorpe, and A. Graham (1999), Surface effects of bottom-generated turbulence in a shallow tidal sea, *Nature*, *400*, 251–254.

Norris, S. J., I. M. Brooks, and D. J. Salisbury (2013), A wave roughness reynolds number parameterization of the sea spray source flux, *Geophysical Research Letters*, *40*(16), 4415–4419, doi:10.1002/grl.50795.

Offen, G. R., and S. J. Kline (1975), A proposed model of the bursting process in turbulent boundary layers, *Journal of Fluid Mechanics*, *70*(02), 209–228.

Pachauri, R. K., M. R. Allen, V. R. Barros, J. Broome, W. Cramer, R. Christ, J. A. Church, L. Clarke, Q. Dahe, P. Dasgupta, et al. (2014), Climate change 2014: synthesis report. contribution of working groups i, ii and iii to the fifth assessment report of the intergovernmental panel on climate change.

Paget, A. C., M. A. Bourassa, and M. D. Anguelova (2015), Comparing in situ and satellite-based parameterizations of oceanic whitecaps, *Journal of Geophysical Research: Oceans*, *120*(4), 2826–2843, doi:10.1002/2014JC010328.

Penner, J. E., M. Andreae, H. Annegarn, L. Barrie, J. Feichter, D. Hegg, A. Jayaraman, R. Leaitch, D. Murphy, and J. Nganga (2001), *Aerosols, their direct and indirect effects*, pp. 289–348, Cambridge University Press.

Peregrine, D. (1976), Interaction of water waves and currents, *Advances in applied mechanics*, *16*, 9–117.

Phillips, O. M. (1985), Spectral and statistical properties of the equilibrium range in wind-generated gravity waves, *Journal of Fluid Mechanics*, *156*, 505–31.

Phillips, O. M., F. L. Posner, and J. P. Hansen (2001), High range resolution radar measurements of the speed distribution of breaking events in wind-generated ocean waves: Surface impulse and wave energy dissipation rates, *Journal of Physical Oceanography*, *31*(2), 450–460, doi:10.1175/1520-0485(2001)031⟨0450:HRRRMO⟩2.0.CO;2.

Plant, W. J., R. Branch, G. Chatham, C. C. Chickadel, K. Hayes, B. Hayworth, A. Horner-Devine, A. Jessup, D. A. Fong, O. B. Fringer, S. N. Giddings, S. Monismith, and B. Wang (2009), Remotely sensed river surface features compared with modeling and in situ measurements, *Journal of Geophysical Research: Oceans*, *114*(C11), C11,002.

Prytherch, J., M. J. Yelland, R. W. Pascal, B. I. Moat, I. Skjelvan, and C. C. Neill (2010), Direct measurements of the co_2 flux over the ocean: Development of a novel method, *Geophysical Research Letters*, *37*(3), 1–5, doi:10.1029/2009GL041482.

Puleo, J. A., T. E. McKenna, K. T. Holland, and J. Calantoni (2012), Quantifying riverine surface currents from time sequences of thermal infrared imagery, *Water Resources Research*, *48*(1), W01,527, doi:10.1029/2011WR010770.

Qiao, F., Y. Yuan, Y. Yang, Q. Zheng, C. Xia, and J. Ma (2004), Wave-induced mixing in the upper ocean: Distribution and application to a global ocean circulation model, *Geophysical Research Letters*, *31*(11), doi:10.1029/2004GL019824.

Qiao, F., Y. Yuan, T. Ezer, C. Xia, Y. Yang, X. Lü, and Z. Song (2010), A three-dimensional surface wave–ocean circulation coupled model and its initial testing, *Ocean Dynamics*, *60*(5), 1339–1355, doi:10.1007/s10236-010-0326-y.

Qiao, F., Z. Song, Y. Bao, Y. Song, Q. Shu, C. Huang, and W. Zhao (2013), Development and evaluation of an earth system model with surface gravity waves, *Journal of Geophysical Research: Oceans*, *118*(9), 4514–4524, doi:10.1002/jgrc.20327.

Quinn, P. K., and T. S. Bates (2011), The case against climate regulation via oceanic phytoplankton sulphur emissions, *Nature*, *480*(7375), 51–56.

Randolph, K., H. M. Dierssen, A. Cifuentes-Lorenzen, W. M. Balch, E. C. Monahan, C. J. Zappa, D. T. Drapeau, and B. Bowler (2016), Novel methods for optically measuring whitecaps under natural wave breaking conditions in the southern ocean, *Journal of Atmospheric and Oceanic Technology*, (2016).

Rapp, R. J., and W. K. Melville (1990), Laboratory measurements of deep-water breaking waves, *Philosophical Transactions of the Royal Society of London A*, *331*(1622), 735–800.

Rascle, N., and F. Ardhuin (2013), A global wave parameter database for geophysical applications. part 2: Model validation with improved source term parameterization, *Ocean Modelling*, *70*, 174–188, doi:http://dx.doi.org/10.1016/j.ocemod.2012.12.001.

Romero, L., W. K. Melville, and J. Kleiss (2012), Spectral energy dissipation due to surface-wave breaking, *J. Phys. Oceanogr.*, pp. 1421–1444, doi:10.1175/JPO-D-11-072.1.

Romero, L., L. Lenain, and W. K. Melville (2017), Observations of surface wave–current interaction, *Journal of Physical Oceanography*, *47*(3), 615–632, doi:10.1175/JPO-D-16-0108.1.

Rowe, M. D., C. W. Fairall, and J. A. Perlinger (2011), Chemical sensor resolution require-

ments for near-surface measurements of turbulent fluxes, *Atmos. Chem. Phys.*, *11*(11), 5263–5275, doi:10.5194/acp-11-5263-2011.

Sabine, C. L., R. A. Feely, N. Gruber, R. M. Key, K. Lee, J. L. Bullister, R. Wanninkhof, C. S. Wong, D. W. R. Wallace, B. Tilbrook, F. J. Millero, T.-H. Peng, A. Kozyr, T. Ono, and A. F. Rios (2004), The oceanic sink for anthropogenic co_2, *Science*, *305*(5682), 367–371, doi:10.1126/science.1097403.

Saha, S., S. Moorthi, H.-L. Pan, X. Wu, J. Wang, S. Nadiga, P. Tripp, R. Kistler, J. Woollen, D. Behringer, H. Liu, D. Stokes, R. Grumbine, G. Gayno, J. Wang, Y.-T. Hou, H.-Y. Chuang, H.-M. H. Juang, J. Sela, M. Iredell, R. Treadon, D. Kleist, P. V. Delst, D. Keyser, J. Derber, M. Ek, J. Meng, H. Wei, R. Yang, S. Lord, H. V. D. Dool, A. Kumar, W. Wang, C. Long, M. Chelliah, Y. Xue, B. Huang, J.-K. Schemm, W. Ebisuzaki, R. Lin, P. Xie, M. Chen, S. Zhou, W. Higgins, C.-Z. Zou, Q. Liu, Y. Chen, Y. Han, L. Cucurull, R. W. Reynolds, G. Rutledge, and M. Goldberg (2010), The ncep climate forecast system reanalysis, *Bulletin of the American Meteorological Society*, *91*(8), 1015–1057, doi:10.1175/2010bams3001.1.

Salisbury, D. J. (2014), Global distribution and seasonal dependence of satellite-based whitecap fraction, *Geophysical research letters*, *41*(5), 1616–1623, doi:10.1002/2014GL059246.

Salisbury, D. J., M. D. Anguelova, and I. M. Brooks (2013), On the variability of whitecap fraction using satellite-based observations, *Journal of Geophysical Research: Oceans*, *118*(11), 6201–6222, doi:10.1002/2013JC008797.

Salter, M. E., E. D. Nilsson, A. Butcher, and M. Bilde (2014), On the seawater temperature dependence of the sea spray aerosol generated by a continuous plunging jet, *Journal of Geophysical Research: Atmospheres*, *119*(14), 9052–9072, doi:10.1002/2013JD021376.

Saunders, P. M. (1967), Aerial measurement of sea surface temperature in the infrared, *Journal of Geophysical Research*, *72*(16), 4109–4117.

Scanlon, B., and B. Ward (2013), Oceanic wave breaking coverage separation techniques for active and maturing whitecaps, *Methods in Oceanography*, *8*(0), 1–12, doi:http://dx.doi.org/10.1016/j.mio.2014.03.001.

Scanlon, B., and B. Ward (2016), The influence of environmental parameters on active and maturing oceanic whitecaps, *Journal of Geophysical Research: Oceans*, *121*(5), 3325–3336, doi:10.1002/2015JC011230.

Schwendeman, M., and J. Thomson (2015a), Observations of whitecap coverage and the relation to wind stress, wave slope, and turbulent dissipation, *Journal of Geophysical Research: Oceans*, *120*(12), 8346–8363, doi:10.1002/2015JC011196.

Schwendeman, M., and J. Thomson (2015b), A horizon-tracking method for shipboard video stabilization and rectification, *Journal of Atmospheric and Oceanic Technology*, *32*(1), 164–176, doi:10.1175/JTECH-D-14-00047.1.

Schwendeman, M., J. Thomson, and J. R. Gemmrich (2014), Wave breaking and dissipation in a young wind sea, *Journal of Physical Oceanography*, *44*(1), 104–127, doi:10.1175/JPO-D-12-0237.1.

Sharqawy, M. H., J. H. Lienhard, and S. M. Zubair (2010), Thermophysical properties of seawater: a review of existing correlations and data, *Desalination and Water Treatment*, *16*(1-3), 354–380, doi:10.5004/dwt.2010.1079.

Shu, Q., F. Qiao, Z. Song, C. Xia, and Y. Yang (2011), Improvement of mom4 by including surface wave-induced vertical mixing, *Ocean Modelling*, *40*(1), 42–51, doi:http://dx.doi.org/10.1016/j.ocemod.2011.07.005.

Shvidchenko, A. B., and G. Pender (2001), Macroturbulent structure of open-channel flow over gravel beds, *Water Resources Research*, *37*(3), 709–719.

Smith, G. B., R. J. Volino, R. A. Handler, and R. I. Leighton (2001), The thermal signature of a vortex pair impacting a free surface, *J. Fluid Mech.*, *444*, 49–78.

Soloviev, A. V., and P. Schlüssel (1994), Parameterization of the cool skin of the ocean and of the air-ocean gas transfer on the basis of modeling surface renewal, *Journal of Physical Oceanography*, *24*(6), 1339–46.

Song, Z., F. Qiao, and Y. Song (2012), Response of the equatorial basin-wide sst to non-breaking surface wave-induced mixing in a climate model: An amendment to tropical bias, *Journal of Geophysical Research: Oceans*, *117*(C11), doi:10.1029/2012JC007931.

Spillane, M., E. Monahan, P. Bowyer, D. Doyle, and P. J. Stabeno (1986), *Whitecaps and global fluxes*, pp. 209–218, Springer.

Springer, T. G., and R. L. Pigford (1970), Influence of surface turbulence and surfactants on gas transport through liquid interfaces, *Industrial & Engineering Chemistry Fundamentals*, *9*(3), 458–465, doi:10.1021/i160035a025.

Sreenivasan, K. R. (1984), On the scaling of the turbulence energy dissipation rate, *Physics of Fluids (1958-1988)*, *27*(5), 1048–1051.

Steele, J. H., S. A. Thorpe, and K. K. Turekian (2009), *Elements of physical oceanography: a derivative of the encyclopedia of ocean sciences*, Academic Press.

Stokes, G. G. (1880), Considerations relative to the greatest height of oscillatory irrotational waves which can be propagated without change of form, *Mathematical and physical papers*, *1*, 225–228.

Sugihara, Y., H. Tsumori, T. Ohga, H. Yoshioka, and S. Serizawa (2007), Variation of whitecap coverage with wave-field conditions, *Journal of Marine Systems*, *66*(1–4), 47–60, doi:http://dx.doi.org/10.1016/j.jmarsys.2006.01.014.

Sutherland, P., and W. K. Melville (2013), Field measurements and scaling of ocean surface wave-breaking statistics, *Geophys. Res Lett.*, *40*(doi:10.1002/grl.50584), 3074–3079.

Sutherland, P., and W. K. Melville (2015), Field measurements of surface and near-surface turbulence in the presence of breaking waves, *Journal of Physical Oceanography*, *45*(4), 943–965, doi:10.1175/JPO-D-14-0133.1.

Sweeney, C., E. Gloor, A. R. Jacobson, R. M. Key, G. McKinley, J. L. Sarmiento, and R. Wanninkhof (2007), Constraining global air-sea gas exchange for co_2 with recent bomb 14c measurements, *Global Biogeochemical Cycles*, *21*(2), 1–10, doi:10.1029/2006GB002784.

Takahashi, T., S. C. Sutherland, R. Wanninkhof, C. Sweeney, R. A. Feely, D. W. Chipman, B. Hales, G. Friederich, F. Chavez, C. Sabine, A. Watson, D. C. E. Bakker, U. Schuster, N. Metzl, H. Yoshikawa-Inoue, M. Ishii, T. Midorikawa, Y. Nojiri, A. Körtzinger, T. Steinhoff, M. Hoppema, J. Olafsson, T. S. Arnarson, B. Tilbrook, T. Johannessen, A. Olsen, R. Bellerby, C. S. Wong, B. Delille, N. R. Bates, and H. J. W. de Baar (2009), Climatological mean and decadal change in surface ocean pco_2, and net sea–air co_2 flux over the global oceans, *Deep Sea Research Part II: Topical Studies in Oceanography*, *56*(8–10), 554–577, doi:http://dx.doi.org/10.1016/j.dsr2.2008.12.009.

Talke, S. A., A. R. Horner-Devine, C. C. Chickadel, and A. T. Jessup (2013), Turbulent kinetic energy and coherent structures in a tidal river, *Journal of Geophysical Research: Oceans*, *118*(12), 6965–6981, doi:10.1002/2012JC008103.

Tedford, E. W., J. R. Carpenter, R. Pawlowicz, R. Pieters, and G. A. Lawrence (2009), Observation and analysis of shear instability in the fraser river estuary, *Journal of Geophysical Research-Oceans*, *114*, doi:ArtnC1100610.1029/2009jc005313.

Tennekes, H., and J. Lumley (1972), *A First Course in Turbulence*, MIT Press, Cambridge, Mass.

Terray, E. A., M. A. Donelan, Y. C. Agrawal, W. M. Drennan, K. K. Kahma, I. A. J. Williams, P. A. Hwang, and S. A. Kitaigorodskii (1996), Estimates of kinetic energy dissipation under surface waves, *Journal of Physical Oceanography*, *26*(5), 792–807.

Thomson, J., J. R. Gemmrich, and A. T. Jessup (2009), Energy dissipation and the spectral distribution of whitecaps, *Geophys. Res Lett.*, *35*, L11,601, doi:10.1029/2009GL038201.

Thomson, J., E. D'Asaro, M. Cronin, W. Rogers, R. Harcourt, and A. Shcherbina (2013), Waves and the equilibrium range at ocean weather station p, *Journal of Geophysical Research: Oceans*, *118*(11), 5951–5962.

Thorpe, S. A., and A. J. Hall (1983), The characteristics of breaking waves, bubble clouds, and near-surface currents observed using side-scan sonar, *Continental Shelf Research*, *1*(4), 353–384.

Toba, Y. (1973), Local balance in the air-sea boundary processes, *Journal of Oceanography*, *29*(5), 209–220.

Toba, Y., and M. Koga (1986), *A Parameter Describing Overall Conditions of Wave Breaking, Whitecapping, Sea-Spray Production and Wind Stress*, *Oceanographic Sciences Library*, vol. 2, book section 4, pp. 37–47, Springer Netherlands, doi:10.1007/978-94-009-4668-2_4.

Tolman, H. L., and D. Chalikov (1996), Source terms in a third-generation wind wave model, *Journal of Physical Oceanography*, *26*(11), 2497–2518, doi:doi:10.1175/1520-0485(1996)026⟨2497:STIATG⟩2.0.CO;2.

Tolman, H. L., B. Balasubramaniyan, L. D. Burroughs, D. V. Chalikov, Y. Y. Chao, H. S. Chen, and V. M. Gerald (2002), Development and implementation of wind-generated ocean surface wave modelsat ncep, *Weather and Forecasting*, *17*(2), 311–333, doi:doi:10.1175/1520-0434(2002)017⟨0311:DAIOWG⟩2.0.CO;2.

Trowbridge, J. H., W. R. Geyer, M. M. Bowen, and A. J. Williams (1999), Near-bottom turbulence measurements in a partially mixed estuary: Turbulent energy balance, velocity structure, and along-channel momentum balance*, *Journal of Physical Oceanography*, *29*(12), 3056–3072, doi:10.1175/1520-0485(1999)029⟨3056:NBTMIA⟩2.0.CO;2.

Turk, D., C. J. Zappa, C. S. Meinen, J. Christian, D. T. Ho, A. G. Dickson, and W. R. McGillis (2010), Rain impacts on co_2 exchange in the western equatorial pacific, *Geophysical Research Letters*, *37*, L23,610, doi:10.1029/2010GL045520.

Turney, D. E., W. C. Smith, and S. Banerjee (2005), A measure of the near-surface fluid motions that predicts air-water gas transfer in a wide range of conditions, *Geophysical Research Letters*, *32*, L04,607, doi:10.1029/2004GL021671.

Vanoni, V. A., and L.-S. Hwang (1967), *Relation between bed forms and friction in streams*, WM Keck Laboratory of Hydraulics and Water Resources California Institute of Technology.

Vassilicos, J. C. (2015), Dissipation in turbulent flows, *Annual Review of Fluid Mechanics*, *47*, 95–114.

Veron, F. (2015), Ocean spray, *Annual Review of Fluid Mechanics*, *47*, 507–538.

Veron, F., and W. K. Melville (2001), Experiments on the stability and transition of wind-driven water surfaces, *Journal of Fluid Mechanics*, *446*, 25–65.

Veron, F., W. Melville, and L. Lenain (2008), Infrared techniques for measuring ocean surface processes, *J. Atmos. Oceanogr. Technol.*, *25*(2), 307–326.

Vlahos, P., and E. C. Monahan (2009), A generalized model for the air-sea transfer of dimethyl sulfide at high wind speeds, *Geophysical Research Letters*, *36*(21), n/a–n/a, doi:10.1029/2009GL040695, l21605.

Volino, R. J., and G. B. Smith (1999), Use of simultaneous ir temperature measurements

and dpiv to investigate thermal plumes in a thick layer cooled from above, *Experiments in Fluids*, *27*(1), 70–78, doi:10.1007/s003480050330.

Volk, T., and M. I. Hoffert (1985), Ocean carbon pumps: Analysis of relative strengths and efficiencies in ocean-driven atmospheric co_2 changes, *The Carbon Cycle and Atmospheric CO: Natural Variations Archean to Present*, pp. 99–110.

Wallace, D. W. R., and C. D. Wirick (1992), Large air-sea fluxes associated with breaking waves, *Nature*, *356*(6371), 694–696.

Wanninkhof, R. (1992), Relationship between wind speed and gas exchange over the ocean, *Journal of Geophysical Research*, *97*(C5), 7373–7382, doi:10.1029/92JC00188.

Wanninkhof, R. (2014), Relationship between wind speed and gas exchange over the ocean revisited, *Limnology and Oceanography: Methods*, *12*(6), 351–362, doi:10.4319/lom.2014.12.351.

Wanninkhof, R., and M. Knox (1996), Chemical enhancement of co_2 exchange in natural waters, *Limnol. Oceanogr.*, *41*(4), 689–697.

Wanninkhof, R., and W. R. McGillis (1999), A cubic relationship between air-sea co_2 exchange and wind speed, *Geophys. Res. Lett.*, *26*(13), 1889–1892.

Wanninkhof, R., J. R. Ledwell, and W. S. Broecker (1985), Gas exchange-wind speed relation measured with sulfur hexafluoride on a lake, *Science*, *227*(4691), 1224–1226, doi:10.1126/science.227.4691.1224.

Wanninkhof, R., W. Asher, and E. Monahan (1995), The influence of bubbles on air-water gas exchange: Results from gas transfer experiments during wabex-93, in *Selected Papers from the Third International Symposium on Air–Water Gas Transfer*, pp. 239–253, Hanau, Germany: AEON Verlag.

Watson, A. J., R. C. Upstill-Goddard, and P. S. Liss (1991), Air-sea gas exchange in rough and stormy seas measured by a dual-tracer technique, *Nature*, *349*, 145–147.

Woolf, D. K. (1997), *Bubbles and their role in air–sea gas exchange*, pp. 173–206, Cambridge Univ Press, Cambridge, UK.

Woolf, D. K. (2005), Parameterization of gas transfer velocities and sea-state-dependent wave breaking, *Tellus*, *57B*, 87–94.

Woolf, D. K., and S. A. Thorpe (1991), Bubbles and the air-sea exchange of gases in near saturation conditions, *J. Mar. Res.*, *49*, 435–466.

Woolf, D. K., I. S. Leifer, P. D. Nightingale, T. S. Rhee, P. Bowyer, G. Caulliez, G. de Leeuw, S. E. Larsen, M. Liddicoat, J. Baker, and M. O. Andreae (2007), Modelling of bubble-mediated gas transfer: Fundamental principles and a laboratory test, *Journal of Marine Systems*, *66*(1–4), 71–91, doi:http://dx.doi.org/10.1016/j.jmarsys.2006.02.011.

Wrobel, I., and J. Piskozub (2016), Effect of gas-transfer velocity parameterization choice on air–sea co_2 fluxes in the north atlantic ocean and the european arctic, *Ocean Sci.*, *12*(5), 1091–1103, doi:10.5194/os-12-1091-2016.

Wu, J. (1988), Variations of whitecap coverage with wind stress and water temperature, *Journal of Physical Oceanography*, *18*(10), 1448–53.

Wu, L., A. Rutgersson, and E. Sahlée (2015), Upper-ocean mixing due to surface gravity waves, *Journal of Geophysical Research: Oceans*, pp. 8210 – 8228, doi:10.1002/2015JC011329.

Yalin, M. S. (1992), *River Mechanics*, 219 pp., Pergamon.

Yang, M., B. W. Blomquist, C. W. Fairall, S. D. Archer, and B. J. Huebert (2011), Air-sea exchange of dimethylsulfide in the southern ocean: Measurements from so gasex compared to temperate and tropical regions, *Journal of Geophysical Research: Oceans*, *116*(C4), C00f05, doi:10.1029/2010JC006526.

Yang, M., B. Blomquist, and P. D. Nightingale (2014), Air-sea exchange of methanol and acetone during hiwings: Estimation of air phase, water phase gas transfer velocities, *Journal of Geophysical Research: Oceans*, *119*(10), 7308–7323, doi:10.1002/2014JC010227.

Zappa, C. J., and A. T. Jessup (2005), High-resolution airborne infrared measurements of ocean skin temperature, *Geoscience and Remote Sensing Letters, IEEE*, *2*(2), 146–150, doi:10.1109/LGRS.2004.841629.

Zappa, C. J., A. T. Jessup, and H. H. Yeh (1998), Skin-layer recovery of free-surface wakes: Relationship to surface renewal and dependence on heat flux and background turbulence, *Journal of Geophysical Research*, *103*(C10), 21,711–21,722.

Zappa, C. J., P. A. Raymond, E. Terray, and W. R. McGillis (2003), Variation in surface turbulence and the gas transfer velocity over a tidal cycle in a macro-tidal estuary, *Estuaries*, *26*(6), 1401–1415.

Zappa, C. J., W. E. Asher, A. T. Jessup, J. Klinke, and S. R. Long (2004), Microbreaking and the enhancement of air-water transfer velocity, *Journal of Geophysical Research*, *109*, C08S16, doi:10.1029/2003JC001897.

Zappa, C. J., W. R. McGillis, P. A. Raymond, J. B. Edson, E. J. Hintsa, H. J. Zemmelink, J. W. H. Dacey, and D. T. Ho (2007), Environmental turbulent mixing controls on the air-water gas exchange in marine and aquatic systems, *Geophysical Research Letters*, *34*(10), L10,601, doi:10.1029/2006GL028790.

Zappa, C. J., M. L. Banner, J. R. Gemmrich, H. Schultz, R. P. Morison, D. A. LeBel, and T. Dickey (2012), An overview of sea state conditions and air-sea fluxes during radyo, *Journal of Geophysical Research – Oceans*, *117*, C00H19, doi:10.1029/2011JC007336.

Zappa, C. J., M. L. Banner, R. P. Morison, and S. E. Brumer (2016), On the variation of the effective breaking strength in oceanic sea states, *Journal of Physical Oceanography*, *46*(7), 2049–2061, doi:10.1175/JPO-D-15-0227.1.

Zhao, D., and Y. Toba (2001), Dependence of whitecap coverage on wind and wind-wave properties, *Journal of Oceanography*, *57*(5), 603–616, doi:10.1023/A:1021215904955.

Zhao, D., Y. Toba, Y. Suzuki, and S. Komori (2003), Effect of wind waves on air–sea gas exchange: proposal of an overall co_2 transfer velocity formula as a function of breaking-wave parameter, *Tellus, Series B: Chemical and Physical Meteorology*, *55B*, 478–487, doi:10.1034/j.1600-0889.2003.00055.x.

Riverine skin temperature response to subsurface processes in low wind speeds

Adapted from: Brumer, S.E., C.J. Zappa, S.P. Anderson and J.P. Dugan (2016). Riverine Skin Temperature Response to Subsurface Processes in Low Wind Speeds, J. Geophys. Res. Oceans, 121, doi:10.1002/2015JC010746

A.1 Abstract

Both surface and subsurface processes modulate the surface thermal skin and as such the skin temperature may serve as an indicator for coastal, estuarine, and alluvial processes. Infrared (IR) imagery offers the unique tool to survey such systems, allowing not only to assess temperature variability of the thermal boundary layer, but also to derive surface flow fields through digital particle image velocimetry, optical flow techniques, or spectral methods. In this study, IR time-series imagery taken from a boat moored in the Hudson River estuary is used to determine surface flow, turbulent kinetic energy dissipation rate, and characteristic temperature and velocity length scales. These are linked to subsurface measurements provided by in situ instruments. Under the low wind conditions and weak stratification, surface currents and dissipation rate are found to reflect subsurface mean

flow ($r^2 = 0.89$) and turbulence ($r^2 = 0.75$). For relatively low dissipation rates, better correlations are obtained by computing dissipation rates directly from wavenumber spectra rather than when having to assume the validity of the Taylor hypothesis. Furthermore, the subsurface dissipation rate scales with the surface length scales (L) and mean flow (U) using $\varepsilon \propto \frac{U^3}{/} L(r^2 = 0.9)$. The surface length scale derived from the thermal fields is found to have a strong linear relationship ($r^2 = 0.88$) to water depth (D) with (D/L) $\sim$ 13. Such a relation may prove useful for remote bathymetric surveys when no waves are present.

A.2 Introduction

In alluvial and coastal waters, turbulence is driven both by wind forcing at the air-water interface and friction at the bottom boundary layer. In such environments, tidal flow enhances near-surface turbulence through shear over topography and can be the dominant driver of turbulent kinetic energy in low to moderate wind regimes [*Zappa et al.*, 2003, 2007]. In a shallow, weakly stratified water column, bottom generated turbulence may propagate to the surface and result in distinct coherent features observable at the surface under low wind conditions. When winds exceed $\sim$5 m s^{-1} and the tidal flow is low, winds become the dominant driver of turbulence in the upper boundary layer and the air-water interface is dominated by wind stress and other near-surface secondary flows such as Langmuir circulation [*Leibovich*, 1983; *Melville et al.*, 1998; *Veron and Melville*, 2001].

The large-scale surface signatures of bottom-generated turbulence are termed boils. They are thought to be produced by upwelling water which, upon impinging on the surface, spreads radially. Boils are discernable in visible imagery as the upwelled water is sediment laden. They are also associated with regions of increased bubble concentration and can be detected in sonograph images [*Nimmo-Smith et al.*, 1999].

Observations of boils have been reported both for relatively shallow rivers [*Jackson*, 1976; *Talke et al.*, 2013] and the shallow tidal North Sea [*Nimmo-Smith et al.*, 1999]. The analysis of

bottom-generated turbulence over riverbeds dates back to shortly after World War II [*Matthes*, 1947]. It has since been recognized that large-scale vortical motions are omnipresent forms of turbulence in rivers and estuaries. The evolution of an ideal turbulent eddy in the wall region of a turbulent boundary layer was described by *Allen* [1985]. In turbulent boundary layer flow, velocity increases away from solid boundary and momentum in continuously exchanged from the outer flow towards the boundary. At the wall, low momentum fluid is periodically gathered into coherent structures which are subsequently pulled or thrusted upward into the faster outer current. As the upper portion moves faster than that near the bed, the coherent structure becomes wedge shaped. As it grows in height, the fluid in the lower lee is increasingly sheltered and the coherent structures are increasingly sheared. Viewed from above, the coherent structure resembles an elongated horseshoe or hairpin with the center portion that is the farthest from the boundary moving the fastest and furthest and the flanks being carried forward less rapidly. The generation of coherent structures and boils over river dunes is reviewed by *Best* [2005].

Bubble or dye injection experiments showed evidence of vertical streaks in the innermost turbulent boundary layer [*Grass*, 1971; *Kline et al.*, 1967]. These low speed streaks are locally and intermittently subject to a cyclic process described as bursting [*Kline et al.*, 1967]. The burst cycles generated in the bottom boundary layer have been described in two comparable conceptual models [*Offen and Kline*, 1975] illustrated in Figures 1 and 2 in *Jackson* [1976]. In these models, the boundary layer is subdivided in an inner zone and an outer zone. The outer region can be further subdivided into zones of uniform momentum or into an intermediate region and a surface influenced region [*Adrian et al.*, 2000; *Hurther et al.*, 2007; *Nezu and Nakagawa*, 1993].

The majority of the turbulence is produced in the inner zone in which the innermost viscous layer is made of low speed streaks that are periodically lifted up by transverse vortices that arise from the high flow shear at the boundary between the zones. The lifted streak grows, as do the vortices, until it breaks up creating a burst. Being a buffer layer process,

the bursting phenomenon involves inner scales that are an order of magnitude smaller than outer scales [*Hurther et al.*, 2007]. *Heathershaw* [1974] made measurements of near bottom turbulence in the Irish Sea and showed evidence of bursts in time series of turbulent velocity fluctuations. *Matthes* [1947] labeled the upward-tilted stream wise vortices that arise from bursts as "kolks". These kolks ultimately result in boils when reaching the surface.

Differing views have emerged as to the evolution of the vortices or eddies after their generation. *Yalin* [1992] suggested that these grow almost to the vertical extent of the water column before breaking up into new eddies whereas *Shvidchenko and Pender* [2001] reported depth scales eddies which remain frozen in the flow. Whether there is cyclic growth and destruction of eddies leading to surface velocity fluctuations or whether these arise from ordered sequences of 3-D eddies moving with the bulk flow has important implications as to the relation between surface scales, depth and velocity as well as surface renewal.

How the turbulence generated at the river bed affects the water column and subsequently the surface determines the nature of the surface indicators detected by remote sensing. There is extensive literature on bottom-generated turbulence and free stream turbulent near plane boundary, especially with regards to sediment transport [e.g. *Gordon*, 1975; *Grass*, 1971; *Matthes*, 1947; *Vanoni and Hwang*, 1967]. Most studies rely on visual observation and only recently have efforts been made to link bottomgenerated turbulence to InfraRed (IR) observations [*Chickadel et al.*, 2011; *Talke et al.*, 2013; *Zappa et al.*, 2003].

IR imagery allows for measurements of the skin temperature. The skin temperature is governed by both surface and subsurface processes. The net air-water heat flux typically leads to a cooler thermal boundary layer (TBL) compared to the underlying bulk layer. Even a modest net surface heat flux leads to a detectable IR signal, which makes IR remote sensing possible both during day and night. In the open ocean, the temperature difference skin and the interior is typically 0.28℃ [*Katsaros*, 1980; *Liu and Businger*, 1975; *Saunders*, 1967]. Turbulent motions resulting from wind forcing at the air-sea interface and from turbulent eddies generated within the water column, disrupt the TBL, mixing it with the bulk layer. In

the open ocean, surface temperature modulation can be associated with large scale processes such as surface and internal gravity waves [*Farrar et al.*, 2007; *Veron et al.*, 2008; *Zappa and Jessup*, 2005]. In channel flows such as estuaries or river, a variety of phenomena lead to disruption of the TBL and even total removal of the TBL for short periods of time [e.g., *Zappa et al.*, 2004; *Chickadel et al.*, 2009; *Plant et al.*, 2009; *Smith et al.*, 2001]. The large surface divergence associated with boils leads to disruption of the TBL.

Here we aim to infer characteristics of subsurface turbulence and bulk water properties from skin temperature measurement. The study is based on infrared imagery recorded at nighttime under low wind conditions from a barge in the Hudson River. A strong relationship between surface length scales derived directly from infrared imagery and water column depth is shown to exist under low wind conditions when the TBL is dominated by bottom-generated turbulence. Under such conditions, we find surface velocities derived from IR time-series imagery correspond to subsurface current velocities. Furthermore, we find turbulent kinetic energy dissipation rates calculated directly from wavenumber spectra of surface velocity fields correlate with subsurface dissipation rates. Finally, we show how subsurface dissipation may be inferred from surface currents and length scales. The paper is organized as follows: the study area and field campaign is briefly described in the methods section; the methods section also contains the data processing procedure; results are described in section A.4 and discussed in section A.5.

A.3 Methods

A.3.1 Study Area

The field campaign was undertaken in the Hudson River estuary on the nights of 18 and 19 November 2010. The study area, shown in Figure A.1, was located by the State Line Lookout in the Palisades Interstate Park, NJ, ∼32 km north of Manhattan. The data collection was made outside of the tidal channel, in a region of relative uniformity over a muddy riverbed,

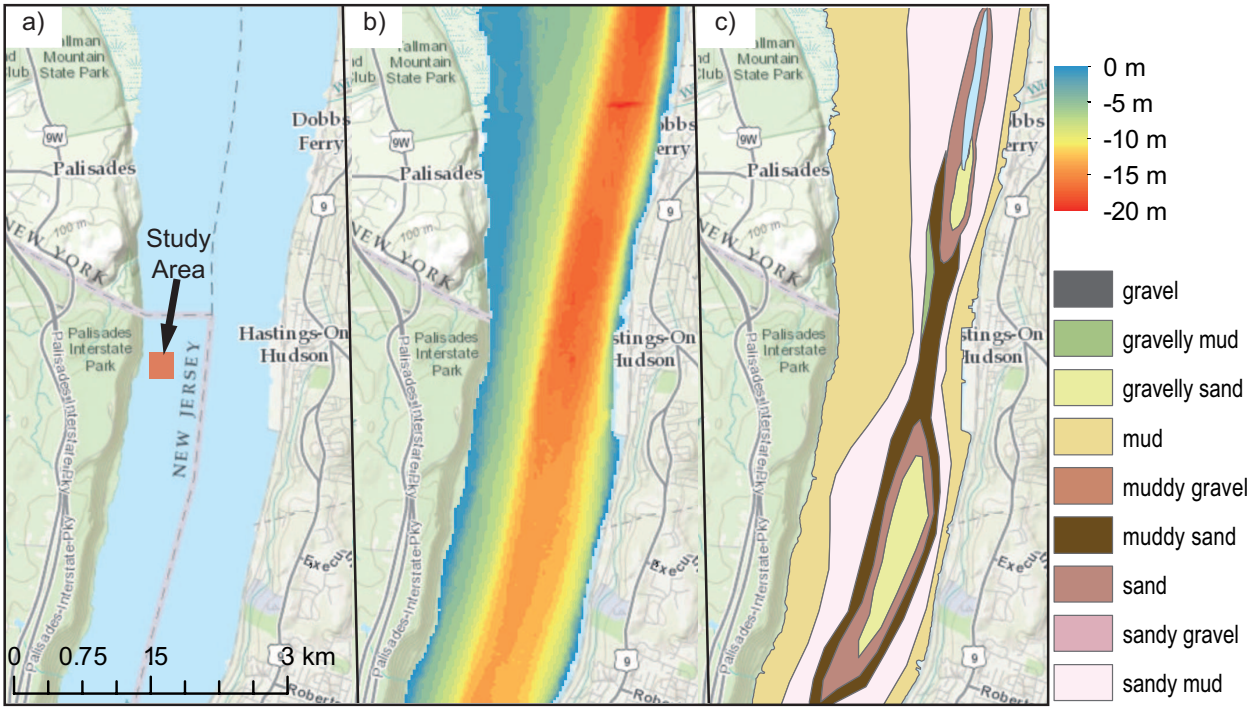

Figure A.1: (a) Map of the Hudson River estuary. The study area is highlighted in red. (b) Bathymetric map derived from soundings collected between 1930 and 1945, and fed into a Digital Elevation Model with 30 m resolution by NOAA. (c) Map showing riverbed sediment types determined from interpretation of sediment size measured from cores and grabs by *Bell et al.* [2006].

where the water depth, inferred from the pressure sensors of subsurface instruments, varied between 3.8 and 5.2 m during the survey period. Higher resolution bathymetry (not shown) confirms lack of bed forms in the study region. The Hudson River estuary is microtidal with a semidiurnal tidal range of ∼1.4 m and tidal currents of ∼1-2.5 m s^{-1} (values at Dobbs Ferry, taken from http://tidesandcurrents.noaa.gov/). The mean tidal discharge varies from about 12,000 m^3s^{-1} at The Battery where the Hudson flows into New York Harbor to zero at Troy [*Abood*, 1974]. River discharge estimates are only available in the freshwater part of the Hudson, the southernmostbeing below Poughkeepsie (USGS 01372058), where the discharge was of 991 m^3s^{-1} on the 18th and 728 m^3s^{-1} on the 19th.

A.3.2 Data and Instrumentation

A series of 10 min IR videos were taken of the river surface from a crew boat (Marguerite Miller, from Miller's Launch) moored in proximity of a pilling on which various instruments

were mounted. The IR data were collected every 30 min between 0100-0600 UTC on the 18th (year day 322), and 0400-1000 UTC on the 19th (year day 323) amounting to a total of 23 runs. Surface and subsurface in situ instruments mounted on the piling provided measurements of environmental parameters such as wind speed, heat fluxes, air and water temperatures, humidity as well as subsurface currents, turbulence, and salinity (Figure A.2).

The IR camera used, was a CEDIP Jade III longwave (7.7-9.3 μ m) camera which was mounted on a pan/tilt system on the A-frame of the moored ship. This setup permitted movement of the camera with the current as to always have a vantage point upstream of the ship. The camera was mounted at $\sim$5.5 m above the water level with and incidence angle of about 258. An Xsens IMU (Inertial Measurement Unit) mounted on the pan/tilt system next to the camera measured the roll and pitch of the boat motion at a frequency of 10 Hz, allowing for projection correction. The field of view angles of the camera are 21.78×16.48 giving an image area of 4.57 m^2 with an average pixel size of 0.59 cm^2. The CEDIP Jade III offers better than 15 mK temperature resolution, 14 bit digitization, and 320×240 pixels resolution. The sampling frequency was set to 60 Hz. The atmospheric boundary layer was measured with a Campbell air-sea flux package. This meteorological station was mounted on the piling neighboring the ship at a height of 7.5 m above the river bed. It provided measurements of wind speed and direction, relatively humidity, atmospheric pressure, air temperature, solar insolation, and downwelling longwave radiation. In situ subsurface instrumentation (Figure A.2) consisted of among others a 2 MHz Nortek model Vector ADV, mounted on the aforementioned piling at 3.35 m above the riverbed. The ADV collected data in 10 min bursts at the top of every 1/2 h, with a sampling frequency 32 Hz. Additionally, two high resolution 2 MHz Nortek model Aquadopp profilers were mounted on the piling at 0.91 m and 1.83 m above the riverbed. The Aquadopps measured velocity fluctuations along three beams with a 25 mm spatial resolution over 0.75 m. The two horizontal beams were nominally at 45° from the mean flow. The profilers collected data in 59 min bursts at the top of every hour, with a sampling frequency 2 Hz. Currents were

also measured by a bottom-mounted upward-looking 1200 kHz RDI ADCP. The ADCP was located 35 m to the northwest of the pilling. The ship remained within 130 m of the pilling and 100 m of the ADCP during data collection. The ADCP provided velocities over vertical bins are 25 cm apart, starting at 81 cm above the riverbed at a frequency of 1 Hz. 2 CTDs were mounted on the piling at 99.4 cm (3") and 3.35 m (11") above the river bed, sampling at 0.5 Hz. CTD profiles were also taken from the side of the barge before and after each IR video. All instruments mounted on the piling were oriented toward the middle of the river channel and were never in the wake of the piling under any flow conditions.

A.3.3 Surface Current Retrieval

Surface velocity fields were been determined by two approaches:

1. Feature tracking or Digital Particle Velocimetry (DPIV)

2. From the advective surface in 3-D spectra of the skin temperature (SAS)

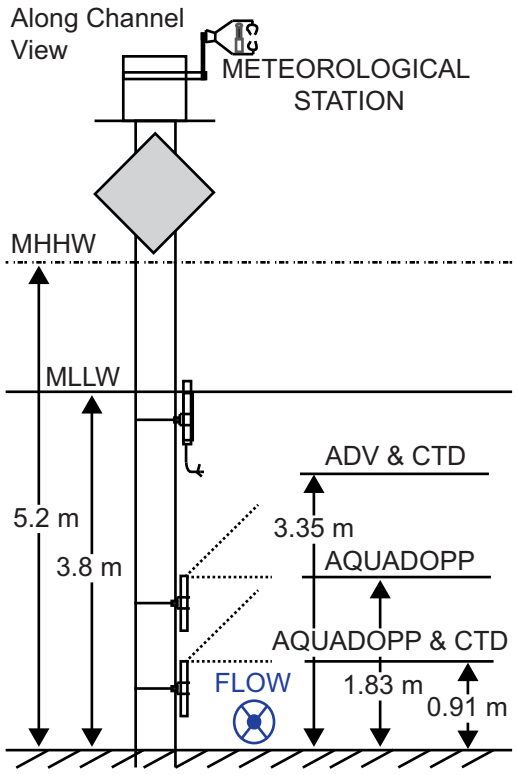

Figure A.2: An along channel schematic of the in situ instrumentation set up on the pilling.

The feature tracking DPIV method is based on 2-D spatial cross-correlations ($\phi_{fg}(x,y) = \sum_{i=0}^{I-1}\sum_{j=0}^{J-1} f(i,j)g(x+1,y+j)$) between 16 $\times$ 16 pixels correlation windows in a first frame and 32 $\times$ 32 pixel search window in a second frame. The two frames are consecutive, taken 1/10th of a second apart. Velocities are determined on nodes spaces eight pixels apart in the x and y direction. The distance between the centers of the windows and the location of the maximum cross-correlation (MCC) divided by the time between image A and B give the magnitude of the current speed and the vector connecting centers to MCC gives the direction of the displacement. The location of the MCC is approximated with two 3-point Gaussian curve fits, one in each direction so as to improve the subpixel accuracy. MCC-based surface current retrievals from IR time-series imagery have been shown to be successful in riverine environments [e.g., *Puleo et al.*, 2012; *Dugan et al.*, 2014]. Performing the cross-correlation in the spatial domain is numerically more intensive than computing it in the frequency space via a Fast Fourier Transform. However, it is more accurate and flexible [*McKenna and McGillis*, 2002].

The advective surface approach is based on *Dugan and Piotrowski* [2012] method. They showed how to determine the surface flow magnitude and direction by fitting the 2-D planar surface, which arises from advective variance detectable in 3-D spectra of airborne visible imagery. Computing 3-D spectra of the every 3000 frames of each run, the advective signal is clearly visible. For less than 3000 frames, the energy of advective signal tends to be too low. A linear least square fit of the advective surface in wavenumber frequency slices of the 3-D spectra was performed at various angles relative to the image. The slope of the linear fit is the magnitude of the advection at a given angle. Fitting a cosine function to the obtained magnitudes as a function of angle, we determine the magnitude and direction of the surface flow as the maximum of the fit and the corresponding angle.

A.3.4 Turbulent Kinetic Energy Dissipation

The turbulent kinetic energy (TKE) dissipation rate e is estimated by fitting the inertial subrange of wavenumber spectra ($\Phi(k)$) with a $k^{5/3}$ slope following the Kolmogorov turbulence cascade which dictates that:

$$\Phi(k) = \alpha \varepsilon^{\frac{2}{3}} k^{-\frac{5}{3}} \tag{A.1}$$

where k denotes the wavenumber and a is a constant equal to 1.5. Wavenumber spectra were computed directly from both the IR-derived velocity fields and Aquadopp profiles (cf. FigureA.3). For time series measurement of velocities such as collected by ADVs, one has to make a further assumption before deriving TKE dissipation rates. Assuming that the frozen Taylor hypothesis is valid, i.e., that turbulent eddies remain unchanged while being advected by the mean flow, one can convert frequency spectra $S(f)$ into wavenumber spectra as follows:

$$\Phi(k) = S(f) \cdot \frac{\langle v \rangle}{2\pi}, \tag{A.2}$$

with $k = 2\pi f / \langle v \rangle$, where f is the frequency and $\langle v \rangle$ the mean velocity.

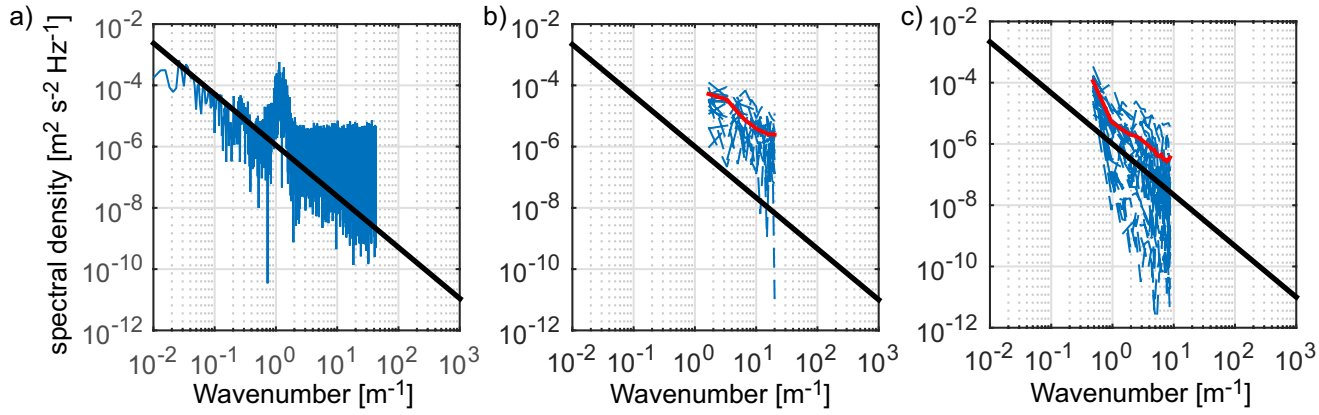

Figure A.3: Examples of wavenumber spectra computed from (a) the ADV, (b) the bottom Aquadopp, with individual profiles in blue and a 10 min mean in red, and (c) DPIV surface velocity fields, in blue for an individual row and in red a frame mean. The solid black line represents the $k^{-5/3}$ slope.

A.3.5 Surface Length Scales

Characteristic surface length scales are determined directly from the skin temperature imagery and from the DPIV velocity fields from which the frame mean velocity was removed. In order to do so, it is necessary to scale the imagery and transform the camera coordinates to water level coordinates. This is achieved through a rotation matrix using the roll, pitch, and yaw angles measured by the IMU as exemplified in Figure A.4.

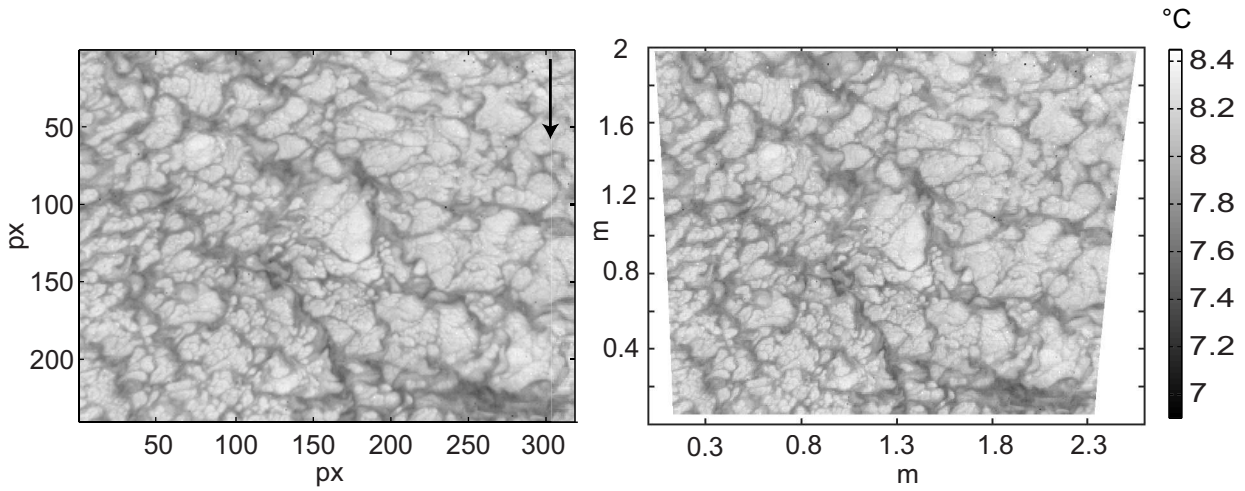

Figure A.4: a) An example of a calibrated IR image preprojection correction; the black arrow indicates the mean flow direction. (b) The same frame scaled and projected correctly.

From the scaled fields, normalized auto-covariance functions were computed for each row and column of each frame (an example of which is shown in Figure A.5). The normalized auto-covariance is given by:

$$C_{XX}(\delta) = \frac{\sum_{p=0}^{P-\delta} x(p)x(p+\delta)}{\sum_{p=0}^{P} x(p)^2} \tag{A.3}$$

where δ is the lag, P is the number of pixels in a row or column, and $x(p)$ is the temperature of a given pixel. For each frame, two mean normalized auto-covariance functions were subsequently computed, one for each dimension. Characteristic skin temperature length scales ($L1$ and $L2$) were determined as the distance at which the skin temperatures are

no longer correlated, i.e., corresponding to the smallest lag at which the frame mean auto-covariance function are equal to zero. From the DPIV fields, we first computed four length scales, one for each component of the velocity vector for both dimensions of the image which were averaged to give one single scale for each run.

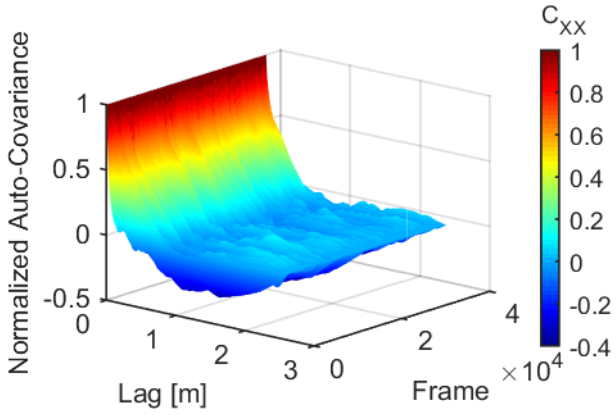

Figure A.5: Sample time series of the frame averaged normalized spatial autocovariance (C_{XX}) of the thermal imagery for various lags. The color map reflects the autocovariance.

A.4 Results

A.4.1 Environmental Conditions Including Surface and Subsurface Currents

IR measurements were taken under varying wind conditions, with 30 min average wind speed ranged from 0.12 to 3.62 m s^{-1} (Figure A.6). The wind speed averaged 2.29 ± 1.31 m s^{-1} on the night of the 18th (year day 322) and 1.06±0.67 m s^{-1} on the night of the 19th (year day 323). As a result, the momentum flux was much stronger on the 18th with a mean and standard deviation of 0.30±0.23 kg m^{-1} s^{-2}; on the 19th it only reached 0.13±0.08 kg m^{-1} s^{-2}.

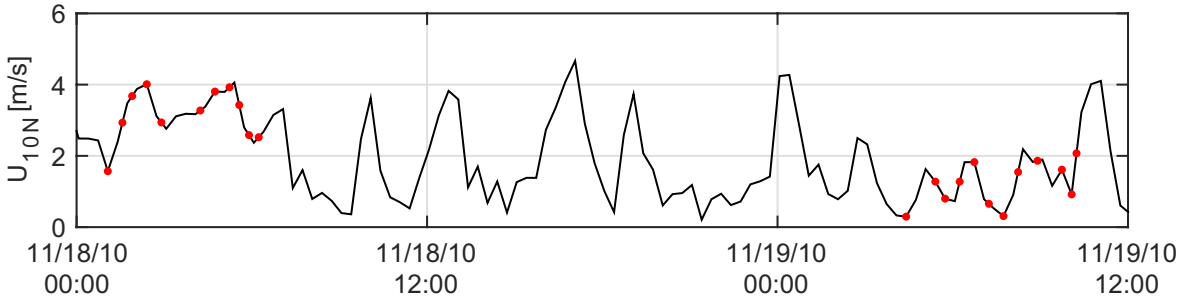

Figure A.6: Time series of the 20 min averaged U_{10} neutral measured by the meteorological station on the piling, the red dots represent the IR data collection periods.

Measurements coincided with the ebbing tide on the first night and low water to flood tide during the second night (Figure A.7a). An estimate of the bulk current speed was obtained by computing a column averaged velocity from the ADCP from the deepest bin (81 cm above the river bed) to the top good bin about 50–75 cm below the water surface. A time series of the column-averaged velocity is plotted in Figure A.7a and 10 min-averaged velocity corresponding to periods of imagery recording are reported in Table A.1. Over the time period IR imagery was recorded, the 10 min-averaged current speed measured by the ADCP ranged from 0.07 to 0.73 m s^{-1}. These strongly correlated to the 10 min average ADV measurements ($r^2 = 0.9$, cf. Figure A.8a). Even though one could expect the surface flow to be wind driven, the winds experienced were so weak that the surface velocities derived from the imagery match the column-averaged ADCP ($r^2 = 0.89$ for SAS and $r^2 = 0.82$ for DPIV, cf. Figure A.8b and A.8c) velocities and ADV velocities ($r^2 = 0.79$ for SAS and $r^2 = 0.71$ for DPIV). Surface currents matching subsurface flow may be expected in a tidally forced system in extremely low winds. The surface velocities were also found to correlate with the bottom ADCP measurements ($r^2 = 0.78$ for SAS and $r^2 = 0.68$ for DPIV). Both surface current retrieval methods agree very well with an $r^2 = 0.95$.

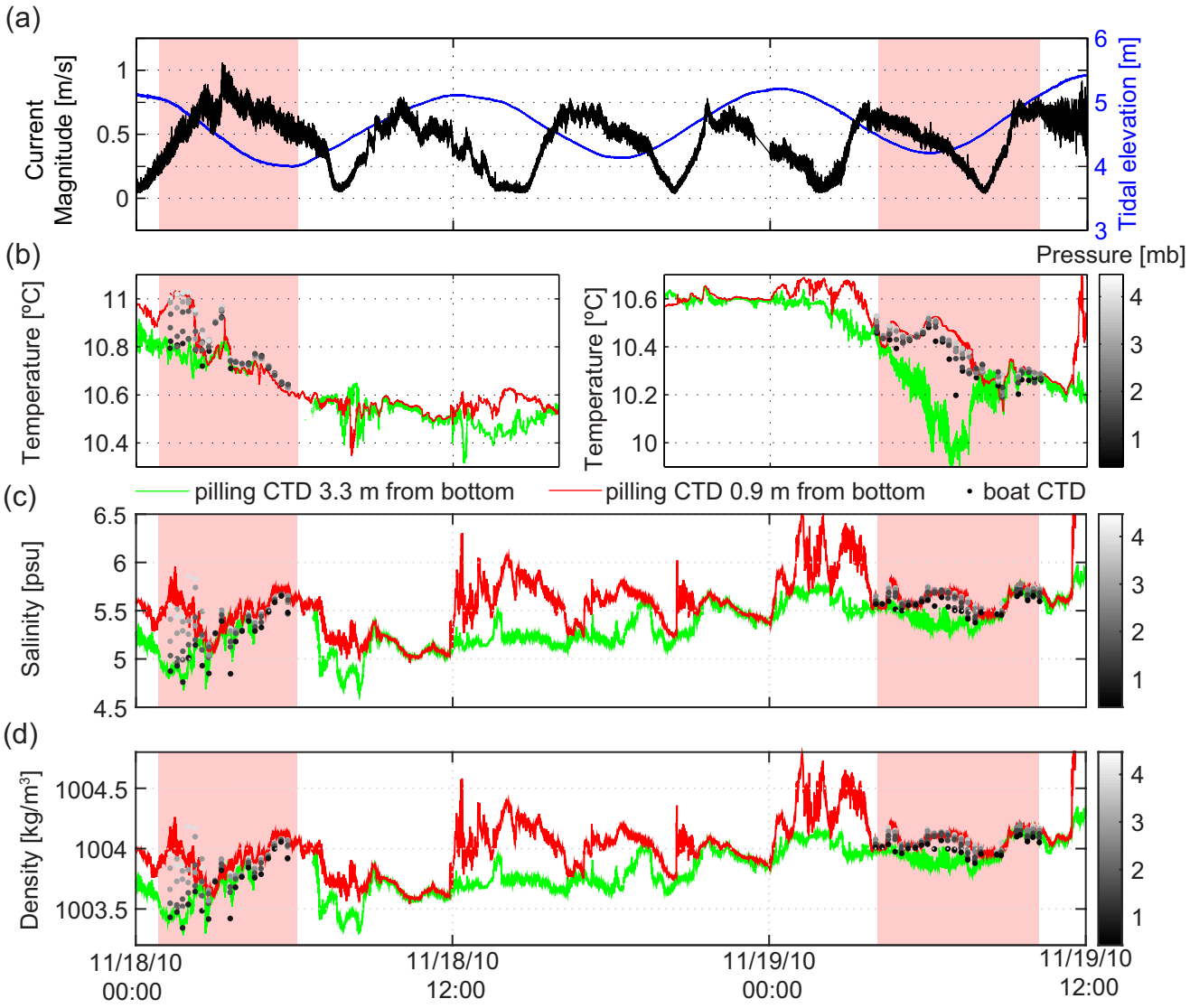

Figure A.7: Time series of (a) column-averaged currents and tidal elevation given by the ADCP, (b) measured temperature, (c) measured salinity, and (d) derived density from the two CTD mounted on the pilling at 3.3 (green) and 0.9 (red) meters from the bottom, respectively, as well as from the CTD profiles taken from the barge. The pink-shading delimits the periods of IR measurements. At the end of the first night and toward the middle of the second night, the surface CTD (mounted 3.3 m above the river bed) was out of the water leading to erroneous measurements which were excluded from the graphs.

U(m s^{-1})	U direction to	Depth (m)	Re	Re_T	L (cm)	$L1$ (cm)	$L2$ (cm)
0.27	W	5.05	1.35E06	1.07E05	40.1±5.6	26.8±5.5	53±8.2
0.56	W	4.27	2.38E06	1.85E05	33.1±5.3	30.5±5.1	35.5±8.3
0.41	W	4.23	1.72E06	1.29E05	31.7±6.1	24.5±5.2	39.2±8.5
0.31	W	4.29	1.33E06	8.68E04	28.1±5.8	21.8±4.4	34.8±0.6
0.2	W	4.37	8.75E05	6.81E04	34.1±7.9	29.8±5.6	38.4±12.8
0.07	W	4.49	3.12E05	2.35E04	34.0±8.0	30.5±4.9	37.6±12.9
0.29	NE	4.69	1.36E06	1.10E05	37.8±6.0	30.4±5.0	45.2±8.8
0.67	ENE	4.94	3.30E06	2.61E04	39.1±5.6	31±4.5	47±7.9
0.67	ENE	5.02	3.35E06	2.88E04	43.2±7.2	34.9±5.5	50.9±10.2
0.70	ENE	5.09	3.56E06	3.05E04	43.5±7.3	34.5±7.1	51.9±8.2

Table A.1: Table of the 10 min Column-Averaged ADCP Current Magnitude (U), Flow Direction, Depth (D), the Bulk Reynolds Number($Re = \frac{UD}{\nu}$), the Turbulent Reynolds Number ($Re_T = \frac{UL}{\nu}$), Mean Decorrelation Length-Scale (L), Mean Length-Scale Roughly Perpendicular to the Flow ($L1$) and Mean Scale Roughly Parallel to the Flow ($L2$).

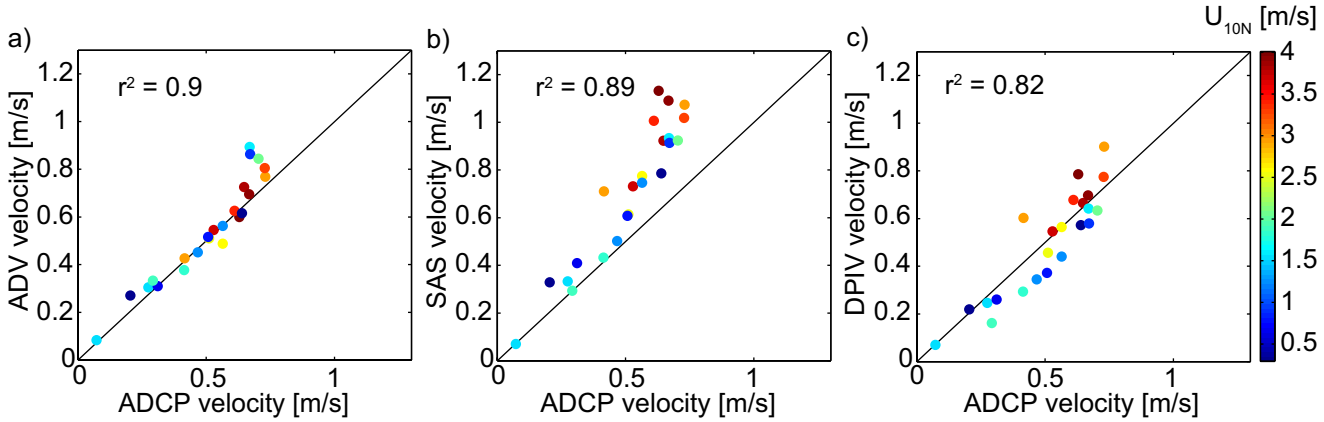

Figure A.8: Scatter plots of the run mean flow magnitudes derived from the ADCP versus the (a) ADV, (b) SAS, and (c) DPIV. The data are color-coded according to wind speed (U_{10N}). The 1:1 line is shown in black.

Subsurface turbulence was strong enough for the water column to be well mixed throughout the majority of the IR imaging measurement period as seen in Figure A.7. Only during the first couple of runs does, there appear to be a small degree of stratification (see Figure A.7d). The column mean Brunt-Vaisala frequency ($N = \sqrt{\frac{g}{\rho_0}\frac{d\rho(z)}{dz}}$) calculated during IR imagery was recorded was of 0.0327±0.0259 s^{-1} based on the pilling CTDs and of 0.0194±0.001 s^{-1} based on the CTD casts taken from the barge Figure A.9 shows the mean profile of N^2 (times 4) based on the CTD casts. Several data points and profiles were removed from the analysis as they correspond to periods of time when thermal reflections contaminated the infrared imaged surface temperature field. These data are excluded from data presented in Figures A.9-A.12. This eliminated all but the first run of the first night of measurements as well as two runs taken during the second night. Such low buoyancy frequency reinforces the idea of a weakly stratified water column. The Richardson number ($Ri = \frac{N^2}{\frac{du}{dz}^2}$) calculated from the pilling and boat CTDs and the ADCP was below the critical Richardson number of 1/4 throughout most of the survey. This is indicative of a turbulent flow regime where shear can overcome the stabilizing effects of the stratification. Only during the first three runs did the Ri go above critical; increasing from 0.4 in run 1-0.77 in run 2 and decreasing to 0.55 in run 3. The shear determined from the ADCP was relatively uniform within the water column; averaging 0.003 s^{-2} with signs of enhanced shear (0.005-0.013 s^{-2}) toward the bottom of the

water column (Figure A.9). Experimental set up did not allow for an estimate of the shear in the bottom boundary, the deepest velocity measurement being at 81 cm above the river bed.

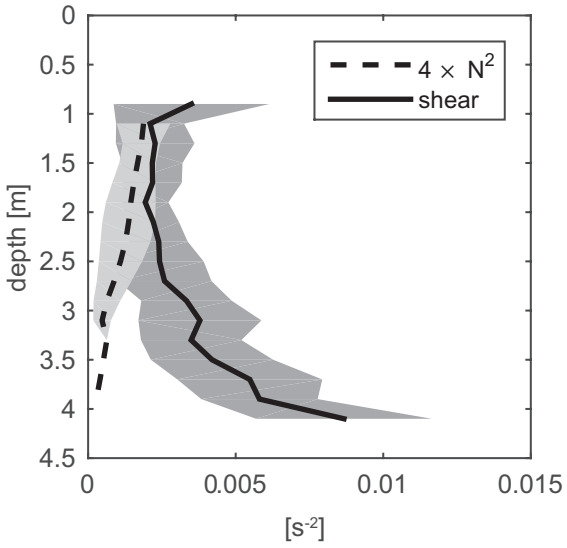

Figure A.9: Mean profiles of four times the buoyancy frequency determined from shipborne CTD casts (dashed line) and shear computed from the ADCP (solid line). The light and dark gray shadings indicate the one standard deviation bounds for the buoyancy frequency times 4 and the shear, respectively.

During the low water period on 18 November, the CTD mounted to the piling 3.3 m above the riverbed emerged above the water level and was exposed to the atmosphere leading to erroneous measurements. These were excluded from Figure A.7. The CTD profiles taken from the barge closely follow the measurements taken at the pilling confirming the horizontal homogeneity of the study site and the low level of stratification.

A.4.2 Turbulent Kinetic Energy Dissipation

Surface-derived TKE dissipation rates correlate with the subsurface dissipation rates (cf. Figure A.10). As described in section A.3.4, both DPIV and Aquadopp TKE dissipation rates were computed directly from wavenumber spectra, whereas the ADV TKE dissipation rates were derived from frequency spectra assuming the validity of the Taylor hypothesis of frozen flow. All runs with reflection have been discarded since they generate unreliable DPIV fields. Since the TKE dissipation rates range over several orders of magnitude, computing a

linear correlation coefficients gives a biased result reflecting mostly the tightness of fit of the higher values. In order to avoid that bias, correlation coefficients are reported for $\log_{10}(\varepsilon)$. The linear correlation coefficient is 0.59 between the surface εand the ADV εand 0.75 between the surface εand the Aquadopp mounted at 0.91 m above the river bed. The correlation coefficient between the surface εand the Aquadopp mounted at 1.83 m above the surface is of 0.38. The mostly strong correlation throughout the water column is expected due to the low stratification and low wind conditions described in section A.4.1

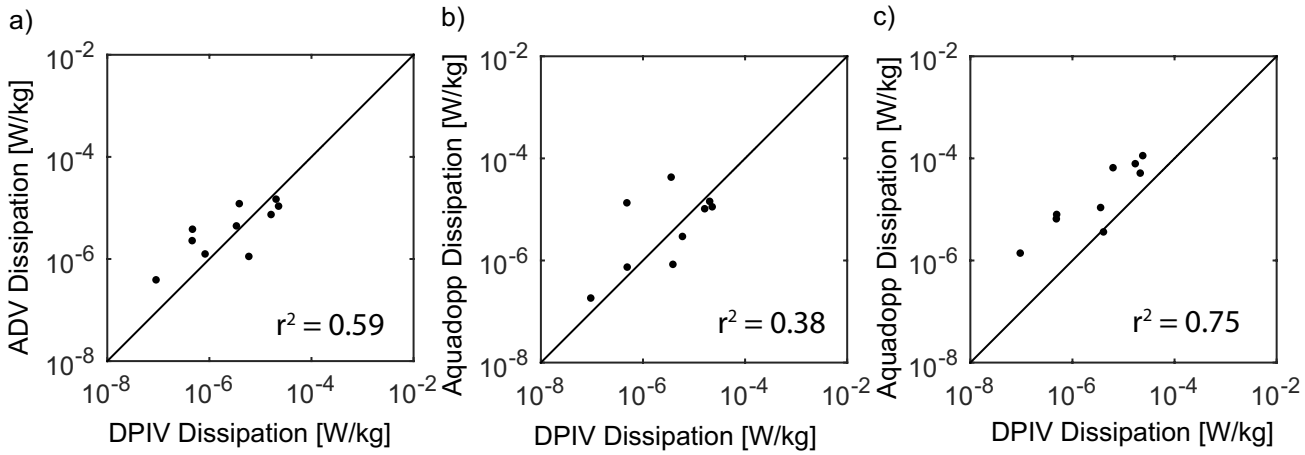

Figure A.10: DPIV-derived TKE dissipation rates versus (a) that from the ADV at 3.35 m above the river bed, (b) that from the bottom Aquadopp at 1.83 m above the river bed, and (c) that from the bottom Aquadopp at 0.91 m above the river bed. The 1:1 line is shown in black.

A.4.3 Surface Length-Scale Determined From Imagery and Correlation With Depth

As seen in Figure A.4, the river surface is covered by warm features, depicted in lighter gray, surrounded by colder, darker filaments. The warm skin temperatures result from bulk water brought to the surface. The scale of these macroturbulent features seem to remain relatively constant over the duration of the 10 min runs allowing for surface length scales to be defined. The warm features are slightly anisotropic, often elongated in the direction of the flow. In some videos taken during the first night, reflection from the A-frame can be seen in the imagery as a cold artifact. These videos coincide with the period of time when the water

column was more stratified and winds were stronger as noted in the previous section and are excluded from the subsequent analysis purely based on the presence of reflection.

For each run, a mean length scale was computed from $L1$ and $L2$. Figure A.11a shows a scatter plot of the length scales derived from the skin temperature fields versus water depth. The results show the scale of the surface features (L) is strongly linearly correlated ($r^2 = 0.88$) to the water depth (D), with a slope of (D/L) $\sim$ 13. As noted above, several outliers were excluded from this analysis and are not plotted in Figure A.11. These outliers correspond to periods of time when the water column was more stratified and reflections dominated the temperature field. The correlation is slightly stronger ($r^2 = 0.93$) with $L2$ which roughly corresponds to the direction of flow and weakly correlated with $L1$ ($r^2 = 0.37$).

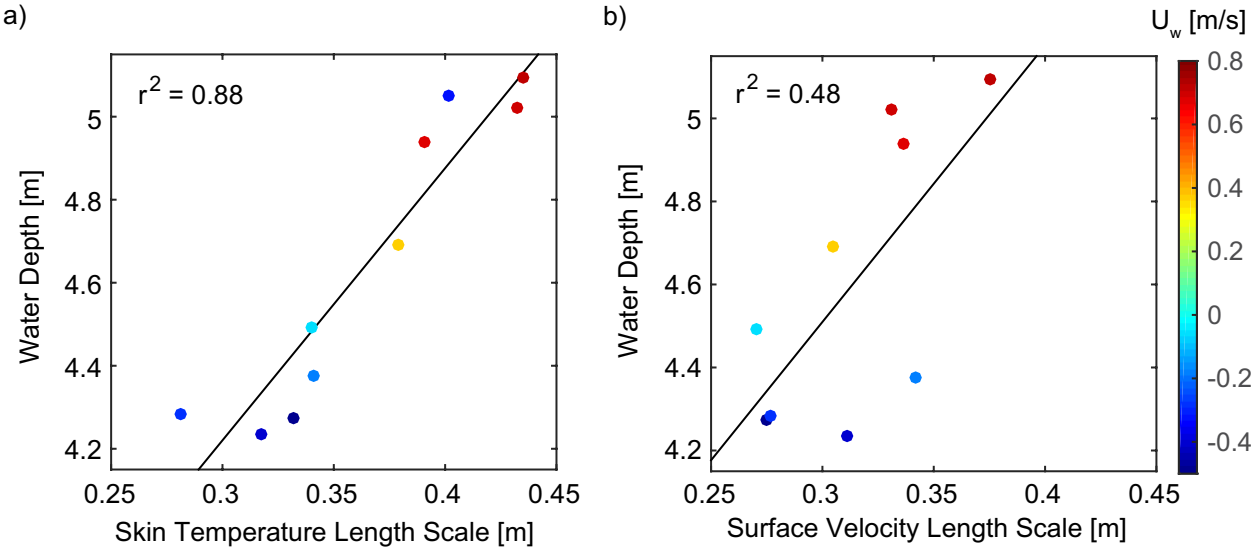

Figure A.11: Scatter plot of the surface scales derived from the spatial autocorrelation functions of (a) the skin temperature and (b) the DPIV velocity fields against height of the water column. The data are color-coded according to wind speed (U_{10N}) and the black line shows the linear fit.

Although the mean length scale derived from the DPIV increases with water depth (cf. Figure A.11b), the linear correlation is much smaller ($r^2 = 0.48$). On average, the mean DPIV scales are found to differ by $\sim$7 cm from the temperature scales. This can mostly be attributed to the difference in resolution of the fields used to determine the scales. Indeed, the temperature scale has a pixel resolution i.e. $\sim$0.8 cm, whereas the scale derived from the DPIV has a resolution of $\sim$6.4 cm.

A.4.4 Determining Subsurface Dissipation Rates From Surface Current and Surface Length Scales

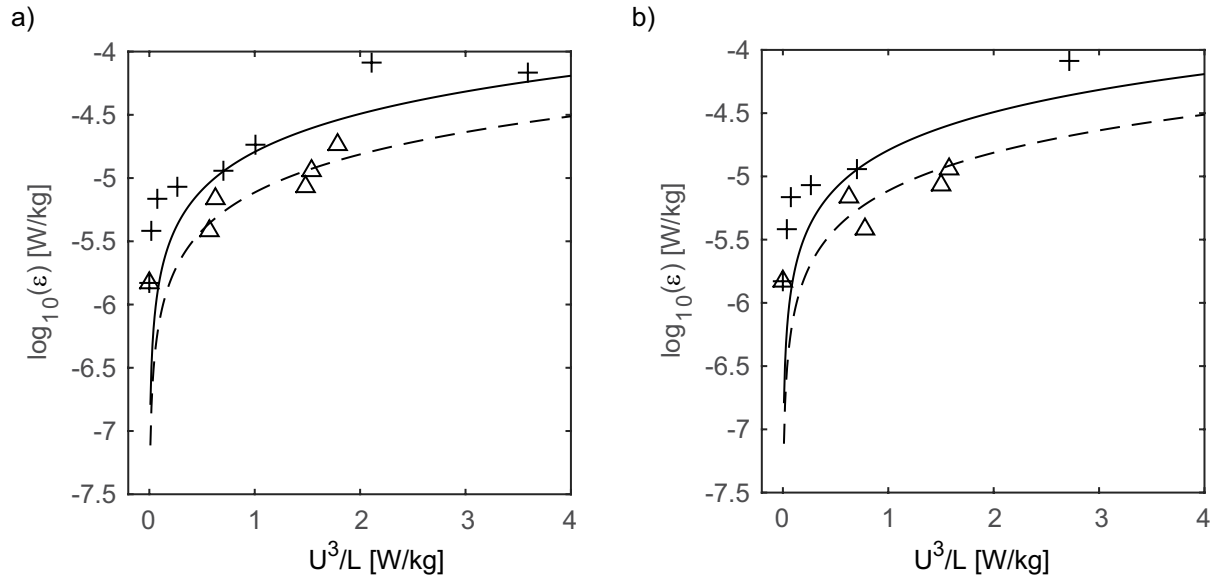

Figure A.12: Scatter plots of the dissipation measured by the bottom Aquadopp against U^3/L where U is the mean velocity derived from the SAS (triangle) and DPIV (plus) and L is the temperature length scale in (a) and the DPIV scale in (b). The solid and dashed lines show the best fit of the form $y = a \times x$ when using the DPIV and SAS velocity, respectively. The proportionality coefficient or slope to the best fit in Figure A.12a is 4.7×10^{-5} for SAS and 1.6×10^{-4} for DPIV and in Figure A.12b 3.9×10^{-6} for SAS and 1×10^{-4} for DPIV.

The turbulent kinetic energy dissipation rate can be estimated from the both the flow speed (U) and the dominant length scale in the flow (L). On the one hand, the dissipation rate equals the kinetic energy production rate which is proportional to U^2. One the other hand, the rate of kinetic energy supply can be thought as proportional to the inverse turnover time of large eddies: L/U. This implies $\varepsilon \sim \frac{U^2}{L/U} \sim \frac{U^3}{L}$ [*Tennekes and Lumley*, 1972]. As seen in Figure A.12, $\frac{U^3}{L}$ computed from surface length scales and surface currents is highly linearly correlated to εderive from the Aquadopp. Correlations are the strongest when using SAS velocities ($r^2 = 0.9$) and slightly lower when using DPIV ($r^2 = 0.82$) velocities. The strength of the correlation is comparable when the length scales derived directly from the temperature field or derived from the DPIV are used. Since the surface length scales L are

highly correlated to D (see FigureA.10), the correlations are comparable. Using DPIV mean flow, we get $r^2 = 0.8$ and using SAS mean flow we get $r^2 = 0.86$. Note that while L varies by about 50%, $|u^3|$ spans three orders of magnitude. Therefore, it is the velocity magnitude and not L that controls the large variation in the dissipation rate and explains the major part of the high correlations coefficients found here. Indeed a quick sensitivity test shows that keeping U equal to the mean flow measured throughout the experiment and letting L vary, the correlations drop to $r^2 = 0.16$, whereas keeping L constant and varying U keeps correlations high with $r^2 = 0.77 - 0.84$.

A.5 Discussion

This study shows a clear linear relation between the scales of the surface temperature features and the water column depth. It also demonstrates that subsurface TKE dissipation rate can be estimated from surface length scales and mean flow speed. The ability to successfully determine subsurface and bulk flow properties from surface data is likely due to the low wind and weak stratification experienced during the measurement period. The agreement between the IR-derived mean surface current and subsurface velocities as well as the surface and subsurface TKE dissipation rate estimates suggest that the system was dominated by bottom-generated turbulence that propagated through the water column. Therefore, the bottomgenerated turbulence governs properties of the TBL that are discernible in IR imagery. This is in agreement with the idea that in estuaries, under low wind conditions, turbulence is mainly tidally driven. Indeed, *Zappa et al.* [2007] showed that for winds <5.5 m s^{-1}, the TKE dissipation rate near the surface (<38 cm) varied with tidal current. Although there is an apparent correlation between the length scales and the wind speed ($r^2 = 0.35$), the limited data available does not allow us to separate the wind speed effects from the depth dependence. Also, note that the strongest winds occurred during high tide. While the wind and tide should be independent of each other, the data were taken when the tidal elevation

was highly correlated ($r^2 = 0.68$ in Figure A.11) to the wind.

Under quiescent wind, elevated upward heat fluxes at the air-water interface lead to free convection [*Handler et al.*, 2001; *Katsaros*, 1977; *Kudryavtsev and Soloviev*, 1985; *Volino and Smith*, 1999; *Zappa et al.*, 1998]. This typically occurs during the night time when the near surface water experiences strong cooling. Although being a less energetic process than shear, free convection leads to disruption of the thermal boundary layer, with Bernard cells clearly detectable in IR imagery. When free convection dominates, the TKE dissipation rate is proportional to the buoyancy flux [*Lombardo and Gregg*, 1989]. The buoyancy flux estimated from the flux data measured at the piling using the COARE3.5 algorithm was not found to be correlated to the TKE dissipation ($r^2 = 0.1$) .However, the TKE dissipation rate was found to strongly correlate to the shear production ($\overline{u'w'}\frac{du}{dz}$ where the prime indicate the turbulent components of u and w the horizontaland flow vertical components, respectively) computed from the ADCP ($r^2 = 0.92$ for the deepest Aquadopp and $r^2 = 0.75$ for DPIV derived ε). Calculation of the momentum flux $\overline{u'w'}$ was done via Reynolds decomposition of the velocity components for each good subsurface ADCP bin over 10 min periods corresponding to times of IR image recording. The momentum flux was then multiplied by the horizontal shear between the depth above and below each bin to get the shear production. From these shear production profiles, we determined that both the bottom and the top, and as well as column mean shear production, were all highly correlated to the TKE dissipation rate. The correlation values reported above are for the column mean shear production.

The bulk shear (U/D) was found to be highly correlated both with surface dissipation estimates from the DPIV ($r^2 = 0.8$) and subsurface dissipation estimates from the Aquadopp ($r^2 = 0.78$). However, the surface temperature length scales where found to be only weakly correlated to the bulk shear ($r^2 = 0.19 - 0.28$ with the lowest for $L2$ and the highest for L) and the shear production ($r^2 = 0.11 - 0.32$ with the lowest for $L1$ and the highest for $L2$).

It is important to note here that the spectral models for turbulence used to estimate the TKE dissipation rates in this paper hinge on the assumption of isotropy [*Kolmogorov*,

1991]. However, at the surface, the kinematic boundary condition specifies a zero vertical velocity across the material surface. As *Talke et al.* [2013] discuss in spectral models on the assumption of "approximate isotropy". IR remote sensing for studies of estuarine and riverine turbulence as such environments are ubiquitously turbulent. *Chickadel et al.* [2011] have shown that IR derived dissipation rates correlate with in situ measured near-surface dissipation rate. They validate IR-derived e with estimates from an ADV located 2 cm below the surface. While there were near surface dissipation measurements made during the current study, the surface estimates of dissipation are seen to reflect the deeper subsurface estimates of ε. *Chickadel et al.* [2011] made use of the Taylor hypothesis for the imagery estimates of ε, choosing to compute dissipation at a single location of the ADV at the surface. Our analysis suggests one can avoid having to assume the validity of the Taylor hypothesis. Our results show a strong correlation between surface and subsurface dissipation rate estimates from DPIV wavenumber spectra. Good correlation between DPIV dissipation rate estimates and near bottom ε is expected in a system dominated by bottom-generated turbulence. Surface modification of turbulence explains the order of magnitude difference between surface and near bottom ε. The lower correlation of midcolumn and surface $\varepsilon$is related to two high dissipation estimates of the Aquadopp. Recalculating the correlation coefficient without those outliers $r^2 = 0.89$.

Grid-turbulence experiments [*Batchelor*, 1953; *Sreenivasan*, 1984] in wind tunnels have provided evidence that at high Reynolds numbers, the TKE dissipation rate is independent of viscosity and when scaled by the integral length scale (L_i) and the root mean square velocity fluctuation (u') it is a constant of order unity: $C_\varepsilon \frac{u'}{L_i}$ with $C_\varepsilon = 1$. This is in agreement with the Richardson-Kolmogorov cascade at equilibrium. In a recent review, *Vassilicos* [2015] report growing evidence of a nonequilibrium region where the TKE spectrum has Kolmogorov's $-5/3$ wave number and C_ε is a constant that depends on types of flow and boundary condition independently of Reynolds number. Here we show evidence of εscaling as the cubed mean velocity rather than ${u'}^3$. This explains why the slopes in Figure A.12 are not

of order unity. Rather, the slope can be related to an interfacial drag coefficient. Assuming a wall layer scaling for ε, the law of the wall dictates:$\varepsilon = \frac{u_*^3}{\kappa z}$, where u_* is the friction velocity, κ the von K/'arm/'an constant, and z the vertical distance from the wall. The drag coefficient (C_d) is defined as: $u_*^2 = C_d U^2$, where U is the mean velocity. It follows that: $\varepsilon = \frac{u_*^3}{\kappa z} = C_d^{\frac{3}{2}} \frac{U^3}{\kappa z}$ or $\varepsilon = C_d^{\frac{3}{2}} \beta \frac{U^3}{L} = C_{\varepsilon B} \frac{U^3}{L}$, where $\beta = \frac{L}{\kappa z}$ and $C_{\varepsilon B} = C_d^{\frac{3}{2}} \beta$ the bulk C_ε or slope in Figure A.12. Figure A.11, suggests that L/z is a constant of $\mathcal{O}(10^{-2})$ giving a β of $\mathcal{O}(10^{-1})$. Assuming a typical C_d over mud of $\mathcal{O}(10^{-3})$ [*Gabioux et al.*, 2005; *Trowbridge et al.*, 1999], we derive a $C_{\varepsilon B}$ (or slope) of $\mathcal{O}(10^{-5} - 10^{-6})$ for the data reported here.

The weak stratification of the water column is propitious for the transport of bottom-generated turbulence to the surface that disturbs the thermal boundary layer. The discernible surface temperature features that result allow for the observed relationship between the surface length scales and depth. As the system is tidally driven, the water depth and tidal velocity are related and out of phase. This suggests that the length scales are also related to the tidal velocity. However, the picture is complicated because study area was located outside the main channel where the water level and tidal current vary out of phase with a varying lag. Furthermore, due to the limited space sample available in this study, the effect of tidal asymmetry between ebb an flood could not be explored nor the how very slow currents around slack tide affect the surface length scales.

The relation between length scales and depth is likely to vary with the degree of stratification and may break down above some threshold. Under higher wind conditions, one could expect properties of the TBL to show less signature of bottom-generated turbulence. In a wind-driven TBL, there may be no boils discernible in IR imagery and the surface length scales would likely not be related to the water column depth. More data under higher wind conditions are necessary to verify the above statement.

Imagery taken during periods of stronger winds had to be excluded from the analysis because it was contaminated by reflections generated from small-scale surface gravity waves. Furthermore, even during periods of "enhanced" stratification, the Ri was mostly below

0.25 meaning that the degree of stratification did not vary enough to assess its potential effects on the results reported here. Therefore, the data available for the present study does not span a large enough variety of environmental conditions to determine objective criteria for when the skin temperature no longer shows signatures of bottom-generated turbulence. These objective criteria will include dependence on tidal current, stratification, net heat flux, surfactants, and wind speed. Since the temperature features studied here are generated at the river bed by the shear of the overflowing water, these would be observed once the flow is strong enough. There is therefore likely a minimum flow ($<$7 cm s^{-1}, according the data presented here) below which the results reported here are no longer valid. One could assume that once the velocity threshold has been exceeded depth becomes the limiting factor controlling L. Note that due to the limited parameter space sample of this tidal current threshold cannot be determined. Based on the study of *Zappa et al.* [2003] and *Zappa et al.* [2007], one could assume the results no longer to be valid for wind speeds exceeding 5.5 m s^{-1}. As for the degree of stratification, a feasible criterion could be based on the Richardson number, with the relation between length scale and depth likely to not hold for Ri greater than a critical value (Ri_c) somewhere between 1/4 and 1. The critical Richardson number was first determined for steady, two-dimensional, stably stratified, horizontal shear flows of an ideal Boussinesq fluid by *Miles* [1961] and *Howard* [1961] who determined that such flows are stable for $Ri > Ri_c = 1/4$ everywhere in the fluid. However, multiple studies [*Abarbanel et al.*, 1984; *Geyer and Smith*, 1987; *Giddings et al.*, 2011; *Nepf and Geyer*, 1996; *Tedford et al.*, 2009] have found that Ri_c may be higher than the theoretical value and may lay anywhere between 0.2 and 1.0. Studying stratification in the Hudson River estuary *Nepf and Geyer* [1996] use $Ri_c < 0.4$ to indicate regions of potential mixing.

It is fair assume that scales observed at the surface may be as long as the water is deep. However it is important to note that the footprint of the IR imagery is only 2-3 m whereas the water depth is 4-5 m. This means that those larger scales are not captured in this study. Indeed, wavenumber spectra of the imagery (not shown) reveal no leveling or drop of energy at

the lowest wavenumbers observed, suggesting that there is significant energy at higher scales than those captured in our limited field of view. A much larger footprint would be needed such as can easily be obtained from airborne platforms. Analysis of ADV spectra showed inconsistent roll off at low wavenumbers but also hint to existence of turbulent scales larger than the field of view. Clear peaks were detected in a small number of ADV wavenumber spectra at length scales of $\mathcal{O}$(1-10 m), an example of which is seen in Figure A.3. This hints to the presence of subsurface coherent structures of similar scale as those detected at the surface.

The relation between the length scales and the water depth shown here differs in magnitude to that reported in previous studies. The scales reported here are decorrelation lengths and represent the radius of surface coherent structures rather than the diameter which is typically reported. Further discrepancies could be explained by the different origin of the signal observed. Here, a temperature signal is detected, whereas previous work was based on visual and acoustic observations of boil diameters or on flow visualizations of eddies and surface velocity field derived length scales. No boils were visually observed during the field experiment. This suggests that the scales reported here while being intrinsic scales of bottom-generated turbulence are unlikely associated with boils. Length scales associated with disruption of the thermal boundary layer, with counter-rotating vortices detected in the flow field, and with boils observed with the naked eye may differ significantly even though all signatures evolved from bottom-generated turbulence. As these scales all seem to be related to depth, it should be possible to find a unifying relationship between them. A first guess could be deduced from previous studies, but simultaneous observation would be required to verify it.

One could expect velocity scales related to boils scales to be half the temperature length scales. This is because the velocity anomaly will go to zero at the center of the boil and outside, while the temperature has a single minimum. Our data does not, however, show such a relation between the temperature and velocity scales. This is related to the inability to measure the largest integral scale given our limited image size. Early observations in the

Polomet River Russia, where depth varied 0.7 and 2.1 m [*Korchokha*, 1968] suggest that D/d lies between 3.7 and 1.75, where D is the water depth and d boil diameter. *Jackson* [1976] documented boils of up to 2-4 m diameter in lower Wabash River where depth ranged from 0.7 to 5.6 m, suggesting $D/d \sim 2.5$. *Nimmo-Smith et al.* [1999] reported boils in a well-mixed and tidal region of the North Sea where depth ranged from 17 to 33 m. Covering 20-30% of surface, the boil diameters seen in visible images were 1.04-1.44 times the water depth. They also determined boils size from an upward-pointing side scan sonar mounted on the sea floor, based on the backscatter of bubble accumulating in surface convergence. The diameters measured acoustically were around 0.93 times D.

Early flow visualization work by [*Klaven*, 1966, 1968; *Klaven and Kopaliani*, 1973] in a 0.05 m deep water columns, suggested the presence of eddies or stream wise counter rotating vortices with vertical scales equal to the water depth and lengths of 4-7 times the water depth for rough and smooth beds, respectively. Further flow visualization laboratory experiments by *Shvidchenko and Pender* [2001] performed in 0.025-0.1 m depth suggested an average eddy length of 4.5 times the water depth. In a more recent study, *Johnson and Cowen* [2014] computed the length scales associated with such eddies from visible imagery using PIV derived flow fields. They report the transverse and stream wise length scale as $0.5D$ and $2.5D$, respectively for water depth ranging from 10 to 30 cm.

Johnson and Cowen [2014] also showed that the length scale normalized by the flow depth is linearly dependent on the turbulent Reynolds number ($Re_T = \frac{UL}{\nu}$, where $U$is the current speed). The Hudson River data (cf. Table A.1) suggest a weak linear correlation between L/D and Re_T ($r^2 = 0.44$). The correlation is equally weak ($r^2 = 0.45$) between L and the bulk Reynolds number ($Re = \frac{UD}{\nu}$). One could expect the surface features not only to depend on bulk water column properties, but also on surface generated turbulence, mainly on wind speed. However, under the low wind conditions experienced during this field experiment, variation in the wind only accounts for 35 percent of the variation in length scale.

Several factors affect the burst cycle and the evolution of subsequent coherent structures.

Bed roughness was found to affect the inner layer. *Grass* [1971] observed how rough beds lead to less copious wall streaks. However, periodic energetic growth and breakups were observed over both rough and smooth beds. Multiple studies reported [e.g., *Matthes*, 1947] that the presence of suspended sediment leads to dampened turbulence. Whether suspended sediments would lead to less frequent or to smaller kolks and eddies traveling toward the surface could have significant impact on the surface signature of bottom-generated turbulence and potentially alter the proportionality factor between surface length scales and water column depth. Finally, surface waves and especially breaking wave overwhelm less turbulent structures of bursting. In such unsteady flow fields, bursting and its surface signature may not be recognizable.

A.6 Conclusion

The strong linear relation between surface length scale determined from IR imagery and water column depth is a promising result and should be explored further in a variety of environments. The ability to remotely derive bathymetry is also valuable for estimating river discharge as suggested by *Johnson and Cowen* [2014]. Using IR imagery offers an advantage over visible imagery as it has been shown that DPIV and SAS algorithms can directly be applied to the IR imagery to get surface velocities without needing to seed the water. DPIV flow fields can be used to estimate surface dissipation rates from IR imagery. These surface dissipation rates estimate subsurface dissipation in tidally driven systems under low wind and weak stratification. Under such conditions, it is also possible to determine subsurface dissipation rates from surface length scales and a mean flow using $\varepsilon \sim \frac{U^3}{L}$. Although imagery analyzed here was taken from a barge, the methods used can easily adaptable to a variety of potential platforms including helicopters, aircraft, and unmanned air systems, as well as fixed platforms.